Magneto-Rayleigh–Taylor instability in resistive liquid metals

Paria Makaremi–Esfarjani

Department of Mechanical Engineering

McGill University, Montreal

August, 2024

A thesis submitted to McGill University

in partial fulfillment of the requirements of the degree of

Doctor of Philosophy

To my mother, Maryam.

Also, to all the fearless women in my country, Iran, fighting for their rights and freedom.

برای زن، زندگی، آزادی

Abstract

The use of an imploding shell to compress plasma into a high-energy-density state is a viable pathway toward attaining fusion energy. Magnetized target fusion, for instance, achieves the necessary high temperatures and densities for a fusion reaction by dynamically compressing the initially formed plasma through the inward motion of a liquid-metal liner. Similarly, magnetized liner inertial fusion utilizes a solid liner to compress an initially pre-heated and pre-magnetized plasma, bringing it to fusion conditions.

Despite differences in the underlying physics and engineering of these methods, they share a common concern: maintaining the stability of the liner interface during the compression. Any instability at the liner interface adversely affects the fusion reactor performance, destabilizing and contaminating the plasma, leading to lower energy production and plasma quenching. The magneto-Rayleigh–Taylor (MRT) instability is an important instability appearing at the liner interface and is of significant concern in such applications. This study focuses on better understanding the MRT instability growth and feedthrough in a resistive liquid-metal liner of finite thickness.

To achieve this objective, a novel level set-based two-phase solver for addressing incompressible ideal/resistive magnetohydrodynamics (MHD) flows is introduced. This solver is developed within the finite-difference framework. Initially, a second-order accurate two-phase incompressible solver is implemented for the hydrodynamic case, building upon previous efforts made in the literature. Subsequently, this solver is expanded to accommodate magnetic flows. The extended solver is extensively verified by employing different test cases, such as the deformation of ferrofluid droplets in both quiescent and shear flows, followed by an investigation of Rayleigh–Taylor instability in magnetic fluids.

The solver is further developed to solve the complete set of resistive MHD equations for two-phase incompressible flows in a two-dimensional, planar geometry. This computational capability is then used to examine the MRT instability growth and feedthrough in an initially magnetic-field-free liquid-metal liner surrounded by two lower-density regions. In the lower layer, a horizontal magnetic field is imposed, and the impact of the Alfvén number on the MRT growth rate is explored across various wavenumber values. The findings reveal that the stabilizing effect of the magnetic field is more pronounced for higher wavenumber values.

Additionally, the influence of magnetic diffusion on MRT growth is analyzed, indicating that considering the finite resistivity of the liquid liner leads to a higher MRT growth rate compared to the ideal scenario, thereby diminishing the stabilizing effect of the magnetic tension. The effect of resistivity is further investigated across different magnetic Reynolds numbers and wavenumbers, delineating the growth rate across regimes of pure hydrodynamics, ideal MHD, and resistive MHD. The results indicate that magnetic diffusion primarily affects the MRT growth rate for higher wavenumbers, while the effect of finite resistivity is mainly observed over a longer duration of instability development for smaller wavenumbers. Furthermore, it is demonstrated that decreasing the Alfvén number results in the faster emergence of the magnetic diffusion effect on the MRT growth rate.

Lastly, the feedthrough effect at the upper interface of the liquid liner is also studied across different regimes and wavenumbers. The feedthrough effect is shown to be more evident for higher wavenumbers. The effect of initially seeded perturbations at the upper interface on the MRT instability and feedthrough is also examined.

Résumé

L'utilisation d'une coquille implosive pour comprimer le plasma dans un état de haute densité énergétique est une voie viable pour atteindre l'énergie de fusion. La fusion par cible magnétisée, par exemple, permet d'atteindre les températures et les densités élevées nécessaires à une réaction de fusion en comprimant dynamiquement le plasma initialement formé par le mouvement vers l'intérieur d'un revêtement en métal liquide. De même, la fusion inertielle par revêtement magnétisé utilise un revêtement solide pour comprimer un plasma initialement préchauffé et pré-magnétisé, l'amenant ainsi aux conditions de fusion.

Malgré les différences dans la physique et l'ingénierie sous-jacentes de ces méthodes, elles partagent une préoccupation commune: le maintien de la stabilité de l'interface de la gaine pendant la compression. Toute instabilité à l'interface de la gaine affecte négativement les performances du réacteur de fusion, en déstabilisant et en contaminant le plasma, ce qui entraîne une baisse de la production d'énergie et une extinction du plasma. L'instabilité magnéto-Rayleigh–Taylor (MRT) est une instabilité importante apparaissant à l'interface de la gaine et constitue une préoccupation majeure dans de telles applications. Cette étude se concentre sur une meilleure compréhension de la croissance de l'instabilité MRT et de la pénétration dans une gaine liquide-métal résistive d'épaisseur finie.

Pour atteindre cet objectif, un nouveau solveur biphasique basé sur les ensembles de niveaux est introduit pour traiter les écoulements magnétohydrodynamiques (MHD) idéale et résistive incompressibles. Ce solveur est développé dans le cadre des différences finies. Dans un premier temps, un solveur biphasique incompressible précis au second ordre est mis en œuvre pour le cas hydrodynamique, en s'appuyant sur les efforts précédents réalisés dans la littérature. Par la suite, ce solveur est étendu pour prendre en compte les écoulements magnétiques. Le solveur étendu est largement vérifié en utilisant différents cas de test, tels

que la déformation de gouttelettes de ferrofluide dans des écoulements quiescents et de cisaillement, suivie d'une étude de l'instabilité de Rayleigh–Taylor dans les fluides magnétiques.

Le solveur est ensuite développé pour résoudre l'ensemble des équations MHD résistives pour les écoulements incompressibles à deux phases dans une géométrie plane bidimensionnelle. Cette capacité de calcul est ensuite utilisée pour examiner la croissance de l'instabilité MRT et la pénétration dans un revêtement liquide-métal initialement dépourvu de champ magnétique et entouré de deux régions de plus faible densité. Dans la couche inférieure, un champ magnétique horizontal est imposé et l'impact du nombre d'Alfvén sur le taux de croissance de la MRT est exploré pour différentes valeurs du nombre d'ondes. Les résultats révèlent que l'effet stabilisateur du champ magnétique est plus prononcé pour les valeurs élevées du nombre d'ondes.

En outre, l'influence de la diffusion magnétique sur la croissance de la MRT est analysée, indiquant que la prise en compte de la résistivité finie du revêtement liquide conduit à un taux de croissance de la MRT plus élevé par rapport au scénario idéal, diminuant ainsi l'effet stabilisateur de la tension magnétique. L'effet de la résistivité est étudié plus en détail pour différents nombres de Reynolds et nombres d'ondes magnétiques, délimitant le taux de croissance dans les régimes d'hydrodynamique pure, de MHD idéale et de MHD résistive. Les résultats indiquent que la diffusion magnétique affecte principalement le taux de croissance de la MRT pour les nombres d'ondes élevés, tandis que l'effet de la résistivité finie est principalement observé sur une plus longue durée de développement de l'instabilité pour les nombres d'ondes plus faibles. En outre, il est démontré que la diminution du nombre d'Alfvén entraîne une émergence plus rapide de l'effet de diffusion magnétique sur le taux de croissance de la MRT.

Enfin, l'effet de traversée à l'interface supérieure du revêtement liquide est également étudié dans différents régimes et à différentes hauteurs d'ondes. Il s'avère que l'effet de traversée est plus évident à des hauteurs d'ondes plus élevées. L'effet des perturbations initialement semées à l'interface supérieure sur l'instabilité de la MRT et l'effet de traversée est également examiné.

Table of Contents

Acknowledgements

I would like to begin this section by sincerely thanking my supervisor, Prof. Andrew Higgins, for all his unconditional support during my Ph.D. study. I am so grateful for all his invaluable advice and guidance, which tremendously helped me throughout my Ph.D. path (which turned out to be rather bumpy). I will always be appreciative of his patience and confidence in me and my abilities, and his constant exploration of ways to assist me during my Ph.D. research. I will always be in his debt, and I will carry all I learned from him not only in my future career path but also in my personal life.

I also want to thank Dr. Alireza Najafi-Yazdi for his valuable suggestions and feedback, especially on the implementation of the numerical solver. I appreciate all his help and support during my doctoral research.

My gratitude is also extended to Prof. Jovan Nedić for kindly having me as a member of his research group and providing me with helpful comments. I gratefully acknowledge all the useful discussions we had on different aspects of my research. Additionally, I thank my fellows in the McGill Fluids Laboratory, Dylan Caverly and Ivo Dawkins, for offering insightful input on my research.

Spending a six-month internship at General Fusion Inc. was an unforgettable experience during my Ph.D. It provided me with insight into the fusion world and helped me carve out my research question. For this, I thank my colleagues at General Fusion Inc. for making this experience as pleasant as possible, especially Meritt Reynolds, Peter de Vietien, and Colin McNally. I would also like to thank Jean-Sebastien Dick, Piotr Forysinski, and Nick Sirmas for their helpful discussions that contributed to this work. I owe a great debt of gratitude to Ivan Khalzov for his insightful comments and valuable guidance in defining the research problems to which I could contribute, as well as insightful discussions on the analysis.

I would like to express my gratitude to my parents for their unconditional support not only throughout my Ph.D. studies but also for encouraging me at every stage of my education since I was seven. They always went out of their way to ensure I reach my goals and become the best version of myself. Additionally, big thanks to my sister, Niloufar, who has always been there for me. Even during my lowest moments, when I would spend hours debugging my code, she cheered me up and gave me the energy to persevere. I also thank my brother-in-law, Nojan, for sending me humorous memes reminding me that I would eventually complete my Ph.D., worst case scenario, in my 50s! Additionally, I am grateful for all the friends that I found at McGill, who became my family here.

To my best friend and loving partner, Khashayar: Thank you for being my rock, my ride or die during every step of my doctoral study. I appreciate you for unconditionally supporting me and believing in me even when I did not myself. Thanks for tolerating me talking nonstop about my research (most of the time nagging, of course) and for all your useful comments on my work. Our discussions always helped me through this journey, and thanks for being my research teammate.

Contribution to original knowledge

The present work establishes a numerical examination of magneto-Rayleigh–Taylor (MRT) instability growth and feedthrough in a resistive liquid-metal liner of finite thickness. The specific aim is to analyze the effect of magnetic tension and diffusion on MRT instability growth in an initially magnetic-field-free liquid-metal slab. This investigation is performed by utilizing a novel numerical solver for two-phase magnetohydrodynamic (MHD) flows developed in this study. The primary contributions of this research follow:

- A novel level set-based two-phase incompressible solver for ideal/resistive MHD flows within the finite-difference framework is introduced. In the initial phase of development, a two-phase numerical solver for magnetic flows is presented. The accuracy and performance of this solver are extensively verified. Subsequently, the complete set of Maxwell's equations is incorporated into the numerical solver to accurately model the behaviour of perfectly conductive and finite resistive flows.

- The deformation of ferrofluid droplets in sheared flows across different susceptibility values is investigated, employing the implemented solver for magnetic fluids. It is shown that in low capillary regimes, increasing the magnetic susceptibility of a droplet leads to a more pronounced deformation. In higher capillary flows, increasing the magnetic permeability ratio between the droplet and the surrounding medium results in a more notable rotation and elongation, potentially leading to droplet breakup.

- The MRT instability and feedthrough of a liquid-metal liner are numerically examined across different Alfvén numbers and magnetic Reynolds numbers. The presence of an axial magnetic field decreases the MRT instability growth of the liner, especially for smaller Alfvén numbers and higher wavenumbers. The finite resistivity of liquid metal

is shown to diminish the stabilizing effect of the magnetic field compared to its ideal counterpart, in which the liner is assumed to be perfectly conductive. The effect of magnetic diffusion on MRT instability growth is found to be more evident for smaller magnetic Reynolds numbers and higher wavenumbers, while the effect of resistivity on the MRT growth for smaller wavenumbers appears in a later stage of instability development. The feedthrough effect at the upper interface of the liquid liner is also studied across different regimes, with or without initially seeded perturbations at this interface.

Contribution of authors

This dissertation consists of one published and one journal article in preparation. These papers are co-authored with my supervisor, Prof. Andrew J. Higgins, who provided guidance on numerical simulations, offered insightful comments, and reviewed the manuscripts. Additionally, my co-supervisor, Dr. Alireza Najafi-Yazdi contributed to the numerical simulation aspect of the first paper (Chapter 2). The work reported in this thesis is entirely the author's own. The following chapters correspond to the aforementioned manuscripts:

- **Paper 1 (Makaremi-Esfarjani *et al.*, 2023, Chapter 2)**: "A level set-based solver for two-phase incompressible flows: Extension to magnetic fluids", published in the International Journal of Computational Fluid Dynamics.
  https://doi.org/10.1080/10618562.2024.2334073

- **Paper 2 (Makaremi-Esfarjani & Higgins, 2024, Chapter 3)**: "Magneto-Rayleigh–Taylor instability and feedthrough in a resistive liquid-metal liner of finite thickness", published in Physics of Fluids as an *Editor's Pick*.
  https://doi.org/10.1063/5.0220816

The following conference proceedings also emerged from the material presented in this dissertation:

- Makaremi-Esfarjani, P. & Higgins, A. J. 2023 Numerical investigation of perturbation growth in a liquid metal liner slab using a level set-base two-phase solver. In *Proceedings of*

the 76th Annual Meeting of the APS Division of Fluid Dynamics, Washington, DC.
https://meetings.aps.org/Meeting/DFD23/Session/G23.4

- Makaremi-Esfarjani, P., Najafi-Yazdi, A. & Higgins, A. J. 2022 Modelling Surface Instabilities of Incompressible Nonconducting and Conducting Fluids. In *Proceedings of the 75th Annual Meeting of the APS Division of Fluid Dynamics*, Indianapolis, Indiana.
https://meetings.aps.org/Meeting/DFD22/Session/T15.7

- Makaremi-Esfarjani, P. & de Vietien, P. 2020 Coupled CFD/MHD Simulations of Plasma Compression by Resistive Liquid Metal. In *Proceedings of the 62nd Annual Meeting of the APS Division of Plasma Physics*, Online.
https://meetings.aps.org/Meeting/DPP20/Session/CP19.21

List of Figures

List of Tables

Nomenclature

This section lists the important nomenclature used throughout the study.

Roman Symbols

$\boldsymbol{A}$	magnetic vector potential
a	interface acceleration
$\boldsymbol{B}$	$= (B_x, B_y, B_z)$, magnetic flux density
c	speed of sound
D	deformation parameter
$\boldsymbol{E}$	electrical field intensity
E	energy
$\boldsymbol{F}_{\text{sv}}$	volume force
g	gravitational acceleration
$\boldsymbol{H}$	$= (H_x, H_y, H_z)$, magnetic field intensity
h	upper/lower layer thickness
h^*	dimensionless upper/lower layer thickness
$\boldsymbol{J}$	$= (J_x, J_y, J_z)$, electric current density
$\boldsymbol{k}$	$= (k_x, k_y, k_z)$, wavenumber vector

k^*	dimensionless wavenumber
$\boldsymbol{M}$	magnetization vector
m	mass
$\boldsymbol{n}$	$= (n_x, n_y, n_z)$, normal vector
p	pressure field
R	droplet radius
t	time
$\boldsymbol{u}$	$= (u_x, u_y, u_z)$, velocity field
$\boldsymbol{x}$	$= (x, y, z)$, spatial coordinate vector

Greek Symbols

$\dot{\gamma}$	shear rate
Δ	grid spacing
δ	liquid liner thickness
δ_{ij}	Kronecker delta
ϵ	level set thickness
θ	angle of rotation
κ	curvature
λ	wavelength
λ_{m}	magnetic diffusivity
μ	dynamic viscosity
μ_{r}	dynamic viscosity ratio ($\mu_{\mathrm{gas}}/\mu_{\mathrm{liquid}}$)

μ_{m}	magnetic permeability
$\mu_{\mathrm{m},0}$	vacuum magnetic permeability
ν	kinematic viscosity
ξ	perturbation amplitude
ρ	density
ρ_{r}	density ratio ($\rho_{\mathrm{gas}}/\rho_{\mathrm{liquid}}$)
σ	surface tension coefficient
σ_{e}	electrical conductivity
$\sigma_{\mathrm{e,r}}$	electrical conductivity ratio ($\sigma_{\mathrm{e,gas}}/\sigma_{\mathrm{e,liquid}}$)
τ	fictitious time
τ^{M}	Maxwell stress tensor
ϕ	signed distance level set
χ	magnetic susceptibility
ψ	level set
ω	growth rate
ω^*	dimensionless growth rate

Acronyms

Al	Alfvén number
AMR	arbitrary mesh refinement
At	Atwood number
$\mathrm{Bo_m}$	magnetic Bond number

Bo	Bond number
Ca	capillary number
CFL	Courant–Friedrichs–Lewy
CLSVOF	coupled-level-set and volume-of-fluid
CLS	conservative level set
CSF	continuum surface force
D − T	deuterium and tritium
GFM	ghost fluid method
HOUC	high order upstream central
HPLS	hybrid particle level set
ICF	inertial confinement fusion
LBM	lattice Boltzmann method
LULI	laboratoire pour l'utilisation des lasers
MagLIF	magnetized liner inertial fusion
MCF	magnetic confinement fusion
MHD	magnetohydrodynamics
MRT	magneto-Rayleigh–Taylor
MTF	magnetized target fusion
NASA	National Aeronautics and Space Administration
NRL	National Research Laboratory
NSTX	National Spherical Torus Experiment

PETSc	portable, extensible toolkit for scientific computation
PLMI	plasma/liquid-metal interface
$\mathrm{Re_m}$	magnetic Reynolds number
Re	Reynolds number
RLSG	refined level set grid
RM	Richtmyer–Meshkov
RT	Rayleigh–Taylor
SPH	smoothed particle hydrodynamics
TVD	total variation diminishing
VOF	volume-of-fluid
WENO	weighted essentially non-oscillatory

CHAPTER 1

Introduction

1.1 Background

There is a growing need for an energy production approach that is sustainable and practical while having a minimal environmental footprint. Fusion power holds great promise as an alternative energy source for fossil fuels. Fusion is the energy generation mechanism in which two light nuclei such as deuterium and tritium (D-T), hydrogen isotopes, undergo a reaction to produce a heavier nucleus. The mass of the resulting nucleus is less than the sum of the reacting nuclei. This mass difference is transformed into a large amount of energy, which can be computed using Einstein's equation $E = mc^2$*(Freidberg, 2014).

To initiate fusion reactions, positively charged nuclei need to overcome their mutual repulsion and get close enough to fuse via quantum tunnelling through the Coulomb barrier. Thermal fusion happens at significantly high temperatures, typically in the order of millions of Kelvin. At such high temperatures, any gas becomes ionized and forms a plasma (Boyd & Sanderson, 2003). Subsequently, the random thermal motion of heated reactants provides the necessary energy for fusion. For a self-sustaining thermonuclear reaction to occur, a sufficient density of reactant ions, i.e., hydrogen isotopes, must be confined at a desirable temperature for a specified duration, known as the Lawson triple product criterion (Lawson, 1957). Holding reactants for a sufficient amount of time allows for the self-heating of the plasma by energetic alpha particles, thereby sustaining the reaction. The Lawson criterion,

* Variables E, m, and c represent energy, mass, and the speed of light, respectively.

which comprises a fundamental requirement for achieving fusion burn, states that the rate of energy deposition into the plasma by alpha particles generated by the fusion reaction should exceed losses due to transport and radiation. In the field of fusion power, various approaches have been investigated, yet many technical issues need to be addressed to make fusion energy a viable energy source for commercial power plants.

1.1.1 Fusion approaches and challenges

Magnetized target fusion (MTF) is a fusion approach based on compressing the initially formed plasma target to fusion conditions using a conductive imploding surface (Robson, 1975). The MTF approach is the middle ground between the two conventional methods, namely, magnetic confinement fusion (MCF) and inertial confinement fusion (ICF). The MCF reactors use strong magnetic fields to confine the low-density plasma, while the ICF method is based on producing extremely high-density plasma using high-power laser beams (Boyd & Sanderson, 2003). However, in the MTF method, the medium-density plasma reaches the thermonuclear condition by increasing its pressure using compression, which can be achieved dynamically (Laberge, 2019). Siemon *et al.* (1999) concluded that MTF offers lower-cost reactors compared with other approaches. Using compression to heat the magnetized plasma targets to fusion conditions has been proposed in the literature many years ago. For instance, the Linus project conducted by the United States Naval Research Laboratory (NRL) made a seminal contribution in investigating the viability of using compression for heating the closed-flux magnetized plasmas (Miller & Krakowski, 1980; Turchi, 2008). The compression method has advantages compared with other proposed approaches since a high amount of energy can be delivered to plasma during compression, and therefore plasma temperature and pressure can increase effectively. Moreover, if a liquid lithium-lead flux conserver is utilized to compress the plasma, the liquid-metal blanket can be used to ad-

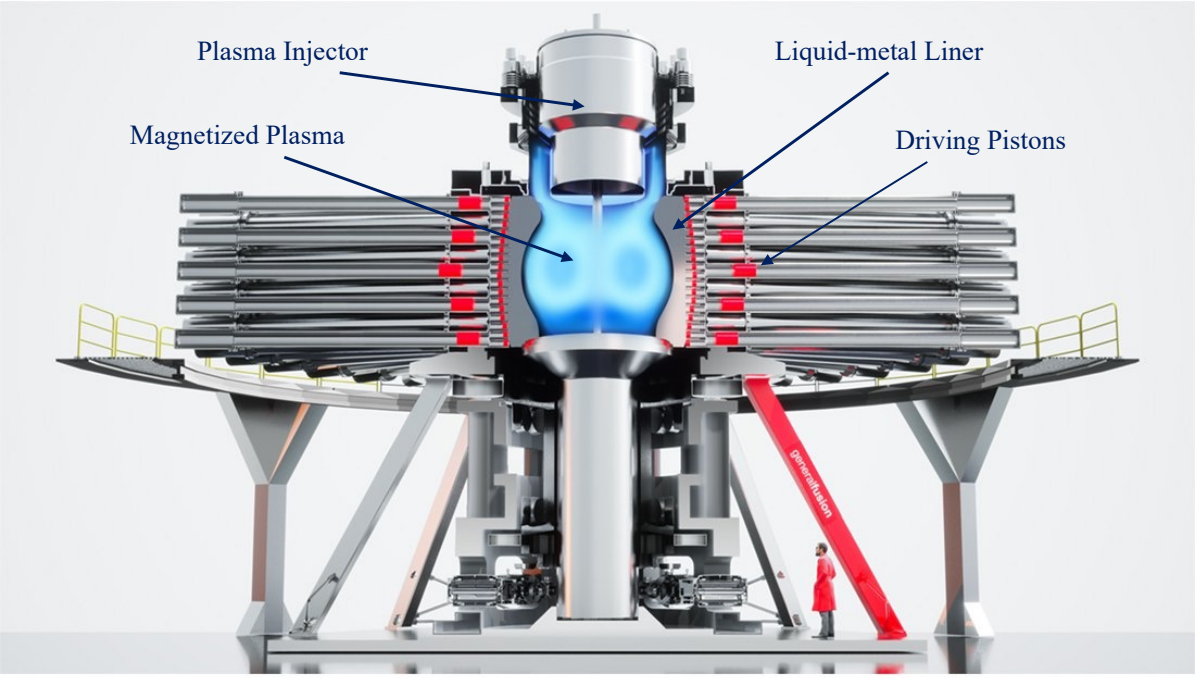

Figure 1.1: General Fusion's MTF reactor.

dress tritium breeding[†] and the *first wall problem*[‡], which are the common hurdles in fusion reactors (Brennan *et al.*, 2020).

Of particular interest, General Fusion Inc. is introducing a novel fusion reactor based on the MTF concept, shown in Fig. 1.1. In their fusion reactor, the initially formed *magnetized plasma* is introduced from a *plasma injector* into a cylindrical cavity formed by the rotation of a *liquid-metal liner*. Subsequently, the plasma is compressed to reach fusion conditions through the inward motion of the liquid-metal liner, facilitated by a system of *driving pistons* (Laberge, 2019).

One of the primary challenges in the MTF approach is maintaining the geometrical integrity of the imploding liner (Itoh & FUJII-E, 1979, 1980). As noted by Itoh *et al.* (1982) in investigating the stabilization of an imploding liquid-metal liner, two main mechanisms impair the geometrical integrity of the liner: (i) the Rayleigh–Taylor (RT) instability and

[†] Tritium fuel can be produced in fusion reactors as a result of lithium reacting with neutrons which are the products of the thermonuclear reaction.

[‡] The first wall problem refers to the damage to the inner surface of the reactor chamber caused by neutron bombardment at high temperatures, which could be avoided in the MTF approach where a liquid is used as the first wall.

(ii) cavitation formation induced by pressure waves (Itoh & FUJII-E, 1979; Itoh *et al.*, 1982). The aforementioned mechanisms result in liner disruption and plasma contamination. Many studies have suggested different solutions to overcoming these issues (Harris, 1962; Book & Winsor, 1974; Book & Turchi, 1979; Itoh & FUJII-E, 1979). For example, Book & Winsor (1974) concluded that using a rotating liner can oppose RT instability formation, further investigated in other studies such as the study by Huneault *et al.* (2019). Besides the RT instability, other hydrodynamic and magnetohydrodynamic instabilities appearing during large compression ratios result in decreased plasma temperature, which can lead to plasma quenching and cause low energy production (Brennan *et al.*, 2020). Furthermore, these instabilities can cause penetration of liner materials into the plasma, resulting in plasma impurities and contamination (Turchi, 2008).

In addition to MTF, other fusion approaches also consider the importance of RT instability, such as ICF and liner Z-pinch implosion. In the ICF approach, a cryogenic D-T target is compressed by utilizing laser-driven ablation of a thin shell within a nanosecond timescale. During the acceleration stage, the outer surface of the shell experiences RT instability, leading to perturbation growth at this interface. These perturbations then propagate through the thin shell, inducing perturbations at its outer interface, known as the feedthrough effect. Near the peak compression point, as a result of the deceleration of the inner surface of the shell by the internal light hot spot, this interface also becomes RT unstable (Wang *et al.*, 2015). Therefore, the initially seeded perturbation on this interface as a result of feedthrough will be further amplified. In ICF implosions, RT instability along with other mechanisms such as Richtmyer–Meshkov instability, the Bell–Plesset effect, and feedthrough (Wang *et al.*, 2017) results in the mixing of ablated material and D-T fuel. This mixing adversely affects reactor performance and energy production (Wang *et al.*, 2015).

Another promising fusion approach is magnetized liner inertial fusion (MagLIF), presently being developed by Sandia National Laboratories, in which an initially pre-heated and pre-magnetized fuel is compressed by the implosion of a cylindrical Z-pinch liner (Slutz *et al.*, 2010). Figure 1.2 represents a schematic of a MagLIF implosion. In this approach, a metal liner, a cylindrical shell approximately one centimetre in height, is initially filled with deuterium fuel. A high current is driven along this liner, inducing a magnetic field that wraps

around it (see Fig. 1.2[left]). Prior to the implosion, the plasma inside the liner is heated via laser to increase its temperature (see Fig. 1.2[middle]). The interaction between the current and magnetic fields generates the Lorentz force, causing the shell to implode and compress the deuterium fuel (see Fig. 1.2[right]). Similar to previous approaches, this fusion concept is also susceptible to the RT instability (Weis *et al.*, 2014). The RT instability in MagLIF occurs in two stages, i.e., during the implosion and also at the final stages of compression when the liner is decelerated into the deuterium fuel at the outer and inner interfaces of the liner, respectively (Weis, 2015). Hence, investigating the RT instability growth and understanding how instability growth on one interface may affect the other, i.e., the feedthrough effect or interface coupling, is imperative among different fusion approaches (Weis *et al.*, 2014; Wang *et al.*, 2015; Weis, 2015).

1.1.2 Instabilities in fusion reactors

Formation of any instability at the plasma/liquid-metal interface (PLMI) is undesirable; however, various forms of hydrodynamic and magnetohydrodynamic instabilities are prone to occur at the PLMI during the fusion process. The magnetohydrodynamic instabilities include but are not limited to edge-localized mode instability, tilt instability, and vertical displacement events (Hassanein *et al.*, 2005). It is worth mentioning that a wide range of instabilities can emerge in plasma as well while operating in a fusion reactor, e.g., kink instability, sausage instability, tearing mode instability, and drift instability. Introducing these instabilities is beyond the scope of this thesis; however, interested readers can refer to studies such as Furth *et al.* (1973), Glasser *et al.* (1975), Kerner *et al.* (1998), Freidberg (2014), and Glasser *et al.* (2016).

Different studies have examined hydrodynamic instabilities at the liquid liner using theoretical and numerical approaches. However, due to its complexity, hydrodynamic instabilities remain an active field of research. Four types of instabilities related to different fusion applications are susceptible to emerge at the liner interface, namely, Kelvin–Helmholtz instability,

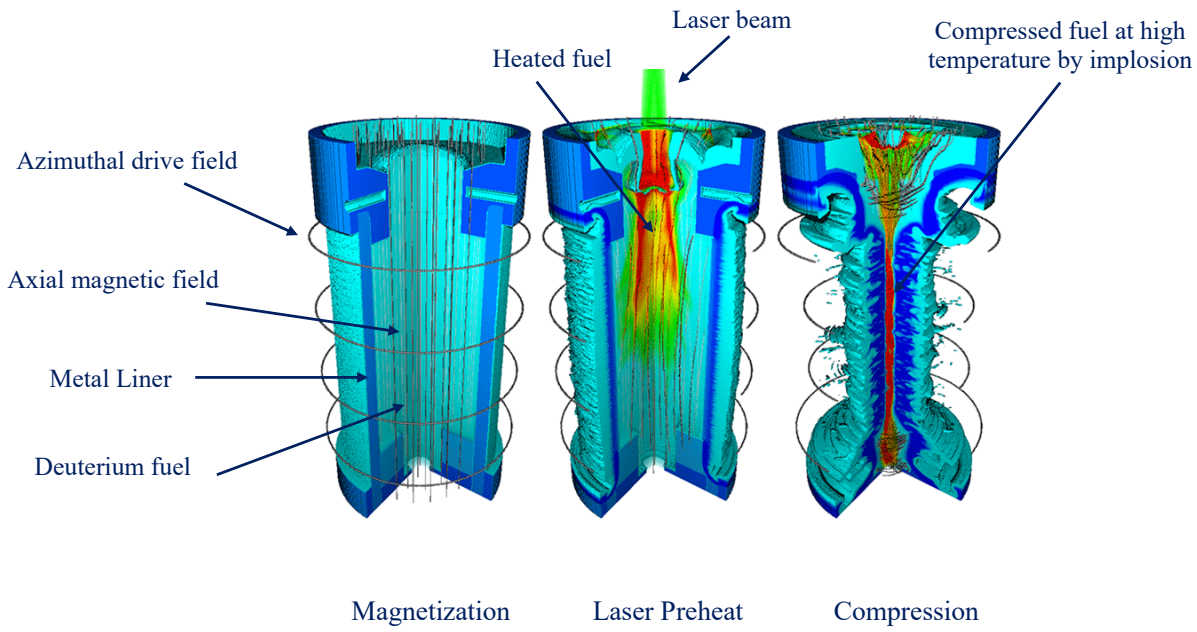

Figure 1.2: Three stages of a MagLIF implosion is illustrated. [left] A current running along the metal liner induces an azimuthal drive field that wraps around the liner. The axial magnetic field is imposed to magnetize the plasma, which aids in its confinement and containment of the heat required for the fusion reaction to occur. [middle] Plasma is initially heated before compression by employing high-power lasers. [right] The liner implosion results in an increased axial magnetic field, as well as the density and temperature of the plasma (Betti, 2014).

bubble bursting, Rayleigh–Plateau instability, and RT instability[§]. In this section, we will briefly review these instabilities, with a primary focus on the RT instability, especially in the presence of a magnetic field, known as the magneto-Rayleigh–Taylor (MRT) instability.

The Kelvin–Helmholtz instability arises from the velocity difference across the interface of two fluids. The Kelvin–Helmholtz instability has been widely examined in tokamak reactors[¶], where it mainly appears due to plasma jets, plasma exhaust, and liquid flows in-

[§] In some cases, such as ICF implosion, the RT instability is induced due to the propagation of a shock wave across the interface between two fluids, which is known as the Richtmyer–Meshkov (RM) instability (Zhou *et al.*, 2021).

[¶] A tokamak is a torus reactor which confines the hot plasma through magnetic field lines that wind around the torus in a helix.

teracting with the liquid-metal divertor[‖] with an oblique angle. This instability can lead to the formation of droplets at the PLMI, resulting in droplets splashing into the plasma. The ejection of droplets causes plasma impurity and enhances erosion at the plasma and liquid interface.

Bubble bursting at the liquid-metal surface was first mentioned by Hassanein & Konkashbaev (1994) while studying the droplet ejection from melted surfaces in tokamaks. These bubbles may arise from the liquid vaporization or the absorption of gases, creating blisters on the plasma-facing surfaces. The thin film covering these bubbles may burst and result in the formation of droplets, followed by a rising jet of liquid, which will decompose to a spray of droplets due to the Rayleigh–Plateau instability. The Rayleigh–Plateau instability occurs when a falling column of liquid breaks into a chain of droplets to reduce the liquid's total surface area, thereby reducing the surface tension. Studies on this type of instability for the plasma and liquid interactions have been somewhat limited. Gomes *et al.* (2008) conducted one of the first studies on this instability, examining the interaction of a liquid gallium jet with plasma inside a small-sized tokamak.

1.1.2.1 Rayleigh–Taylor instability

The RT instability emerges when a lighter fluid is accelerated towards a denser fluid, or conversely, if the situation is reversed and a denser fluid is decelerated by a lighter one. This instability is commonly observed on Earth when a denser fluid overlays a lighter fluid (Zhou *et al.*, 2021). In this scenario, gravity disrupts the boundary between the two fluids, leading to the development of perturbations and eventually resulting in turbulent mixing. In a broader context, RT instability occurs when an opposing density gradient, $\nabla\rho$, and pressure gradient, ∇p, coexist. This condition can be mathematically represented as $\nabla\rho \cdot \nabla p < 0$, indicating the coexistence of density and pressure gradients in different directions. The RT instability was first introduced by Rayleigh (1882) and examined in a later study by Taylor (1950).

[‖] Divertor is located at the bottom of the vacuum vessel inside the fusion reactor and protects the surrounding wall from the thermal and neutronic loads, as well as removing waste products from a reactor operating at steady-state condition.

The RT instability arises from continuous acceleration, while the Richtmyer–Meshkov (RM) instability is characterized by impulsive acceleration of an interface (Richtmyer, 1960; Meshkov, 1969). For instance, RM instability appears when a shock wave crosses the perturbed interface between two fluids, causing a sudden acceleration of the interface and rendering it unstable. Consequently, the RM instability can be treated as an impulsive analog to the RT instability. One significant difference between RT and RM instabilities is that an interface between fluids of different densities is inherently RM unstable, regardless of the direction of the travelling shock wave (Zhou *et al.*, 2021). In contrast, RT instability only occurs when the acceleration is directed towards the denser fluid. RT and RM instabilities are crucial features appearing in a wide range of physical phenomena, such as the formation of the Crab Nebula in astrophysics (Hester, 2008), supernova dynamics (Janka, 2012), geological flows (Seropian *et al.*, 2018), as well as various engineering applications, including high-energy-density regimes like ICF and plasma instabilities in fusion reactors (Zhou *et al.*, 2021).

The RT instability growth rate, denoted by ω, depends on the relative densities of the two fluids (ρ_{light}, ρ_{heavy}), interface acceleration (a), and the wavenumber of the initial perturbation (k), given as Rayleigh (1882)

$$\omega = \left(\frac{\rho_{\text{heavy}} - \rho_{\text{light}}}{\rho_{\text{heavy}} + \rho_{\text{light}}} \, k \, a \right)^{\frac{1}{2}} . \tag{1.1}$$

The RT instability causes small-amplitude perturbations at the unstable interface to grow exponentially over time, t, with the growth rate outlined in Eq. (1.1). Therefore, by denoting the initial amplitude of the perturbation by ξ_0, the temporal evolution of the perturbation can be expressed as $\xi(t) \propto \xi_0 \mathrm{e}^{\omega t}$, within the linear regime. The RT growth rate can be simplified as $\omega = \sqrt{ka}$ when the density of the light fluid is negligible compared to the heavy one ($\rho_{\text{light}} \ll \rho_{\text{heavy}}$).

In his seminal work, Taylor (1950) investigated the instability of a liquid layer of finite thickness, δ, subjected to acceleration by air pressure acting on the upper interface, assuming $\rho_{\text{light}} \ll \rho_{\text{heavy}}$. Taylor (1950) demonstrated that the RT growth rate, described as $\sqrt{ka}$, remains independent of the thickness of the fluid slab. Furthermore, he explored the

feedthrough effect, revealing that the amplitude of seeded ripples on the stable surface of the liquid layer experiences growth reduced by a factor of $e^{-k\delta}$ compared to ripples on the unstable interface.

Generally, the evolution of an RT unstable interface can be divided into three distinct regimes:

(i) The linear phase initiates the process, during which the amplitude of interfacial perturbations grows exponentially. The corresponding growth rate of this phase is derived from the linearization of the perturbation equations, as expressed in Eq. (1.1).

(ii) Following the linear phase, the nonlinear phase ensues, in which perturbation amplitudes are further amplified, resulting in the emergence of characteristic mushroom shapes.

(iii) In the late-time development phase, turbulence develops as perturbations continue to grow, leading to enhanced mixing of the two fluids across a wide range of scales.

These stages are depicted in Fig. 1.3**, where the aforementioned characteristic features can be observed. In the presented results, initially, a heavier fluid is situated above a lighter one in a gravitational field; therefore, the corresponding interface between the two fluids is unstable. The potential energy of the system decreases when the heavy (light) fluid forms protrusions that extend into the lighter (heavier) fluid, causing spike and bubble structures to appear. According to the stability analysis, Eq. (1.1), the RT instability growth rate is greater for perturbations with greater wavenumbers, i.e., shorter wavelengths. Consequently, narrow spike configurations grow faster compared to wider bulges at the interface.

Different factors such as surface tension, viscosity, material strength, and magnetic tension can affect the RT instability development and play a stabilizing role during its growth. This stabilizing effect depends on local gradients of the corresponding variables, such as surface curvature or velocity field; therefore, it is more pronounced at larger wavenumbers. The competition between the RT instability growth rate of the most unstable mode and the most dominant stabilizing effect for large wavenumbers results in the introduction of a

** The results demonstrating the RT instability growth are from numerical simulations performed using the implemented two-phase solver in this study.

cut-off wavenumber. This cut-off wavenumber indicates that instabilities with wavenumbers higher than the cut-off value will be stabilized (Piriz *et al.*, 2006, 2018).

As mentioned earlier, Rayleigh (1882) and Taylor (1950) conducted pioneering studies on the classical RT instability. This was followed by other researchers; for instance, Mikaelian (1982) investigated the RT instability growth at the interfaces of an arbitrary number of stratified fluids to address the design challenge of a multishell target approach for ICF. Later, Mikaelian (1990) extended the previous study to investigate the effect of surface tension on RT and RM instabilities in multilayer fluids. Additionally, Mikaelian (1995) examined the perturbation growth and interface coupling of a liquid layer of finite thickness for both RT and RM instabilities. All the aforementioned studies were performed analytically. Subsequent analytical studies investigated the effects of magnetic field presence on the RT and RM instabilities in both scenarios of multilayer and single liquid layers of finite thickness. For example, Cao *et al.* (2009) showed that when a multilayer stratified fluid is suddenly accelerated towards a transverse magnetic field, the RM instability is suppressed compared to the case where there is no magnetic field. In the study by Sun *et al.* (2022), the effect of an inclined magnetic field was investigated on RT and RM instabilities. The subsequent section will further provide an overview of the studies focusing on MRT instability.

1.1.2.2 Magneto-Rayleigh–Taylor instability

Introducing a magnetic field can significantly impact the growth rate of the RT instability and complicate the underlying physics. The effort to investigate magnetohydrodynamic (MHD) instabilities dates back to the 1950s and 1960s, primarily motivated by understanding the instabilities observed in Z-pinches. Kruskal & Schwarzschild (1954) investigated the instability growth in an ionized plasma slab supported by the magnetic pressure against gravity. The study conducted by Harris (1962) is one of the key investigations into the MRT instability growth in a collapsing shell within a magnetic field, including the feedthrough effect. The main limitation of this study is attributed to the fact that Harris (1962) only considered MHD modes that do not bend magnetic field lines during instability growth. Consequently, the obtained results were similar to the classical RT case, and the main characteristic of MRT instability, its anisotropic nature, was not discussed.

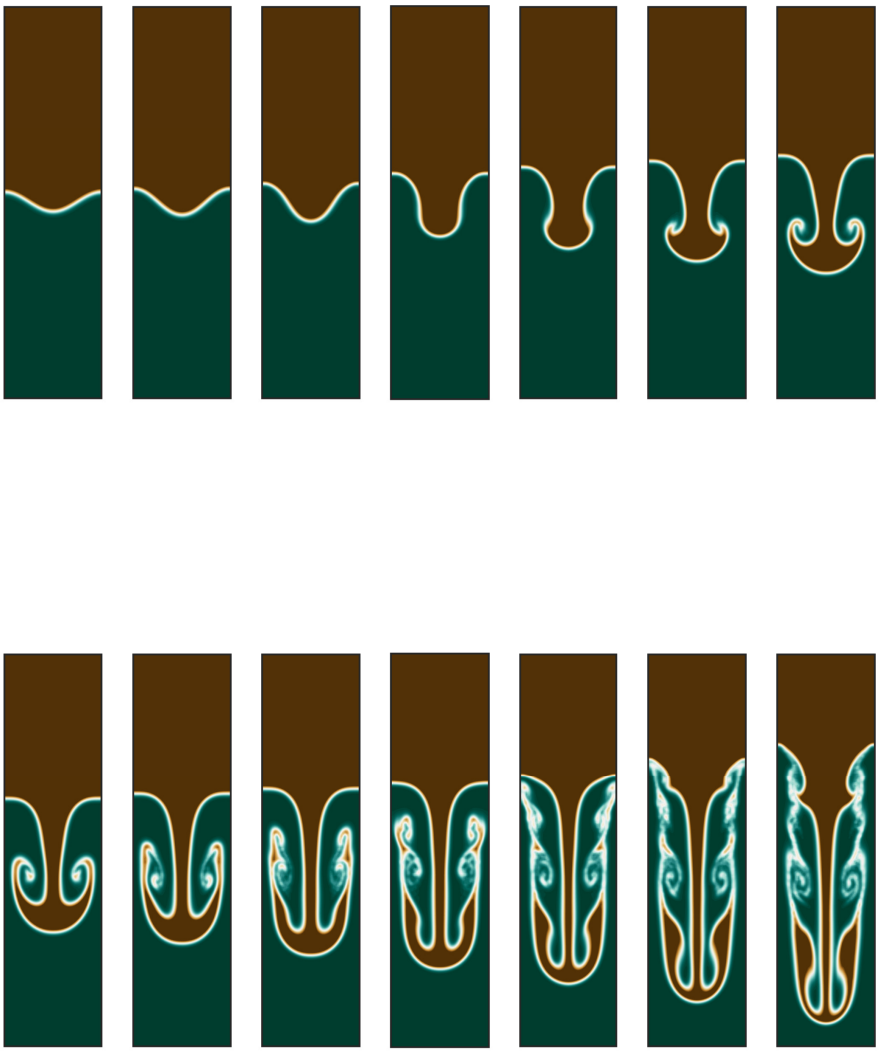

Figure 1.3: The growth of the RT instability when a denser fluid (brown) overlays a lighter fluid (green) in the presence of a gravitational field. The evolution of the RT instability is illustrated through snapshots from the top-left (initial time) to the bottom-right (late-time development). The first four panels approximately correspond to the linear stage of RT instability growth, while in the following four snapshots, characteristic bubbles and spikes corresponding to the second regime of RT instability appear. Subsequently, as perturbations continue to grow, a turbulent regime develops.

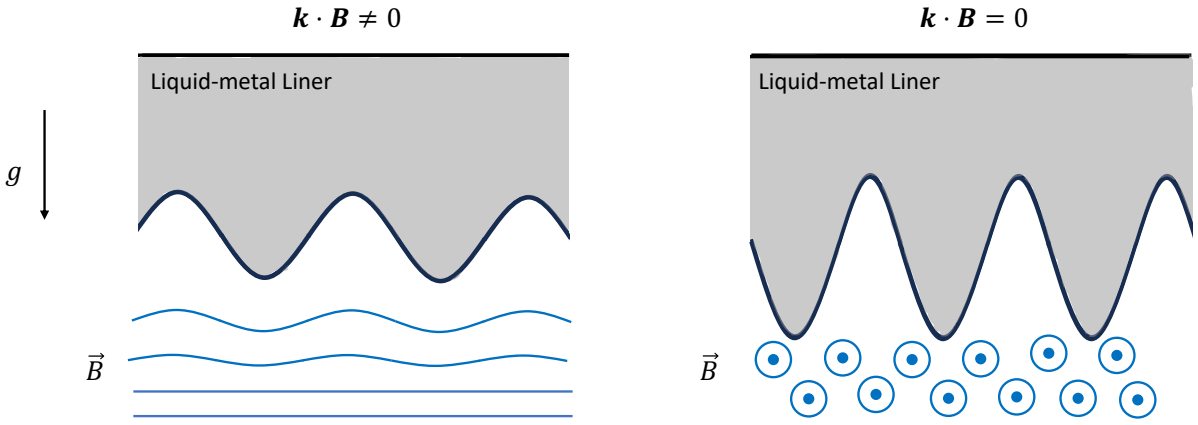

Figure 1.4: The MRT instability growth for two cases: on the left, perturbation growth bends magnetic field lines, while on the right, instability growth does not affect the magnetic field lines. In the scenario where $\boldsymbol{k} \cdot \boldsymbol{B} \neq 0$, the observed instability growth is less compared to the pure hydrodynamic RT case. However, for $\boldsymbol{k} \cdot \boldsymbol{B} = 0$, the instability growth is the same as in the classical RT.

To elucidate the anisotropic nature of MRT instability, consider a scenario where a perfectly conductive liquid-metal liner is located on top of a lower-density region, such as air, in which a constant horizontal magnetic field is present, as depicted in Fig. 1.4. When magnetic field lines are parallel to the initial perturbation of the interface, as the instability initiates, the magnetic field lines begin to bend following the frozen-in law[††] (see Fig. 1.4[left]). Consequently, the induced magnetic tension stemming from the bent magnetic field lines serves as an energy sink, resulting in a reduced growth rate compared to the classical RT case. Conversely, when magnetic field lines are perpendicular to the interface perturbation (see Fig. 1.4[right]), they remain unbent throughout the instability growth, resulting in a growth rate consistent with that of the hydrodynamic case.

[††] The frozen-in law states that for the ideal MHD case, magnetic field lines are attached to the velocity field and vice versa.

In the presence of the magnetic field $\boldsymbol{B}$, the classical RT growth rate reported in Eq. (1.1) is modified as (Weis, 2015)

$$\omega^2 = \frac{\rho_{\text{heavy}} - \rho_{\text{light}}}{\rho_{\text{heavy}} + \rho_{\text{light}}}\, k\, g - \frac{(\boldsymbol{k}\cdot\boldsymbol{B})^2}{\mu_{\text{m},0}\,(\rho_{\text{heavy}} + \rho_{\text{light}})}, \tag{1.2}$$

where the variable $\mu_{\text{m},0}$ denotes the magnetic permeability of vacuum. The minus sign in the right-hand side of Eq. (1.2) conveys the stabilizing effect of the magnetic field when $\boldsymbol{k}\cdot\boldsymbol{B} \neq 0$. As the RT instability initiates, magnetic field lines bend and experience tension, resulting in the generation of Alfvén waves. Alfvén waves travel along the magnetic field lines and for a magnetic field, $\boldsymbol{B}_0$, the Alfvén velocity, $\boldsymbol{v}_{\text{Al}}$, is given as

$$\boldsymbol{v}_{\text{Al}} = \boldsymbol{B}_0/\sqrt{\mu_{\text{m}}\rho}, \tag{1.3}$$

where μ_{m} and ρ are the magnetic permeability and density of the corresponding medium, respectively. Assuming the density of the lighter region to be negligible compared to the heavier one, the second term of the left-hand side of Eq. (1.2) is simplified as $(\boldsymbol{k}\cdot\boldsymbol{v}_{\text{Al}})^2$, showing the magnetic tension effect on the MRT instability growth through the generation of Alfvén waves. The stabilizing effect of the magnetic field is more pronounced for perturbations with larger wavenumbers as it induces stronger tension in magnetic field lines.

The behaviour of magnetic field lines resembles that of elastic bands, introducing a restoring force as they experience tension. This restoring force is stronger for perturbations with shorter wavelengths (i.e., higher wavenumbers), suggesting that magnetic tension suppresses instability growth at high wavenumbers. For instance, when the perturbation wavenumber aligns with the initially imposed magnetic field, the cut-off wavenumber is determined as $k_{\text{cut-off}} = (g\rho_{\text{heavy}}\mu_{\text{m},0})/B^2$ using Eq. (1.2). Therefore, perturbations with wavenumbers greater than $k_{\text{cut-off}}$ are stabilized.

The anisotropic nature of the MRT instability was investigated by later studies. For instance, the study by Lau *et al.* (2011), further extended by Weis *et al.* (2014), led to the development of an analytical solution for the MRT instability growth in a plasma slab of finite thickness surrounded by two lower-density regions. The derived theoretical expression is based on the ideal MHD assumption, and each region is assumed to be incompressible

with an arbitrary magnetic field value and direction parallel to the interface. This study is performed in the Cartesian coordinate system. The analytical model presented by Weis *et al.* (2014) proved to be very insightful and was further validated with MagLIF experiments at Sandia National Laboratories. However, according to Weis (2015), the analytical solution was found to be less accurate for cases involving large wavenumber perturbations, strong magnetic tension, and especially when the resistivity of the liner cannot be neglected. It is noteworthy to mention that the analytical model was also reproduced for the cylindrical geometry, which is closer to the Z-pinch (Weis, 2015). Studying cylindrical geometry is important when investigating instabilities in Z-pinch configurations, as two well-known current-carrying instabilities, namely, sausage and kink modes, only appear in the cylindrical geometry.

1.1.3 Motivation

Although various analytical, experimental, and numerical investigations have explored the MRT instability for the ideal MHD case, observations regarding the effect of resistivity on MRT growth are somewhat limited. Jukes (1963) was the first to analytically examine the effect of finite resistivity on RT growth in the presence of a constant horizontal magnetic field. Later, Sun *et al.* (2023) revisited this problem, identifying an error in the boundary conditions proposed by Jukes (1963), and introduced an updated dispersion relation for MRT growth in the MHD case with finite resistivity. According to their findings, the stabilizing effect of the magnetic field is further diminished for larger growth rates, and the density ratio noticeably impacts the growth rate. In the study conducted by Yang *et al.* (2019*a*), the impact of finite resistivity on MRT growth in a conductive liquid film of finite thickness was examined analytically. They showed that a horizontal magnetic field decreases the growth rate in both ideal and resistive MHD scenarios. However, this stabilizing effect is more pronounced in the cases with stronger magnetic fields and higher conductivity of the liquid layer.

Song & Srinivasan (2020) numerically investigated the effect of magnetic diffusion on MRT instability growth in two stratified fluids with a constant horizontal magnetic field applied in the domain. They observed that resistivity decreases the peak magnitude of the magnetic field compared to the ideal case and reduces the stabilization effect. The effect

of resistivity on shock-driven MRT instability in high-energy-density plasma regimes is important for ICF implosion and has obtained significant attention in recent studies (Manuel *et al.*, 2021; Barbeau *et al.*, 2022; Samulski *et al.*, 2022). For example, Manuel *et al.* (2021) experimentally investigated this effect. In their experimental setup at Laboratoire pour l'utilisation des lasers intenses (LULI), a 43-micrometre-thick target with initially seeded perturbations at the interface was tested when a laser induces a shock wave, causing the interface to become unstable. These experiments were performed without and with a background magnetic field of 10 Tesla. According to the experimental results, no measurable difference was observed between these two cases, which did not agree with the numerical results from the ideal MHD solver, suggesting that a proper resistive MHD model is needed to accurately model the effect of magnetic diffusion.

Investigating the impact of magnetic diffusion on MRT instability growth remains a crucial area for further study. Consequently, this thesis aims to enhance the existing understanding of this research question. To achieve this objective, a novel two-phase incompressible resistive MHD solver is introduced. This solver serves as a practical toolkit for modelling MRT instability growth and feedthrough in a liquid-metal liner of finite thickness. In the following section, the implementation of this solver and the adopted numerical schemes for solving the governing equations are briefly presented.

1.2 Numerical Campaign

To model the MRT instability growth and feedthrough in a liquid-metal liner, a two-phase incompressible resistive MHD solver is required. While various studies have focused on developing a two-phase incompressible solver for the hydrodynamic case in the literature (Sussman & Puckett, 2000; Olsson *et al.*, 2007; Desjardins *et al.*, 2008*b*), existing two-phase MHD solvers are limited due to their complexity and multiphysics nature. That is why one of the objectives of this study is to present a robust two-phase resistive MHD solver that is straightforward to implement and can be employed in various applications.

The implemented solver is developed from scratch in-house, with a thorough examination of its accuracy and performance at every stage of the development, as will be detailed in

the subsequent chapters. While various open-source codes could be potentially utilized and built upon to serve this purpose, a decision was made to conduct a comprehensive numerical campaign as a part of this study. This is due to the fact that one needs to fully understand the underlying structure and numerical schemes embedded within the code to be able to address complex research questions accurately. This approach allows for detailed verification of the numerical solutions to ensure their accuracy and physical validity, as well as providing control over the underlying numerical methods. Therefore, one of the contributions of this study is presenting a novel second-order level set-based two-phase solver for incompressible resistive MHD flows in the finite-difference framework.

The governing set of equations for an incompressible resistive MHD solver is given as

$$\frac{\partial \boldsymbol{u}}{\partial t} + \nabla \cdot (\boldsymbol{u}\boldsymbol{u}) = -\frac{1}{\rho}\nabla p + \frac{1}{\rho}\nabla \cdot \mu \left(\nabla \boldsymbol{u} + \nabla \boldsymbol{u}^{\mathrm{T}}\right) + \boldsymbol{g} + \frac{1}{\rho}\boldsymbol{F}_{\mathrm{sv}} + \frac{1}{\rho}\nabla \cdot \tau_{ij}^{\mathrm{M}}, \tag{1.4a}$$

$$\nabla \cdot \boldsymbol{u} = 0, \tag{1.4b}$$

$$\frac{\partial \boldsymbol{B}}{\partial t} = \nabla \cdot (\boldsymbol{B}\boldsymbol{u} - \boldsymbol{u}\boldsymbol{B}) + \nabla \cdot \lambda_{\mathrm{m}} (\nabla \boldsymbol{B}), \tag{1.4c}$$

$$\nabla \cdot \boldsymbol{B} = 0, \tag{1.4d}$$

where $\boldsymbol{u}$ and $\boldsymbol{B}$ denote the velocity and magnetic fields, respectively. Variables p, μ, and ρ are pressure, dynamic viscosity, and density, respectively. The gravitational acceleration is denoted by $\boldsymbol{g}$ and $\boldsymbol{F}_{\mathrm{sv}}$ represents any volume force that might be present such as surface tension.

The force experienced by conductive fluids due to the presence of electromagnetic fields is known as the Lorentz force and is given as $\boldsymbol{J} \times \boldsymbol{B}$, where $\boldsymbol{J}$ is the electric current. This force can be written in the form of the Maxwell stress tensor, τ^{M}, which is given as

$$\nabla \cdot \tau_{ij}^{\mathrm{M}} = \nabla \cdot \left(\frac{B_i B_j}{\mu_{\mathrm{m}}} - \frac{\boldsymbol{B}^2}{2\mu_{\mathrm{m}}}\delta_{ij}\right), \tag{1.5}$$

where variable μ_{m} denotes the magnetic permeability. The Lorentz force is included in the momentum equation, Eq. (1.4a), to account for the effect of magnetic forces on fluid motion. According to Eq. (1.5), the Lorentz force consists of two components, i.e., the

magnetic pressure, $(\boldsymbol{B}^2)/2\mu_\mathrm{m}$, and the magnetic tension, B_iB_j/μ_m. The latter term produces a restoring force when magnetic field lines bend and experience tension (Walsh, 2022). Due to the incompressibility assumption, the momentum equation should be solved under the divergence-free condition for the velocity field, as expressed in Eq. (1.4b).

The induction equation, Eq. (1.4c), describes the evolution of a magnetic field due to the convection and diffusion mechanisms. The variable λ_m represents the magnetic diffusivity and is given as $\lambda_\mathrm{m} = 1/(\mu_\mathrm{m}\sigma_\mathrm{e})$, where σ_e is the electrical conductivity. Owing to the fact that magnetic fields are solenoidal vectors and magnetic monopoles do not exist, the solution to the induction equation must also satisfy the divergence-free constraint for the magnetic field, Eq. (1.4d).

Among the main available methods to model two-phase flows, i.e., the lattice Boltzmann method (LBM) (Li *et al.*, 2022), smoothed particle hydrodynamics (SPH) (Fonty *et al.*, 2019), two-fluid, and one-fluid models, the one-fluid formulation is adopted in the present solver. In this approach, the Navier–Stokes equations are solved across the entire computational domain, accounting for properties such as density, viscosity, and electrical conductivity discontinuity at the interface. Proper boundary conditions for velocity, pressure, and magnetic field across the interface separating the two fluids are implicitly imposed in this method.

The conservative level set (CLS) approach introduced by Olsson & Kreiss (2005) and Olsson *et al.* (2007) is utilized as the interface capturing method. The fifth-order upwind-based numerical discretization is employed to solve the transport equation for the level set function. A conservative re-initialization step is integrated into the level set transport equation to maintain the thickness of the interface profile and conserve mass during the simulation. This interface capturing scheme is coupled with the projection method proposed by Chorin (1997) on a staggered grid arrangement to model the behaviour of two-phase incompressible flows. Subsequently, this solver is extended to incorporate Maxwell's equations of electromagnetism for simulating magnetic and conductive fluids. Maxwell's set of equations is presented as

follows

$$\nabla \cdot \boldsymbol{B} = 0, \qquad \text{(Gauss's law)} \tag{1.6a}$$

$$\nabla \times \boldsymbol{E} = -\frac{\partial \boldsymbol{B}}{\partial t}, \qquad \text{(Faraday's law)} \tag{1.6b}$$

$$\nabla \times \boldsymbol{B} = \mu_{\mathrm{m}} \boldsymbol{J}, \qquad \text{(Maxwell–Ampère law)} \tag{1.6c}$$

$$\nabla \cdot \boldsymbol{J} = 0, \qquad \text{(charge conservation)} \tag{1.6d}$$

$$\boldsymbol{J} = \sigma_{\mathrm{e}}(\boldsymbol{E} + \boldsymbol{u} \times \boldsymbol{B}), \qquad \text{(Ohm's law)} \tag{1.6e}$$

where $\boldsymbol{E}$ and σ_{e} denote the electric field intensity and electrical conductivity, respectively. Combining Faraday, Maxwell–Ampère, and Ohm's laws results in the induction equation, which should be solved under the divergence-free constraint for the magnetic field, as dictated by Gauss's law.

During the first phase of the conducted numerical campaign (Chapter 2), the reduced Maxwell's equations under the magnetostatic assumption are solved. The magnetostatic solver proved to be a suitable capability for modelling magnetic fluids and ferrofluids. Ferrofluids, originally introduced by the National Aeronautics and Space Administration (NASA) in the 1960s, consist of colloidal suspensions of magnetic nanoparticles dispersed in a carrier fluid. Ferrofluids find diverse applications, including biomedical applications such as targeted drug delivery and the treatment of retinal detachment (Voltairas *et al.*, 2001; Mefford *et al.*, 2007), droplet generation from nozzles (Bijarchi & Shafii, 2020), and microfluidics (Bijarchi *et al.*, 2021). When subjected to an external magnetic field, nanoparticles within ferrofluids become magnetized and align with the field direction. Owing to their special structure, the imposed magnetic field changes slowly over time compared to the characteristic timescales of the fluid motion, validating the magnetostatic assumption. The excellent performance exhibited by the solver in handling high density and magnetic permeability ratios at the interface has enabled the investigation of ferrofluid droplet deformation across various susceptibility values in both quiescent and shear flows. It is observed that increasing the magnetic permeability jump leads to greater ferrofluid deformation, which can result in droplet breakup in some cases.

The solver is further extended to account for the full resistive MHD equations (Chapter 3) to study the behaviour of both perfectly conductive fluids and fluids with finite resistivity. The implemented solver can address large electrical conductivity discontinuities at the interface, making it a robust capability for studying the problem of interest, presented in the next section.

1.3 Objectives

The primary objective of this thesis is to expand and contribute to the understanding of the impact of magnetic tension and diffusion on the MRT instability growth in a liquid-metal slab. In this study, a scenario where an initially magnetic-field-free liquid-metal liner of finite thickness overlays a lower-density region containing a constant horizontal magnetic field is investigated, as depicted in Fig. 1.5. The lower and upper layers are assumed to have the same material properties, such as density, magnetic permeability, and electrical conductivity. All three layers are assumed to be incompressible. As illustrated in Fig. 1.5, due to the body force g acting downward, the lower interface of the liquid-metal liner becomes RT unstable. Consequently, any initially seeded perturbation at this interface begins to grow due to this instability. However, the presence of the magnetic field in the lower layer can influence this instability growth. Additionally, perturbations at the lower interface propagate to the upper interface of the liquid liner and induce perturbations at this interface. This interface coupling effect depends on different parameters, such as liner thickness, perturbation growth, and perturbation wavenumber.

It should be noted that this study specifically focuses on the initial stages of perturbation growth that are parallel to the imposed horizontal magnetic field, before convergence effects become significant. Consequently, the two-dimensional Cartesian computational domain (see Fig. 1.5) and the treatment of the liquid liner as an incompressible flow are considered valid assumptions. Although the assumption of incompressibility becomes invalid throughout the entire liner compression process, the primary interest of this work is in studying MRT instability growth during the initial stages, where the liquid liner can be treated as incompressible. This incompressibility assumption allows for larger time steps and improved computational

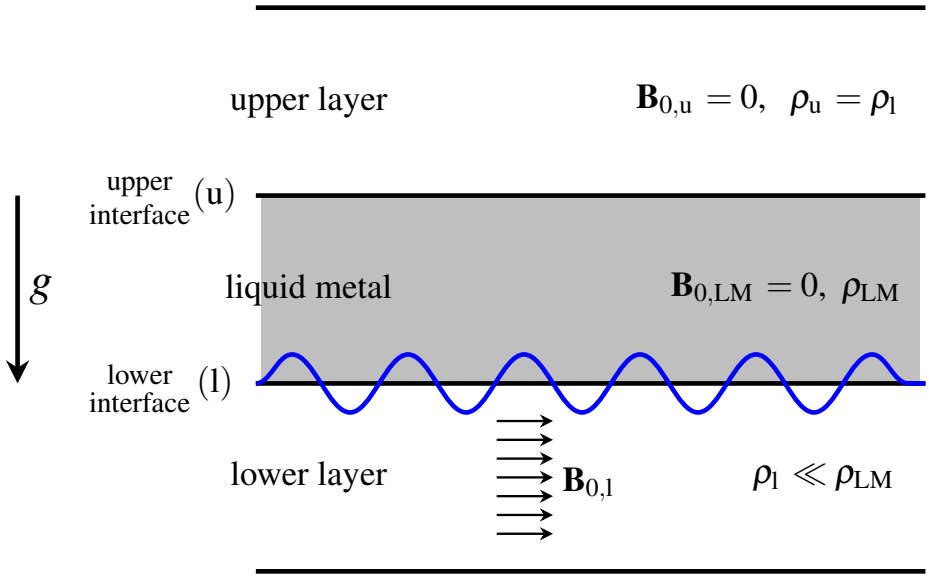

Figure 1.5: The schematic of the problem of interest.

efficiency. In the compressible regime, due to the high sound speed in liquid metals, smaller time steps and more computational resources would be required by the CFL condition, which is deemed unnecessary for the current case.

The specific research questions that are aimed to be addressed in this thesis are:

- What is the effect of the imposed magnetic field strength on the MRT growth rate at the lower interface and its feedthrough effect at the upper interface in both ideal and resistive MHD cases?
- What is the effect of the liquid liner's finite resistivity on perturbation growth and interface coupling? Additionally, how would the electrical conductivity ratio between the liquid liner and the surrounding medium affect the obtained results?
- How would surface tension impact MRT instability growth in both ideal and resistive MHD cases?
- What is the effect of the liner's thickness and perturbation wavenumber on the MRT growth and feedthrough for ideal and resistive MHD cases?

- What is the effect of magnetic diffusion on the morphology of the MRT instability spikes and bubbles in the initial stages of instability growth, as well as in highly nonlinear regimes?

These research questions are answered in this work using the introduced second-order numerical solver for two-phase incompressible resistive MHD flows. Although analytical studies have proven to be insightful, they are mainly limited to the linear regime. Moreover, existing analytical solutions fail to address scenarios where magnetic diffusion exists or where surface tension is an important factor, especially in the three-layer configuration of interest. However, these limitations can be addressed in this study.

On a final note in this section, to systematically investigate the raised questions and extend the applications of this study, key non-dimensional parameters appearing in the governing equations are utilized for stability analyses. The four dimensionless numbers governing the physics of this problem are the Reynolds number (Re), the Bond number (Bo), the Alfvén number (Al), and the magnetic Reynolds number ($\mathrm{Re_m}$). The Reynolds number defines the ratio between inertia forces and shear forces, while the Bond number quantifies the intensity of capillary forces. The magnetic Reynolds number measures the relative strength of the magnetic advection mechanism to magnetic diffusion. The Alfvén number indicates the ratio between inertial forces and magnetic forces. The dimensionless set of governing equations and these listed parameters are discussed in detail in Chapter 3.

1.4 Organization of the Thesis

The thesis is presented in the form of a manuscript-based dissertation. This chapter serves as the introduction. Chapter 2 contains a detailed numerical implementation of a two-phase incompressible solver for magnetic fluids. In this chapter, the behaviour of ferrofluid droplets in different flow regimes for various susceptibility values of the droplets is studied. Additionally, the RT instability growth in magnetic fluids is investigated.

Chapter 3 extends the numerical effort represented in Chapter 2 to account for ideal/resistive MHD equations. This chapter primarily focuses on the obtained numerical results addressing the specific questions raised in the previous section. The impact of the introduced dimen-

sionless parameters on the liquid-metal liner instability growth and feedthrough is discussed in this chapter. Furthermore, there is a brief section between Chapters 2 and 3, i.e., a logical bridge, explaining the connection between the topics and how they contribute to answering the research questions.

Chapter 4 offers a discussion of the findings, followed by a further investigation of the interface coupling effect for different scenarios. These scenarios explore cases where the upper interface is initially smooth or perturbed, with perturbations either in-phase or out-of-phase compared to the perturbation at the lower interface of the liquid liner. Finally, in Chapter 5, a summary of the main results and concluding remarks is presented.

CHAPTER 2

A level set-based solver for two-phase incompressible flows: Extension to magnetic fluids

This chapter reports on the first phase of the conducted numerical campaign, which involves developing a two-phase incompressible solver for magnetic flows. In the presented solver, the Navier–Stokes equations are solved along with Maxwell's equations under the magnetostatic assumption. This chapter is based on:

Makaremi-Esfarjani, P., Higgins, A. J. & Najafi-Yazdi, A. 2023 A level set-based solver for two-phase incompressible flows: Extension to magnetic fluids. *International Journal of Computational Fluid Dynamics* **37** (7), 565–606.

Abstract

Development of a two-phase incompressible solver for magnetic flows in the magnetostatic case is presented. The proposed numerical toolkit couples the Navier–Stokes equations of hydrodynamics with Maxwell's equations of electromagnetism to model the behaviour of magnetic flows in the presence of a magnetic field. To this end, a rigorous implementation of a second-order two-phase solver for incompressible nonmagnetic flows is introduced first. This solver is implemented in the finite-difference framework, where a fifth-order conservative level set method is employed to capture the evolution of the interface, along with an incompressible solver based on the projection scheme to model the fluids. The solver demonstrates excellent performance even with high density ratios across the interface (Atwood number

≈ 1), while effectively preserving the mass conservation property. Subsequently, the numerical discretization of Maxwell's equations under the magnetostatic assumption is described in detail, utilizing the vector potential formulation. The primary second-order solver for two-phase flows is extended to the case of magnetic flows, by incorporating the Lorentz force into the momentum equation, accounting for high magnetic permeability ratios across the interface. The implemented solver is then utilized for examining the deformation of ferrofluid droplets in both quiescent and shear flow regimes across various susceptibility values of the droplets. The results suggest that increasing the susceptibility value of the ferrofluid droplet can affect its deformation and rotation in low capillary regimes. In higher capillary flows, increasing the magnetic permeability jump across the interface can further lead to droplet breakup as well. The effect of this property is also investigated for the Rayleigh–Taylor instability growth in magnetic fluids.

2.1 Introduction

Modelling multi-phase (interfacial) flows involves simulating systems with the presence of two or more immiscible fluids with different physical properties and distinguishable interfaces. Multi-phase flows, particularly two-phase flows, have garnered substantial interest in various applications, including spray atomization (Desjardins *et al.*, 2008*b*), bubbly flows (Clift *et al.*, 2005), and nuclear reactors (Radman *et al.*, 2021). The complexity of analytically and experimentally studying the physics of two-phase flows (Prosperetti & Tryggvason, 2009) has necessitated the development of accurate, cost-effective, and consistent numerical methods. Numerous studies have been conducted to establish a comprehensive numerical toolkit in the field. Despite these efforts, developing a numerical solver to study two-phase flows remains a challenging task. The difficulty originates from modelling fluid property discontinuities across thin interfaces, particularly when large density ratios are present. The inability to accurately capture discontinuities in fluid properties can result in numerical instabilities. Errors arising from the inadequate discretization of fluid property discontinuities can become particularly pronounced for large density ratios, thereby limiting simulations to low density ratios. However, most realistic problems of interest involve large density ratios, such as the

formation and dynamics of bubbles, molten metal flows in atmospheric air, gas entrainment in liquid phases, and the aerodynamic effects of gas on the liquid phase (Bussmann *et al.*, 2002). Enforcing mass and momentum conservation is also crucial to obtain physical results and to avoid numerical instabilities in simulations. Therefore, the numerical solver must be able to provide consistent mass and momentum exchange across interfaces throughout the simulation. It is essential for the two-phase solver to be able to address topology changes of the interface and accommodate a wide range of time and length scales as well. In numerical solvers for two-phase flows, it is crucial to properly couple the governing equations of fluids with an appropriate interface-tracking method.

Existing techniques for simulating two-phase flows can be grouped into four categories: the lattice Boltzmann method (LBM), smoothed particle hydrodynamics (SPH), two-fluid, and one-fluid models. The first two methods examine the behaviour of the fluid by representing it as a collection of particles (Li *et al.*, 2022; Lai *et al.*, 2023; Fonty *et al.*, 2019; Cui *et al.*, 2021), while the last two approaches assume the fluid as a continuum medium that can be described by solving the Navier–Stokes equations. The two-fluid method treats the two phases as separate fluids that interact with each other. This model has demonstrated success in simple problems but has been shown to be inadequate for more complex scenarios (Prosperetti & Tryggvason, 2009). In this study, we adopt the one-fluid formulation and implement it on a fixed Eulerian grid to develop a two-phase incompressible numerical solver. The Navier–Stokes equations are solved for the entire computational domain, accounting for the density and viscosity jump at the interface while implicitly imposing appropriate boundary conditions across the interface separating the two fluid regions. Among different numerical schemes for treating high density ratios across the interface and modelling surface tension forces, the ghost fluid method (GFM) (Fedkiw *et al.*, 1999) and the continuum surface force (CSF) (Brackbill *et al.*, 1992) method stand out as robust solutions. The GFM is based on a generalized Taylor series expansion and explicitly accounts for the density jump at the interface; as a result, it is not sensitive to the amplitude of the density jump. The surface tension force is also directly incorporated in the pressure jump condition, leading to a sharp numerical treatment of this singular term (Desjardins *et al.*, 2008*b*). However, in the CSF approach, instead of including the surface tension force directly in the

pressure jump condition, this force is represented as a volumetric force spread over a few grid points surrounding the interface. While this approach may result in a slightly less accurate interface representation, particularly in cases with small front structures, it is generally considered to be less numerically challenging. Furthermore, discretizing the viscous terms using the GFM can be difficult and complex to implement numerically, making it less desirable for some applications (Desjardins *et al.*, 2008*b*). Thus, many researchers employ the CSF approach to discretize the viscous term. In this study, we used the CSF method to model both the surface tension and the viscosity terms. Albeit slightly less accurate as compared to GFM for surface tension modelling, the CSF approach is more straightforward to implement and can provide robust and accurate results.

The available methods to numerically transport an interface can be divided into two categories: interface-tracking and interface-capturing (Mirjalili *et al.*, 2017). One well-known approach in the interface-tracking category is the front-tracking method introduced by Unverdi & Tryggvason (1992). This method involves breaking down the fluid interface into discrete material points, referred to as front-tracking points, which are then transported using a moving mesh that follows a Lagrangian approach. While this approach benefits from purely Lagrangian transport, it faces difficulties in preserving liquid volume due to the requirement for frequent mesh rearrangements (Desjardins *et al.*, 2008*b*). Additionally, parallelization of the front-tracking method presents a significant challenge. Furthermore, any break-up or merging of the interface should be addressed manually due to the inability of this technique to inherently handle topology changes. As a result, front-tracking methods are not well-suited for simulations with frequent topological changes, such as primary atomization (Desjardins *et al.*, 2008*b*).

Interface-capturing methods such as the volume-of-fluid (VOF) method (Scardovelli & Zaleski, 1999) and level set method (Sethian, 1999) implicitly capture the interface and can robustly address complex topological changes in the simulation. The VOF method employs a liquid volume fraction transport equation to depict the interface, ensuring mass conservation. However, since the VOF scalar is discontinuous across the interface, specific numerical treatments are required for the discretization of the transport equation. The

discontinuous nature of the VOF scalar presents difficulties in computing interface properties such as normal and curvature values as well.

The level set method, introduced by Sethian (1999) in the field of image processing and computer graphics, represents an interface implicitly using the iso-level of a smooth function, i.e., the signed distance function. The smoothness of the level set function is maintained with the re-initialization process, and the Eulerian scalar transport equation can be solved using high-order numerical schemes. In addition, parallelization of the solver can be accomplished efficiently, and interface characteristics such as normal and curvature values are easily calculable due to the smoothness of the level set function. Despite all the mentioned advantages of the level set method, this method does not inherently conserve mass during the simulations, leading to potentially significant errors. Various hybrid methods have been introduced to overcome the stated drawback of the level set method, such as the coupled-level-set and volume-of-fluid method (CLSVOF) by Sussman & Puckett (2000). The CLSVOF method incorporates the mass conservation property of the VOF method with the smoothness of the level set function (Meng *et al.*, 2022). Another hybrid method is the hybrid particle level set method (HPLS) proposed by Enright *et al.* (2002). This method updates the interface location computed using the Eulerian transport equation through the use of Lagrangian markers, resulting in improved mass conservation. Although all of these hybrid methods improved the mass conservation property of the original level set method, they lack the main benefits of the original level set method, i.e., the cost-effective, straightforward implementation of the Euler transport equations using different existing high-order schemes (Mirjalili *et al.*, 2017).

Furthermore, several studies have explored the use of mesh refinement techniques to mitigate errors in mass conservation. For instance, Herrmann (2008) proposed the refined level set grid (RLSG) method, in which the level set equation is solved on an auxiliary high-resolution grid. Another approach is the standard arbitrary mesh refinement (AMR) method, in which the mesh is made finer near the interface (Gibou *et al.*, 2018; Chen *et al.*, 2023). Although mesh refinement techniques offer improved mass conservation, they can be computationally expensive, difficult to implement in parallel systems, and constrained by small time steps due to the finer mesh resolution.

Studies by Olsson & Kreiss (2005) and later Olsson *et al.* (2007) addressed the conservation issue of the classical level set method by proposing a modification while maintaining its simplicity. They replaced the traditional signed distance level set function with the diffuse interface profile defined by the hyperbolic tangent function and solved the transport and re-initialization equations in a conservative form. This approach showed an improvement in mass conservation by an order of magnitude compared to results using the signed distance function (Olsson & Kreiss, 2005). In this study, we will use the conservative level set (CLS) approach to capture the interface between two flows.

The implemented interface-capturing scheme should then be coupled with a proper incompressible flow solver to simulate the physics of two-phase incompressible flows. Here, we will utilize the projection method introduced by Chorin (1997) to model the behaviour of incompressible flows. In this approach, the momentum equation is split into two parts. The first one solves the momentum equation while ignoring the pressure term to calculate the intermediate velocity field, which does not necessarily satisfy the divergence-free constraint. Subsequently, the second equation uses pressure to project the intermediate velocity field into a divergence-free velocity field.

Magnetic fields exert a considerable influence on the behaviour of conducting fluids. The motion of these fluids in the presence of magnetic fields is described through the coupling of the Navier–Stokes equations with Maxwell's equations of electromagnetics. This coupling gives rise to a set of equations known as the magnetohydrodynamics (MHD) equations. The interaction between electromagnetic fields and incompressible conducting fluids finds applications in fusion reactors, the metallurgical industry, MHD generators, and aluminum reduction cells (Davidson, 2001). To investigate the physics of these problems, a two-phase MHD solver is required. While numerous numerical studies have been conducted on simulating one-phase incompressible or compressible MHD problems (Jiang & Wu, 1999; Wu, 2007; Makaremi-Esfarjani & Najafi-Yazdi, 2022), the existing two-phase MHD solvers are highly limited due to their complexity and multi-physics nature. For instance, Huang *et al.* (2002) developed a three-dimensional free-surface MHD solver to simulate the evolution of the liquid lithium film free-surface due to the existing magnetic forces in a fusion reactor known as NSTX (National Spherical Torus Experiment). Their implemented MHD model

is based on the magnetic field induction equation, and the free boundary is tracked using the concept of a fractional volume of fluid method. On the other hand, Gao *et al.* (2004) simulated the motion of a liquid lithium droplet under a strong non-uniform magnetic field in a vacuum environment without the influence of gravity. In their approach, the VOF model is incorporated to capture the interface, and the CFS method is used to account for the surface tension. Later, Tagawa (2006) developed a numerical solver to investigate the movement of a falling droplet of liquid metal into a pool of liquid metal under a uniform magnetic field in the cylindrical geometry. The primary level set approach of Sussman *et al.* (1994) has been used in the study by (Tagawa, 2006) to capture the interface without the re-initialization step. In that study, the mass conservation, convergence, and consistency of the solver have not been verified for other benchmarks. Additionally, various studies have been also conducted to simulate the two-phase MHD flows in the finite-element framework. For example, Yang *et al.* (2019*b*) proposed a diffuse interface model to numerically simulate the two-phase MHD flows and studied the performance of their solver for two-phase Hartmann flows, which is the MHD version of the classical Poiseuille flows.

Despite various numerical efforts in MHD flows in compressible liquid, there remains a need for a general and systematic implementation of a numerical framework with a higher order of accuracy. This is crucial for effectively capturing the formation of instabilities at the interface, which is of high importance in different applications, particularly when dealing with abrupt changes in magnetic properties across the interface. In this study, the magnetostatic case of Maxwell's equations is studied and integrated into the implemented two-phase incompressible solver. Two-phase magnetostatic solvers are widely employed to simulate the deformation of ferrofluid droplets in various flow fields, with applications in different fields, including biomedicine and rheology (Afkhami *et al.*, 2008, 2010; Majidi *et al.*, 2022). In the presence of a magnetic field in two-phase magnetic flows, magnetic permeability experiences a discontinuity across the interface, leading to the induction of the Lorentz force. This force significantly influences the evolution of the interface. Therefore, it is essential to incorporate the role of the Lorentz force into the governing equations. The proposed two-phase magnetostatic solver adequately addresses the magnetic permeability jumps across the

interface, imposes proper boundary conditions for the magnetic field at the interface, and satisfies the divergence-free constraint for the magnetic field.

The objective of this study is two-fold. First, it primarily aims to present a detailed second-order numerical toolkit for simulating the physics of two-phase incompressible flows and its extension to magnetic flows. The mathematical formulation and numerical grid implementation will be given in Sec. 2.2. While investigating the surface instabilities necessitates the use of higher-order numerical solvers, most numerical studies in this area are limited to first-order accuracy. Thus, a fifth-order mass-conservation level set approach is presented in Sec. 2.3, which includes a conservative re-initialization step to minimize the mass loss. The accuracy and robustness of the implemented level set solver are also analyzed using several benchmarks existing in the literature. A high-order conservative incompressible solver based on the projection method is discussed in Sec. 2.4 to solve the momentum equation under the divergence-free constraint of the velocity field. The level set and incompressible solvers are then coupled in Sec. 2.5, and the detailed implementation of a second-order two-phase incompressible solver is demonstrated. This numerical approach solves the governing equations in a conservative form and effectively handles high density ratios and viscosity jumps across the interface without introducing numerical instabilities. Furthermore, a consistent method for calculating the interface curvature is utilized, which is cost-effective and straightforward to implement. The robustness and accuracy of this two-phase solver are examined through three benchmarks. This effort is followed by introducing a two-phase magnetohydrodynamics solver under the magnetostatic assumption, achieved by extending the implemented second-order two-phase solver to the magnetic case. To the knowledge of the authors, studies on developing a high-order two-phase solver for magnetic flows are limited, and there is no specific study focusing on the development of a two-phase magnetostatic solver in the finite-difference framework using a high-order level set method to capture the interface between two fluids. Thus, in Sec. 2.6, a procedure for adding the magnetic terms to the solver is established. The introduced solver successfully accounts for significant magnetic permeability variations across the interface while satisfying the divergence-free condition of the magnetic field. The performance of the solver is evaluated by proposing three

test cases: The deformation of a ferrofluid droplet in quiescent and shear flow regimes and the magneto-Rayleigh–Taylor instability in magnetic fluids.

The second and principal contribution of this paper is the investigation of sheared ferrofluid droplet deformation for various values of the droplet's susceptibility in both low and high capillary flow regimes. While previous studies have examined the effects of various factors on droplet deformation, such as the viscosity ratio between the droplet and the surrounding medium and the strength and direction of the imposed magnetic field, exploring deformations for different susceptibility values remains a crucial avenue to explore. Therefore, in Sec. 2.6, this paper also investigates the impact of droplet susceptibility values on its deformation, rotation, and potential breakup.

2.2 Grid arrangement and mathematical formulation

The use of a staggered grid in an incompressible solver ensures the accurate coupling between the velocity and pressure fields. The staggered arrangement, as illustrated in Fig. 2.1, eliminates oscillations in the pressure field and avoids the checker-board problem, a common issue for incompressible numerical simulations (Morinishi *et al.*, 1998). In this computational grid system, scalar values such as pressure are defined at the cell centers and velocity components are defined at the cell faces. As a result, the continuity equation is solved at cell center points, while the momentum equation corresponding to each velocity component is defined at cell faces.

In this study, we have employed similar notation of the conservative centred high-order finite-difference scheme of Morinishi *et al.* (1998) and Desjardins *et al.* (2008*a*), briefly introduced in this section for the sake of completeness. According to their notation, the second-order finite-difference operator with the stencil size n for a variable ϕ in the x_1-direction in the computational domain $\boldsymbol{x} = (x_1, x_2, x_3)$ is defined as

$$\frac{\delta_n \phi}{\delta_n x_1} = \frac{\phi\left(x_1 + n\,\Delta x/2,\, x_2,\, x_3\right) - \phi\left(x_1 - n\,\Delta x/2,\, x_2,\, x_3\right)}{n\,\Delta x}. \tag{2.1}$$

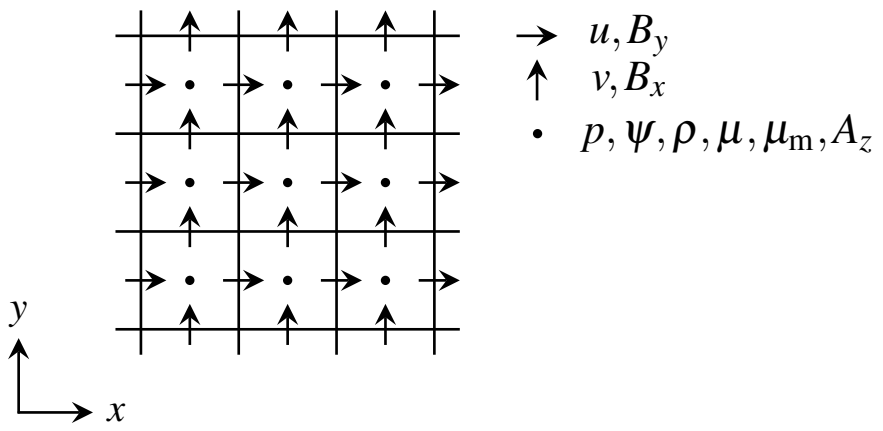

Figure 2.1: Staggered grid system in Cartesian coordinates. In the staggered grid arrangement, the values of scalar fields such as pressure (p), level set function (ψ), density (ρ), dynamic viscosity (μ), magnetic permeability (μ_m), and $z-$component of the vector potential (A_z), are defined at cell centers. Velocity components, u and v, as well as magnetic field components, B_x and B_y, are defined at cell faces.

The second-order differential operator with respect to the x_2- and x_3-directions, $\frac{\delta_n \phi}{\delta_n x_2}$ and $\frac{\delta_n \phi}{\delta_n x_3}$, can be defined in the same manner. The second-order interpolation of a quantity ϕ defined on the computational domain $\boldsymbol{x} = (x_1, x_2, x_3)$ with the stencil size n in the x_1-direction is given as

$$\overline{\phi}^{n\,x_1} = \frac{\phi\,(x_1 + n\,\Delta x/2,\, x_2,\, x_3) + \phi\,(x_1 - n\,\Delta x/2,\, x_2,\, x_3)}{2}, \tag{2.2}$$

and is defined similarly in the x_2- and x_3-directions.

The $n^{\mathrm{th}}-$order central finite-difference operator in x_i-direction is defined as

$$\frac{\delta_{n\mathrm{th}}\,\phi}{\delta_{n\mathrm{th}}\,x_i} = \sum_{l=1}^{n/2} \alpha_l \frac{\delta_{(2l-1)}\,\phi}{\delta_{(2l-1)}\,x_i}, \tag{2.3}$$

where weight values, α_l, are calculated as

$$\sum_{l=1}^{n/2} (2l-1)^{2(k-1)}\,\alpha_l = \delta_{kl}, \quad k \in [1,\, n/2]. \tag{2.4}$$

Additionally, the $n^{\text{th}}-$order interpolation in the x_i-direction is given as

$$\overline{\phi}^{n\text{th } x_i} = \sum_{l=1}^{n/2} \alpha_l \, \overline{\phi}^{(2l-1)\, x_i}. \tag{2.5}$$

The introduced $n^{\text{th}}-$order finite-difference and interpolation schemes will be later used to discretize the governing equations.

2.3 Implementation of level set

The traditional level set function introduced by Sethian (1999) is a smooth signed distance function given as

$$|\phi\,(\boldsymbol{x}, t)\,| = |\boldsymbol{x} - \boldsymbol{x}_\Gamma|, \tag{2.6}$$

where variable $\boldsymbol{x}_\Gamma$ denotes the closest point on the interface from point $\boldsymbol{x}$. The positive and negative values of $\phi(\boldsymbol{x}, t)$ indicate the location of a point relative to the interface, with convention determining which side is positive or negative. Therefore, the zero iso-contour of the defined signed distance function, $\phi(\boldsymbol{x}, t)$=0, corresponds to the interface itself. The level set motion under the velocity field $\boldsymbol{u}$ can be described using the following transport equation

$$\frac{\partial \phi}{\partial t} + \boldsymbol{u} \cdot \nabla \phi = 0. \tag{2.7}$$

Advecting the interface employing Eq. (2.7) for a few time steps can cause the ϕ function to lose its signed distance property, becoming distorted and losing its smoothness, thereby causing issues in the simulation (Desjardins *et al.*, 2008*b*). To prevent this issue, different re-initialization methods have been introduced to reconstruct the ϕ function to be a smooth signed distance function during the simulation. One of the well-known re-initialization techniques is solving a Hamilton–Jacobi equation, introduced by Sussman *et al.* (1994), which can be solved using high-order numerical discretization schemes and recover the distance function accurately. This method is proven to have various limitations, thoroughly discussed in the literature (Desjardins *et al.*, 2008*b*; Sethian, 1999), which are outside the scope of this paper. However, the main disadvantage of using this approach for simulating two-phase

flows is that both the transport equation and re-initialization process fail to conserve the volume of the region enclosed by the zero iso-contour. This can result in mass gain or loss in numerical simulations, leading to unphysical results. In this study, the conservative level set method (CLS) is employed to address this issue.

In the CLS approach (Olsson & Kreiss, 2005), the interface between two immiscible flows is defined using a diffuse profile in the form of a hyperbolic tangent function, ψ, as below

$$\psi(\boldsymbol{x}, t_0) = \frac{1}{2}\left(\tanh\left(\frac{\phi(\boldsymbol{x}, t_0)}{2\epsilon}\right) + 1\right), \tag{2.8}$$

where ϵ is a parameter to indicate the interface thickness and is commonly defined as a function of the mesh resolution. In the hyperbolic tangent definition, the iso-contour 0.5, $\psi\left(\boldsymbol{x}, t\right)$=0.5, specifies the location of the interface. For an incompressible flow, $\nabla \cdot \boldsymbol{u} = 0$, the transport equation can then be re-written as

$$\frac{\partial \psi}{\partial t} + \nabla \cdot (\boldsymbol{u}\psi) = 0. \tag{2.9}$$

In order to recover the hyperbolic tangent form of the level set profile, maintain the interface thickness, and prevent diffusion and smearing of the interface during the simulation, a re-initialization step should be introduced. The derived conservative re-initialization step by Olsson & Kreiss (2005) is given as

$$\frac{\partial \psi}{\partial \tau} + \nabla \cdot \left(\psi\left(1-\psi\right)\boldsymbol{n}\right) = \nabla \cdot \left(\epsilon \nabla \psi\right), \tag{2.10}$$

where the variable τ is the pseudo-time, $\boldsymbol{n}$ is the normal vector at $\tau = 0$, calculated as $\boldsymbol{n} = \nabla\psi/|\nabla\psi|$, and the equation is solved until convergence is reached. In the proposed re-initialization step, the compression flux, $\psi\left(1-\psi\right)\boldsymbol{n}$, is included to maintain the resolution of the interface and sharpen the profile which may smear due to the numerical diffusion occurring during the simulation of the transport equation. Also, in order to make sure that the level set profile remains of thickness ϵ and avoids the formation of discontinuities at the interface, the diffusion flux, $\epsilon\nabla\psi$, with a small amount of viscosity is added to the re-initialization equation. In Eq. (2.10), the diffusion in the normal direction to the interface

would be balanced by the compression term. However, diffusion might also occur in the direction tangential to the interface, causing the interface to move (Olsson *et al.*, 2007). For that reason, in the later study by Olsson *et al.* (2007), the diffusion term has been modified as $\nabla \cdot (\epsilon (\nabla\psi \cdot \boldsymbol{n}) \boldsymbol{n})$ to avoid any tangential movement of the interface due to diffusion, improving the re-initialization process.

2.3.1 High-order level set transport

Employing the notation introduced in Section 2.2, the $n^{\text{th}}-$order level set transport can be discretized as

$$\nabla \cdot (\boldsymbol{u}\psi) = \sum_{i=1}^{3} \left(\frac{\delta_{2\text{nd}}}{\delta_{2\text{nd}}\, x_i} \left[u_i \overline{\psi}^{n\text{th}\, x_i} \right] \right) \tag{2.11}$$

where $\overline{\psi}^{n\text{th}\, x_i}$ is a $n^{\text{th}}-$order interpolation of the variable ψ to the cell face in $i-$direction and u_i is the $i^{\text{th}}-$component of the velocity vector. Instead of using central interpolation schemes, it is better to use an upwind-biased scheme to prevent numerical oscillations appearing around $\psi = 0.5$. Thus, different upwind-biased approaches can be employed in order to calculate interpolated ψ values at the cell faces, such as WENO-type schemes (Liu *et al.*, 1994; Jiang & Shu, 1996; Su & Kim, 2018) or High Order Upstream Central (HOUC) schemes (Nourgaliev & Theofanous, 2007). The use of higher order schemes improves the conservation of the transported level set, reducing the need for re-initialization and yielding more accurate results. In this study, we utilize the fifth-order WENO interpolation method, described in detail in Appendix A. This approach is non-oscillatory and aims to mitigate unwanted oscillations, especially near sharp gradients, providing a smooth solution at each time step. The third-order total variation diminishing (TVD) Runge–Kutta scheme is used for the temporal integration, presented in Appendix B. Employing TVD spatial and temporal numerical schemes suppresses the formation of unwanted oscillations in the numerical simulation of the ψ profile, which is one of the main considerations in solving Eq. (2.9).

2.3.2 Level set conservative re-initialization

As mentioned earlier, it is essential to maintain a consistent thickness of the hyperbolic tangent profile during the transport of the level set function. However, numerical schemes

may diffuse the interface, resulting in a violation of mass conservation in the simulation. To address this issue, the re-initialization step is incorporated into the level set transport equation. The implemented re-initialization equation in this study, given as

$$\frac{\partial \psi}{\partial \tau} + \nabla \cdot (\psi (1-\psi) \boldsymbol{n}) = \nabla \cdot (\epsilon (\nabla \psi \cdot \boldsymbol{n}) \boldsymbol{n}), \tag{2.12}$$

is taken from the work by Olsson *et al.* (2007), although their discretization method is based on the finite-element approach. Therefore, we will establish a robust, consistent finite-difference approach inspired by the study of Desjardins *et al.* (2008*b*) to numerically discretize Eq. (2.12). To proceed, we denote the diffusive and compressive fluxes as $\boldsymbol{F}_{\mathrm{D}} = \epsilon (\nabla \psi \cdot \boldsymbol{n}) \boldsymbol{n}$ and $\boldsymbol{F}_{\mathrm{C}} = \psi (1-\psi) \boldsymbol{n}$, respectively. According to the analysis shown by Desjardins *et al.* (2008*b*), employing a more compact computational stencil to discretize Eq. (2.12) will lead to a more accurate and robust reconstruction of the interface while eliminating the appearance of spurious oscillations; hence, the second-order discretization is employed. For the sake of clarity, we rewrite Eq. (2.12) for a two-dimensional case as below

$$\frac{\partial \psi}{\partial \tau} + \overbrace{\frac{\partial}{\partial x}(\psi (1-\psi) n_x) + \frac{\partial}{\partial y}(\psi (1-\psi) n_y)}^{\text{compression}} = \underbrace{\epsilon \frac{\partial}{\partial x}\left(\frac{\partial \psi}{\partial x} {n_x}^2 + \frac{\partial \psi}{\partial y} n_x n_y\right) + \epsilon \frac{\partial}{\partial y}\left(\frac{\partial \psi}{\partial x} n_x n_y + \frac{\partial \psi}{\partial y} {n_y}^2\right)}_{\text{diffusion}}. \tag{2.13}$$

In order to update the cell center ψ values, compression and diffusion fluxes should be calculated at cell faces, and components of the normal vector should be found at cell faces. To this end, normal values at cell faces, i.e., face normals (Desjardins *et al.*, 2008*b*), are calculated, determining $x-$ and $y-$components of the normal vector at cell faces in both $x-$ and $y-$directions. The x_i-component of ψ gradient across the x_i-face is given as

$$(\nabla \psi)_i^{x_i-\text{face}} = \left.\frac{\partial \psi}{\partial x_i}\right|_{x_i-\text{face}} = \frac{\delta_{2\text{nd}} \psi}{\delta_{2\text{nd}}\, x_i}, \tag{2.14}$$

while for the x_j-component, a second-order interpolation of ψ in the x_i-direction is needed, and the face gradient value is calculated as

$$(\nabla\psi)_j^{x_i-\text{face}} = \left.\frac{\partial\psi}{\partial x_j}\right|_{x_i-\text{face}} = \frac{\delta_{2\text{nd}}\overline{\psi}^{2\text{nd}\,x_i}}{\delta_{2\text{nd}}\ x_j}. \tag{2.15}$$

Normalized face gradient values will correspond to normal vector values at cell faces, defining the normal vector at x_i-face as $\boldsymbol{n}^{x_i} = (\nabla\psi)^{x_i-\text{face}} / |\,(\nabla\psi)^{x_i-\text{face}}\,|$. Therefore, the discrete version of diffusion and compression terms can be written as

$$\nabla\cdot\left(\epsilon\left(\nabla\psi\cdot\boldsymbol{n}\right)\boldsymbol{n}\right) = \epsilon\sum_{i=1}^{3}\left(\frac{\delta_{2\text{nd}}}{\delta_{2\text{nd}}\ x_i}\left[\boldsymbol{n}_i^{x_i}\left(\boldsymbol{n}^{x_i}\cdot(\nabla\psi)^{x_i-\text{face}}\right)\right]\right), \tag{2.16}$$

and

$$\nabla\cdot\left(\psi\left(1-\psi\right)\boldsymbol{n}\right) = \sum_{i=1}^{3}\left(\frac{\delta_{2\text{nd}}}{\delta_{2\text{nd}}\ x_i}\left[\boldsymbol{n}_i^{x_i}\overline{\psi\left(1-\psi\right)}^{2\text{nd}\,x_i}\right]\right), \tag{2.17}$$

respectively. According to Olsson *et al.* (2007), the re-initialization equation converges quickly. In their study, it has been shown that for the case of $\Delta x \sim \Delta t \sim \epsilon$, the solution of the conservative re-initialization will converge within one or two steps.

Desjardins *et al.* (2008*b*) demonstrated that by employing the length scale analysis, the proper $\Delta\tau$ and the number of steps needed to obtain the steady state solution of the re-initialization equation can be determined. They showed that by taking the CFL number of the convection equation, Eq. (2.9), to be n times greater than the CFL number corresponding to the compression term in the re-initialization equation, Eq. (2.12), $n\,\text{CFL}_{\text{comp}} = \text{CFL}_{\text{conv}}$, the solution of the re-initialization equation converges after n steps. Thus, there is no requirement to evaluate the convergence criteria during the simulation. Our simulations utilize this approach and produce decent, robust results for the re-initialization step, further explained in the following section.

2.3.3 Level set test cases

In Appendix C, the numerical order of accuracy of the implemented level set solver is demonstrated through the rotating circle test case. In this section, the accuracy, consistency, and

robustness of the level set solver along with the re-initialization procedure are verified and discussed using two additional test cases, i.e., the circle in a deformation field and Zalesak's disk problems.

2.3.3.1 Circle in a deformation field

The main purpose of this test case is to evaluate the ability of the solver to properly resolve thin filament structures, mainly appearing in stretching and tearing flows (Enright *et al.*, 2002). Here, the initial center of the circle interface is located at $(0.5, 0.75)$, with the radius of $r = 0.15$. The interface thickness equals to $\epsilon = (\Delta x)^{0.7}/2$, and the simulation is performed on the computational domain $[x, y] \in [0, 1] \times [0, 1]$, with the grid resolution of 256×256. The velocity field is defined as

$$u = \sin(\pi x) \sin(\pi x) \sin(2\pi y), \tag{2.18}$$

and

$$v = -\sin(\pi y) \sin(\pi y) \sin(2\pi x), \tag{2.19}$$

causing the circle interface to stretch out into a long, thin fluid element that continuously wraps around itself. The CFL values are set as 0.5 and 0.25 for transport and re-initialization equations, respectively, and the re-initialization process is applied every five steps. Figure 2.2(a) displays the evolution of the interface, $\psi = 0.5$, at eight different time steps: $t = 0.5, 1, 1.5, 2, 2.5, 3, 3.5$, and 4 in black. Figure 2.2(a) visually confirms that the implemented solver is capable of sustaining thin, elongated filament structures of the interface for a long simulation time. The calculated maximum area loss during the simulation, from $t = 0$ to 4, is equal to 2.8%, demonstrating the area-conserving character of the level set solver, even after stretching the vortex for a long time and causing the trailing ligament thickness to become of the order of the mesh resolution. Additionally, in order to evaluate how the thickness of the transition layer changes, $\psi = 0.05$ and $\psi = 0.95$ contours are also depicted in blue and purple, respectively, for the first six time steps, as for the final stages of the vortex stretching, the thickness becomes too thin, and visualization of the transition layer is a bit difficult. According to the presented contours, the thickness of the transition layer

remains almost constant even after drastic changes in the interface. However, at the tail of the stretched vortex, it can be seen that the transition layer is not constant. This is mainly due to the fact that the thickness of the stretched circle becomes similar to the thickness of the interface. This behaviour was also observed in other studies like the one by Olsson & Kreiss (2005) and is called a pinch-off effect. The pinch-off is a numerical effect and can be prevented if the interface's thickness is smaller than the distance between two interfaces.

Figure 2.2(b) presents the interface location of the vortex at $t = 4.5$ in black, while the blue iso-contour depicts the solution at the same time without applying the re-initialization step during the simulation, from $t = 0$ to 4.5. Figure 2.2(b) makes evident that incorporating the re-initialization process in the simulation leads to a smoother solution with better area conservation. The zoomed-in insets in Fig. 2.2(b) better illustrate that employing the re-initialization step during the simulation results in a better reconstruction of the thin filaments and prevent the tearing of the interface in the solution, leading to a more conservative solution.

To achieve a better quantitative analysis and error calculation, the vortex field can be reversed in time by multiplying the velocity components by $\cos(\pi t/T)$, where T denotes the time that the circle returns to its initial state, and, therefore, the interface location is known. In our simulation, the periodicity is set to $T = 2$, and the simulation is run from $t = 0$ to $t = 4$, hence, the interface goes through two complete rotations. Figure 2.3(a) illustrates the interface from $t = 0$ to 4 with increments of 0.5, showing that the circle interface goes through two complete rotations and returns to its original place at $t = 4$. The calculated root mean square (rms) of the error for the level set field at $t = 2$ and 4, are 4.8×10^{-3} and 7×10^{-3}, respectively.

The area loss during the simulation and the convergence of the numerical result for increasing mesh resolutions are studied by repeating this test case for four other resolutions, 16×16, 32×32, 64×64, and 128×128. In order to investigate the mass conservation property of the implemented level set, A/A_0 is calculated, where A_0 represents the initial area and A is the computed area at each time step, for all five grid resolutions. In Fig. 2.3(b), the conservative behaviour of the implemented level set is demonstrated by a decrease in area loss as the mesh is refined and the value of A/A_0 becomes closer to one as the grid resolution

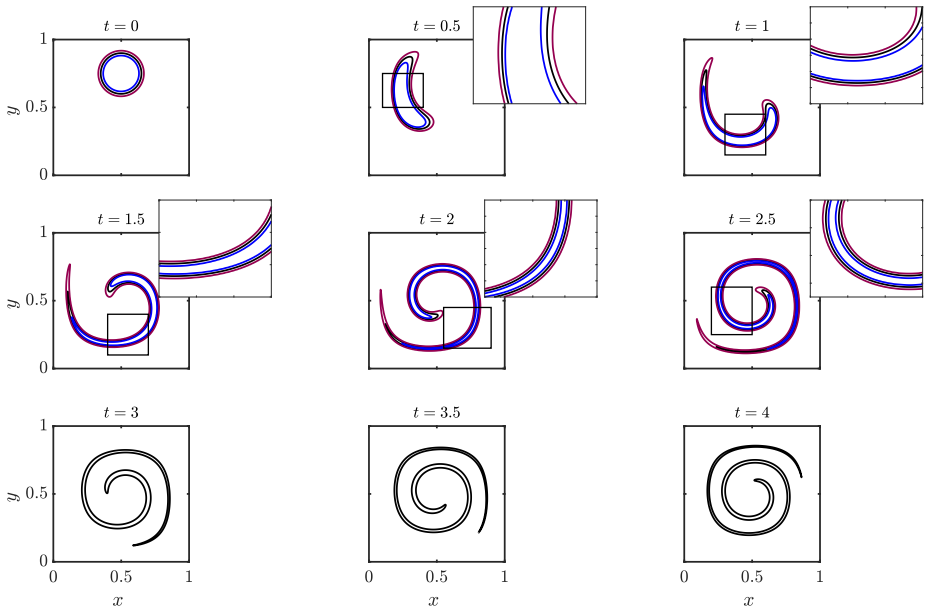

(a)

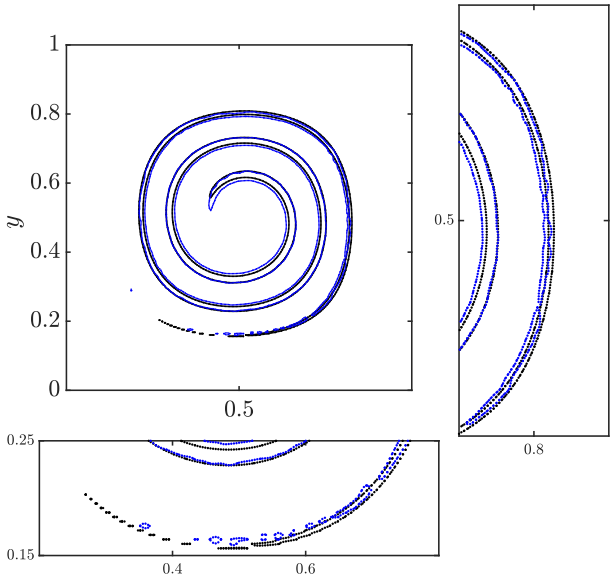

(b)

Figure 2.2: (a) The interface location, $\psi = 0.5$ (in black), of the single vortex in the velocity field defined by Eqs. (2.18-2.19), from $t = 0$ to $t = 4.0$, with the grid resolution of 256×256 and CFL$= 0.5$. For $t = 0$ to 2.5, $\psi = 0.05$ and $\psi = 0.95$ contours are also plotted in blue and purple, respectively. (b) Interface location of the vortex in the deformation field, black: with re-initialization process applied every five time steps, and blue: without re-initialization step.

is increased. Figure 2.3(b) also compares the numerical and analytical results for different mesh resolutions. Furthermore, increasing the grid resolution leads to the convergence of the numerical result to its analytical counterpart. The conservative property noticeably improved when the mesh resolution is increased from 16×16 to 32×32. For mesh resolutions 64×64, 128×128, and 256×256, the calculated $\psi = 0.5$ contour is close to the analytical interface, and for 128×128 and 256×256, the computed interface is indistinguishable from the exact one. In order to evaluate the accuracy of the solver, the L_∞ error of the area loss during the simulation from $t = 0$ to 4 is calculated for all five mesh resolutions. In Fig. 2.3(c), the calculated error values are plotted against the computational grid size using a logarithmic scale. According to Fig. 2.3(c), the error decreases as the mesh is refined, and a second-order convergence is achieved. This convergence analysis indicates that the solver is able to maintain second-order accuracy for the mass conservation property even for more pronounced interface deformations over prolonged periods of simulation. It is worth noting that the complexity of the interface evolution may necessitate more frequent re-initialization steps to ensure optimal mass conservation during the simulation. The re-initialization step is second-order accurate and can affect the global order of accuracy of the solver. That is why the convergence rate here is expected to be less than that of the test case presented in Appendix C.

2.3.3.2 Zalesak's disk

The Zalesak's disk problem, widely used in the literature to indicate the robustness of a solver towards diffusion errors (Mizuno *et al.*, 2022), is studied in this section. In this test case, the ability of the solver to transport sharp corners and thin structures without introducing noticeable diffusion errors can be examined. This test case includes a notched circle in solid body rotation under the velocity field of $u = 2\pi\,(y - 0.5)$ and $v = -2\pi\,(x - 0.5)$. Initially, a notched circle of radius $r = 0.15$ is centred at $(0.5, 0.5)$ with a notch of width 0.05 and height 0.25 in the computational domain of $(x, y) \in [0, 1] \times [0, 1]$. At $t = 1$, the disk goes through one complete rotation and returns to its primary location. The level set thickness and CFL values are similar to the previous case, and a Dirichlet boundary condition is imposed at all boundaries. Figure 2.4 displays the solution at $t = 1$ for three different grid resolutions

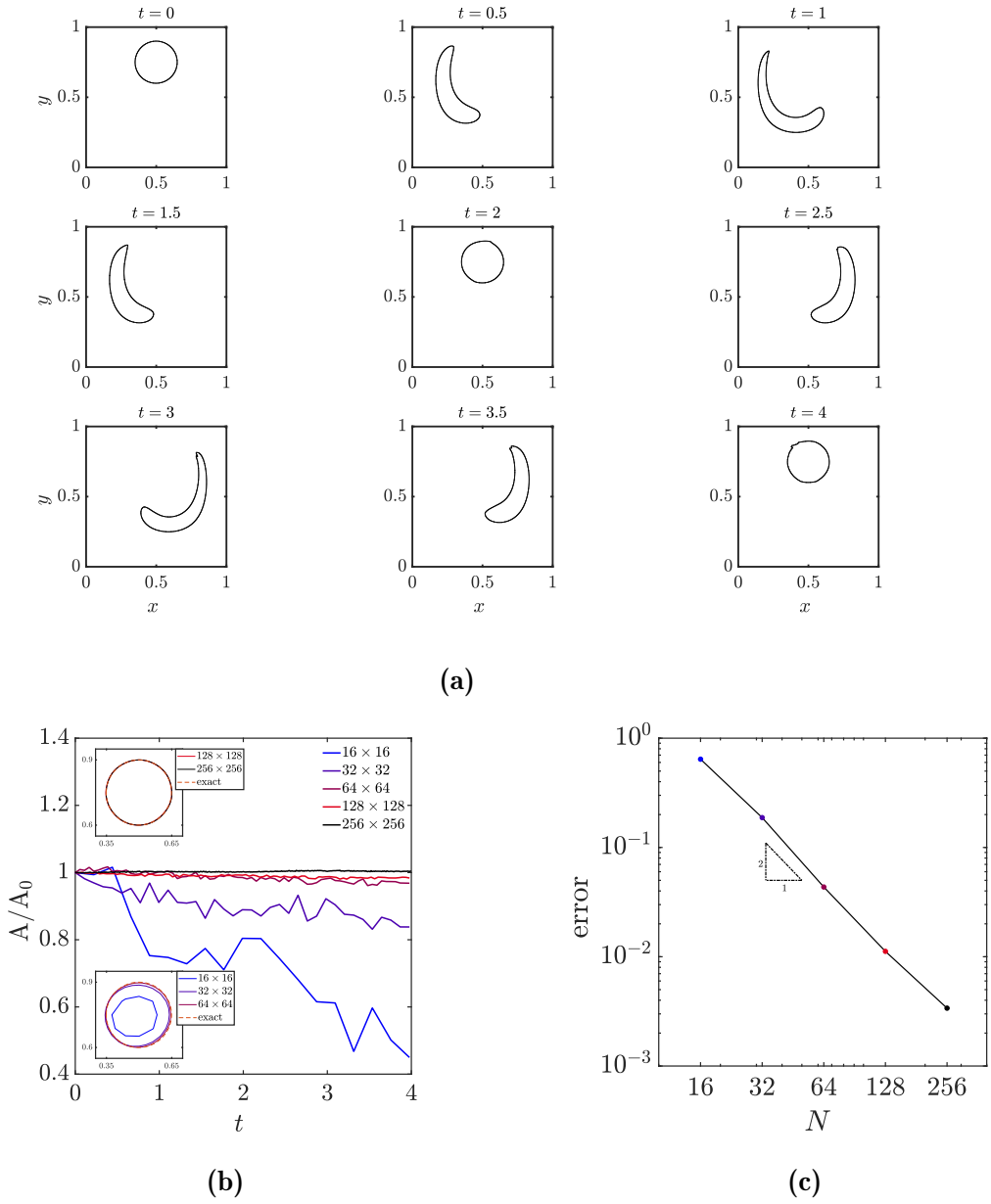

Figure 2.3: (a) The interface location of the circle in the vortex field with the periodicity of $T = 2$ at nine different time steps, $t = 0, 0.5, 1, 1.5, 2, 2.5, 3, 3.5$, and 4. The simulation is performed in the two-dimensional computational domain, $[x, y] \in [0, 1] \times [0, 1]$, with the grid resolution of 256×256, and CFL$= 0.5$. The re-initialization step is applied every five time steps. (b) The temporal evolution of the normalized area for the circle in the vortex field is compared for five different mesh resolutions of 16×16, 32×32, 64×64, 128×128, and 256×256. Additionally, the interface location of the circle, $\psi = 0.5$, is shown for all five different grid resolutions. (c) Order of convergence analysis of the area loss property. The L_∞ error values of the area loss are computed for five different grid resolutions and plotted against the grid size.

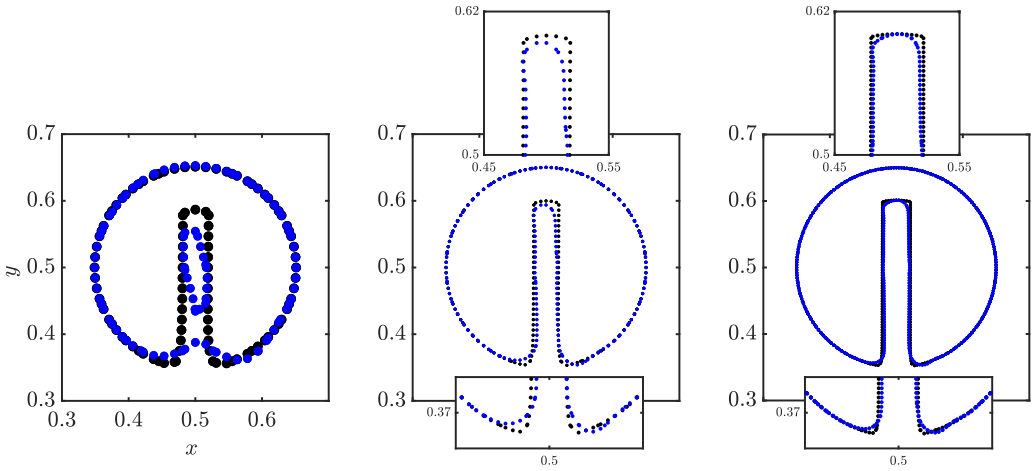

Figure 2.4: The interface of the Zalesak's disk, $\psi = 0.5$, for three different grid resolutions, $64 \times 64, 128 \times 128$, and 256×256, from left to right. The black contour shows the initial interface while the blue one represents the calculated interface at $t = 1$. The numerical solution converges to the exact solution by increasing the mesh resolution, accurately capturing the corners and structure of the interface.

64×64, 128×128, and 256×256. As can be seen in Fig. 2.4, increasing the grid resolution reduces the diffusion of the interface, and the final solution is close to the initial description of the interface, recovering the edges and corners of the disk more accurately (see zoomed-in insets). The calculated area loss for the three grid resolutions from coarse to fine are 0.43%, 0.25%, and 0.07%, respectively, showing the convergence of the solution by increasing the grid resolution.

2.4 Implementation of incompressible Navier–Stokes solver

In this section, the implementation of a high-order incompressible solver is presented. The density of each fluid particle does not change as it moves in the incompressible flow regime. Therefore, the mass conservation equation simplifies to a divergence-free condition for the velocity field, which must be satisfied while solving the momentum equation. To this end,

the projection method is adopted in our algorithm, and two test cases are examined to verify the accuracy and robustness of the implemented solver.

2.4.1 Governing equations

The incompressible form of the Navier–Stokes equations are given as

$$\frac{\partial \boldsymbol{u}}{\partial t} + \nabla \cdot (\boldsymbol{u}\boldsymbol{u}) = -\frac{1}{\rho}\nabla p + \frac{1}{\rho}\nabla \cdot \mu \left(\nabla \boldsymbol{u} + \nabla \boldsymbol{u}^{\mathrm{T}}\right) + \boldsymbol{g}, \tag{2.20a}$$

$$\nabla \cdot \boldsymbol{u} = 0, \tag{2.20b}$$

where $\boldsymbol{u}$ is the velocity vector, ρ is the density field, and p is the pressure field. Variables μ and $\boldsymbol{g}$ denote the dynamic viscosity and gravitational acceleration, respectively. It is noteworthy to mention that the momentum equation is solved in a conservative form, ensuring momentum conservation and avoiding unphysical numerical solutions. The presented incompressible numerical solver employs a spatial staggered-variable formulation, described in Section 2.2. Compared to a collocated formulation, staggering offers the benefit of localized derivative stencils in space that enhance the precision of the stencil. In order to solve the momentum equation, the pressure gradient is required at cell faces, where the velocity values are defined. In the staggered arrangement, the second-order pressure gradient can be calculated using pressure values that are one cell apart. However, in the collocated formulation, the pressure values that span three cells are needed to compute the second-order pressure derivative. The localized stencils accessible in staggered approaches are considerably more precise than the broader stencils that would be used in a collocated approach on the same mesh (Pierce, 2001). Furthermore, the staggered grid system offers a strong coupling between the pressure and velocity field when a Poisson equation is solved for the pressure compared to the collocated grids (Morinishi *et al.*, 1998). As a result, the unphysical solution obtained in the collocated grid system due to weak coupling is prevented.

2.4.2 Projection method

The main difficulty of numerically solving the incompressible Navier–Stokes equations is the lack of an explicit time-derivative term in the continuity equation. Consequently, the velocity divergence-free constraint must be satisfied by implicitly coupling the mass equation with the pressure term in the momentum equation (Kim & Moin, 1985). To this end, this study incorporates the projection method initially introduced by Chorin (1997), which is based on the Helmholtz–Hodge decomposition that states any vector field can be decomposed into two components: solenoidal (divergence-free), and irrotational (curl-free). In this operator splitting approach, the momentum equation is divided into two separate equations, given as

$$\frac{\tilde{\boldsymbol{u}}^{n+1}-\boldsymbol{u}^{n}}{\Delta t}=-\nabla\cdot(\boldsymbol{u}^{n}\boldsymbol{u}^{n})+\frac{1}{\rho}\nabla\cdot\mu\left(\nabla\boldsymbol{u}^{n}+(\nabla\boldsymbol{u}^{n})^{\mathrm{T}}\right)+\boldsymbol{g}, \tag{2.21a}$$

and

$$\frac{\boldsymbol{u}^{n+1}-\tilde{\boldsymbol{u}}^{n+1}}{\Delta t}+\frac{\nabla p^{n+1}}{\rho}=0, \tag{2.21b}$$

where $\tilde{\boldsymbol{u}}$ denotes the intermediate velocity which does not necessarily satisfy the divergence-free constraint. Adding Eq. (2.21a) and Eq. (2.21b) recovers the original momentum equation, i.e., Eq. (2.20a). Equation (2.21a), also known as the intermediate step, is straightforward to solve since only one unknown is present in the equation, that is, the intermediate velocity, $\tilde{\boldsymbol{u}}$. However, Eq. (2.21b) has two unknown variables and cannot be solved in its present form. To address this issue, by taking the divergence of Eq. (2.21b) and knowing that the velocity field solution at time step $n+1$ should be divergence-free, $\nabla\cdot\boldsymbol{u}^{n+1}=0$, the following equation will be obtained

$$\nabla\left(\frac{1}{\rho}\nabla p^{n+1}\right)=\frac{1}{\Delta t}\nabla\cdot\tilde{\boldsymbol{u}}^{n+1}, \tag{2.22}$$

which is a Poisson equation for pressure. Since the density is constant, Eq. (2.22) can be simplified as

$$\Delta p^{n+1}=\frac{\rho}{\Delta t}\nabla\cdot\tilde{\boldsymbol{u}}^{n+1}. \tag{2.23}$$

In this way, the intermediate velocity field, which was initially computed without forcing incompressibility, is projected into the divergence-free field, satisfying Eq. (2.20b). Solving the Poisson equation for pressure results in the solution for the pressure field. Lastly, the velocity field at time step $n+1$ can be updated by rearranging Eq. (2.21b) to be read as

$$\boldsymbol{u}^{n+1} = \tilde{\boldsymbol{u}}^{n+1} - \left(\frac{\Delta t}{\rho}\right) \nabla p^{n+1}. \tag{2.24}$$

Here, the projection method is explained using the first-order Euler scheme to discretize time derivative terms. The projection method can be easily extended to other numerical temporal-integration schemes, such as the third-order Runge–Kutta method employed in this study.

Using the notation introduced in Section 2.2, the $n^{\text{th}}-$order spatial discretization of the diffusion term for the x_1-component can be written as

$$\begin{aligned}\left[\nabla \cdot \mu \left(\nabla \boldsymbol{u} + \nabla \boldsymbol{u}^T\right)\right]_{x_1}^{n\text{th}-\text{order}} = & \frac{\delta_{n\text{th}}}{\delta_{n\text{th}}\, x_1}\left[2\mu\left(\frac{\delta_{n\text{th}}\, u_1}{\delta_{n\text{th}}\, x_1}\right)\right] \\ & + \frac{\delta_{n\text{th}}}{\delta_{n\text{th}}\, x_2}\left[\overline{\overline{\mu}^{2\text{nd}\, x_1}}^{2\text{nd}\, x_2}\left(\frac{\delta_{n\text{th}}\, u_1}{\delta_{n\text{th}}\, x_2} + \frac{\delta_{n\text{th}}\, u_2}{\delta_{n\text{th}}\, x_1}\right)\right] \\ & + \frac{\delta_{n\text{th}}}{\delta_{n\text{th}}\, x_3}\left[\overline{\overline{\mu}^{2\text{nd}\, x_1}}^{2\text{nd}\, x_2}\left(\frac{\delta_{n\text{th}}\, u_1}{\delta_{n\text{th}}\, x_3} + \frac{\delta_{n\text{th}}\, u_3}{\delta_{n\text{th}}\, x_1}\right)\right],\end{aligned} \tag{2.25}$$

where $\boldsymbol{u} = (u_1, u_2, u_3)$. In this study, the second-order finite-difference scheme is implemented to discretize the diffusion term. Hence, the x_1- and x_2-components of the diffusion term, $\nabla \cdot \mu \left(\nabla \boldsymbol{u} + \nabla \boldsymbol{u}^{\mathrm{T}}\right)$, can be computed as

$$\left[\nabla \cdot \mu \left(\nabla \boldsymbol{u} + \nabla \boldsymbol{u}^{\mathrm{T}}\right)\right]_{x_1}^{2\text{nd}-\text{order}} = \frac{\delta_2\, T_{x_1 x_1}}{\delta_2\, x_1} + \frac{\delta_2\, T_{x_1 x_2}}{\delta_2\, x_2}, \tag{2.26a}$$

and

$$\left[\nabla \cdot \mu \left(\nabla \boldsymbol{u} + \nabla \boldsymbol{u}^{\mathrm{T}}\right)\right]_{x_2}^{2\text{nd}-\text{order}} = \frac{\delta_2\, T_{x_1 x_2}}{\delta_2\, x_1} + \frac{\delta_2\, T_{x_2 x_2}}{\delta_2\, x_2}, \tag{2.26b}$$

where

$$T_{x_1x_1} = 2\mu \left(\frac{\delta_2 \, u_1}{\delta_2 \, x_1} \right), \tag{2.26c}$$

$$T_{x_1x_2} = \mu \left(\frac{\delta_2 \, u_1}{\delta_2 \, x_2} + \frac{\delta_2 \, u_2}{\delta_2 \, x_1} \right), \tag{2.26d}$$

and

$$T_{x_2x_2} = 2\mu \left(\frac{\delta_2 \, u_2}{\delta_2 \, x_2} \right). \tag{2.26e}$$

The discretization can be simply extended to the three-dimensional case, $\boldsymbol{x} = (x_1, x_2, x_3)$.

Most previous numerical studies have employed a second-order discretization for the convection term, $\nabla \cdot (\boldsymbol{uu})$, in the context of two-phase flows. This choice is made because discontinuities are expected to arise in the velocity fields across the interface, and transitioning to a higher-order finite-difference scheme introduces numerical challenges. In this study, instead of utilizing second-order interpolation, we adopted fifth-order WENO interpolation for discretizing the convection term. This approach has been demonstrated to yield approximately third-order accuracy for the single-phase incompressible solver (please refer to Appendix D) and provides second-order accuracy for the two-phase solver. This improvement is notable when compared to other second-order based numerical discretizations. The employed discretization of $\nabla \cdot (\boldsymbol{uu})$ term for $\boldsymbol{x} = (x_1, x_2)$ in this study is given as

$$\begin{aligned} \left[\nabla \cdot (\boldsymbol{uu})\right]_{x_1} = & \frac{\delta_2}{\delta_2 \, x_1} \left(\overline{u_1}^{5^{\text{th}}\text{WENO } x_1} \; \overline{u_1}^{5^{\text{th}}\text{WENO } x_1} \right) \\ & + \frac{\delta_2}{\delta_2 \, x_2} \left(\overline{u_1}^{5^{\text{th}}\text{WENO } x_2} \; \overline{u_2}^{5^{\text{th}}\text{WENO } x_1} \right), \end{aligned} \tag{2.27a}$$

and

$$\begin{aligned} \left[\nabla \cdot (\boldsymbol{uu})\right]_{x_2} = & \frac{\delta_2}{\delta_2 \, x_1} \left(\overline{u_1}^{5^{\text{th}}\text{WENO } x_2} \; \overline{u_2}^{5^{\text{th}}\text{WENO } x_1} \right) \\ & + \frac{\delta_2}{\delta_2 \, x_2} \left(\overline{u_2}^{5^{\text{th}}\text{WENO } x_2} \; \overline{u_2}^{5^{\text{th}}\text{WENO } x_2} \right). \end{aligned} \tag{2.27b}$$

The Poisson equation for the pressure is discretized using the second-order central finite-difference scheme. The solution of the Poisson equation is computed at each iteration of the

simulation by employing Krylov methods and multi-grid preconditioning implemented in the PETSc package library (Balay *et al.*, 1997).

In the staggered grid arrangement shown in Fig. 2.1, boundary conditions for the velocity components normal to the boundary can be readily implemented. However, imposing the proper boundary condition for the tangential components of the velocity can be more challenging. Thus, ghost points are used to apply the desired boundary condition for velocity components tangential to the boundary (Tryggvason *et al.*, 2011). For example, consider a case where the no-slip boundary condition is needed to be implemented for the velocity component in the $y-$direction, v, at the left boundary (see Fig. 2.5). In order to update the value of $v_{i,j+1/2}$, which has a half-cell offset from the left boundary, and to impose a proper boundary, the value of $v_{i-1,j+1/2}$ is needed that is located outside of the domain. The tangential velocity at this ghost point can be obtained by using linear interpolation as $v_{\text{boundary}} = \left(v_{i,j+1/2} + v_{i-1,j+1/2}\right)/2$, where v_{boundary} is the velocity value at the boundary, equal to the wall tangential velocity for the no-slip case. Therefore, the value at the ghost point can be calculated as $v_{i-1,j+1/2} = 2v_{\text{boundary}} - v_{i,j+1/2}$, and the no-slip boundary condition is imposed. The same approach can be taken for other boundary conditions as well. For instance, for the slip boundary condition where the derivative of the tangential velocity is zero, the value of the ghost point is given as $v_{i,j+1/2} = v_{i-1,j+1/2}$. In Appendix D, the order of accuracy and performance of the introduced incompressible solver are examined. Interested readers can refer to this section for more details.

2.5 Implementation of two-phase solver for nonmagnetic flows

This section presents the methodology implemented for simulating incompressible two-phase flows. The introduced solver is based on coupling the conservative level set (CLS) approach, detailed in Section 2.3 with the incompressible solver presented in Section 2.4. In two-phase flows, material properties such as density and viscosity experience a jump across the interface, requiring special numerical treatments to avoid the appearance of numerical instabilities. In addition, proper boundary conditions must be imposed across the interface to obtain accurate

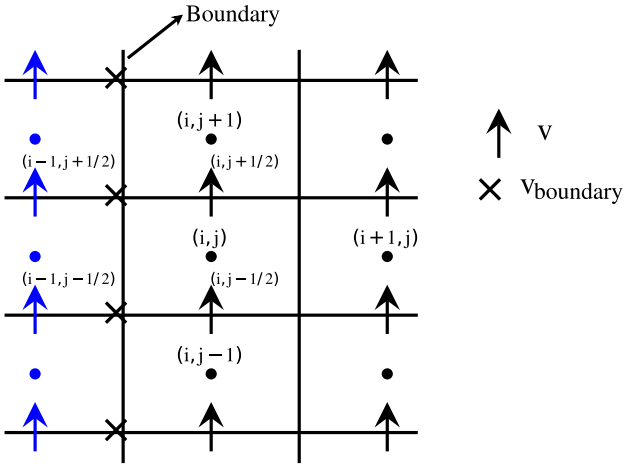

Figure 2.5: The proper boundary condition for the tangential velocity is implemented by employing ghost points located outside of the computational domain, shown in blue. The tangential velocity of these ghost points is specified to enable the linear interpolation to produce the intended tangent velocity at the wall.

physical results. This section, thus, discusses these issues and introduces a complete solution procedure for modelling two-phase flows.

2.5.1 One-fluid formulation

The governing equation for the one-fluid formulation approach to describe the two-phase incompressible flows is given as

$$\frac{\partial \boldsymbol{u}}{\partial t} + \nabla \cdot (\boldsymbol{u}\boldsymbol{u}) = -\frac{1}{\rho}\nabla p + \frac{1}{\rho}\nabla \cdot \mu \left(\nabla \boldsymbol{u} + \nabla \boldsymbol{u}^{\mathrm{T}}\right) + \boldsymbol{g} + \frac{1}{\rho}\boldsymbol{F}_{\mathrm{v}}, \tag{2.28}$$

where $\boldsymbol{F}_{\mathrm{v}}$ represents any volume force that may be present. The solution of Eq. (2.28) should also satisfy the incompressibility constraint. In each phase, the material properties are constant, that is, $\rho = \rho_{\mathrm{l}}$ and $\mu = \mu_{\mathrm{l}}$ for the liquid phase, while $\rho = \rho_{\mathrm{g}}$ and $\mu = \mu_{\mathrm{g}}$ for the gas phase. However, across the thin interface, denoted by Γ, fluid properties experience a jump that can be written as $[\rho]_\Gamma = \rho_{\mathrm{l}} - \rho_{\mathrm{g}}$ and $[\mu]_\Gamma = \mu_{\mathrm{l}} - \mu_{\mathrm{g}}$ for the density and dynamic viscosity, respectively. Since there is no mass exchange between the two phases, the normal

component of the velocity should be continuous across the interface, i.e.,

$$[\boldsymbol{u}\cdot\boldsymbol{n}]_\Gamma = \boldsymbol{u}_\mathrm{l}\cdot\boldsymbol{n} - \boldsymbol{u}_\mathrm{g}\cdot\boldsymbol{n} = 0, \tag{2.29}$$

where $\boldsymbol{n}$ is the normal vector to the interface. For viscous flows, the tangential component of the velocity should also be equal for the two phases at the interface. Thus, the velocity field should be continuous across the interface, and the boundary condition for the velocity can be written as

$$[\boldsymbol{u}]_\Gamma = 0. \tag{2.30}$$

Additionally, applying the momentum conservation principle to a control volume located at the interface leads to the following boundary condition for the pressure jump

$$[\left(-p\boldsymbol{I} + \mu\left(\nabla\boldsymbol{u} + \nabla\boldsymbol{u}^\mathrm{T}\right)\right)\cdot\boldsymbol{n}]_\Gamma = 0, \tag{2.31}$$

where $\boldsymbol{I}$ is the identity tensor. If the surface tension force is considered, the boundary condition for the pressure jump across the interface is modified as

$$[\left(-p\boldsymbol{I} + \mu\left(\nabla\boldsymbol{u} + \nabla\boldsymbol{u}^\mathrm{T}\right)\right)\cdot\boldsymbol{n}]_\Gamma = \sigma\kappa\boldsymbol{n}, \tag{2.32}$$

where variable σ denotes the surface tension coefficient. The curvature of the interface, κ, is calculated as $\kappa = -\nabla\cdot\boldsymbol{n} = -\nabla\cdot(\nabla\psi/|\nabla\psi|)$. In the present study, the corresponding jump condition in the pressure gradient is modelled by employing the continuum surface force (CSF) method of Brackbill *et al.* (1992). The CSF approach defines surface tension as a volume force spreading over the finite interface width, expressed as $F_\sigma = \sigma\kappa\nabla\psi$. Therefore, proper calculation of the interface curvature is essential for accurate and robust surface tension modelling, which will be discussed in more detail in the next section. The viscous term is also discretized using the CSF method.

2.5.2 Projection method and discretization

As previously introduced, the projection method is employed to solve the incompressible Navier–Stokes equations. This method involves two steps, known as prediction and correction. During the prediction step, Eq. (2.28) is solved, ignoring the pressure term, to advance the velocity field $\boldsymbol{u}^n$ to an intermediate velocity $\tilde{\boldsymbol{u}}^{n+1}$. In the correction step, the intermediate velocity is projected to its divergence-free solution, $\boldsymbol{u}^{n+1}$, using the solution of the pressure Poisson equation. The projection method has been discussed in Sec. 2.4.2 for the single incompressible flow case. However, for two-phase flows, special considerations and numerical treatments must be taken into account. The discretization of the convective term, $\nabla\cdot(\boldsymbol{u}\boldsymbol{u})$, can be performed similarly to the one demonstrated earlier in Sec. 2.4.2. The main challenges associated with treating the interface discontinuities in two-phase incompressible flows include properly modelling the viscosity discontinuity across the interface and accurately calculating the curvature. The viscosity term in the momentum equation must be appropriately discretized, particularly in the presence of a dynamic viscosity jump, to ensure the accurate calculation of kinetic energy dissipation near the interface. Additionally, a robust and accurate method to assess the evolution of the interface curvature should be employed to model the surface tension force. Another issue in two-phase flow simulations pertains to the numerical discretization of the pressure gradient term. The pressure gradient component in Eq. (2.28) includes the density term as well, and since the density has a jump across the interface, specific consideration is required. We will conclude this section by discussing these issues in more detail and presenting the discretization used to model viscosity, surface tension, and pressure jump terms.

Viscosity and surface tension modelling

The viscosity term, $\nabla\cdot\mu\left(\nabla\boldsymbol{u}+\nabla\boldsymbol{u}^{\mathrm{T}}\right)$, can be discretized using Eq. (2.25), which displays the general form of the $n^{\mathrm{th}}-$order spatial discretization of this term, considering a non-constant dynamic viscosity field. The implemented two-phase solver employs the second-order finite-difference scheme and second-order linear interpolation to discretize this term. Furthermore, the density and viscosity are assumed to smoothly vary over the interface (Olsson & Kreiss,

2005). Therefore, the density and viscosity fields can be represented using the level set function as

$$\rho\left(\boldsymbol{x},t\right)=\rho_{\mathrm{g}}+\left(\rho_{\mathrm{l}}-\rho_{\mathrm{g}}\right)\psi\left(\boldsymbol{x},t\right) \tag{2.33}$$

and

$$\mu\left(\boldsymbol{x},t\right)=\mu_{\mathrm{g}}+\left(\mu_{\mathrm{l}}-\mu_{\mathrm{g}}\right)\psi\left(\boldsymbol{x},t\right), \tag{2.34}$$

respectively. As a result, the discontinuity in the density and viscosity fields is smoothed out across the interface within a few layers of cells, which is the function of the interface thickness. Thus, numerical instabilities that may appear due to the sharp jump in fluid properties are avoided in the solution.

According to the CSF model introduced by Brackbill *et al.* (1992), the surface tension force per unit interfacial area between two fluids with a constant surface tension coefficient, σ, can be written as

$$\boldsymbol{F}_{\mathrm{sa}}\left(\boldsymbol{x}_{\Gamma}\right)=\sigma\kappa\left(\boldsymbol{x}_{\Gamma}\right)\boldsymbol{n}\left(\boldsymbol{x}_{\Gamma}\right), \tag{2.35}$$

where $\boldsymbol{x}_{\Gamma}$ is an arbitrary point located on the interface. The introduced interfacial surface tension force can be recast as

$$\boldsymbol{F}_{\mathrm{sv}}(\boldsymbol{x})=\sigma\overbrace{\left(-\nabla\cdot\frac{\nabla\psi}{|\nabla\psi|}\right)}^{\kappa}\nabla\psi, \tag{2.36}$$

which represents the surface tension volume force at any point $\boldsymbol{x}$ (Olsson & Kreiss, 2005). The introduced force $\boldsymbol{F}_{\mathrm{sv}}(\boldsymbol{x})$ results in the same total force as that of $\boldsymbol{F}_{\mathrm{sa}}(\boldsymbol{x}_{\Gamma})$, but it is distributed over the width of the interface. This approximation is only valid for small interface thicknesses. Therefore, it is essential to avoid excessively wide interfaces and to maintain a constant thickness for the interface during the simulation, which has been addressed in the implementation of the level set (see Sec. 2.3.2). In order to calculate the surface tension force, the solver should be able to robustly and accurately compute the curvature value. Employing high-order numerical schemes to calculate curvature results in oscillations appearing in the curvature field, leading to an unphysical solution for the velocity field, known as spurious currents. To tackle this issue, first- or second-order schemes are usually used to

calculate curvature values. Various methods have been developed, such as utilizing height functions or implementing the least-squares minimization approach (Boniou *et al.*, 2022), to formulate a robust and consistent framework for curvature calculation. However, most of these approaches are computationally expensive and difficult to implement. In this study, curvature computation is based on using the calculated face normals introduced in Sec. 2.3.2. Therefore, the curvature field for the two-dimensional case is given as

$$\kappa = \frac{\delta_{2\text{nd}} \left(\boldsymbol{n}_x\right)^{x-\text{face}}}{\delta_{2\text{nd}}\, x} + \frac{\delta_{2\text{nd}} \left(\boldsymbol{n}_y\right)^{y-\text{face}}}{\delta_{2\text{nd}}\, y}. \tag{2.37}$$

Equation (2.37) is second-order accurate and can be easily implemented, requiring no additional computational effort. Various test cases have been conducted to evaluate the results obtained from the Eq. (2.37) curvature calculation, demonstrating its robustness. Notably, the results exhibit no discernible oscillations, which will be expounded upon in the subsequent section. Finally, for the two-dimensional case of $\boldsymbol{x} = (x, y)$, the $x-$ and $y-$components of the surface tension force spatial discretization can be written as

$$[\sigma\kappa\nabla\psi]_{x-\text{comp}} = \sigma\overline{\left(\frac{\delta_{2\text{nd}} \left(\boldsymbol{n}_x\right)^{x-\text{face}}}{\delta_{2\text{nd}}\, x} + \frac{\delta_{2\text{nd}} \left(\boldsymbol{n}_y\right)^{y-\text{face}}}{\delta_{2\text{nd}}\, y}\right)}^{2\text{nd}\,x} \frac{\delta_{2\text{nd}}\, \psi}{\delta_{2\text{nd}}\, x} \tag{2.38a}$$

and

$$[\sigma\kappa\,\nabla\psi]_{y-\text{comp}} = \sigma\overline{\left(\frac{\delta_{2\text{nd}} \left(\boldsymbol{n}_x\right)^{x-\text{face}}}{\delta_{2\text{nd}}\, x} + \frac{\delta_{2\text{nd}} \left(\boldsymbol{n}_y\right)^{y-\text{face}}}{\delta_{2\text{nd}}\, y}\right)}^{2\text{nd}\,y} \frac{\delta_{2\text{nd}}\, \psi}{\delta_{2\text{nd}}\, y}, \tag{2.38b}$$

respectively.

Poisson equation

In the two-phase incompressible solver, since the density field is not constant in the computational domain, the Poisson equation cannot be simplified as Eq. (2.23), and the variable coefficients should be considered while discretizing the Poisson equation. Therefore, the second-order discretization of the Poisson equation can be written as

$$
\begin{aligned}
\nabla\left(\frac{1}{\rho}\nabla p\right)\Bigg|_{i,j} &= \frac{\partial}{\partial x}\left(\frac{1}{\rho}\frac{\partial p}{\partial x}\right)\Bigg|_{i,j} + \frac{\partial}{\partial y}\left(\frac{1}{\rho}\frac{\partial p}{\partial y}\right)\Bigg|_{i,j} \\
&= \frac{\left(\frac{1}{\rho}\frac{\partial p}{\partial x}\right)_{i+1/2,j} - \left(\frac{1}{\rho}\frac{\partial p}{\partial x}\right)_{i-1/2,j}}{\Delta x} + \frac{\left(\frac{1}{\rho}\frac{\partial p}{\partial y}\right)_{i,j+1/2} - \left(\frac{1}{\rho}\frac{\partial p}{\partial y}\right)_{i,j-1/2}}{\Delta y} \\
&= \frac{\left(\frac{2}{\rho_{i+1,j}+\rho_{i,j}}\frac{p_{i+1,j}-p_{i,j}}{\Delta x}\right) - \left(\frac{2}{\rho_{i,j}+\rho_{i-1,j}}\frac{p_{i,j}-p_{i-1,j}}{\Delta x}\right)}{\Delta x} \\
&\quad + \frac{\left(\frac{2}{\rho_{i,j+1}+\rho_{i,j}}\frac{p_{i,j+1}-p_{i,j}}{\Delta y}\right) - \left(\frac{2}{\rho_{i,j}+\rho_{i,j-1}}\frac{p_{i,j}-p_{i,j-1}}{\Delta y}\right)}{\Delta y}.
\end{aligned} \tag{2.39}
$$

It is noteworthy to mention that second-order interpolation is used to calculate density values at cell faces, e.g., $(1/\rho)_{i+1/2,j} = 2/\left(\rho_{i+1,j} + \rho_{i,j}\right)$. The same interpolation should also be applied while calculating the $1/\rho$ coefficients for pressure gradient, viscosity, and surface tension terms in Eq. (2.28). Furthermore, it is imperative to use the same finite-difference scheme when computing the gradient of pressure and level set gradient for determining the surface tension force. This ensures that the gradient operator provides the proper force balance between pressure gradient and surface tension across the interface, thereby reducing the formation of unphysical spurious velocities in the solution (Boniou *et al.*, 2022).

2.5.3 Solution procedure

The complete solution procedure for the two-phase incompressible solver can be summarized as follows:

1. The conservative level set (CLS) approach is used to implicitly advance the location of the interface from t^n to t^{n+1}, employing the velocity field at t^n.

2. The updated location of the interface, ψ^{n+1}, is then utilized to obtain the density and viscosity fields at t^{n+1}. Thus, ρ^{n+1} and μ^{n+1} fields are computed using Eqs. (2.33) and (2.34).

3. The intermediate velocity field at time step t^{n+1} is calculated by solving Eq. (2.28), while ignoring the pressure term.

4. The obtained intermediate velocity is then projected into a divergence-free field by solving the Poisson equation for the pressure based on the discretization introduced in Eq. (2.39).

5. The correct velocity field is calculated at time $n+1$ by solving Eq. (2.24). The obtained velocity at t^{n+1} is then employed to advance the level set profile for the next time step.

Based on the CFL condition, the stability constraint for the time step due to convection, viscosity, and surface tension terms is given as (Boniou *et al.*, 2022; Finster *et al.*, 2023)

$$\Delta t \leq \min\left(\frac{\Delta x}{\max(||\boldsymbol{u}||)}, \sqrt{\frac{\Delta x^3\left(\rho_\mathrm{l}+\rho_\mathrm{g}\right)}{4\pi\sigma}}, \frac{1}{4}\frac{\Delta x^2}{\max(\nu_\mathrm{l},\nu_\mathrm{g})}\right). \tag{2.40}$$

Usually, the surface tension limits the time step; however, for large density ratios, the viscosity term may be more restrictive.

2.5.4 Two-phase solver test cases

To investigate the accuracy, robustness, and performance of the implemented two-phase solver, three test cases are studied: the static droplet, damping surface wave, and the Rayleigh–Taylor instability. The static droplet test case, which aims to evaluate the capability of the two-phase solver to accurately calculate curvature and model surface tension forces, is presented in Appendix E, and interested readers are encouraged to refer to this section for more detail. The latter two test cases are examined in this section. The damping surface wave benchmark is employed to investigate the order of accuracy of the implemented solver and the interaction between viscosity and surface tension terms in a simulation. Lastly, the Rayleigh–Taylor instability is investigated to assess the performance of the solver in handling the evolution of a complex interface and also in treating cases where a high-density ratio exists across the interface.

2.5.4.1 Damping surface wave

The viscous damping of a surface wave is a well-known test case in the literature, widely used to assess the capability of the implemented solver to accurately model the interaction

between viscosity and surface tension forces. In this test case, two superimposed fluids with density ρ_1 and ρ_2 are separated by a sinusoidal interface with wavelength λ and amplitude A_0, and thus the perturbed interface profile is given as

$$y = y_0 - A_0 \cos(2\pi x/\lambda). \tag{2.41}$$

For the case where both fluids have the same kinematic viscosity, ν, and constant surface tension, σ, the analytical solution for the evolution of the wave amplitude with time is derived by Prosperetti (1981) by employing the initial value theorem. The initial value solution is obtained as (Prosperetti, 1981)

$$\begin{aligned} A_{\text{exact}}(t) = \frac{4(1-4\beta)k^4\nu^2}{8(1-4\beta)k^4\nu^2 + {\omega_0}^2} A_0 \operatorname{erfc}\left(\sqrt{\nu k^2 t}\right) \\ + \sum_{i=1}^{4} \frac{z_i}{Z_i} \left(\frac{{\omega_0}^2 A_0}{{z_i}^2 - \nu k^2}\right) \exp[\left({z_i}^2 - \nu k^2\right) t] \operatorname{erfc}\left(z_i\sqrt{t}\right), \end{aligned} \tag{2.42}$$

where z_i are the roots of

$$z^4 - 4\beta\sqrt{k^2\nu}\, z^3 + 2\left(1-6\beta\right) k^2\nu\, z^2 + 4(1-3\beta)(k^2\nu)^{\frac{3}{2}}\, z + (1-4\beta)k^4\nu^2 + {\omega_0}^2 = 0. \tag{2.43}$$

The dimensionless parameter β is defined as $\beta = \rho_1\rho_2/\left(\rho_1+\rho_2\right)^2$, while the inviscid frequency of the wave oscillation is given by $\omega_0 = \sqrt{\frac{\sigma k^3}{\rho_1+\rho_2}}$, and $Z_i = \Pi_{\substack{j=1 \\ j\neq i}}^{4} \left(z_j - z_i\right)$.

Here, the simulation is performed in a computational domain of $[0,1]\times[0,1]$, with periodic boundary conditions along the $x-$direction and slip wall boundary along the $y-$direction, and y_0 is set to $y_0 = 0.5$. The wavelength of the perturbation is set to $\lambda = 1$, and the initial amplitude of the wave is $A_0 = 0.01\lambda$. Three scenarios are investigated, namely, density ratios of 1, 10, and 1000, for four different grid resolutions of 8×8, 16×16, 32×32, and 64×64, with the interface thickness being set to $\epsilon = \Delta x/2$. For the first case of unity density ratio, the surface tension coefficient is $\sigma = 2$, with the constant kinematic viscosity for both fluids being set to $\nu = 0.0647$, and $\rho_1 = \rho_2 = 1$. The simulation was run for all different mesh resolutions with the constant time step $\Delta t = 0.0005$. Figure 2.6[top-left] displays the time

evolution of the normalized wave amplitude, i.e., A/λ, for all four meshes, along with the analytical solution. This figure visually confirms that, as mesh resolution is increased, the numerical solution converges to the analytical one. For a better quantitative comparison, the rms value of the error in the wave amplitude is plotted against the mesh resolution in Fig. 2.6[top-right].

As can be concluded from the computed error values, although for the coarsest mesh resolution, the solver is able to capture the proper behaviour of the surface wave, a small error in the numerical oscillation period of the wave has caused a noticeable error value for this mesh. As the mesh resolution is increased, more accurate results are obtained, and according to Fig. 2.6[top-right], close to a second-order convergence rate is observed. It is noteworthy to mention that for the case of $\rho_2/\rho_1 = 1$, there is no dynamic viscosity or momentum jump across the interface. Therefore, the numerical errors solely originate from the solution of the level set transport equation and the curvature computation. However, by increasing the density ratio, due to the existence of the density and dynamic viscosity jump across the interface, both convection and viscosity terms of the momentum equation affect the solution. Therefore, the numerical solver is also evaluated for density ratios of 10 and 100 to investigate whether the numerical model is capable of addressing these jump conditions and momentum transfer across the interface in the presence of a surface tension force. For both density ratios of 10 and 100, the kinematic viscosity of the fluids is set to $\nu = 0.00647$, and time steps are set to $\Delta t = 0.001$ and 0.003, respectively. As expected, as the mesh resolution increases, the numerical results become more accurate for both cases, as shown in Fig. 2.6[middle-left, bottom-left]. According to the convergence study, the approximate convergence rate of 1.6 is achieved for both cases, see Fig. 2.6[middle-right, bottom-right], demonstrating that in the presence of a density and viscosity jump, the solver tends to preserve its order of accuracy.

2.5.4.2 Rayleigh–Taylor instability

The Rayleigh–Taylor instability occurs when a layer of liquid is superimposed to another less dense liquid layer in such a way that by interchanging the fluids, the energy of the system can be reduced. The Rayleigh–Taylor instability has been widely studied in classical hydro-

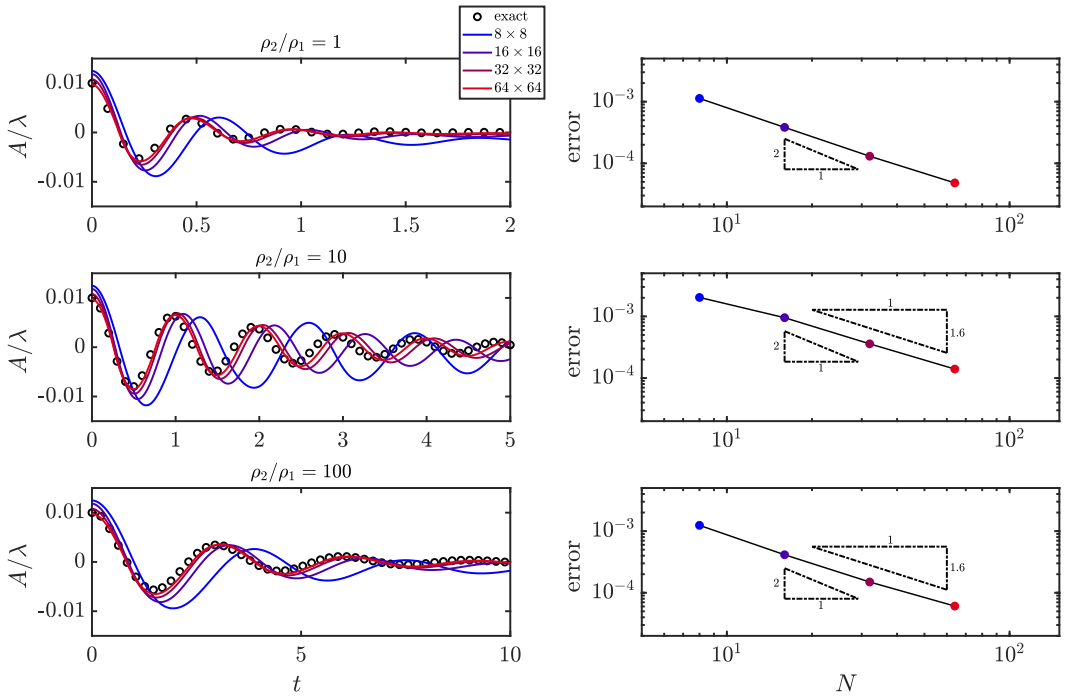

Figure 2.6: The solutions of the damped surface wave problem for three density ratios of [top] unity, [middle] 10, and [bottom] 100, are represented for four different mesh resolutions of 8×8, 16×16, 32×32, and 64×64. The accuracy analysis of the implemented two-phase solver is also illustrated for all three density ratios.

dynamics and is studied as a benchmark to evaluate the performance of the implemented two-phase solver for simulating problems containing the highly nonlinear and multi-scale nature of fluid dynamics. To simulate the Rayleigh–Taylor instability, we consider a two-dimensional rectangular domain $[x, y] \in [0, 1] \times [0, 4]$, with a fluid interface parallel to the horizontal axis at $y_0 = 2.0$. The fluid interface is initialized with a small sinusoidal perturbation, whose wavelength and amplitude are 2π and 0.1, respectively. Following the study by Huang *et al.* (2020), the material properties are set to $\rho_1 = 1$, $\rho_2 = 3$, $\mu_1 = \mu_2 = 0.01$, $\sigma = 10^{-12}$, and the gravity is acting downwards with a magnitude of unity. The simulation is performed for four mesh resolutions of 16×64, 32×128, 64×256, and 128×512. For all cases, the time step is set to $\Delta t = 5 \times 10^{-4}/\sqrt{\mathrm{At}}$, where the Atwood number is defined as $\mathrm{At} = (\rho_2 - \rho_1) \,/\, (\rho_1 + \rho_2)$.

Figure 2.7(a) depicts the results for the four different mesh resolutions at time $t\sqrt{\mathrm{At}} = 0$ to 2.5 with an increment of 0.25. It is visually evident that even for the coarsest mesh resolution case, the main features of the Rayleigh–Taylor instability are captured. However, refining the mesh allows for a better representation of the evolution and growth of bubbles and spikes in the solution. For a more comprehensive quantitative analysis, we validated our results with four different previous studies by Huang *et al.* (2020), Ding *et al.* (2007), Guermond & Quartapelle (2000), and Tryggvason *et al.* (2011). To this end, the transient location of the spike tip and the interface location at the left (right) edge during the simulation are compared to results from previous studies, shown in Fig. 2.7(b). As can be observed from Fig. 2.7(b), by increasing the mesh resolution, our results converge to ones from earlier studies, especially for the mesh resolution of 128×512, the results closely match those reported in the literature. Note that the study performed by Tryggvason *et al.* (2011) only considered the inviscid case, which explains the slight deviation from the other results. Assuming the solution of the finest grid, 128×512, as an analytical solution, the convergence rate of the solution is calculated. To this end, the L_2 norm of the spike and bubble locations during the simulation is computed. Figure 2.7(c) displays the order of accuracy, which is around 1.5. The obtained convergence rate is close to the expected second-order, confirming that the solver is robust and accurate for more complex problems as well.

Finally, the performance of the solver is also evaluated by simulating the Rayleigh–Taylor instability for higher density ratios of 30, 1000, and 3000. The mesh resolution is set as 64×256 and $\Delta t = 5 \times 10^{-4}/\sqrt{\mathrm{At}}$. Figure 2.8 displays the results for density ratios of 30 ($\mathrm{At} = 0.935$), 1000 ($\mathrm{At} = 0.998$), and 3000 ($\mathrm{At} = 0.999$), at time $t\sqrt{\mathrm{At}} = 0$ to 2 with an increment of 0.25. As expected, the interface evolves faster for higher density ratios, and the interface structures are simpler. Therefore, for the minimum density ratio of 30, the rate of penetration of the heavier fluid to the lighter one is less as a result of the reduced growth rate of the Rayleigh–Taylor instability, and the mushroom structure of the Rayleigh–Taylor instability can be observed. Since the Atwood number is comparable for two cases of density ratios of 1000 and 3000, the results of the surface evolution are similar (see Fig. 2.8). However, in the case of the density ratio of 3000, the tip of the spike has penetrated the lower-density region a bit further, and its structure is sharper at the tip (see the insets of

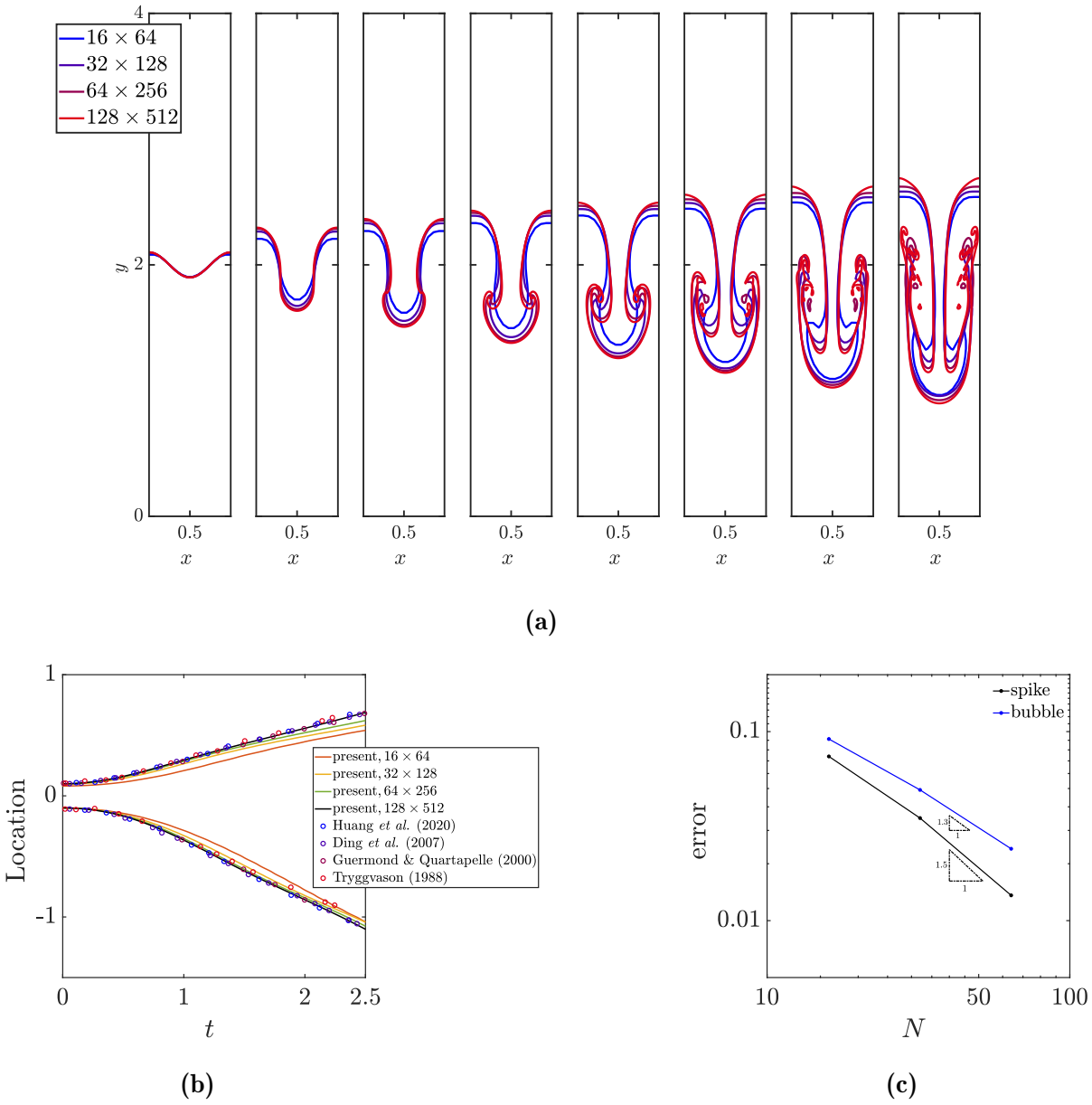

Figure 2.7: (a) The interface of the Rayleigh–Taylor instability with a density ratio of 3 ($\mathrm{At} = 0.5$) at $t\sqrt{\mathrm{At}} = 0, 1, 1.25, 1.5, 1.75, 2, 2.25$, and 2.5, from left to right, for four different mesh resolutions. (b) The transient location of the spike tip and bubble is depicted during the simulation for four different mesh resolutions of 16×64, 32×128, 64×256, and 128×512. The results are compared to four different studies by Huang *et al.* (2020), Ding *et al.* (2007), Guermond & Quartapelle (2000), and Tryggvason *et al.* (2011). (c) L_2 error in spike tip and bubble locations during the Rayleigh–Taylor simulation with the density ratio of three for the mesh resolutions of 16×64, 32×128, and 64×256.

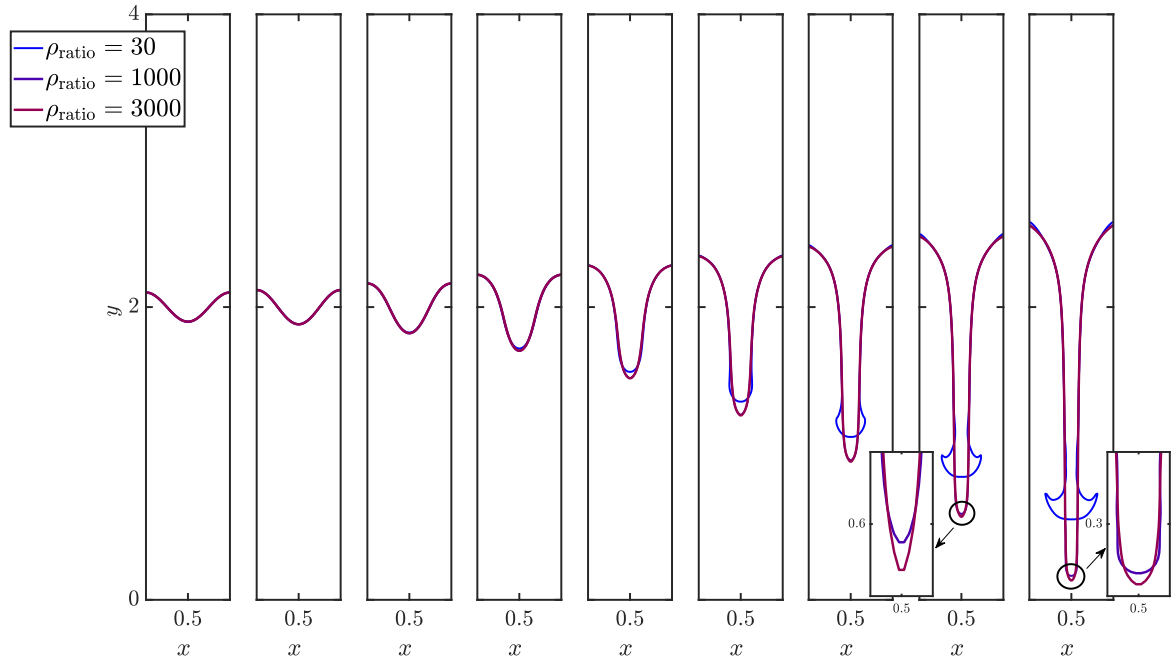

Figure 2.8: The interface of the Rayleigh–Taylor instability for different density ratios of 30 (At = 0.935), 1000 (At = 0.998), and 3000 (At = 0.999) at $t\sqrt{\text{At}} = 0, 0.25, 0.5, 0.75, 1, 1.25, 1.5, 1.75$, and 2, from left to right, for the mesh resolution of 64×256.

Fig. 2.8). The greater density ratio of 3000 indicates a more significant disparity in fluid densities, leading to stronger buoyancy forces. This stronger buoyancy causes the spikes at the interface to penetrate farther into the lower-density region due to the accelerated downward motion of the denser fluid. Additionally, a greater density ratio corresponds to a higher Atwood number, which accelerates the exponential growth of Rayleigh–Taylor instability, further promoting the deeper penetration of spike tips into the low-density region. However, because the Atwood numbers for these cases are relatively close, the difference in results remains relatively small.

2.6 Implementation of two-phase solver for magnetic flows

In this section, the previously introduced two-phase solver is extended to account for magnetic flows. To achieve this, the effect of the Lorentz force is incorporated into the momentum

equation, taking into consideration the magnetic permeability jump across the interface. The governing equations of two-phase flows along with the magnetostatic equation are solved, and the detailed numerical discretization is presented.

2.6.1 Discretization of governing equations for incompressible flows under magnetic fields

The Lorentz force quantifies the force experienced by fluids due to electromagnetic fields, given as $\boldsymbol{J} \times \boldsymbol{B}$, where $\boldsymbol{J}$ and $\boldsymbol{B}$ are electric current and magnetic flux densities, respectively. This force can be written in the form of the Maxwell stress tensor, τ^{M}, given as (Davidson, 2001)

$$\nabla \cdot \tau_{ij}^{\mathrm{M}} = \nabla \cdot \left(\frac{B_i B_j}{\mu_{\mathrm{m}}} - \frac{\boldsymbol{B}^2}{2\mu_{\mathrm{m}}} \delta_{ij} \right), \tag{2.44}$$

where variable μ_{m} denotes the magnetic permeability. This force can be treated as a body force acting on a fluid, and, hence, the updated momentum equation is expressed as

$$\frac{\partial \boldsymbol{u}}{\partial t} + \nabla \cdot (\boldsymbol{u}\boldsymbol{u}) = -\frac{1}{\rho}\nabla p + \frac{1}{\rho}\nabla \cdot \mu \left(\nabla \boldsymbol{u} + \nabla \boldsymbol{u}^{\mathrm{T}} \right) + \boldsymbol{g} + \frac{1}{\rho}\boldsymbol{F}_{\mathrm{sv}} + \frac{1}{\rho}\nabla \cdot \tau_{ij}^{\mathrm{M}}. \tag{2.45}$$

When the field quantities do not change with time, Maxwell's equations are reduced to the electrostatic and magnetostatic case, which are given as

$$\nabla \cdot \boldsymbol{B} = 0, \qquad \text{(Gauss's law)} \tag{2.46a}$$

$$\nabla \times \boldsymbol{E} = 0, \qquad \text{(Faraday's law)} \tag{2.46b}$$

$$\nabla \times \boldsymbol{H} = \boldsymbol{J}, \qquad \text{(Maxwell–Ampère law)} \tag{2.46c}$$

$$\nabla \cdot \boldsymbol{J} = 0, \qquad \text{(equation of continuity)} \tag{2.46d}$$

where variables $\boldsymbol{H}$ and $\boldsymbol{E}$ denote the magnetic field and electric field intensities, respectively. The magnetic flux density, $\boldsymbol{B}$, is related to the magnetic field intensity, $\boldsymbol{H}$, using the magnetic permeability, $\mu_{\mathrm{m}} = \boldsymbol{B}/\boldsymbol{H}$. In the magnetostatic case, the behaviour of the magnetic field can be studied in the absence of electric currents, since the electric charges are either at rest or moving very slowly, so that the magnetic field induced by them can be

neglected. Consequently, there is no interaction between electric and magnetic fields, and an electrostatic case or a magnetostatic case can be studied separately.

Under the magnetostatic assumption, Eqs. (2.46a) and (2.46c) explain the evolution of the magnetic field. One approach to solving the Maxwell–Ampère equation while satisfying the magnetic field divergence-free constraint is the vector potential formulation. In this method, the magnetic field, $\boldsymbol{B}$, is defined as the curl of an auxiliary vector, $\boldsymbol{A}$, with the gauge condition of $\nabla \cdot \boldsymbol{A} = 0$, as $\boldsymbol{B} = \nabla \times \boldsymbol{A}$. As a result, Gauss's law of magnetism is automatically satisfied, and Eq. (2.46c) is recast as

$$\nabla \times \boldsymbol{H} = \nabla \times \left(\frac{1}{\mu_\mathrm{m}} \boldsymbol{B} \right) = \nabla \times \left(\frac{1}{\mu_\mathrm{m}} \nabla \times \boldsymbol{A} \right). \tag{2.47}$$

For the two-dimensional case, $\boldsymbol{B} = (B_x, B_y, 0)$, the vector potential is reduced to $\boldsymbol{A} = (0, 0, A_z)$, and Eq. (2.47) will be simplified as

$$\nabla \times \left(\frac{1}{\mu_\mathrm{m}} \boldsymbol{B} \right) = \nabla \times \left(\frac{1}{\mu_\mathrm{m}} \nabla \times \boldsymbol{A} \right) = \nabla \times \left(\frac{1}{\mu_\mathrm{m}} \frac{\partial A_z}{\partial y} \boldsymbol{i} - \frac{1}{\mu_\mathrm{m}} \frac{\partial A_z}{\partial x} \boldsymbol{j} \right) = \nabla \left(-\frac{1}{\mu_\mathrm{m}} \nabla A_z \right) = J_z. \tag{2.48}$$

Equation (2.48) is a Poisson equation with variable coefficients and can be discretized similarly to the pressure Poisson equation discussed earlier, Eq. (2.39), provided that μ_m and A_z are defined at cell centers (see Fig. 2.1).

Employing the obtained A_z from Eq. (2.48), the components of the magnetic field are given as

$$B_x = \frac{\partial A_z}{\partial y} = \frac{\delta_{2\mathrm{nd}}\ A_z}{\delta_{2\mathrm{nd}}\ y}, \tag{2.49a}$$

and

$$B_y = -\frac{\partial A_z}{\partial x} = -\frac{\delta_{2\mathrm{nd}}\ A_z}{\delta_{2\mathrm{nd}}\ x}, \tag{2.49b}$$

at cell faces in $y-$ and $x-$directions, respectively (see Fig. 2.1). Finally, for the two-dimensional case of $\boldsymbol{x} = (x, y)$, the components of the Lorentz force are discretized as

$$\left[\nabla \cdot \tau_{ij}^\mathrm{M} \right]_{x-\mathrm{comp}} = \frac{\delta_{2\mathrm{nd}}}{\delta_{2\mathrm{nd}}\ x} \left(\frac{\left(\overline{B_x}^{2\mathrm{nd}\ y} \right)^2 - \left(\overline{B_y}^{2\mathrm{nd}\ x} \right)^2}{2\mu_\mathrm{m}} \right) + \frac{\delta_{2\mathrm{nd}}}{\delta_{2\mathrm{nd}}\ y} \left(\frac{\overline{B_x}^{2\mathrm{nd}\ x}\ \overline{B_y}^{2\mathrm{nd}\ y}}{\overline{\mu_\mathrm{m}}^{2\mathrm{nd}\ x\ 2\mathrm{nd}\ y}} \right), \tag{2.50a}$$

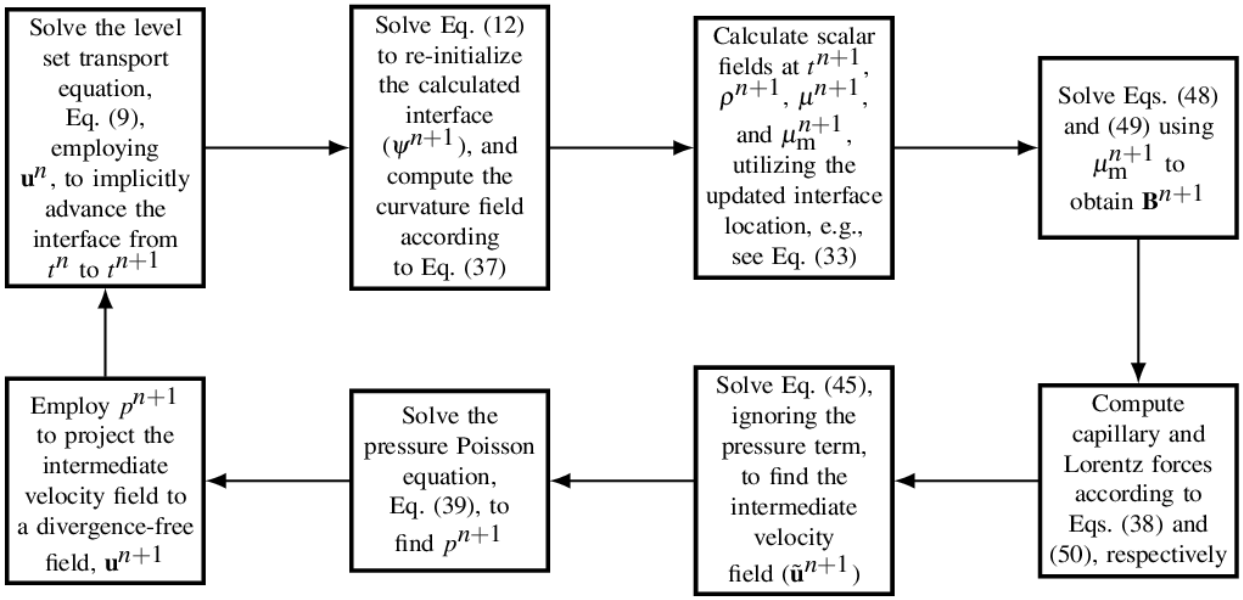

Figure 2.9: A flowchart representing the complete procedure for implementing the two-phase incompressible numerical toolkit for magnetic flows.

$$\left[\nabla \cdot \tau_{ij}^{\mathrm{M}}\right]_{y-\mathrm{comp}} = \frac{\delta_{2\mathrm{nd}}}{\delta_{2\mathrm{nd}}\, x}\left(\frac{\overline{B_x}^{2\mathrm{nd}\ x}\ \overline{B_y}^{2\mathrm{nd}\ y}}{\overline{\mu_{\mathrm{m}}}^{2\mathrm{nd}\ x\,2\mathrm{nd}\ y}}\right) + \frac{\delta_{2\mathrm{nd}}}{\delta_{2\mathrm{nd}}\, y}\left(\frac{\left(\overline{B_y}^{2\mathrm{nd}\ x}\right)^2 - \left(\overline{B_x}^{2\mathrm{nd}\ y}\right)^2}{2\mu_{\mathrm{m}}}\right). \quad (2.50b)$$

The solution procedure introduced in the previous section for two-phase nonmagnetic flows can be applied to the magnetic case as well with some modifications. In step (2), the magnetic permeability field at t^{n+1}, μ_{m}^{n+1}, should be computed according to the updated location of the interface as well. The obtained magnetic permeability field will then be employed to calculate the magnetic field at time step $n+1$, solving Eq. (2.48), which in turn will be utilized to determine the Lorentz force in the momentum equation. Figure 2.9 summarizes the complete procedure for implementing the two-phase incompressible solver for magnetic flows.

2.6.2 Magnetic two-phase test cases

Three test cases are conducted in this section, namely, the deformation of both a static and a sheared ferrofluid droplet as well as Rayleigh–Taylor instability in magnetic fluids, to evaluate the performance and accuracy of the implemented solver. The static droplet test case is designed to assess the capability of the solver to accurately simulate the behaviour of

the Lorentz force at the interface for various magnetic field strengths. The numerical results are validated by comparing them with experimental and analytical data. In the second test, the deformation of a droplet in a shear flow is investigated, considering both low and high capillary flow regimes under varying magnetic field conditions. This test also involves comparing results with theoretical solutions, particularly in the context of low magnetic field values. Furthermore, within this test case, the impact of the magnetic permeability ratio between the ferrofluid droplet and the surrounding flow on its deformation and rotation is examined. The third benchmark is employed to evaluate the solver's performance in modelling the evolution of a complex interface in the presence of different magnetic field densities and high magnetic permeability jumps across the interface. Additionally, the impact of the magnetic field on the growth rate of the Rayleigh–Taylor instability is investigated and compared with the results obtained from linear analysis. It is noteworthy to mention that since ferrofluids do not conduct electric current, and in our test cases, no external current is imposed, the right-hand side value of Eq. (2.48), J_z, is set to zero in the following numerical simulations.

2.6.2.1 Deformation of a stationary magnetic droplet

In this test case, a liquid droplet of diameter $D = 1$ is considered at the center of a two-dimensional domain of $[0, 4] \times [0, 4]$ filled with gas, in a stationary velocity field. In the case of zero gravity, similar to the static droplet test case presented in Appendix E, the droplet remains at rest since the pressure and capillary forces are balanced. However, if the gas and liquid phases have different values of magnetic permeability, in the presence of a magnetic field, the induced Lorentz force at the interface affects the deformation of the droplet; the competition between the Lorentz force and the surface tension force dictates the evolution of the droplet's interface. Suppose the density and viscosity are constant for both phases, $\rho_1 = \rho_2 = 1$ and $\mu_1 = \mu_2 = 0.001$. A uniform magnetic field, $\boldsymbol{B}_0 = 2$ mT, is imposed from bottom to top and $\mu_{\mathrm{m,l}} = 9\,\mu_{\mathrm{m,g}}$. The capillary force attempts to maintain the interface of the droplet in its initial shape. Nonetheless, since the magnetic field lines will be distorted around the droplet's interface, the created Lorentz force causes the droplet to deform and stretch. In order to better interpret the deformation of the droplet for different scenarios and

magnetic strengths, scale analysis is employed. To this end, the following non-dimensional variables are introduced

$$\boldsymbol{u}^* = \boldsymbol{u}/u_0, \quad \boldsymbol{B}^* = \boldsymbol{B}/B_0, \quad \boldsymbol{l}^* = \boldsymbol{l}/l_0, \quad t^* = t\,u_0/l_0, \quad p^* = p/\rho_0\,u_0^2, \tag{2.51}$$

where the zero subscripts refer to the initial value, and l_0 is the length scale of the problem. Rewriting the momentum equation in the non-dimensional form will then result in

$$\frac{\partial \boldsymbol{u}^*}{\partial t^*} + \frac{\partial}{\partial \boldsymbol{l}^*}\left(\boldsymbol{u}^*\boldsymbol{u}^*\right) = -\frac{\partial p^*}{\partial \boldsymbol{l}^*} + \overbrace{\frac{\mu}{u_0\,l_0\,\rho_0}}^{\frac{1}{\mathrm{Re}}}\frac{\partial}{\partial \boldsymbol{l}^*}\left(\frac{\partial \boldsymbol{u}^*}{\partial \boldsymbol{l}^*} + \frac{\partial \boldsymbol{u}^{*\mathrm{T}}}{\partial \boldsymbol{l}^*}\right) - \overbrace{\frac{\sigma}{\rho_0\,u_0^2\,l_0}\left(\nabla\cdot\boldsymbol{n}\right)\nabla\psi}^{\text{surface tension}} + \underbrace{\frac{B_0^2}{\rho_0\,\mu_\mathrm{m}\,{u_0}^2}\frac{\partial}{\partial \boldsymbol{l}^*}\left(\boldsymbol{B}^*\boldsymbol{B}^* - \frac{|\boldsymbol{B}^*|^2}{2}\delta_{i,j}\right)}_{\text{Lorentz force}}. \tag{2.52}$$

The ratio between the Lorentz force and the surface tension force can be qualified by a non-dimensional number defined as

$$\frac{\text{Lorentz force}}{\text{surface tension force}} = \frac{\frac{B_0^2}{\rho_0\,\mu_\mathrm{m}\,{u_0}^2}}{\frac{\sigma}{\rho_0\,u_0^2\,l_0}} = \frac{B_0^2\,l_0}{\mu_\mathrm{m}\sigma}. \tag{2.53}$$

Hence, for the case of $B_0^2\,l_0/\mu_\mathrm{m}\,\sigma \ll 1$, the surface tension force overcomes the Lorentz force and the droplet is expected to retain its shape. Conversely, in the case of $B_0^2\,l_0/\mu_\mathrm{m}\,\sigma \gg 1$, since the Lorentz force is greater than the capillary force, the droplet deforms and stretches. If $B_0^2\,l_0/\mu_\mathrm{m}\,\sigma$ is of the order of one, the Lorentz and surface tension forces are of the same magnitude. As a consequence, oscillations in the deformation of the droplet could be observed, as the Lorentz force stretches the interface and the surface tension force tries to prevent the deformation.

This finding is then used to validate the behaviour of the implemented solver. In the numerical setup, the thickness of the interface is set to $\epsilon = \Delta x/2$, with the grid resolution of 101×101, where a no-slip boundary is imposed at all boundaries. Three cases of $B_0^2\,l_0/\mu_\mathrm{m}\,\sigma \ll 1$, $B_0^2\,l_0/\mu_\mathrm{m}\,\sigma \gg 1$, and $B_0^2\,l_0/\mu_\mathrm{m}\,\sigma \approx 1$ are investigated, where the surface tension coefficient is set to 0.01, 1, and 100, respectively, and the results are represented in Fig. 2.10. It can be appreciated in Fig. 2.10 that for the case of $B_0^2\,l_0/\mu_\mathrm{m}\,\sigma \gg 1$, the Lorentz force is vertically

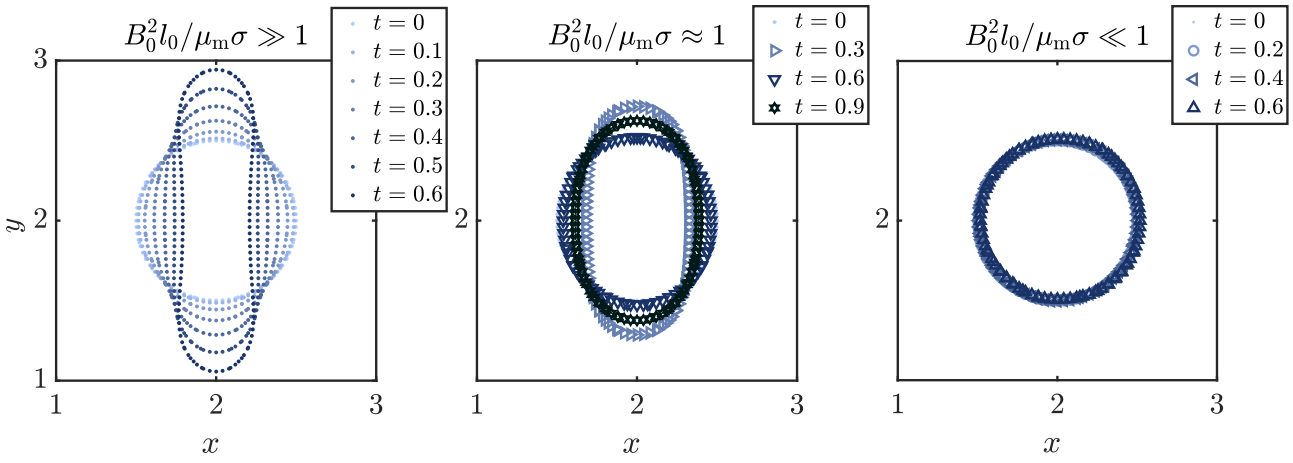

Figure 2.10: The evolution of the droplet under the constant magnetic field imposed from bottom to top of the computational domain, with $\mu_{m,l}/\mu_{m,g} = 9$. Three cases of $B_0^2\, l_0/\mu_m\, \sigma \gg 1$, $B_0^2\, l_0/\mu_m\, \sigma \approx 1$, and $B_0^2\, l_0/\mu_m\, \sigma \ll 1$ are represented from left to right, respectively.

stretching the droplet while for the $B_0^2\, l_0/\mu_m\, \sigma \ll 1$ case, the droplet remains unchanged in time. Additionally, when the Lorentz and capillary forces are of the same order of magnitude, there is an oscillation in the deformation of the droplet's interface, evident in Fig. 2.10.

The non-dimensional number introduced in Eq. (2.53) is the magnetic Bond number, denoted as $\mathrm{Bo_m}$, mostly introduced as $\mathrm{Bo_m} = l_0\, \mu_{m,0}\, H_0^2/2\sigma$ in the literature. This parameter plays a critical role in various applications, including the study of the dynamics and deformation of ferrofluid droplets in the presence of a magnetic field. Ferrofluids are colloidal suspensions of nanoscale magnetic particles, typically around 10 nm in size, dispersed in a base fluid (Majidi *et al.*, 2022). They were initially introduced by NASA in 1963, and since then, ferrohydrodynamics has become a subject of significant interest in the field of fluid mechanics (Rosensweig, 2013). Ferrofluids have found applications across various fields, including microfluidics (Bijarchi *et al.*, 2021), biomedical applications such as the treatment of retinal detachment and targeted drug delivery (Mefford *et al.*, 2007; Voltairas *et al.*, 2001),

droplet generation from nozzles (Bijarchi & Shafii, 2020), and heat transfer augmentation (Zarei Saleh Abad *et al.*, 2019). Understanding the behaviour of ferrofluid droplets in the presence of magnetic fields is essential for their practical applications. When subjected to a uniform magnetic field, a ferrofluid droplet suspended in a viscous medium elongates along the direction of the field, ultimately reaching a stable equilibrium configuration. Researchers have conducted numerous studies to investigate the deformation and dynamics of single ferrofluid droplets under the influence of magnetic fields, employing analytical solutions, numerical simulations, and experimental observations (Bacri *et al.*, 1982; Li *et al.*, 2021; Afkhami *et al.*, 2008, 2010).

To further validate our implemented two-phase solver for magnetic flows quantitatively, we have leveraged the theoretical work presented by Afkhami *et al.* (2010), who explored the deformation of a ferrofluid droplet in a quiescent fluid subjected to a uniform magnetic field. In their study, they established a relation between the deformation of a ferrofluid and the magnetic Bond number. This theoretical solution is derived under the assumption that the droplet maintains its ellipsoidal shape during elongation due to the presence of the magnetic field (Afkhami *et al.*, 2010). Consequently, the extent of deformation of the droplet is quantified by introducing the aspect ratio denoted as b/a, where $2a$ and $2b$ represent the major and minor axes of the droplet, respectively, after it has undergone deformation and reached a steady state. Afkhami *et al.* (2010) modelled the magnetization of the ferrofluid droplet, denoted as $\boldsymbol{M}_{\text{ferrofluid}}$, as a linear function of the applied magnetic field, given as $\boldsymbol{M}_{\text{ferrofluid}} = \chi \boldsymbol{H}$, where $\boldsymbol{H}$ represents the external uniform magnetic field strength, and χ is the magnetic susceptibility of the ferrofluid droplet (Majidi *et al.*, 2022; Afkhami *et al.*, 2010). Magnetic susceptibility, χ, is a material property that quantifies the magnetization response of the ferrofluid droplet to an applied magnetic field. It is expressed as $\chi = (\mu_{\text{m,droplet}}/\mu_{\text{m},0} - 1)$ and is assumed to remain constant in each phase in the analytical solution of Afkhami *et al.* (2010). Consequently, the magnetic induction field is calculated as $\boldsymbol{B} = \mu_{\text{m},0}\,(\boldsymbol{H} + \boldsymbol{M}_{\text{ferrofluid}}) = \mu_{\text{m},0}\,(1+\chi)\,\boldsymbol{H}$ (Afkhami *et al.*, 2010). The theoretical finding regarding the droplet deformation in an external magnetic field reported by Afkhami *et al.*

(2010) is presented as

$$\mathrm{Bo_m} = \left(\frac{1}{\chi} + k\right)^2 \left(\frac{b}{a}\right)^{\frac{1}{3}} \left[2\frac{b}{a} - \left(\frac{b}{a}\right)^{-2} - 1\right], \tag{2.54}$$

where k is the demagnetizing factor that is calculated as

$$k = \left(\frac{1-E^2}{2E^3}\right)\left(\ln\frac{1+E}{1-E} - 2E\right), \quad \text{with} \quad E = \sqrt{1-a^2/b^2}. \tag{2.55}$$

Here, a test case similar to the previous test is conducted to compare our results with the theoretical solution of Eq. (2.54) and other numerical and experimental results existing in the literature. In this test case, a circular ferrofluid droplet with a radius of $R_0 = 0.5$ is placed at the center of a computational domain of $[0, 2] \times [0, 6]$ filled with gas. The mesh resolution of 100×300 and time step $\Delta t = 0.001$ were used for all simulations. The density and viscosity are set to be the same for both phases, $\rho_1 = \rho_2 = 1$ and $\mu_1 = \mu_2 = 0.01$, and a constant surface tension value of $\sigma = 1$ was employed. The magnetic permeability of the gas is set to $\mu_{\mathrm{m,g}} = \mu_{\mathrm{m,0}} = 1$, therefore, to change the magnetic permeability ratio between two phases, the magnetic permeability of the ferrofluid droplet is altered. Figure 2.11(a)[left] illustrates the initial magnetic field configuration for the case where $\chi = 2$ and $\mathrm{Bo_m} = 3$, along with the initial shape of the ferrofluid droplet at $t = 0$, as an example. As can be observed in this figure, the magnetic field lines near the droplet interface are distorted due to the varying magnetic permeability of the two phases. These distorted magnetic field lines induce magnetic forces at the droplet interface, resulting in the deformation of the ferrofluid droplet. The deformed droplet for this specific case at steady state along with the corresponding magnetic field are represented in Fig. 2.11(a)[middle]. As expected, the droplet has elongated along the magnetic field lines due to the presence of magnetic forces. Figure 2.11(a)[right] demonstrates the forces acting on the ferrofluid droplet interface, namely, the magnetic force (depicted in black) and the capillary force (shown in red). It is visually evident from this figure that the magnetic force exhibits a higher amplitude, enabling it to overcome the capillary force and induce elongation. The surface tension force,

primarily concentrated at the poles of the droplet where high curvature is present, opposes the magnetic forces, attempting to preserve the initial shape of the droplet.

Figure 2.11(b) displays the droplet deformation for eight different magnetic Bond numbers of $\mathrm{Bo_m} = 0.25$, 0.5, 1, 2, 3, 6, 8, and 10, with the susceptibility value of $\chi = 2$ for all cases. It can be seen that for higher magnetic Bond numbers, the droplet deformation is more pronounced, owing to the increased magnetic forces, since the surface tension coefficient remains consistent across all cases. As the magnetic Bond number increases, indicating stronger magnetic forces, the magnetic force becomes more effective in overcoming capillary forces, further deforming the droplet.

In Fig. 2.11(c), the deformation of the ferrofluid droplet is explored under three different magnetic susceptibility values of $\chi = 2$, 5, and 20, across various magnetic Bond numbers. The results are compared with analytical solutions, demonstrating a close agreement between numerical and theoretical predictions. As expected, an increase in the magnetic Bond number leads to more significant changes in the aspect ratio. The maximum error between the numerical and analytical results in the studied cases is approximately 4.2%. This discrepancy can be attributed to the theoretical assumption that the droplet is axisymmetric and retains an elliptical shape during deformation (Afkhami *et al.*, 2010). However, this assumption may not hold true, particularly for cases with higher susceptibility and magnetic Bond numbers (Afkhami *et al.*, 2010), where more significant discrepancies with the analytical solution are evident. Additionally, the obtained results for $\chi = 2$, 5, and 20 cases are compared with numerical results from Afkhami *et al.* (2010), showing good agreement, with some discrepancy due to the differences in the nature of simulations (axisymmetric in Afkhami *et al.* (2010) vs. two-dimensional in this study).

Furthermore, in the case where $\chi = 20$, we compare our results with the experimental data obtained by Bacri & Salin (1982). While a reasonable agreement was observed, discrepancies, particularly for higher magnetic Bond numbers, can be attributed to the three-dimensional nature of the experiments and the assumption of constant surface tension in our simulations. In reality, it is observed that the interfacial tension of the ferrofluid droplet depends on the magnetic field, especially for high magnetic field strengths (Afkhami *et al.*, 2010).

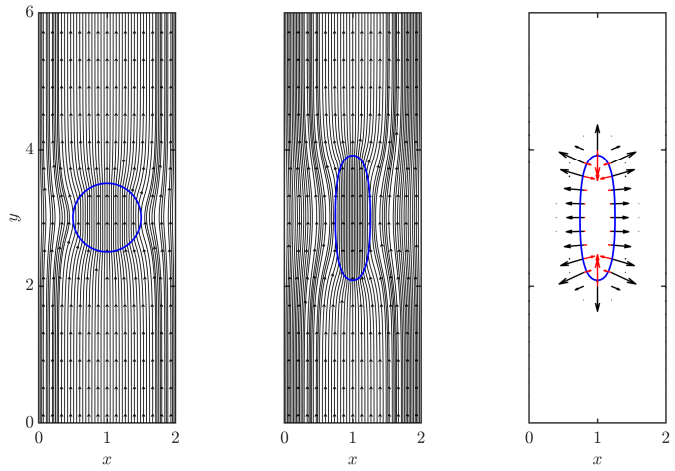

(a)

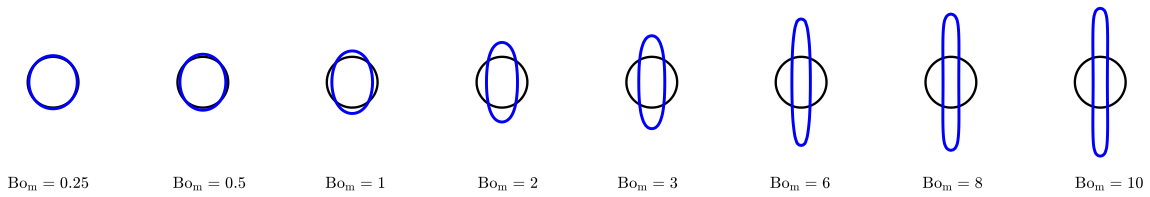

(b)

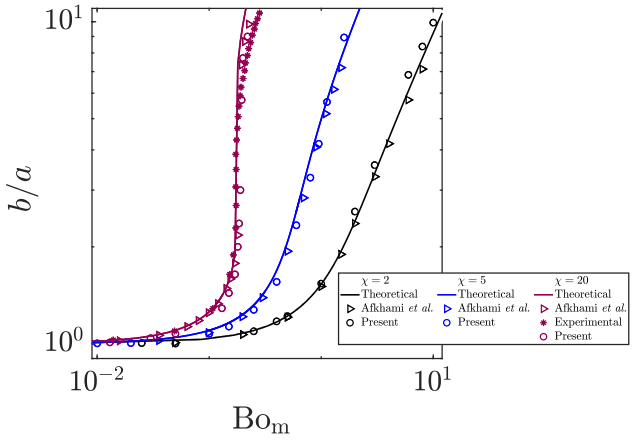

(c)

Figure 2.11: (a) Configuration of the ferrofluid droplet along with magnetic field at [left] $t = 0$, [middle] steady state, and [right] depiction of the magnetic force (in black) and capillary force (in red) acting at the interface for the case $\chi = 2$ and $\text{Bo}_\text{m} = 3$. (b) droplet deformation across eight different magnetic Bond numbers with a susceptibility value of $\chi = 2$. (c) Comparison of analytical, numerical, and experimental results for three different magnetic susceptibility values of $\chi = 2$, 5, and 20, under varying magnetic Bond numbers.

2.6.2.2 Deformation of a sheared magnetic droplet

As previously mentioned, ferrofluid droplets have garnered significant attention from researchers due to their diverse applications in areas such as biomedicine, microfluidics, and rheology (Cunha *et al.*, 2018). In some applications, these droplets are not only subjected to an external magnetic field, as discussed in the previous test case, but also experience the presence of hydrodynamic flow. This flow can influence the droplet's deformation, inclination, and potential breakup into smaller droplets. Consequently, studying the deformation of sheared droplets becomes crucial across various industrial applications that utilize emulsions. The deformation of the sheared droplet depends on various parameters, such as surface tension, shear rate, magnetic field strength, and the viscosity ratio between the droplet and the suspending fluid. In addition to the magnetic Bond number, $\mathrm{Bo_m}$, another non-dimensional parameter known as the capillary number, Ca, which quantifies the ratio between shear and surface tension forces, also influences the droplet deformation. Hassan *et al.* (2018) conducted a numerical study on the deformation of sheared droplets under a uniform external magnetic field using the finite-element method. Their study investigated the effects of shear rate, magnetic field strength, and magnetic field direction on ferrofluid deformation. They found that in the low capillary regime, magnetic forces dominate over shear forces, exerting primary control over droplet dynamics (Hassan *et al.*, 2018). Additionally, increasing the magnetic field strength, i.e., increasing the magnetic Bond number, enhances droplet deformation (Hassan *et al.*, 2018). In a subsequent study by Hassan & Wang (2019), the impact of viscosity ratio and magnetic field direction on droplet deformation and breakup was explored under the constraint of a low Reynolds number ($\mathrm{Re} \leq 0.03$). Their results indicated that when the magnetic field is applied at an angle of 45°, droplet elongation is more pronounced, leading to accelerated droplet breakup. Conversely, varying the magnetic field angle to 0° or 135° suppresses droplet breakup. To our knowledge, no previous study has investigated sheared droplet deformation by varying the susceptibility value of the ferrofluid droplet. Consequently, in this test case, we investigate sheared droplet deformation for low capillary numbers to validate the implemented numerical solver. Additionally, we explore the effect of the magnetic susceptibility ratio between the ferrofluid droplet and its

surrounding medium on the dynamics and deformation of the ferrofluid droplet in both low and high capillary regimes.

Figure 2.12 illustrates the schematic of this test case, including a ferrofluid droplet with radius $R_0 = 0.5$ suspended in another nonmagnetic viscous fluid. The droplet is positioned at the center of a square computational domain with dimension $W_{\text{domain}} = 6$, and a velocity profile of $u = \dot{\gamma} y$ is imposed, where $\dot{\gamma}$ represents the corresponding shear rate. A uniform magnetic field of $\boldsymbol{H}_0$ at the angle of 90° is applied. It is worth noting that numerical studies model simple shear flows by moving two confining walls, which can introduce confinement effects on the deformation of the droplet. Studies by Kennedy *et al.* (1994) and Guido & Villone (1998) on the droplet deformation in a simple shear flow suggest that the confinement effect on droplet deformation is negligible when $2R_0/W_{\text{domain}} < 0.4$. In our simulations, $2R_0/W_{\text{domain}}$ is equal to 0.16, effectively eliminating the confinement effect on droplet deformation. In the presented simulations, the density and viscosity of both phases are assumed to be equal, $\rho = 1$ and $\mu = 0.1$. The top and bottom boundaries of the computational domain are treated as moving walls with velocities of $+\dot{\gamma} W_{\text{domain}}/2$ and $-\dot{\gamma} W_{\text{domain}}/2$, respectively, producing constant shear rate of $\dot{\gamma}$, while the left and right boundaries are periodic. By setting surface tension coefficient and shear rate to 1 and 0.4, respectively, the capillary number is adjusted to $\text{Ca} = \mu_{\text{m},0} R_0 \dot{\gamma}/\sigma = 0.02$, and the deformation of the droplet is investigated for different values of Bo_m and χ. To quantify droplet deformation, Taylor's deformation parameter (Taylor, 1932, 1934) is calculated, given as

$$D = \frac{L - B}{L + B}, \tag{2.56}$$

where L and B represent the major and minor axes of the deformed droplet (see Fig. 2.12). The pioneering work of Taylor indicating the deformation parameter of a buoyant droplet suspended in another viscous fluid under a shear flow in the Stokes flow limit (Taylor, 1932, 1934) was extended by Jesus *et al.* (2018) to a sheared ferrofluid droplet under an external magnetic field in the limit of both small Ca and Bo_m numbers. According to the asymptotic theory derived by Jesus *et al.* (2018), the deformation of a sheared ferrofluid droplet in the

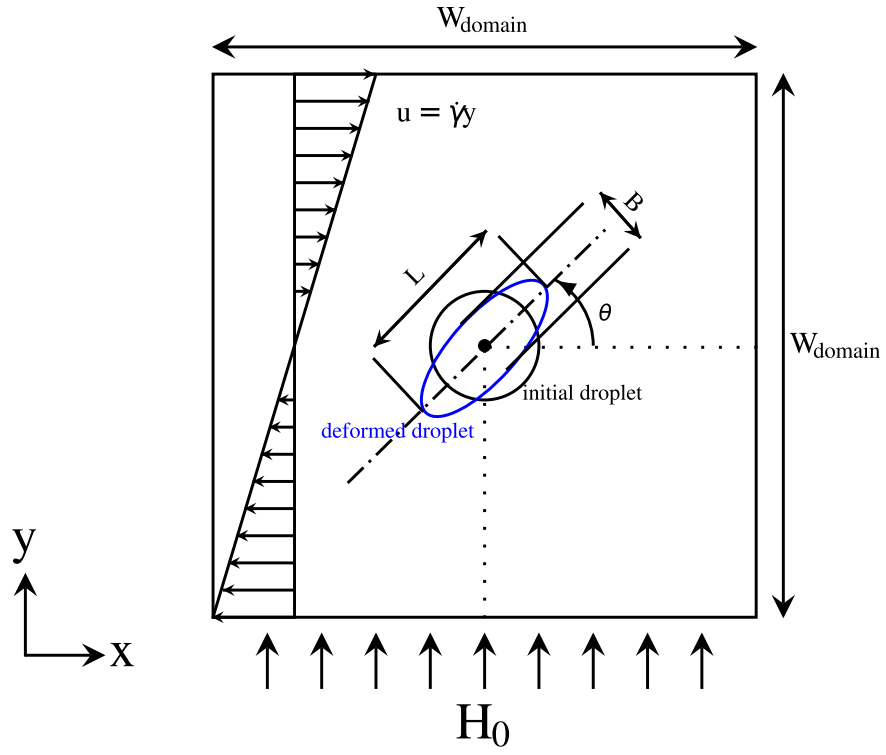

Figure 2.12: Schematic of a ferrofluid droplet suspended in another nonmagnetic viscous fluid in a simple shear flow under a uniform external magnetic field, $\boldsymbol{H}_0$.

presence of a uniform magnetic field is given as

$$D = \frac{\sqrt{\left[\alpha\left(\nu_{\mathrm{r}}\right)\mathrm{Ca}\right]^2 + \left[\beta\left(\chi_{\mathrm{droplet}}\right)\mathrm{Bo_m}\right]^2}}{2 + \frac{1}{3}\beta\left(\chi_{\mathrm{droplet}}\right)\mathrm{Bo_m}}, \tag{2.57}$$

where $\alpha\left(\nu_{\mathrm{r}}\right)$ and $\beta\left(\chi_{\mathrm{droplet}}\right)$ are the functions of the viscosity ratio between the droplet and the surrounding fluid, ν_{r}, and the susceptibility of the ferrofluid droplet, χ_{droplet}, respectively. These functions are calculated as

$$\alpha\left(\nu_{\mathrm{r}}\right) = \frac{19\nu_{\mathrm{r}} + 16}{8(\nu_{\mathrm{r}} + 1)} \tag{2.58a}$$

and

$$\beta\left(\chi_{\mathrm{droplet}}\right) = \frac{3\,\chi_{\mathrm{droplet}}\left(2\,\chi_{\mathrm{droplet}} + 1\right)}{4\left(\chi_{\mathrm{droplet}} + 3\right)^2}. \tag{2.58b}$$

Figure 2.13[left] presents the droplet deformation parameter with $\mathrm{Ca} = 0.02$ for different magnetic bond numbers, ranging from 0 to 6, for three different droplet susceptibility values

of $\chi = 1$, 2, and 3. Since the simulations are performed in the low capillary regime, it is expected that magnetic forces dominate over shear forces and as the magnetic Bond number increases, the droplet deformation is anticipated to increase. Figure 2.13[left] visually confirms that the numerical results capture this expected behaviour. As shown in this figure, the results for $\mathrm{Bo_m} < 1$ are in good agreement with the theoretical solution. Please refer to the inset in this figure, which depicts analytical and numerical solutions for the magnetic Bond number ranging from 0 to 0.8. However, as the magnetic Bond number increases, the numerical results deviate from the theoretical solution derived by Jesus *et al.* (2018). This behaviour is expected since the proposed theoretical solution is only valid for small magnetic Bond numbers ($\mathrm{Bo_m} \ll 1$). Furthermore, it is evident that by increasing the susceptibility value, the numerical results differ more pronouncedly from the small perturbation analysis of the theoretical solution. According to the numerical results, increasing the magnetic susceptibility value of the droplet significantly affects its deformation. For example, for $\chi = 3$ and $\mathrm{Bo_m} = 6$, the deformation parameter is approximately 2 times higher than the same case with $\chi = 1$. Figure 2.13[middle] depicts the steady-state droplet at $\mathrm{Bo_m} = 1$ for the three different magnetic susceptibility values of $\chi = 1$, 2, and 3. As can be seen from this figure, increasing the magnetic susceptibility value by three times results in an elongated, thin droplet shape compared to the $\chi = 1$ case. This behaviour can be explained by investigating the existing Maxwell stresses at the droplet interface for different susceptibility values. In Fig. 2.14, the magnetic field for three different values of $\chi = 1$, 2, and 3 is shown at $t = 0$ and the steady state. According to this figure, a larger χ, or in other words, a larger magnetic permeability discontinuity between the ferrofluid droplet and the surrounding fluid, will result in a greater distortion of magnetic field lines around the droplet interface. This higher bending in the magnetic field lines induces a larger Lorentz force at the interface, which in turn causes greater droplet elongation, as the surface tension (restoring force) is constant for all cases. This conclusion emphasizes that changing the susceptibility of the ferrofluid droplet also plays an important role in its dynamics and deformation. In the study by Hu *et al.* (2018), it was also shown that the magnetic field lines inside the ferrofluid droplet at $t = 0$ are aligned with the externally imposed magnetic field. However, the magnetic field will be distorted near the interface of the droplet. Hu *et al.* (2018) found the analytical solution for

the magnetic field intensity inside and outside of the circular cylinder within an externally vertical uniform magnetic field. According to their analytical solution, the magnetic field intensity inside the cylinder will be given as $\boldsymbol{H} = A\boldsymbol{e}_y$, where $A = H_0\,(2\mu_{\mathrm{m},2})/(\mu_{\mathrm{m},1} + \mu_{\mathrm{m},2})$. Variables $\mu_{\mathrm{m},1}$ and $\mu_{\mathrm{m},2}$ denote the magnetic permeability of the surrounding gas and the ferrofluid droplet, respectively. We measured the numerical magnetic field intensity for the three different cases of $\chi = 1$, 2, and 3, shown in Fig. 2.14, and compared it to the analytical solution. According to our results, the magnetic field intensity for the cases $\chi = 1$, 2, and 3 are $1.32H_0$, $1.51H_0$, and $1.62H_0$, respectively. These results are in good agreement with the numerical findings of $1.33H_0$, $1.5H_0$, and $1.6H_0$ for the cases $\chi = 1$, 2, and 3, respectively.

In Fig. 2.14, the acting magnetic and surface tension forces at the interface are shown in black and red, respectively, at the steady-state situation. Since we are in the low capillary regime, shear forces play a minor role in droplet deformation and are neglected in the figure. For $\chi = 1$, since the droplet is still in a circular shape, the surface tension is present around the entire interface. However, for $\chi = 2$ and 3, as the droplet has elongated, the surface tension force is mainly focused at the poles, competing with the magnetic force. Increasing the magnetic Bond number requires a longer simulation time for the droplet reaches a steady state, as previously reported by Jesus *et al.* (2018).

Another important parameter to consider when investigating ferrofluid droplet deformation is the rotation of the droplet under various conditions, quantified by the angle measured counterclockwise from the positive $x-$direction to the major axis of the droplet, θ. Previous studies have explored the rotational angle of the droplet under different magnetic Bond numbers in both low and high capillary regimes. For instance, Hassan *et al.* (2018) demonstrated that for Ca $\approx$ 0.2 and an imposed perpendicular magnetic field, increasing the magnetic Bond number leads to an increase in θ angle. This effect is attributed to the combined influence of the magnetic field and shear flow. However, the impact of magnetic susceptibility on droplet rotation has not yet been discussed in detail. In Fig. 2.13[right], the rotation of the droplet for Ca=0.02 under different magnetic Bond numbers is presented. For a susceptibility value of 1, similar to the behaviour reported in previous studies (Hassan *et al.*, 2018), an increase in the magnetic Bond number leads to an increase in the angle θ until it reaches a constant value. The shear flow attempts to rotate the droplet at an angle

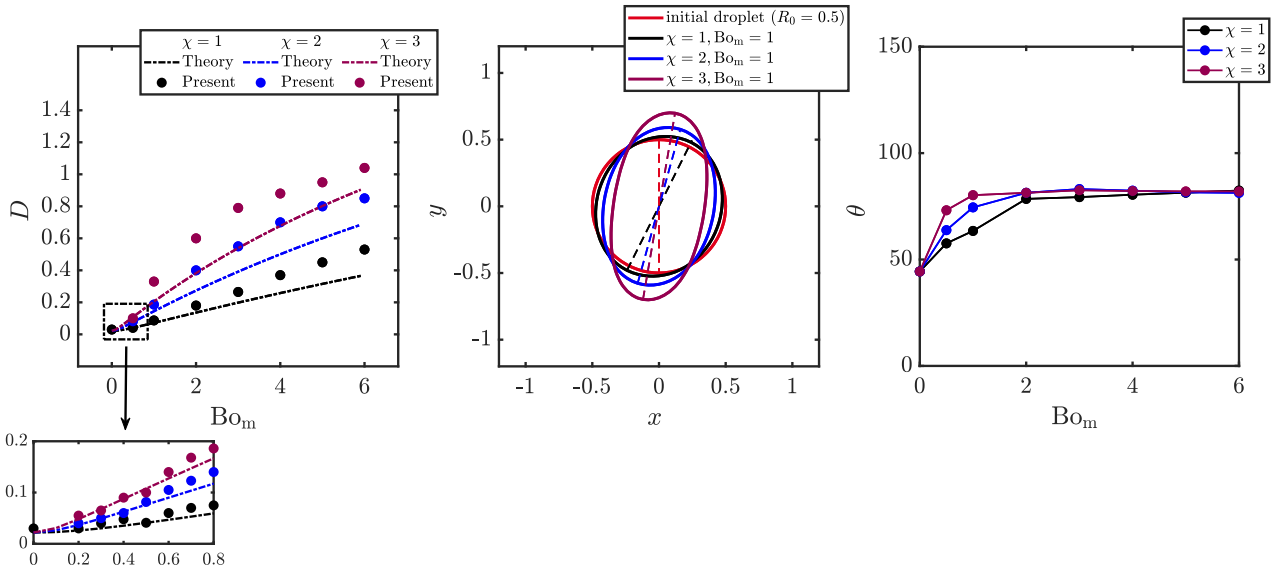

Figure 2.13: [left] Comparison of analytical and numerical results for three different magnetic susceptibility values of $\chi = 1$, 2, and 3 under varying magnetic Bond numbers and fixed capillary number, $\mathrm{Ca} = 0.02$. [middle] Ferrofluid droplet at steady state for three cases of $\chi = 1$, 2, and 3, with the capillary number and magnetic Bond number of 0.02 and 1, respectively. The dashed line connects the poles of the droplet for each case. [right] Ferrofluid droplet inclination, θ, for three different magnetic susceptibility values of $\chi = 1$, 2, and 3 under varying magnetic Bond numbers and fixed capillary number, $\mathrm{Ca} = 0.02$.

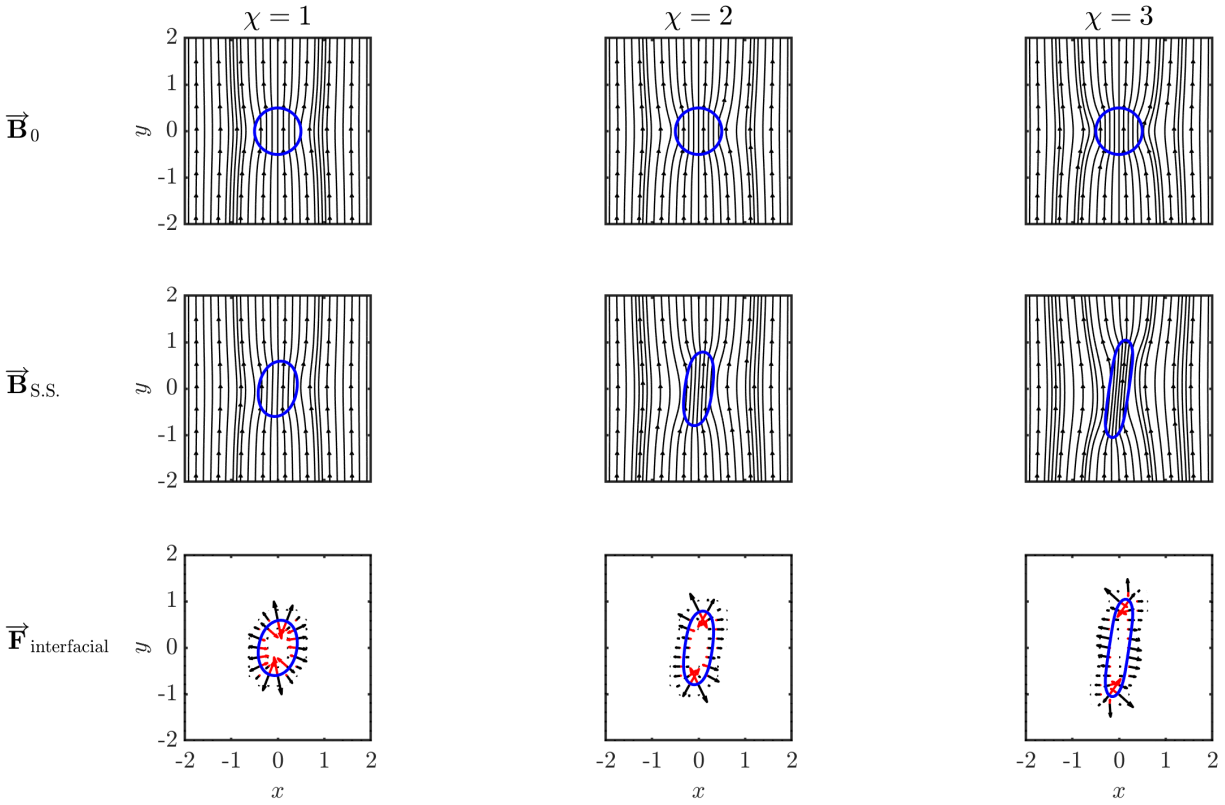

Figure 2.14: [top] Configuration of the ferrofluid droplet along with magnetic field at $t = 0$, [middle] steady state, and [bottom] depiction of the magnetic force (in black) and capillary force (in red) acting at the droplet interface for three cases of $\chi = 1$, 2, and 3, with $\text{Bo}_\text{m} = 2$ and $\text{Ca} = 0.02$.

of 45°, while the external magnetic field aims to elongate the droplet along its vertical field lines. The superposition of these two effects results in the rotation of the droplet. In the low capillary regime, as the magnetic Bond number increases, magnetic forces overcome the shear effect, causing the θ angle to increase along with the droplet deformation parameter. According to the numerical results, for a constant magnetic Bond number less than 2, the higher the droplet's susceptibility, the greater the rotational angle. This can be attributed to the increased Maxwell stress for higher susceptibility values, which further prevents the droplet from deflecting at the 45° angle. However, for magnetic Bond numbers of 3 and greater, the rotational angle becomes almost the same for all different susceptibility values, with no noticeable difference observed between them. These results suggest that not

only does increasing the susceptibility value significantly affect droplet deformation, but also for lower magnetic Bond numbers, higher susceptibility leads to a greater rotational angle, causing the droplet to become more vertical. This is an important observation that can be further utilized when studying sheared droplet deformation in various applications.

The effect of the value of susceptibility on the deformation of a ferrofluid droplet is also investigated in the high capillary regime, Ca=0.2, achieved by increasing the shear rate. In Fig. 2.15(a), the deformation parameters of deformed droplets with two different susceptibilities, $\chi = 1$ and 2, are represented for magnetic Bond numbers ranging from 0 to 4, while keeping Ca=0.2 constant. The theoretical results are also included in this figure. As expected, since we are in the higher capillary regime, the theoretical approach does not accurately predict the D values. The theoretical analysis is valid only for $\mathrm{Ca} \ll 1$, and its predictions become less reliable as the magnetic Bond number increases. According to this figure, for a constant magnetic Bond number, increasing the χ values results in an increase in the deformation parameter, similar to the observations in the previous section. However, it is notable that the obtained deformation parameters in this case are greater than those in the previous case with Ca=0.02. This is because the greater shear rate allows the external shear flow to more effectively influence the droplet's deformation. Moreover, it is evident that by increasing the magnetic Bond number, the angle θ increases and approaches an almost constant value. However, in this case, due to the stronger shear flow, the droplet tends to deflect more toward the 45° shear angle (please compare Fig. 2.13[right] and Fig. 2.15(a)). The calculated deflection angles in the case of $\chi = 2$ for magnetic Bond numbers below 2, are higher than those for $\chi = 1$. This is because for $\chi = 2$, the magnetic field lines are deflected further near the droplet's interface due to a higher magnetic permeability discontinuity across the interface, resulting in a stronger force to elongate the droplet along the field lines and leading to higher θ angles. It is worth noting that the results for $\chi = 2$ under magnetic Bond numbers of 3 and 4 are absent in this figure. This is because for these magnetic Bond number values, the ferrofluid droplet has not reached a steady-state condition, as shown in Fig. 2.15(b), and it continues deforming until it undergoes breakup. Figure 2.15(c) illustrates the sheared droplet's deformation and breakup for the case where $\chi = 2$ and $\mathrm{Bo_m} = 4$ at eight different time steps, up to the moment when breakup occurs. The magnetic Bond

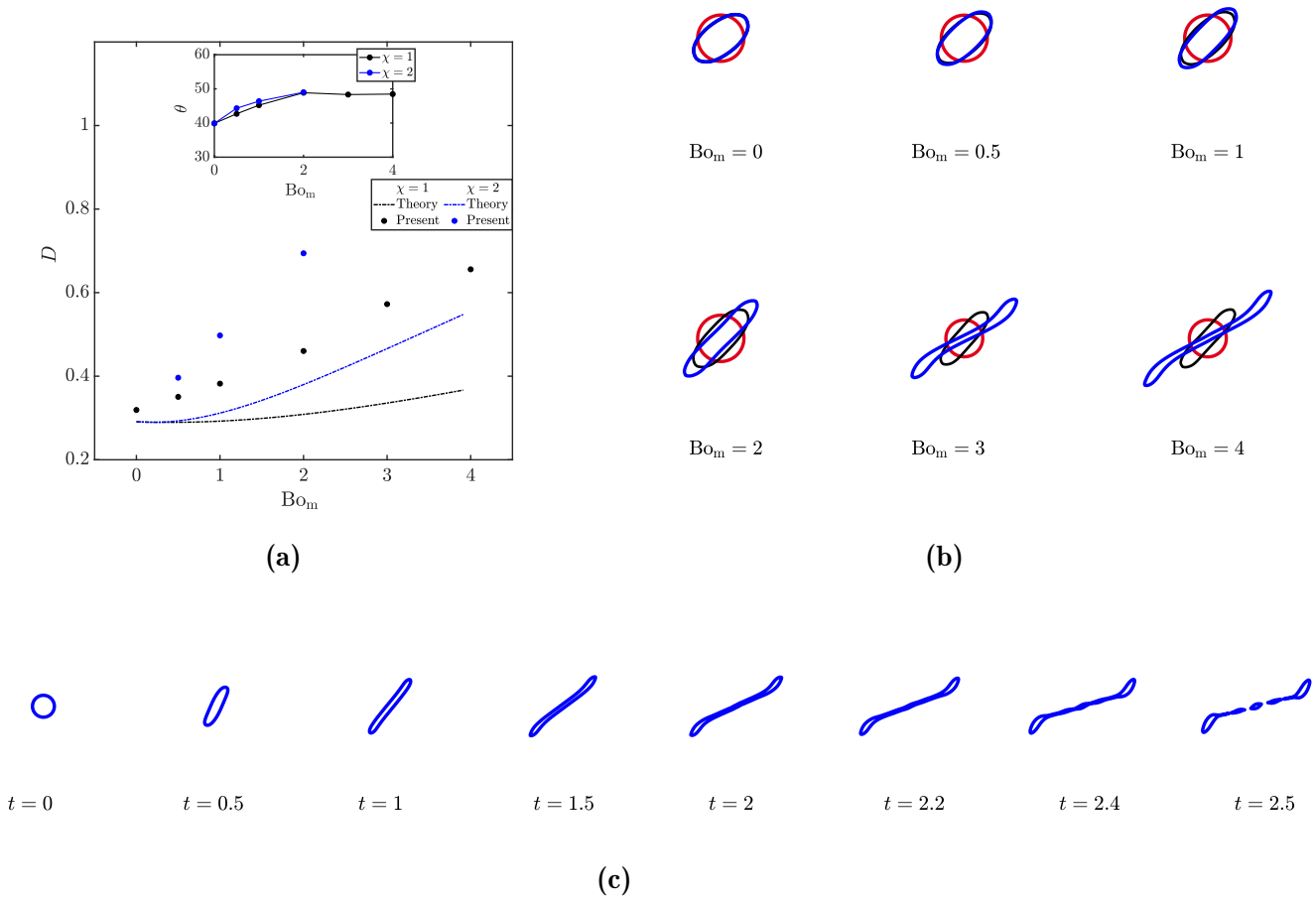

Figure 2.15: (a) Comparison of theoretical and numerical results for two different magnetic susceptibility values, $\chi = 1$ and 2, under varying magnetic Bond numbers, while maintaining a fixed capillary number, Ca = 0.2. The inclination of the ferrofluid droplet, θ, for different cases is also included in this figure. (b) Visualization of a ferrofluid droplet at steady state for two cases with $\chi = 1$ and 2, each at a capillary number of 0.2, across six different magnetic Bond numbers (0, 0.5, 1, 2, 3, and 4). The red contour represents the initial droplet configuration at $t = 0$. Notably, for the case with $\chi = 2$ and magnetic Bond numbers of 3 and 4, the ferrofluid droplet has not reached a steady state, leading to a loss of its ellipsoidal shape as it continues to stretch and thin in the middle. (c) The sheared droplet deformation and breakup for the case $\chi = 2$ with a magnetic Bond number of 4 at $t = 0$, 0.5, 1, 1.5, 2, 2.2, 2.4, and 2.5, presented from left to right, respectively.

number of approximately 3 is the critical value below which the droplet does not rupture. In previous studies, other properties such as the effect of viscosity ratio on droplet breakup were investigated (Hassan & Wang, 2019). In this test case, we have demonstrated that increasing the magnetic susceptibility value of the droplet can also cause droplet breakup, introducing the concept of a critical susceptibility value above which, for a constant Ca and $\mathrm{Bo_m}$ values, breakup occurs. Therefore, the magnetic permeability ratio between the droplet and its surrounding flow not only affects its deformation but can also lead to a breakup mechanism.

2.6.2.3 Rayleigh–Taylor instability in magnetic fluids

The Rayleigh–Taylor instability, which occurs when the interface between fluids of different densities is accelerated towards the direction of the heavy fluid, is widely studied for conducting fluids in the presence of a magnetic field as well. Magneto-Rayleigh–Taylor instability is of importance in different applications, e.g., Z-pinch fusion reactors (Velikovich *et al.*, 1996), magnetic flux compression (Harris, 1962), and laser-driven inertial confinement fusion (Velikovich & Schmit, 2015). In this test case, we investigate the Rayleigh–Taylor instability for magnetic fluids in the presence of a tangential quasi-static magnetic field to validate the performance of the implemented solver. By employing the linear analysis on the Rayleigh–Taylor instability, Awasthi (2014) derived the following quadratic dispersion relation for two viscous, incompressible, and magnetic fluids in the presence of a tangential magnetic field

$$\overbrace{\left[\rho_1+\rho_2\right]}^{\alpha}\omega^2+\overbrace{\left[4k^2(\mu_1+\mu_2)\right]}^{\beta}\omega+\overbrace{\left[(\rho_1-\rho_2)\,gk+\sigma k^3+\frac{k^2H_0^2\left(\mu_{\mathrm{m},2}-\mu_{\mathrm{m},1}\right)^2}{\left(\mu_{\mathrm{m},1}+\mu_{\mathrm{m},2}\right)}\right]}^{\gamma}=0. \quad (2.59)$$

In Eq. (3.13), ω and k variables are the growth rate and wave number of a small perturbation at the interface, respectively, and subscript 1 (2) refers to the lighter (heavier) fluid. According to the instability criteria of Routh–Hurwitz, the stability condition is given as $\alpha > 0$, $\beta > 0$, and $\gamma > 0$ (Awasthi, 2014). Coefficients α and β are always positive, and, therefore, the stability condition is reduced to $\gamma > 0$. The last term of the coefficient γ represents the

effect of the imposed magnetic field on the growth rate of the Rayleigh–Taylor instability. This term is always positive since the value of all the components in this term is positive. Hence, the tangential magnetic field always has a stabilizing effect on the Rayleigh–Taylor instability growth, similar to the effect of surface tension. For the sake of a more consistent analysis, by using the following dimensionless variables as

$$\hat{k} = kL, \quad \hat{\rho} = \frac{\rho_1}{\rho_2}, \quad \hat{\mu} = \frac{\mu_1}{\mu_2}, \quad \hat{\mu}_{\mathrm{m}} = \frac{\mu_{\mathrm{m},1}}{\mu_{\mathrm{m},2}}, \quad \hat{\sigma} = \frac{\sigma}{\rho_2\, g\, L^2}, \quad \hat{H} = \frac{H_0\sqrt{\hat{\rho}}}{\sqrt{(1-\hat{\rho})\; g\, L}}\sqrt{\frac{\mu_{\mathrm{m},2}}{\rho_2}}, \tag{2.60}$$

where L is the characteristic length scale of the domain, the non-dimensional stability condition is expressed as

$$1 - \frac{\hat{\sigma}\hat{k}^2}{(1-\hat{\rho})} - \frac{\hat{k}\hat{H}^2\,(1-\hat{\mu}_{\mathrm{m}})^2}{\hat{\rho}\,(1+\hat{\mu}_{\mathrm{m}})} \leq 0. \tag{2.61}$$

For the state of the marginal stability, when Eq. (2.61) is zero, the critical value of the transverse magnetic field, $\hat{H}_{\mathrm{c}}$, is given as

$$\hat{H}_{\mathrm{c}}{}^2 = \frac{\left[(1-\hat{\rho}) - \hat{\sigma}\hat{k}^2\right]\hat{\rho}\,(1+\hat{\mu}_{\mathrm{m}})}{\hat{k}\,(1-\hat{\rho})\,(1-\hat{\mu}_{\mathrm{m}})^2}. \tag{2.62}$$

Hence, depending on whether the imposed transverse magnetic field is larger or smaller than the critical magnetic field, the system becomes stable or unstable, respectively.

To investigate the performance of the implemented solver for two-phase magnetic flows, the evolution of the Rayleigh–Taylor instability under different magnetic field intensities is simulated. To this end, the same initial condition as those presented in Sec. 2.5.4 for the Rayleigh–Taylor instability test case, with the grid resolution of 32×128, $\hat{\rho} = 1/3\,(\rho_1 = 1, \rho_2 = 3)$, and $\hat{\mu}_{\mathrm{m}} = 0.01\,(\mu_{\mathrm{m},1} = 10^{-3}, \mu_{\mathrm{m},2} = 10^{-1})$ is considered. Three cases of $\hat{H}_0 < \hat{H}_{\mathrm{c}}\,(H_0 = 2)$, $\hat{H}_0 \approx \hat{H}_{\mathrm{c}}\,(H_0 = 5)$, and $\hat{H}_0 > \hat{H}_{\mathrm{c}}\,(H_0 = 10)$ are examined*. The purpose is to qualitatively compare the numerical results with the ones obtained from linear perturbation analysis. Based on Fig. 2.16(a), it is visually evident that the presence of a transverse magnetic field, regardless of its magnitude, tends to suppress the growth of the Rayleigh–Taylor instability. This observation is consistent with the results obtained from

* The critical value of the transverse magnetic field, H_{c}, is expected to be around 4.

other studies (El-Dib, 1994; Awasthi, 2014), stating that the Lorentz force at the interface acts as a restoring force. However, depending on the magnitude of the imposed transverse magnetic field, the evolution of the interface under the Rayleigh–Taylor instability varies. In the case of $\hat{H}_0 < \hat{H}_c$, since the magnitude of the magnetic field is small compared to the critical magnetic field, the growth of the Rayleigh–Taylor instability is expected to be similar to the non-magnetic case, but with a slightly reduced growth rate over time. This behaviour is captured by the implemented numerical solver, as represented in Fig. 2.16(a). On the other hand, when the applied magnetic field is of the order of or greater than the calculated critical magnetic field, the Rayleigh–Taylor instability is anticipated to reach a stable regime. Consequently, the interface between the two fluids oscillates, and the penetration of the heavier fluid to the lighter one is prevented. The solver successfully reproduced these expected results, as demonstrated in Fig. 2.16(a). Additionally, it is apparent from Fig. 2.16(a) that for higher values of the applied magnetic field, the interface oscillates at a faster rate, consistent with the dispersion relation described by Eq. (3.13).

The magnetic permeability ratio between the two fluids, $\hat{\mu}_m$, also influences the evolution of the Rayleigh–Taylor instability. By keeping the imposed transverse magnetic field constant and by varying $\hat{\mu}_m$, the critical magnetic field, $\hat{H}_c$, changes. Consequently, if the Rayleigh–Taylor instability becomes stable for a given $\hat{\mu}_m$ and $\hat{H}_0$, altering the value of $\hat{\mu}_m$ can render it unstable. It is for this reason that the magnetic permeability ratio has a dual role of destabilizing and stabilizing the system, as was mentioned by Awasthi (2014). To assess the solver's capability to accurately handle different magnetic permeability ratios across the interface, three cases of $\hat{\mu}_m = 0.01$, $\hat{\mu}_m = 1$, and $\hat{\mu}_m = 100$ are investigated for a constant imposed $\hat{H}_0$, shown in Fig. 2.16(b). It can be visually confirmed that the case of $\hat{\mu}_m = 1$ is the most unstable one, a finding that is consistent with Eq. (3.13). The Rayleigh–Taylor instability transitions to a stable regime when $\hat{\mu}_m = 0.01$. However, by changing the magnetic permeability ratio to 100, the system becomes unstable, demonstrating the destabilizing effect of the $\hat{\mu}_m$.

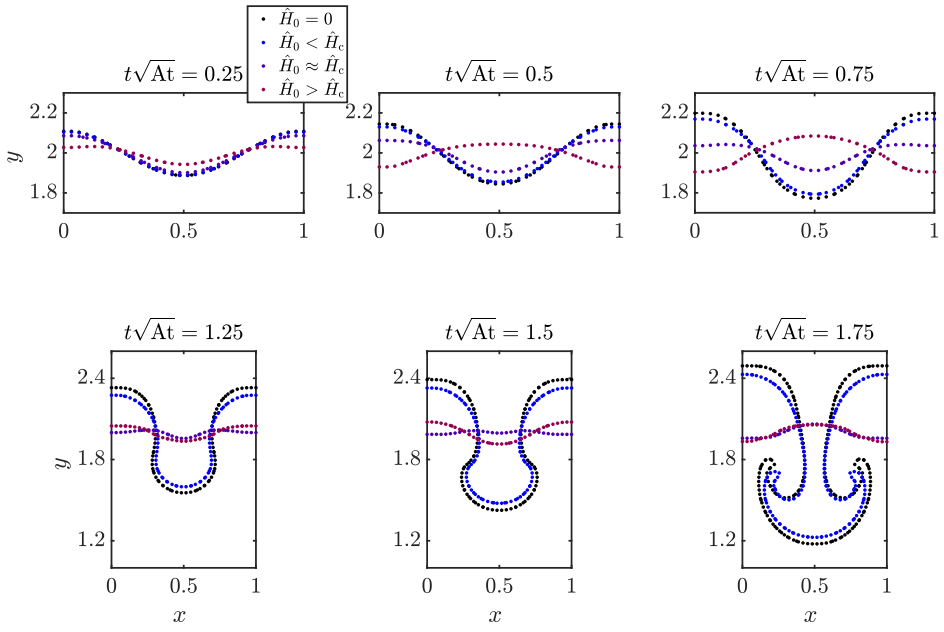

(a)

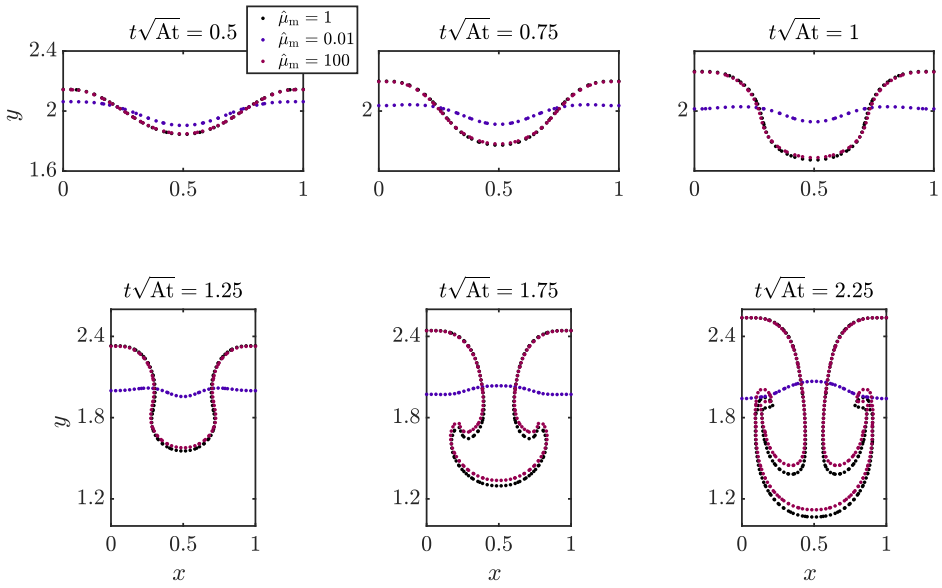

(b)

Figure 2.16: (a) The interface evolution of the Rayleigh–Taylor instability with $\hat{\rho} = 1/3$ and $\hat{\mu}_\mathrm{m} = 0.01$, at $t\sqrt{\mathrm{At}} = 0.25, 0.5, 0.75, 1.25, 1.5$, and 1.75, for three conditions of $\hat{H}_0 < \hat{H}_\mathrm{c}$, $\hat{H}_0 \approx \hat{H}_\mathrm{c}$, and $\hat{H}_0 > \hat{H}_\mathrm{c}$, along with the nonmagnetic case. (b) The interface evolution for three conditions of $\hat{\mu}_\mathrm{m} = 0.01$, $\hat{\mu}_\mathrm{m} = 1$, and $\hat{\mu}_\mathrm{m} = 100$, with a constant $H_0 = 5$ and $\mu_{\mathrm{m},1} = 0.001$, at $t\sqrt{\mathrm{At}} = 0.5, 0.75, 1, 1.25, 1.75$, and 2.25. The simulations are performed on 32×128 mesh resolution and time step $\Delta t = 5 \times 10^{-4}/\sqrt{\mathrm{At}}$.

2.7 Conclusion

This paper presents a numerical development of a two-phase incompressible solver for magnetic flows. The proposed numerical toolkit couples the Navier–Stokes equations of hydrodynamics with Maxwell's equations of electromagnetism, enabling us to model the behaviour of magnetic flows in the presence of a static magnetic field. In order to achieve this goal, first, a detailed implementation of a second-order two-phase solver for incompressible nonmagnetic flows is introduced. This two-phase solver utilizes a fifth-order conservative level set method within the finite-difference framework to capture the interface evolution during the simulation. The accuracy, robustness, and mass conservation properties of the level set solver are verified by conducting three test cases, namely, a rotating circle, a circle in a deformation field, and Zalesak's disk. Additionally, the incompressible Navier–Stokes equations are modelled based on the projection method and solved in the conservative form. The order of accuracy for the implemented two-phase nonmagnetic solver is verified through the capillary wave test case. The Rayleigh–Taylor instability test is also performed to evaluate the performance of the solver for more complicated interface evolution and higher density ratios. For the magnetic case, the reduced Maxwell equations under the magnetostatic assumption are solved based on the vector potential formulation. Subsequently, the primary two-phase solver is extended to account for magnetic flows by incorporating the Lorentz force in the momentum equation. The developed solver demonstrated the capability to handle high magnetic permeability jumps across the interface. Three benchmarks were conducted to evaluate the performance and robustness of the implemented two-phase solver for magnetic flows in the presence of a static magnetic field. The first test case explored droplet deformation under the influence of an external magnetic field in a quiescent flow, examining the interplay between the Lorentz force and capillary force at the interface across varying magnetic field amplitudes. These findings were validated by comparing them with analytical solutions and existing numerical and experimental results from the literature. In the sheared ferrofluid droplet test, the impact of magnetic susceptibility on droplet dynamics was studied. The results revealed that an increase in the susceptibility of the ferrofluid droplet could influence its deformation and rotation in low capillary regimes. However, in higher capillary flows, it

was observed that, under constant capillary and magnetic Bond number values, increasing magnetic susceptibility could lead to droplet breakup. Furthermore, the solver was employed to simulate Rayleigh–Taylor instability in magnetic fluids. Numerical results were compared with linear stability analysis across different magnetic field intensities and magnetic permeability ratios at the interface. This analysis facilitated a discussion regarding the effects of these variables in either stabilizing or destabilizing the Rayleigh–Taylor instability.

Acknowledgments

The authors would like to thank Victor Boniou for his valuable comments on the surface tension implementation and curvature calculations. Paria Makaremi-Esfarjani further acknowledges the helpful suggestions of Khashayar F. Kohan on the initial draft of the manuscript. The authors thank Mathias Larrouturou for useful feedback on the manuscript. This study was supported by the Natural Science and Engineering Research Council of Canada (NSERC) through a NSERC Discovery Grant and Mitacs through the Mitacs Accelerate program.

Appendix A. Fifth-order weighted essentially non-oscillatory (WENO) interpolation

The computation of the level set convective flux requires the interpolation of cell center ψ values to cell faces using an upwind-based scheme. In this study, a fifth-order WENO interpolation is implemented in our numerical solver, explained in greater detail in this section. The concept of the WENO interpolation is similar to the WENO reconstruction. This method involves using a weighted combination of three sub-stencils to calculate the flux values, resulting in a high-order scheme. The weights are chosen to minimize the contribution of stencils with discontinuities, thereby avoiding numerical instability and providing non-oscillatory interpolation.

In Fig. 2.17, the one-dimensional stencil for the fifth-order interpolation in x_i-direction is shown. Subscripts L (left) and R (right) are employed to denote the interpolated values at each cell face based on upwinding considerations. As a result, cell values at $\tilde{\psi}_{\mathrm{L},x_{i+1/2}}$ and

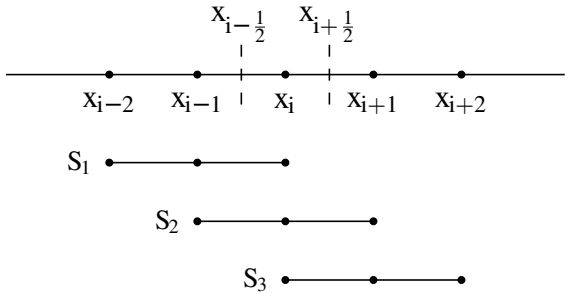

Figure 2.17: The stencil for the fifth-order WENO interpolation scheme to find $\tilde{\psi}_{\mathrm{L},\,x_{i+1/2}}$ and $\tilde{\psi}_{\mathrm{R},\,x_{i-1/2}}$ values at $x_{i+1/2}$ and $x_{i-1/2}$ cell faces, respectively.

$\tilde{\psi}_{\mathrm{R},x_{i-1/2}}$ have the same five-points stencil, shown in Fig. 2.17, and can be divided into three sub-stencils

$$\mathrm{S}_1 = \{x_{i-2},\, x_{i-1},\, x_i\}\,, \tag{2.63a}$$

$$\mathrm{S}_2 = \{x_{i-1},\, x_i,\, x_{i+1}\}\,, \tag{2.63b}$$

and

$$\mathrm{S}_3 = \{x_i,\, x_{i+1},\, x_{i+2}\}\,. \tag{2.63c}$$

Using the third-order interpolation, the cell face values can be obtained for each sub-stencil as

$$\psi^{(1)}_{\mathrm{L},\,x_{i+1/2}} = \frac{3}{8}\psi_{x_{i-2}} - \frac{5}{4}\psi_{x_{i-1}} + \frac{15}{8}\psi_{x_i}, \tag{2.64a}$$

$$\psi^{(2)}_{\mathrm{L},\,x_{i+1/2}} = -\frac{1}{8}\psi_{x_{i-1}} + \frac{3}{4}\psi_{x_i} + \frac{3}{8}\psi_{x_{i+1}}, \tag{2.64b}$$

$$\psi^{(3)}_{\mathrm{L},\,x_{i+1/2}} = \frac{3}{8}\psi_{x_i} + \frac{3}{4}\psi_{x_{i+1}} - \frac{1}{8}\psi_{x_{i+2}}, \tag{2.64c}$$

and

$$\psi^{(1)}_{\mathrm{R},\,x_{i-1/2}} = -\frac{1}{8}\psi_{x_{i-2}} + \frac{3}{4}\psi_{x_{i-1}} + \frac{3}{8}\psi_{x_i}, \tag{2.65a}$$

$$\psi^{(2)}_{\mathrm{R},\,x_{i-1/2}} = \frac{3}{8}\psi_{x_{i-1}} + \frac{3}{4}\psi_{x_i} - \frac{1}{8}\psi_{x_{i+1}}, \tag{2.65b}$$

$$\psi^{(3)}_{\mathrm{R},\,x_{i-1/2}} = \frac{15}{8}\psi_{x_i} - \frac{5}{4}\psi_{x_{i+1}} + \frac{3}{8}\psi_{x_{i+2}}. \tag{2.65c}$$

The fifth-order interpolation is then obtained by combining the calculated third-order interpolation for three sub-stencils using non-linear weights, defined as

$$\tilde{\psi}_{\mathrm{L},\,x_{i+1/2}} = \sum_{k=1}^{3} \omega_{\mathrm{L},\,k}\, \psi^{(k)}_{\mathrm{L},\,x_{i+1/2}}, \quad \text{and} \quad \tilde{\psi}_{\mathrm{R},\,x_{i-1/2}} = \sum_{k=1}^{3} \omega_{\mathrm{R},\,k}\, \psi^{(k)}_{\mathrm{R},\,x_{i-1/2}}, \tag{2.66}$$

where ω variables are the nonlinear weights adopted from Jiang & Shu (1996), given as

$$\omega_{\mathrm{L},\,k} = \frac{\beta_{\mathrm{L},\,k}}{\sum_{m=1}^{3} \beta_{\mathrm{L},m}}, \quad \text{and} \quad \omega_{\mathrm{R},\,k} = \frac{\beta_{\mathrm{R},\,k}}{\sum_{m=1}^{3} \beta_{\mathrm{R},m}}, \tag{2.67}$$

where

$$\beta_{\mathrm{L},\,k} = \frac{\bar{\omega}_{\mathrm{L},\,k}}{(\epsilon + \mathrm{IS}_k)^2}, \quad \text{and} \quad \beta_{\mathrm{R},\,k} = \frac{\bar{\omega}_{\mathrm{R},\,k}}{(\epsilon + \mathrm{IS}_k)^2}. \tag{2.68}$$

Here parameter ϵ is used to prevent the denominators to become zero. The value of ϵ is typically chosen to be between 10^{-5} and 10^{-7} (Jiang & Shu, 1996). In this study, we used a value of $\epsilon = 10^{-6}$. Variables IS_k are the smooth indicators for each sub-stencil, defined as

$$\mathrm{IS}_1 = \frac{1}{3}\left[\psi_{x_{i-2}}\left(4\psi_{x_{i-2}} - 19\psi_{x_{i-1}} + 11\psi_{x_i}\right) + \psi_{x_{i-1}}\left(25\psi_{x_{i-1}} - 31\psi_{x_i}\right) + 10\psi^2_{x_i}\right], \tag{2.69a}$$

$$\mathrm{IS}_2 = \frac{1}{3}\left[\psi_{x_{i-1}}\left(4\psi_{x_{i-1}} - 13\psi_{x_i} + 5\psi_{x_{i+1}}\right) + 13\psi_{x_i}\left(25\psi_{x_i} - \psi_{x_{i+1}}\right) + 4\psi^2_{x_{i+1}}\right], \tag{2.69b}$$

and

$$\mathrm{IS}_3 = \frac{1}{3}\left[\psi_{x_i}\left(10\psi_{x_i} - 13\psi_{x_{i+1}} + 11\psi_{x_{i+2}}\right) + \psi_{x_{i+1}}\left(25\psi_{x_{i+1}} - 19\psi_{x_{i+2}}\right) + 4\psi^2_{x_{i+2}}\right], \tag{2.69c}$$

where $\bar{\omega}_{\mathrm{L},\,k}$ and $\bar{\omega}_{\mathrm{R},\,k}$ are the linear optimal weights for the fifth-order interpolation, calculated using the Lagrange interpolation, and are determined as

$$\bar{\omega}_{\mathrm{L},\,k} = \left\{\frac{1}{16}, \frac{10}{16}, \frac{5}{16}\right\}, \quad \text{and} \quad \bar{\omega}_{\mathrm{R},\,k} = \left\{\frac{5}{16}, \frac{10}{16}, \frac{1}{16}\right\}. \tag{2.70}$$

The same procedure can be applied in each direction for multi-dimensional problems as well.

Appendix B. Third-order Runge–Kutta scheme

The third-order, total variation diminishing (TVD) Runge–Kutta scheme introduced by Gottlieb & Shu (1998) is an explicit temporal integration scheme, which can attenuate spurious oscillations appearing in the solution.

Consider a system of differential equations given by

$$\frac{\partial \boldsymbol{U}}{\partial t} = \boldsymbol{F}(\boldsymbol{U}, t), \tag{2.71}$$

where $\boldsymbol{U}$ is the vector of conservative variables and $\boldsymbol{F}$ is a right-hand-side operator. For a known solution, $\boldsymbol{U}^n$, the third-order Runge–Kutta scheme approximates the solution at the next time step, $\boldsymbol{U}^{n+1}$, using an intermediate step

$$\boldsymbol{U}^1 = \boldsymbol{U}^n + \Delta t \boldsymbol{F}(\boldsymbol{U}^n, t), \tag{2.72}$$

followed by

$$\boldsymbol{U}^2 = \frac{3}{4}\boldsymbol{U}^n + \frac{1}{4}\boldsymbol{U}^1 + \frac{1}{4}\Delta t \boldsymbol{F}(\boldsymbol{U}^1, t), \tag{2.73}$$

which in turn is followed by the final step

$$\boldsymbol{U}^{n+1} = \frac{1}{3}\boldsymbol{U}^n + \frac{2}{3}\boldsymbol{U}^2 + \frac{2}{3}\Delta t \boldsymbol{F}(\boldsymbol{U}^2, t), \tag{2.74}$$

where Δt denotes the time step.

Appendix C. Evaluation of level set solver numerical accuracy: Rotating circle test

The rotating circle test is examined to study the numerical order of accuracy of the level set solver. In this test case, a circular interface of radius $r = 0.15$, with its center initially located at $(x_0, y_0) = (0.25, 0.25)$ is considered. The circle rotates in the two-dimensional computational domain, $[x, y] \in [-0.8, 0.8] \times [-0.8, 0.8]$, under the constant velocity field

$(u, v) = (y, -x)$. According to the initial condition of the problem, the circle should return to its initial place after one revolution at $t = 2\pi$. The initial velocity field and the evolution of the rotating circle from $t = 0$ to $t = 2\pi$ is represented in Fig. 2.18(a). The initial thickness of the level set profile is set to be $\epsilon = (\Delta x)^{0.8}/2$, with the constant time step equal to $\Delta t = 0.001$ and $\Delta\tau = 0.0005$ for transport and re-initialization equations, respectively. The re-initialization process is executed every 20 steps, with a maximum of two iterations per step. The simulation is performed for five different grid resolutions, and L_2 and L_∞ errors are determined for each case. The values of L_2 and L_∞ errors are calculated as

$$L_2 \text{ error} = \sqrt{\frac{\Sigma_{i=1}^{N} \left(\psi_{\text{anal},i} - \psi_{\text{num},i}\right)^2}{N}} \qquad \text{and} \qquad L_\infty \text{ error} = \max \left|\psi_{\text{anal},i} - \psi_{\text{num},i}\right|, \quad (2.75)$$

where $\psi_{\text{anal},i}$ and $\psi_{\text{num},i}$ denote the analytical and numerical results at grid point i, respectively, and N is the total number of the grid points. In Fig. 2.18(b), the error values are plotted versus the number of nodes in the logarithmic scale, and, hence, the slope of the plot depicts the estimated convergence rate of the implemented numerical scheme. As can be observed from Fig. 2.18(b), the order of accuracy is between 4 and 4.5, which is pretty close to the excepted fifth-order accuracy of the implemented method, even for the defined sharp interface case ($\epsilon < \Delta x/2$). However, the re-initialization step is expected to affect the global accuracy of the level set solver.

Appendix D. Incompressible solver test cases

In this section, two test cases are presented, the Taylor–Green vortex and the lid-driven cavity, to examine the order of accuracy and robustness of the implemented incompressible solver.

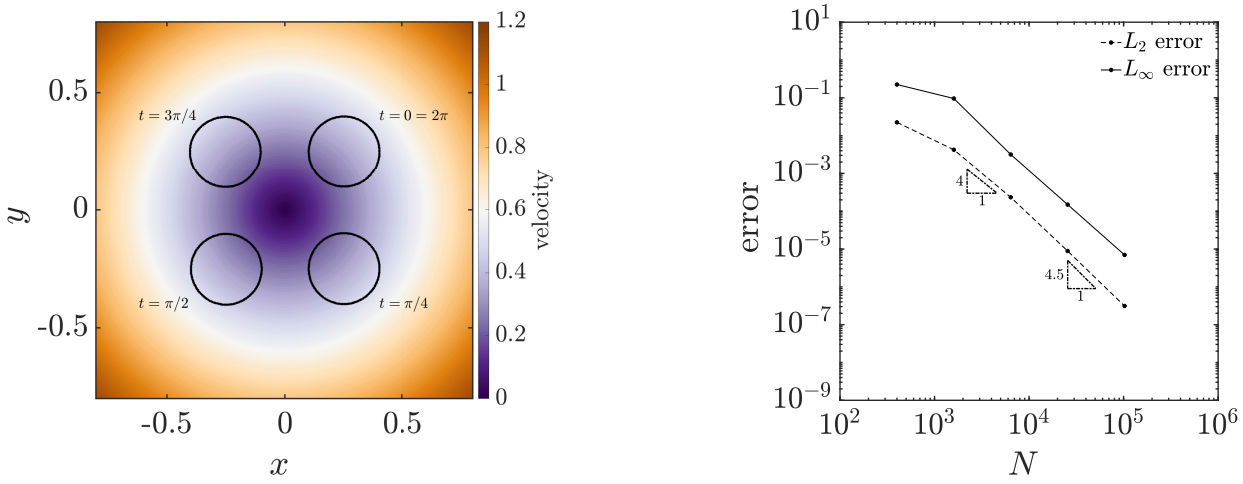

(a) **(b)**

Figure 2.18: (a) The velocity field of the rotating circle test case along with the $\psi = 0.5$ location at $t = 0, \pi/4, \pi/2, 3\pi/4$, and 2π. (b) Order of accuracy analysis for the implemented level set solver using the rotating circle test case. The error values are computed for five different grid resolutions, 20×20, 40×40, 80×80, 160×160, and 320×320, with a constant time step for all simulations.

Decay of a Taylor–Green vortex

The Taylor–Green vortex is a well-known test case in the literature to examine the ability of an incompressible Navier–Stokes numerical solver to simulate transient problems. In this study, the Taylor–Green test is investigated to evaluate the order of accuracy of the implemented incompressible solver. The analytical solution of this benchmark is given as

$$u = \sin(kx)\cos(ky)\exp\left(-2\mu k^2 t/\rho\right), \tag{2.76a}$$

$$v = -\cos(kx)\sin(ky)\exp\left(-2\mu k^2 t/\rho\right), \tag{2.76b}$$

and

$$p = \frac{1}{4}\rho\left[\cos(2kx) + \cos(2ky)\right]\exp\left(-4\mu k^2 t/\rho\right), \tag{2.76c}$$

where k is the wavenumber, set to $k = 1$. The magnitude of the initial velocity field is represented in Fig. 2.19(a), which will be exponentially damped due to the presence of the

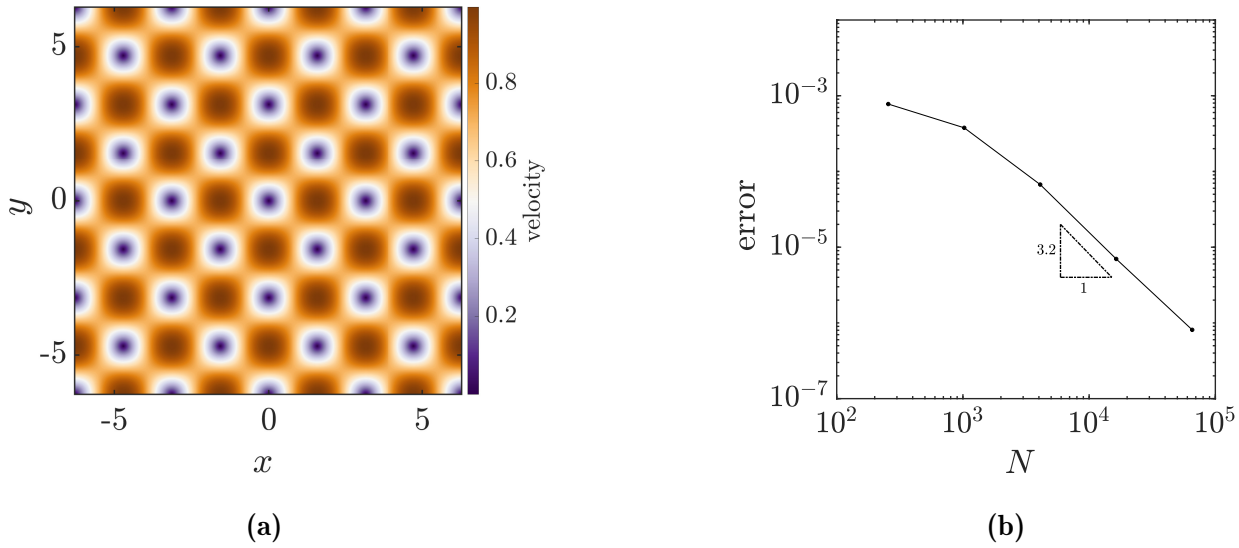

Figure 2.19: (a) Initial velocity field of the Taylor–Green test case. (b) Order of accuracy analysis for the implemented incompressible solver using the decaying Taylor–Green vortex test case. The error values are computed for five different grid resolutions, 16×16, 32×32, 64×64, 128×128, and 256×256, with the constant time step, $\Delta t = 0.001$, for all the simulations.

viscosity. The simulation is performed on the computational domain $[x, y] \in [0, 2\pi] \times [0, 2\pi]$, with a periodic boundary condition implemented at all boundaries. The values of density and dynamic viscosity are set to 1 and 0.01, respectively. The simulation is run for five different grid resolutions, $16 \times 16, 32 \times 32, 64 \times 64, 128 \times 128$, and 256×256, with the constant time step, $\Delta t = 0.001$. The maximum error of the velocity field is calculated at $t = 0.2$ for each case. In Fig. 2.19(b), the error values are plotted against the number of nodes in the logarithmic scale, demonstrating the estimated convergence rate of approximately three for the implemented incompressible solver. It should be noted that the global accuracy of the velocity field is affected by the approximation of the pressure gradient and the discretization of the diffusion term, which are second-order accurate herein. In Table 2.1, second-order convergence is observed for the pressure field as expected. Also, the maximum calculated error for the velocity divergence is quite small, $\mathcal{O}\left(10^{-13}\right)$, showing the proper divergence-free property of the velocity field.

Table 2.1: Calculated L_∞ error of the pressure and velocity divergence for different grid resolutions of the Taylor–Green test case.

Mesh resolution	Error of p	Rate	Error of $(\nabla \cdot \boldsymbol{u})$
16×16	5.28×10^{-2}	——	9.92×10^{-14}
32×32	1.69×10^{-2}	1.64	2.50×10^{-13}
64×64	5.44×10^{-3}	1.63	3.96×10^{-13}
128×128	1.50×10^{-3}	1.85	7.54×10^{-13}
256×256	3.91×10^{-4}	1.94	9.85×10^{-13}

Lid-driven cavity

The lid-driven cavity flow test case is used to evaluate the performance of the implemented solver for complicated flow fields and its capability to reach a steady state solution. This test case includes the square cavity, $[x, y] \in [0, 1] \times [0, 1]$, initially filled with an incompressible fluid, with the top wall moving with the constant velocity, $u = 1$, while the other three walls are stationary. The simulation is performed for two cases of Reynolds numbers of 100 and 1000, with a no-slip boundary condition imposed at all boundaries. The two simulations are run for the grid resolution of 100×100 and $\Delta t = 0.001$. Figure 2.20(a) depicts the streamlines of the velocity fields for $\mathrm{Re} = 100$ and $\mathrm{Re} = 1000$ cases at $t = 10$ and $t = 50$, respectively. This figure visually confirms that the calculated velocity field follows the expected behaviour, which is the formation of a primary vortex towards the center of the cavity and the generation of smaller corner vortices at the bottom corners. For a better evaluation, the computed results for the u and v velocities at the vertical and horizontal centerlines, respectively, are compared with the corresponding results from the study by Huang *et al.* (2019), shown in Fig. 2.20(b,c). As can be observed in this figure, there is a good agreement between the results of the two studies for both cases of $\mathrm{Re} = 100$ and $\mathrm{Re} = 1000$.

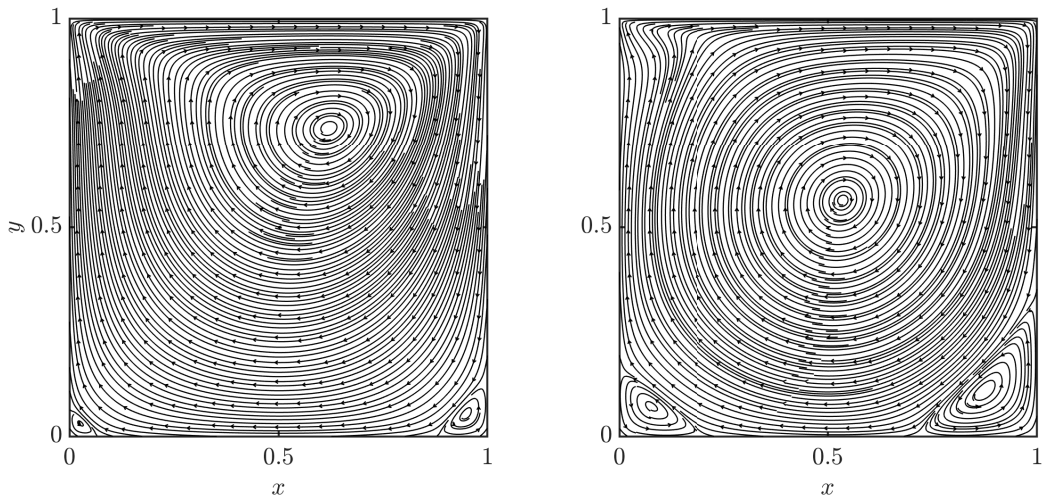

(a)

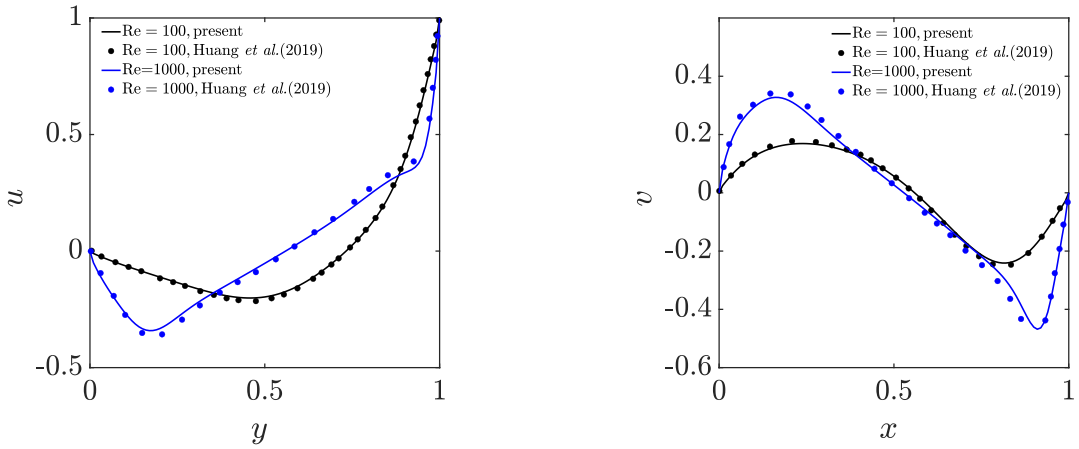

(b) **(c)**

Figure 2.20: (a) Velocity streamlines of the lid-driven cavity test case for [left] Re = 100 and [right] Re = 1000 cases, at $t = 10$ and $t = 50$, respectively. Calculated results of the lid-driven cavity test case for (b) u along the vertical line passing through the center, and (c) v along the horizontal line passing through the center, for Re = 100 (black) and Re = 1000 (blue) cases, at $t = 10$ and $t = 50$, respectively. Results obtained from this study and the study by Huang *et al.* (2019) are plotted using a solid line and a circle symbol, respectively.

Appendix E. Formation of spurious currents: Static droplet test

In this test case, a two-dimensional droplet is considered in a stationary velocity field, $\boldsymbol{u} = 0$. By setting the velocity field to zero and ignoring gravity, the equilibrium solution of the Navier–Stokes equation will result in $\Delta p = \boldsymbol{F}_\sigma = \sigma\kappa$, which satisfies the pressure jump condition, $[p] = \sigma\kappa$. This equilibrium condition is the well-known Laplace's relation between pressure and surface tension forces of a droplet in an equilibrium condition (Popinet, 2018). Therefore, the droplet is expected to remain at rest since the pressure force balances the capillary force. If the numerical solver cannot accurately calculate the curvature and, hence, fails to recover the equilibrium solution, quasi-stationary velocity patterns known as parasitic or spurious currents will appear in the solution (Boniou *et al.*, 2022). Thus, this test case has been widely used by researchers to investigate the capability of their solver to properly balance pressure and surface tension forces across the interface and its accuracy in computing the interface curvature (Boniou *et al.*, 2022). Additionally, the viscosity discontinuity between two flows results in discontinuity of the velocity derivative across the interface, which is more pronounced for larger viscosity ratios. This discontinuity can cause numerical errors in the divergence calculation of the velocity field, which leads to a source of error for pressure (Huang *et al.*, 2019). The inaccuracy in pressure calculation will generate errors when balancing forces across the interface and leads to the formation of unphysical spurious currents. Therefore, the spurious velocity formation is also investigated for different viscosity ratios across the interface in this benchmark.

In the initial condition, a circle of diameter $D = 0.4$ is considered at the center of the two-dimensional computational domain $[0, 1] \times [0, 1]$, where a no-slip boundary condition is imposed at all boundaries. The thickness of the interface is set to $\epsilon = \Delta x/2$. In order to study the magnitude of the spurious flow that will be generated due to the inaccuracies while computing the interface curvature, the proposed test case by Desjardins & Pitsch (2009) is followed. In their test case, the surface tension coefficient is set to $\sigma = 1$, with the same viscosity of $\mu = 0.1$ for both fluids and a constant density ratio of one, i.e., $\rho_1 = \rho_2$. The

Table 2.2: Calculated Ca values for different La numbers for the static droplet test case on the mesh resolution of 32×32, with density and viscosity ratios of one.

$\rho_1(\rho_2)$	La	Ca
0.3	12	5.029×10^{-5}
3	120	3.378×10^{-5}
30	1200	3.612×10^{-5}
300	12000	9.428×10^{-5}
3000	120000	2.657×10^{-4}

Laplace number, represented by $\mathrm{La} = \sigma\rho D/\mu^2$, is then altered by changing the density of both fluids to examine the performance of the solver for various ratios of surface tension and viscous forces. The intensity of the unwanted spurious currents appearing in the solution can be quantified by measuring the capillary number, $\mathrm{Ca} = |u_{\max}|\mu/\sigma$, for different Laplace numbers. The mesh resolution is set to 32×32, and the calculated capillary numbers at a non-dimensional time $t\sigma/(\mu D) = 250$ for five different Laplace numbers are reported in Table 2.2. For each Laplace number, the time step should be determined according to the CFL constraint introduced in Eq. (3.12). According to the calculated capillary numbers, the magnitude of spurious currents, even after a long simulation time, is minimal and independent of the Laplace number, confirming the well-balanced results between pressure and surface tension forces across the interface in the solver. It is worth mentioning that the order of calculated capillary numbers for different Laplace numbers is close to the ones obtained by Desjardins & Pitsch (2009), showing that the magnitude of the spurious errors is consistent with other studies in the literature.

In order to investigate the influence of the shear stress discontinuity across the interface due to the viscosity jump on the formation of spurious velocity, a benchmark akin to that of Huang *et al.* (2019) is also adopted. In this test case, a circle with the diameter of $D = 2$ in a computational domain $[0, 8] \times [0, 8]$ with the grid resolution of 101×101 is considered. For the initial condition of $\sigma = 730$, $\rho_1 = \rho_2 = 1$, and $\mu_1 = 0.001$, the calculated L_2 and L_∞ error norms of the velocity field after 1 and 1000 time steps are given in Table 2.3 for four different viscosity ratios of 1, 10, 100, and 1000, along with the inviscid case. It is appreciated from Table 2.3 that even for large viscosity ratios, the intensity of spurious currents is small and is

Table 2.3: Calculated L_2 and L_∞ norms of the velocity field for four different viscosity ratios along with the inviscid case for the static droplet test case.

	at 1^{st} time step		at 1000^{th} time step	
μ_2/μ_1	L_2	L_∞	L_2	L_∞
0	2.198×10^{-5}	2.286×10^{-4}	1.534×10^{-3}	7.919×10^{-3}
1	6.608×10^{-6}	6.903×10^{-5}	4.619×10^{-4}	2.522×10^{-3}
10	6.608×10^{-6}	6.903×10^{-5}	4.618×10^{-4}	2.521×10^{-3}
100	6.608×10^{-6}	6.903×10^{-5}	4.613×10^{-4}	2.509×10^{-3}
1000	6.608×10^{-6}	6.903×10^{-5}	4.562×10^{-4}	2.394×10^{-3}

close to the inviscid case. In other words, the strength of the parasite current is independent of the viscosity jump, and the solver accurately balances pressure and surface tension forces across the interface in the presence of a shear stress jump. Also, the calculated L_2 and L_∞ errors for both cases, after 1 and 1000 time steps, are in the same order as those reported by Huang *et al.* (2019) study.

Logical bridge

The previous chapter introduced a two-phase incompressible solver to model the behaviour of magnetic fluids, where Maxwell's equations are solved under the magnetostatic assumption. The implemented solver provides a suitable numerical capability for studying the behaviour of ferrofluid droplets and magnetic flows. However, to model liquid-metal liners—whether perfectly conductive or with finite resistivity—the full set of MHD equations must be solved. Accordingly, the following chapter extends the numerical toolkit to solve the complete set of resistive MHD equations. Subsequently, the solver is utilized to model the growth of MRT instability and feedthrough in resistive liquid-metal liners.

CHAPTER 3

Magneto-Rayleigh–Taylor instability and feedthrough in a resistive liquid-metal liner of finite thickness

This chapter builds upon the numerical solver introduced in Chapter 2 and extends its capabilities to solve the complete set of resistive MHD equations for two-phase incompressible flows. The implemented numerical toolkit is utilized to investigate the MRT instability growth in liquid-metal slabs. This chapter is based on:

Makaremi-Esfarjani, P. & Higgins, A. J. 2024 Magneto-Rayleigh–Taylor instability and feedthrough in a resistive liquid-metal liner of finite thickness. *Physics of Fluids* **36** (8).

Abstract

The effect of magnetic tension and diffusion on the perturbation growth of a liquid-metal liner subjected to magneto-Rayleigh–Taylor (MRT) instability is investigated. An initially magnetic-field-free liquid-metal slab of finite thickness is surrounded by two lower-density regions. Within the lower region, a constant axial magnetic field of arbitrary magnitude is applied. The numerical examination of the MRT instability growth, initiated by a seeded perturbation parallel to the magnetic field at the liner's unstable interface, is performed for both perfectly conductive and resistive liners. To this end, a novel level set-based two-phase incompressible solver for ideal/resistive magnetohydrodynamic (MHD) flows within

the finite-difference framework is introduced. Utilizing the implemented numerical toolkit, the impact of different Alfvén numbers and magnetic Reynolds numbers on the MRT growth rate and feedthrough at the upper interface of the liner is studied. Accounting for the finite resistivity of the liner results in an increase in the MRT growth and feedthrough compared to the ideal MHD case. The results indicate that magnetic diffusion primarily affects the MRT growth rate for higher wavenumbers, while for smaller wavenumbers, the effect of finite resistivity is only observed over a longer duration of instability development. We further demonstrate that decreasing the Alfvén number results in the faster emergence of the magnetic diffusion effect on the MRT growth rate. It is also observed that a greater electrical conductivity jump across the liner results in an increased perturbation growth. Lastly, the impact of surface tension on MRT instability growth for both ideal and resistive MHD cases is studied across different wavenumbers, specifically for Bond numbers related to fusion applications.

3.1 Introduction

The Rayleigh–Taylor (RT) instability emerges when a lighter fluid undergoes an acceleration towards a denser fluid (Rayleigh, 1882; Taylor, 1950). In a broader context, RT instability arises when opposing density and pressure gradients coexist, a condition that can be expressed mathematically as $\nabla\rho \cdot \nabla p < 0$. When perturbations are of small amplitude, the RT instability leads to an exponential growth of these perturbations over time at an unstable interface. The rate of perturbation growth (ω) is contingent upon factors such as interface acceleration (g), the relative densities of the two fluids (ρ_{light}, ρ_{heavy}), and the wavenumber of the initial perturbation (k), as depicted by the following equation (Taylor, 1950)

$$\omega = \left(\frac{\rho_{\text{heavy}} - \rho_{\text{light}}}{\rho_{\text{heavy}} + \rho_{\text{light}}} \, k \, g \right)^{\frac{1}{2}}. \tag{3.1}$$

Therefore, if the perturbation amplitude at time $t = 0$ is denoted as ξ_0, the perturbation growth over time within the linear regime is expressed as $\xi(t) \propto \xi_0 \mathrm{e}^{\omega t}$.

The introduction of a magnetic field can profoundly influence the growth of RT instability. Consequently, the magneto-Rayleigh–Taylor (MRT) instability has received great attention in the literature. While the mathematical representation of the RT instability, $\nabla\rho \cdot \nabla p < 0$, remains applicable to the MRT case, the pressure term should be modified to also include the effect of the magnetic pressure (Weis, 2015). The growth of the MRT instability is a significant concern for fusion concepts, specifically in scenarios involving a liner implosion (Weis *et al.*, 2014), such as inertial confinement fusion (ICF), magnetized liner inertial fusion (MagLIF), and magnetized target fusion (MTF). In the context of ICF, the process involves compressing a cryogenic deuterium-tritium target by employing laser-driven ablation of a thin shell within a nanosecond time frame. The acceleration stage, driven by laser-ablated material, induces MRT-driven perturbation growth at the shell's outer surface. These perturbations can propagate to the inner surface and experience further amplification around the point of maximum compression, where the inner surface of the shell is decelerated by the lighter deuterium-tritium target (Wang *et al.*, 2015; Huneault *et al.*, 2019). MagLIF is a magnetically driven ICF approach presently being developed by Sandia National Laboratories, in which a pre-heated and pre-magnetized plasma is compressed to fusion conditions through the compression of an imploding shell of finite thickness (Sefkow *et al.*, 2014; Gomez *et al.*, 2015). This approach is based on the idea proposed by Linhart (1961) and Harris (1962) to utilize an imploding conducting shell to increase the magnetic flux density and reach thermonuclear fusion conditions.

Initially proposed in the 1970s Linus project, MTF is an alternative fusion approach which focuses on achieving fusion conditions by compressing plasma using a conductive imploding surface (Turchi *et al.*, 1980; Brunelli, 2013). This concept employs a mechanically collapsed cylindrical or spherical rotating liquid shell to compress the plasma target. The shell absorbs the ensuing energy released from the fusion reaction in the form of heat and kinetic energy, which is subsequently extracted from the liquid through a heat exchanger. A critical factor for successful fusion in this approach is maintaining stability at the plasma/liquid-metal interface (PLMI) during the experiment. The PLMI is prone to several forms of hydrodynamic and magnetohydrodynamic instabilities, including MRT instability, during the compression

phase. The growth of instability at the PLMI disrupts implosion symmetry and introduces plasma contamination.

Of particular interest, General Fusion Inc. (Laberge, 2008; Suponitsky *et al.*, 2014) is pioneering a novel implementation of the MTF concept. This approach involves the injection of plasma into the reactor core, which is subsequently compressed to achieve fusion conditions through the inward motion of a liquid-metal liner. The inward motion of the liquid liner can be accomplished either mechanically, by using pistons (Pardo *et al.*, 2022), or by utilizing magnetic forces (Turchi *et al.*, 1976). One of the critical challenges within this approach pertains to maintaining the stability of the PLMI during the compression process. The occurrence of any instabilities at the PLMI has the potential to disrupt the plasma's purity, leading to plasma quenching. Throughout the compression process, the inner interface of the liquid metal is susceptible to RT instability. Numerous studies within the literature have studied the growth of RT instability at this inner interface, often exploring the implementation of liner rotation as a strategy to mitigate such instability (**?**Avital *et al.*, 2020). Through rotation, a centrifugal force is generated, acting in opposition to the inward acceleration of the liner—an important mechanism for stabilization. On the other hand, during the magnetic compression of a liner, instabilities might arise from a combination of magnetic and hydrodynamic pressure. Consequently, a more comprehensive investigation is warranted to understand how perturbations on the MRT unstable interface would grow during the compression.

When a liquid liner of finite thickness is decelerated towards a low-density region such as a vacuum or plasma, one interface is subjected to MRT instability, while the other interface is stable. However, perturbations present on the unstable interface may feed through to the stable one. Additionally, the development of perturbations on the stable interface affects the temporal evolution of instabilities on the unstable interface throughout a complete cycle of a fusion reactor's operation. As a result, the feedthrough factor, which quantifies the effect of perturbation growth at one interface on the other interface, is introduced to quantify the impact of feedthrough for different scenarios. The MRT instability along with the feedthrough issue holds significant implications across different fusion approaches such as ICF, MTF, various Z-pinch configurations (Chittenden & Jennings, 2008), and other liner-

driven implosion applications. Among the earliest studies on the RT instability feedthrough one can refer to the study of Taylor (1950). This effort was followed by other researchers, e.g., Mikaelian (1985, 1990, 1995) studied RT and Richtmyer–Meshkov instabilities and the feedthrough effect in finite thickness fluid layers.

The pioneering study of Harris (1962) on MRT feedthrough analytically examined the MRT instability of a collapsing cylindrical shell. This study was limited to cases where magnetic field lines remained unbent, resulting in a feedthrough factor identical to that reported by Taylor (1950) for the pure hydrodynamic case (Lau *et al.*, 2011). Subsequently, more comprehensive investigations were undertaken, accounting for factors such as magnetic tension and the anisotropic nature of MRT instability. Lau *et al.* (2011) conducted an analytical study on the MRT instability and feedthrough in a finite slab thickness using an ideal magnetohydrodynamic (MHD) model. Their examination allowed for the slab to experience acceleration resulting from the interplay of magnetic and fluid pressures. The Lau *et al.* (2011) study highlights the distinguishing characteristic of MRT instability—its anisotropic nature—setting it apart from the hydrodynamic RT instability.

To elaborate further on the anisotropic nature of the MRT instability, one may consider a plasma slab supported by magnetic pressure in the presence of a downward gravitational force. In this scenario, plasma, a denser fluid, overlays the lighter medium of magnetic field lines; therefore, the interface is RT unstable. In instances where the magnetic field lines are orthogonal to initial perturbations of the interface, the growth rate of the instability aligns with that of the hydrodynamic case, $(kg)^{\frac{1}{2}}$. However, for situations where $\boldsymbol{k} \cdot \boldsymbol{B} \neq 0$, the MRT instability growth rate falls below $(kg)^{\frac{1}{2}}$ due to the influence of magnetic tension originating from the bent magnetic field lines (Weis, 2015). This observation highlights the anisotropic behaviour intrinsic to MRT instability, setting it apart from classical RT instability. Subsequently, Weis *et al.* (2014) developed a theoretical expression to characterize the evolution of a surface ripple on a finite plasma slab which is MRT unstable over a limited time span. In their investigation, a finite plasma slab was confined between two perfect conductors and the obtained solution relied on the WKBJ approach. Each region may have an arbitrary magnetic field value with an arbitrary direction parallel to the interface. In their study, the ideal MHD model, along with linear theory, was employed, assuming all three

regions to be incompressible with constant properties in each region. The general dispersion relation in the Cartesian coordinate system, a generalization of prior works (Taylor, 1950; Harris, 1962; Chandrasekhar, 1981), was derived along with the feedthrough factor. While the introduced model proved generally useful for studying instabilities in liner implosions, its accuracy is mainly limited to when relatively large wavelength perturbations are present on the unstable interface. In cases where short wavelength perturbations exist and the resistivity of the regions cannot be neglected, the analytical solution is not quantitatively valid and can only be used for qualitative analysis (Weis, 2015). Later on, this effort was extended to the cylindrical coordinate system, which is closer to the geometry of Z-pinch and allows the two well-known current carrying instabilities in cylindrical liners, i.e., sausage and kink modes, to appear (Weis, 2015). For cylindrical geometries, Weis (2015) also presented the analytical solution for the instability growth rate using the sharp boundary model in cylindrical coordinates under the ideal MHD assumption. The combined MRT and kink mode was reported as one of the main sources of instability in magnetized implosions in cylindrical geometries based on the obtained analytical results (Weis, 2015). These findings were also verified by experimental and numerical studies (Weis *et al.*, 2014; Weis, 2015).

One of the main shortcomings in the aforementioned studies is the lack of consideration for the effect of liner resistivity. Generally, in cases where magnetic field lines and perturbation vectors are aligned, the MRT instability growth rate decreases due to the additional energy required to bend magnetic field lines according to the frozen-in law of ideal MHD cases. However, the existence of resistivity can reduce the stabilizing effect of the magnetic field (Weis *et al.*, 2014). This behaviour was observed in several studies focusing on the magnetic diffusion effect on the RT growth of the unstable interface of high-energy-density plasma in a constant background magnetic field in the whole domain (Bera *et al.*, 2022; Samulski *et al.*, 2022; Barbeau *et al.*, 2022). However, for our problem of interest, i.e., an initially magnetic-field-free liquid-metal liner undergoing MRT instability with the axial magnetic field present in the lower-density region, a more rigorous study is warranted to examine the effect of liner resistivity on perturbation growth and feedthrough.

The present study focuses on addressing this gap and aims to expand the existing knowledge of the impact of liner finite resistivity on perturbation growth. This will provide insight

into how transitioning from the ideal MHD case to the resistive case affects the initial stages of MRT instability growth. The effect of surface tension—which is relatively high in liquid metals as compared to other fluids–on instability growth is also investigated. While surface tension may be negligible in comparison to the large driving forces encountered in inertial fusion, surface tension can be considered as an analog to the stabilizing effects of ablation (Mikaelian, 1990). To this end, a novel level set-based two-phase incompressible MHD solver capable of examining both perfectly conductive and resistive fluids is introduced within the finite-difference framework. To the authors' knowledge, this introduced second-order solver for two-phase MHD flows has never been implemented in previous studies. The implemented solver uses the level-set method for interface capturing, which is coupled with the projection method for solving the incompressible set of equations for MHD flows. One of the contributions of this study is the development and introduction of this solver. The detailed description of the problem investigated in this study is presented in Sec. 3.2, followed by the derivation of the dimensionless parameters describing the physics of the problem. The implementation of the numerical solver and the numerical setup employed for the simulations are discussed in Sec. 3.3. The analytical solution of the problem under the ideal MHD assumption is given in Sec. 3.4. Subsequently, the numerical results regarding the MRT instability growth and feedthrough in an initially magnetic-field-free liquid-metal slab in different regimes are reported in Sec. 3.5. Lastly, a detailed discussion of the results is provided in Sec. 3.6, and the study is summarized in Sec. 3.7.

3.2 Problem description and formulation

This section provides a detailed description of the problem under study, followed by the corresponding set of governing equations solved within the implemented numerical solver.

3.2.1 Problem of interest

The schematic of the studied problem is depicted in Fig. 3.1, where a liquid-metal liner of thickness δ is bounded by two lighter regions, referred to as lower and upper layers. The lower and upper layers are assumed to have the same material properties such as density

and electrical conductivity. Additionally, for simplification, the thickness of these two layers is assumed to be similar, denoted by h.

For the fusion applications described in Sec. 3.1, the MRT instability arises from the acceleration of the liner bounded by a lower density region, with the acceleration of the lower density region toward the greater density region being unstable. For the purposes of the present study, we will consider an analogous problem with the analysis being performed in the reference frame of the liner. Rather than accelerating the liner, a body force term denoted by g will be introduced that has a similar effect on liner dynamics. In this reference frame, the body force term will be directed *downwards*, from the heavier fluid (i.e., the liquid liner) toward the lighter one (i.e., the lower layer), a scenario that is RT unstable, as shown in Fig. 3.1. The upper interface ideally remains stable; however, perturbations on the lower interface can affect the upper surface (i.e., feedthrough effect). Our interest lies in examining the RT instability growth and feedthrough at the lower and upper interfaces, respectively. Each region is assumed to be incompressible, with the lower and upper layers bounded by perfect conductors. Initially, no magnetic field is present in the liquid-metal liner and the upper layer, while a constant horizontal magnetic field, $B_{0,l}$, is imposed in the lower region.

In the course of the numerical campaign conducted in this study, the effect of magnetic field strength present in the lower region on MRT growth and feedthrough is investigated for different liner thicknesses and perturbation wavenumbers. This analysis is then repeated for the case of a resistive liquid-metal liner. For a more rigorous examination and to facilitate the application of this analysis across various scenarios, a set of non-dimensional equations is solved, presented in Sec. 3.2.2, and the influence of governing dimensionless numbers on instability growth is explored.

3.2.2 Governing equations

To better characterize the effect of different parameters such as magnetic tension, magnetic diffusion, and surface tension on the MRT instability growth, the dimensionless form of the governing equations is presented. The reference values used to non-dimensionalize the

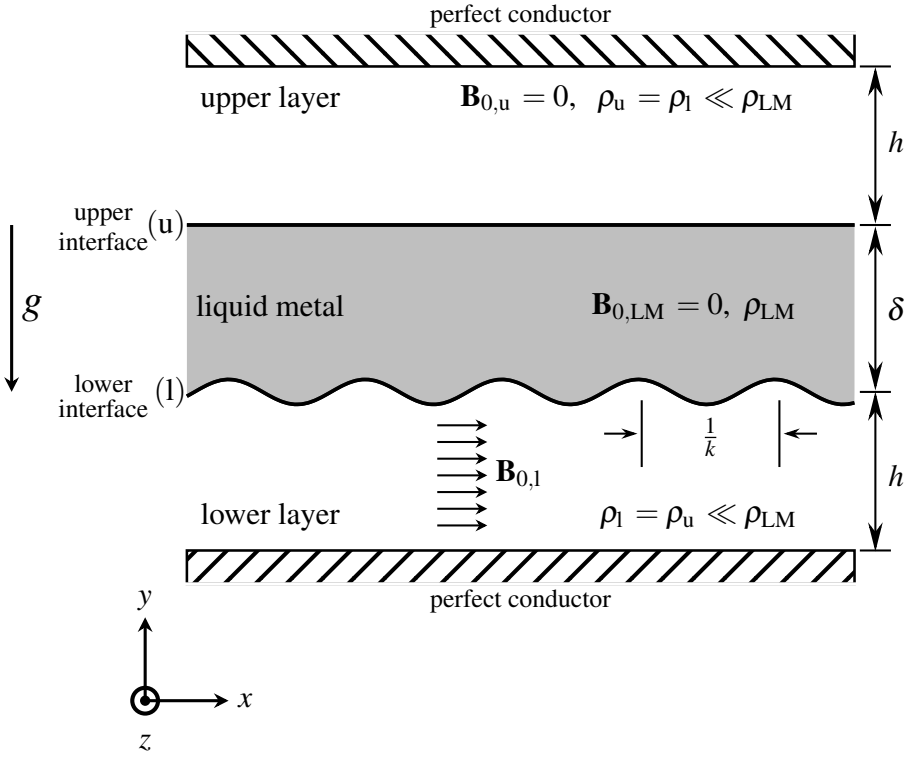

Figure 3.1: The schematic of the problem of interest. The MRT growth of the initially seeded perturbation with the wavenumber denoted by k at the lower interface and its impact on the upper interface are examined.

equations are as follows

$$\boldsymbol{x}^* = \frac{\boldsymbol{x}}{L_{\text{ref}}} = \frac{\boldsymbol{x}}{\delta}, \quad \boldsymbol{u}^* = \frac{\boldsymbol{u}}{U_{\text{ref}}} = \frac{\boldsymbol{u}}{\sqrt{\delta g}}, \quad t^* = \frac{t}{T_{\text{ref}}} = t\sqrt{\frac{g}{\delta}},$$
$$\boldsymbol{B}^* = \frac{\boldsymbol{B}}{B_{\text{ref}}} = \frac{\boldsymbol{B}}{B_{0,\text{l}}}, \quad \text{and} \quad p^* = \frac{p}{\rho_\text{l} U_{\text{ref}}^2}, \tag{3.2}$$

where the superscript "$*$" represents the dimensionless variables. The thickness of the liner, the gravitational acceleration, and the initial uniform axial magnetic field at the lower region are denoted by δ, g, and $B_{0,\text{l}}$, respectively. Variables $\boldsymbol{u}$ and p are the velocity and pressure fields, respectively, and ρ_l is the density of the liquid-metal liner.

Consequently, the non-dimensional form of the two-phase incompressible resistive MHD

equations for inviscid flows is written as

$$\frac{\partial \boldsymbol{u}^*}{\partial t^*} + \nabla \cdot (\boldsymbol{u}^* \boldsymbol{u}^*) = -\frac{1}{\rho}\nabla p^* + \frac{\boldsymbol{g}}{g} + \frac{1}{\rho}\frac{1}{\mathrm{Bo}}\boldsymbol{F}_{\mathrm{ST}} + \frac{1}{\rho}\frac{1}{\mathrm{Al}^2}\nabla \cdot \tau^{\mathrm{M}}, \tag{3.3a}$$

$$\nabla \cdot \boldsymbol{u}^* = 0, \tag{3.3b}$$

$$\frac{\partial \boldsymbol{B}^*}{\partial t^*} = \nabla \cdot (\boldsymbol{B}^* \boldsymbol{u}^* - \boldsymbol{u}^* \boldsymbol{B}^*) + \frac{1}{\mathrm{Re_m}}\nabla \cdot \left(\frac{1}{\sigma_{\mathrm{e}}}\nabla \boldsymbol{B}^*\right), \tag{3.3c}$$

$$\nabla \cdot \boldsymbol{B}^* = 0, \tag{3.3d}$$

where the three dimensionless parameters, Bond number, Bo, Alfvén number, Al, and magnetic Reynolds number, $\mathrm{Re_m}$, are defined as

$$\mathrm{Bo} = \frac{\rho_{\mathrm{l}} L_{\mathrm{ref}} U_{\mathrm{ref}}^2}{\sigma}, \quad \mathrm{Al} = \frac{U_{\mathrm{ref}}}{U_{\mathrm{Alfvén}}}, \quad \text{and} \quad \mathrm{Re_m} = \frac{L_{\mathrm{ref}}\, U_{\mathrm{ref}}}{\lambda_{\mathrm{m,l}}}. \tag{3.4}$$

Variables ρ and σ_{e} are the dimensionless density and electrical conductivity, respectively, given as

$$\rho = \rho_{\mathrm{r}} + (1 - \rho_{\mathrm{r}})\,\psi \quad \text{and} \quad \sigma_{\mathrm{e}} = \sigma_{\mathrm{e,r}} + (1 - \sigma_{\mathrm{e,r}})\,\psi, \tag{3.5}$$

where $\rho_{\mathrm{r}} = \rho_{\mathrm{g}}/\rho_{\mathrm{l}}$ and $\sigma_{\mathrm{e,r}} = \sigma_{\mathrm{e,g}}/\sigma_{\mathrm{e,l}}$, with subscripts "l" and "g" representing the liquid and gas phases, respectively. The scalar variable ψ is the level set function utilized to capture the interface between the liquid and gas phases, varying between 0 (gas phase) to 1 (liquid phase). More detail regarding the implemented level set method is given in the next section.

The Bond number quantifies the intensity of the surface tension force, $\boldsymbol{F}_{\mathrm{ST}}$, with variable σ denoting the surface tension coefficient of the liquid liner. In order to account for the effect of magnetic forces on the fluid motion, the Lorentz force is incorporated into the momentum equation, Eq. (3.3a). The Lorentz force, which quantifies the force experienced by conducting fluids due to electromagnetic fields, is given as $\boldsymbol{J} \times \boldsymbol{B}$, where $\boldsymbol{J}$ is the electric current density. This force can be written in the form of the Maxwell stress tensor, τ^{M}, given as (Davidson, 2001)

$$\nabla \cdot \tau_{ij}^{\mathrm{M}} = \left(B_i^* B_j^* - \frac{|B^*|^2}{2}\delta_{ij}\right), \tag{3.6}$$

which is the conservative representation of this force employed for numerical discretization, as explained in the subsequent section.

The dimensionless Alfvén number is the ratio between the characteristic velocity to the Alfvén wave speed which is defined as

$$U_{\text{Alfvén}} = \frac{B_0}{\sqrt{\mu_{\text{m}}\,\rho_{\text{l}}}}, \tag{3.7}$$

where μ_{m} stands for the magnetic permeability of the corresponding medium. The Alfvén number, $\text{Al} = (U_{\text{ref}}\sqrt{\mu_{\text{m}}\,\rho_{\text{l}}})/(B_0)$, indicates the relative strengths of the magnetic and inertial forces present in MHD flows. A high Alfvén number implies that inertial forces dominate over the existing magnetic forces, while reducing the Alfvén number results in regimes where magnetic forces are more pronounced.

Equation (3.3c), known as the induction equation, represents the evolution of the magnetic field due to the advection, $\nabla \cdot (\boldsymbol{B}^*\boldsymbol{u}^* - \boldsymbol{u}^*\boldsymbol{B}^*)$, and diffusion, $\nabla \cdot \left(\frac{1}{\sigma_{\text{e}}}\nabla \boldsymbol{B}^*\right)$. The induction equation comes from combining the Faraday, Maxwell–Ampère, and Ohm's laws, and the magnetic Reynolds number quantifies the relative strengths of advection and diffusion of a magnetic field, where $\lambda_{\text{m,l}} = 1/\left(\mu_{\text{m}}\,\sigma_{\text{e,l}}\right)$ illustrates the magnetic diffusivity of the liquid liner.

It is noteworthy to mention that momentum and induction equations, Eqs. (3.3a) and (3.3c), should be solved while satisfying the divergence-free constraint for both velocity and magnetic fields, Eqs. (3.3b) and (3.3d). The following section describes the implemented numerical toolkit to solve Eqs. (3.3a-3.3d) in more detail.

3.3 Implementation of a two-phase MHD numerical solver

This section presents the methodology employed for simulating two-phase MHD flows, along with a description of the initial conditions and boundary conditions imposed in the simulations.

3.3.1 Grid arrangement and discretization

The staggered grid arrangement is used in the implemented solver, shown in Fig. 3.2. In this computational grid system, velocity and magnetic field values are represented at cell faces, $(i+\frac{1}{2},j)$ and $(i,j+\frac{1}{2})$, while other scalar variables such as pressure, level set, and properties such as density and electrical conductivity are defined at cell centers, (i,j).

The implemented two-phase resistive MHD solver is an extension to the work of Makaremi-Esfarjani *et al.* (2023), where a detailed description of a two-phase incompressible solver for magnetic flows is provided. In that study, a fifth-order conservative level set method was employed to capture the evolution of the interface, coupled with the projection-based incompressible solver. The solver demonstrated second-order accuracy and showed excellent performance in handling high density ratios across the interface. Additionally, the surface tension force was modelled using the continuum interface force (CSF) approach. In this section, we focus on extending the mentioned solver to the resistive MHD case. Therefore, the discretization of the magnetic forces along with the implementation of the induction equation while satisfying the divergence-free condition are discussed. Interested readers may refer to Makaremi-Esfarjani *et al.* (2023) for more details regarding the implementation of the two-phase solver for hydrodynamic and magnetic flows.

Using the notation introduced in previous studies for the second-order finite-difference and second-order interpolation operators (Morinishi *et al.*, 1998; Desjardins *et al.*, 2008*a*; Makaremi-Esfarjani *et al.*, 2023), the discretization of the $x-$component of the Lorentz force in the two-dimensional computational domain, (x,y), with velocity and magnetic fields denoted by (u,v) and (B_x,B_y), respectively, is given as

$$F_{\text{Lorentz},x}\Big|_{i+\frac{1}{2},j} = \frac{1}{\rho}\frac{1}{\text{Al}^2}\left[\frac{\partial B_x B_x}{\partial x}+\frac{\partial B_x B_y}{\partial y}-\frac{1}{2}\left(\frac{\partial B_x^2}{\partial x}+\frac{\partial B_y^2}{\partial x}\right)\right]$$

$$= \frac{1}{\overline{\rho}^{2\text{nd}\,x}}\frac{1}{\text{Al}^2}\left[\frac{\delta_2\left(\overline{B_x}^{2\text{nd}\,x}\,\overline{B_x}^{2\text{nd}\,x}\right)}{\delta_2\,x}+\frac{\delta_2\left(\overline{B_x}^{2\text{nd}\,y}\,\overline{B_y}^{2\text{nd}\,x}\right)}{\delta_2\,y}-\frac{1}{2}\left(\overline{\frac{\delta_2\,B_x^2}{\delta_2 x}}^{2\text{nd}\,x}+\overline{\frac{\delta_2\,B_y^2}{\delta_2\,x}}^{2\text{nd}\,y}\right)\right] \quad (3.8)$$

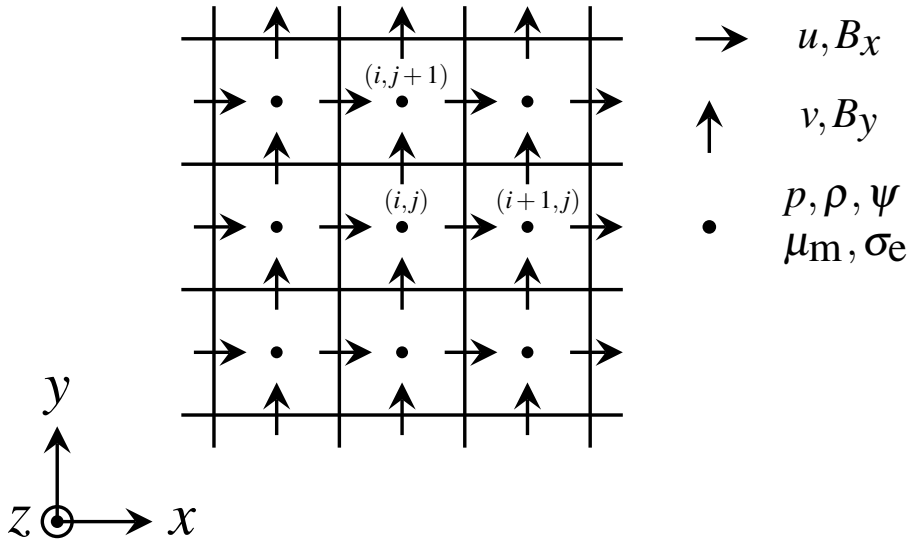

Figure 3.2: Staggered grid system in Cartesian coordinates. In the staggered grid arrangement, the values of scalar fields such as pressure (p), level set function (ψ), density (ρ), magnetic permeability (μ_m), and electrical conductivity (σ_e) are defined at cell centers. Velocity components, u and v, along with magnetic field components, B_x and B_y, are defined at cell faces.

The term $F_{\mathrm{Lorentz},x}$ signifies the Lorentz force present in the $x-$component of the momentum equation. Consequently, these values need to be computed at cell faces along the $x-$direction, $(i+\frac{1}{2}, j)$. Similarly, the $y-$component of the Lorentz force is determined at cell faces $(i, j+\frac{1}{2})$.

The discretization of the induction equation for the B_x component, while considering the electrical conductivity jump across the interface, is given as

$$\left.\frac{\partial B_x}{\partial t}\right|_{i+\frac{1}{2},j} = \frac{\partial}{\partial y}\left(uB_y - B_x v\right) + \frac{\partial}{\partial x}\left(\frac{1}{\sigma_\mathrm{e}}\frac{\partial B_x}{\partial x}\right) + \frac{\partial}{\partial y}\left(\frac{1}{\sigma_\mathrm{e}}\frac{\partial B_x}{\partial y}\right)$$

$$= \frac{\delta_2\left(\overline{u}^{2\mathrm{nd}\,y}\ \overline{B_y}^{2\mathrm{nd}\,x}\right)}{\delta_2\, y} - \frac{\delta_2\left(\overline{B_x}^{2\mathrm{nd}\,y}\ \overline{v}^{2\mathrm{nd}\,x}\right)}{\delta_2\, y} + \frac{\delta_2\left(\frac{1}{\sigma_\mathrm{e}}\ \frac{\delta_2 B_x}{\delta_2 x}\right)}{\delta_2\, x} + \frac{\delta_2\left(\frac{1}{\overline{\overline{\sigma_\mathrm{e}}^{2\mathrm{nd}\,x}}^{2\mathrm{nd}\,y}}\ \frac{\delta_2 B_x}{\delta_2 y}\right)}{\delta_2\, y}, \quad (3.9)$$

at cell faces $(i+\frac{1}{2}, j)$. The electrical conductivity value, σ_e, should also be updated alongside other properties such as density, according to the updated location of the interface deter-

mined by the level set function at each time step. In a similar fashion, the B_y component discretization is derived at cell faces across the $y-$direction, $(i, j+\frac{1}{2})$.

The solution of the induction equation, Eq. (3.3c), does not necessarily satisfy the magnetic field divergence-free constraint. Maintaining the divergence-free condition of the magnetic field significantly influences the accuracy of the numerical solver, and violating this constraint results in unphysical numerical solutions. Various schemes, such as the eight-wave formulation, constrained transport, and projection scheme have been proposed in the literature to impose the divergence-free condition of the magnetic field (Tóth, 2000). In this study, we have employed the projection scheme, where the computed magnetic field from the induction equation is projected into a divergence-free field (Brackbill & Barnes, 1980). The calculated magnetic field from Eq. (3.3c) at time step $n+1$, denoted by $\tilde{\boldsymbol{B}}^{n+1}$, can be written as a summation of a curl and a gradient as $\tilde{\boldsymbol{B}}^{n+1} = \nabla \times \boldsymbol{A} + \nabla\phi$, where only the curl of vector potential $\boldsymbol{A}$ represents the physical part of the magnetic field solution. Taking the divergence of the mentioned equation results in the following Poisson equation for the scalar field ϕ

$$\nabla \tilde{\boldsymbol{B}}^{n+1} = \nabla^2 \phi. \tag{3.10}$$

Solving this Poisson equation and finding the scalar field ϕ, the magnetic field $\tilde{\boldsymbol{B}}^{n+1}$ will be projected into the divergence-free field as

$$\boldsymbol{B}^{n+1} = \tilde{\boldsymbol{B}}^{n+1} - \nabla\phi, \tag{3.11}$$

where $\boldsymbol{B}^{n+1}$ is the magnetic field solution at time step $n+1$ which satisfies the divergence-free constraint.

The third-order explicit Runge–Kutta method is used for the temporal integration (Gottlieb & Shu, 1998), and based on the CFL condition, the stability constraint for the time step due to convection, diffusion, and surface tension terms is given as

$$\Delta t \leq \min\left(\frac{\Delta x}{\max(||\mathbf{u}|| + ||\mathbf{u}_{\text{Alfvén}}||)}, \frac{1}{4}\frac{\Delta x^2}{\max(\lambda_{\text{m,l}}, \lambda_{\text{m,g}})}, \sqrt{\frac{\Delta x^3\,(\rho_{\text{l}} + \rho_{\text{g}})}{4\pi\sigma}}\right). \tag{3.12}$$

As can be observed in Eq. (3.12), the velocity of the Alfvén wave and magnetic diffusivity should also be considered in determining the time step compared to the hydrodynamic case. Consequently, for high magnetic field values or low magnetic Reynolds numbers, the system of governing equations becomes stiff, resulting in excessively small time steps. Due to this numerical stiffness, different semi-implicit and implicit schemes for resistive MHD equations have been proposed in the literature to address the stiffness issue associated with Alfvén waves, such as the implicit solver introduced for reduced resistive MHD equations by Chacón *et al.* (2002). However, for our problem of interest, the explicit Runge–Kutta scheme was deemed to be sufficient and straightforward to implement.

In Appendix A, the accuracy, convergence, and performance of the introduced two-phase incompressible MHD solver are examined. Interested readers can refer to this section for more details.

3.3.2 Numerical simulation setup

The description of the numerical simulation setup and boundary conditions is discussed herein. In this study, the MRT instability of a planar liquid liner slab in a two-dimensional domain is investigated. Although in most cases three-dimensional simulations are needed to fully capture instability growth, two-dimensional studies still provide valuable insights. Furthermore, since our primary focus lies on the initial stages of perturbation growth parallel to the initially imposed axial magnetic field, the perturbation growth mainly occurs within the $x-y$ plane; and, as a result, the two-dimensional assumption is reasonable.

In the initial condition, an inviscid liquid liner with the density and thickness of $\rho_\mathrm{l} = 500\,\mathrm{kg/m^3}$ and $\delta = \pi/6$, respectively, is surrounded by air in the computational domain of $(x, y) \in [0, \pi] \times [0, \pi]$. The density ratio is set to $\rho_\mathrm{r} = 0.002$ for all the presented simulations. Therefore, the Atwood number is almost 1, which is defined as $\mathrm{At} = (\rho_\mathrm{l} - \rho_\mathrm{g})/(\rho_\mathrm{l} + \rho_\mathrm{g})$. The lower interface of the liquid liner is initially perturbed with a sinusoidal perturbation with the amplitude of $\pi/40$, and a uniform magnetic field $B_{0,\mathrm{l}}$ is imposed in the lower region consisting of air. All simulations are performed with a constant CFL number of 0.1.

A periodic boundary condition is set along the $x-$direction, and the top and bottom boundaries are assumed to be perfectly conducting rigid walls. Therefore, the slip boundary

condition is used for the velocity field at the top and bottom boundaries. To impose the perfectly conducting boundary condition for the magnetic field, the normal component of the magnetic field at the walls is set to zero.

To ensure the results of this study are relevant to the various fusion approaches discussed in the introduction, the parameter space for the three key non-dimensional numbers is presented in Table 3.1 for two fusion approaches utilizing a metal liner for compression: MTF and MagLIF. For the MTF approach, the characteristic properties of the General Fusion Inc. power plant design are used, and the working liquid metal is assumed to be liquid lithium. The properties reported in Table 3.1 for MagLIF are based on the Sandia National Laboratory (SNL) Z facility, where a beryllium liner is utilized to compress the deuterium-tritium (D-T) fuel.

Table 3.1 offers insight into the approximate values of the three dimensionless parameters encountered in practical scenarios. In this study, we mainly focus on time scales during which the RT instability remains in laminar regimes and smaller-scale structures have yet to emerge. Although over the entire liner compression process the incompressibility assumption may no longer hold, studying MRT instability growth in the initial stages of compression, where the liquid liner can be treated as incompressible, is of primary interest. The parameters represented in Table 3.1 are helpful in guiding our focus on regimes comparable to those in fusion reactors. Considering the capabilities and limitations of the implemented solver, the conducted test cases are designed so that the corresponding parameters fall within the parameter space introduced here, as presented in the result section.

3.4 Analytical solution

In the present study, the numerical toolkit developed in Sec. 3.3 is employed to study the effect of magnetic tension and diffusion on the MRT instability growth. However, the analytical solution obtained by Weis *et al.* (2014) can be used to predict the MRT instability growth under the ideal MHD assumption within the linear regime and be compared to the numerical results. In their study, Weis *et al.* (2014) derived the analytical dispersion relation for the MRT instability growth of a finite plasma slab confined by two incompressible regions,

Table 3.1: The parameter space of the Bond number, Alfvén number, and magnetic Reynolds number for two fusion approaches: MTF and MagLIF.

		MTF[b]	MagLIF[c]
properties[a]	ρ_l [kg m^{-3}]	500	1850
	σ [N m^{-1}]	0.4	1.5[d]
	σ_e [S m^{-1}]	4×10^6	2.5×10^7
	μ_m [H m^{-1}]	$4\pi \times 10^{-7}$	$4\pi \times 10^{-7}$
	δ [m]	0.4	10^{-4}
	B_0 [T]	0.7 (Uncompressed) 70 (Compressed)	10 (Uncompressed) 100 (Compressed)
	g [m s^{-2}]	10^5	10^{11}
parameters	Bo	$\approx 10^7$	$\approx 10^6$
	Al	$0.07 - 7$	$1.5 - 15$
	$\mathrm{Re_m}$	400	10

[a] The presented values are approximations, as the properties of liquid metal undergo significant changes at high temperatures, and in most cases, exact values are not known.
[b] The liquid lithium properties are taken from Davison (1968).
[c] The analytical expressions of beryllium properties are given by Tolias (2022).
[d] Taken from Kumikov (1983).

assuming all regions to be perfectly conductive. This dispersion relation is reformulated for the problem described in Sec. 3.2.1 based on the defined reference values. The resulting non-dimensional dispersion relation is as follows

$$A^* \omega^{*4} - B^* \omega^{*2} + C^* = 0, \tag{3.13}$$

where ω^* is the dimensionless growth rate, $\omega^* = \omega / \sqrt{k\, g}$, and coefficients A^*, B^*, and C^* are given as

$$A^* = 1 + \rho_\mathrm{r}^2 \coth(k^* h^*) \coth(k^* h^*) + 2\, \rho_\mathrm{r} \coth(k^* h^*) \coth(k^*), \tag{3.14a}$$

$$B^* = \frac{k^*}{\mathrm{Al}^2} \coth(k^* h^*) \coth(k^*) + \frac{\rho_\mathrm{r}\, k^*}{\mathrm{Al}^2} \coth(k^* h^*) \coth(k^* h^*), \tag{3.14b}$$

and

$$C^* = (1 - \rho_\mathrm{r}) \left(\rho_\mathrm{r} + \frac{k^*}{\mathrm{Al}^2} \coth(k^* h^*) - 1 \right). \tag{3.14c}$$

Variables k^* and h^* are dimensionless wavenumber and lower/upper layer thickness, respectively, and are calculated as $k^* = k\,\delta$ and $h^* = h/\delta$. The solution of the dispersion equation, Eq. (3.13), gives

$$\omega^{*2} = \frac{1}{2A^*}\left(B^* \pm \sqrt{B^{*2} - 4A^*C^*}\right). \tag{3.15}$$

According to the energy principle for the MRT instability in the ideal MHD case, ω^{*2} is always real; therefore, $B^{*2} - 4A^*C^* \geq 0$ (Boyd & Sanderson, 2003). Owing to this property, the solution of Eq. (3.15) results in four ω^* values which are either purely real or imaginary and are in negative and positive pairs. Since instability occurs when $\omega^{*2} < 0$, the imaginary solution of ω^* with the greater value corresponds to the MRT instability growth rate of the most unstable mode.

For the initial condition described in Sec. 3.3.2 and nine different Alfvén numbers of ∞, 16, 8, 4, 2, 1.4, 1.1, 1, and 0.5, the MRT growth rate, ω^*, is calculated for different wavenumbers. The schematic of the problem for two different wavenumbers and the corresponding magnetic field configurations are depicted in Fig. 3.3(a), while the corresponding analytical results are presented in Fig. 3.3(b). It is appreciated that generally, decreasing the Alfvén number, i.e., increasing the initial magnetic field present in the lower layer, $B_{0,1}$, results in a reduced MRT growth rate. As shown in Fig. 3.3(b), for Al = 16, the calculated MRT growth rate is slightly smaller compared to the case of pure hydrodynamic, Al = ∞, and this difference becomes more pronounced for higher k^* values. This behaviour is consistent as the Alfvén number is decreased to 8 and below. As the magnetic field is increased, a critical magnetic field strength is reached beyond which the MRT instability is fully stabilized, attributed to the presence of an axial magnetic field. For example, for Al = 0.5 in the studied problem, the calculated MRT growth rate is zero (see Fig. 3.3b).

Another noteworthy observation from Fig. 3.3(b) is the presence of a critical wavenumber, k^*_{critical}, at which the MRT instability growth reaches its maximum value for a constant Alfvén number. For instance, according to Fig. 3.3(b), for Alfvén numbers of 2 and 1.4, the critical wavenumber is close to $k^* = 2/\pi$, corresponding to the peak MRT growth. This critical wavenumber decreases as the Alfvén number decreases, approaching zero for fully stable

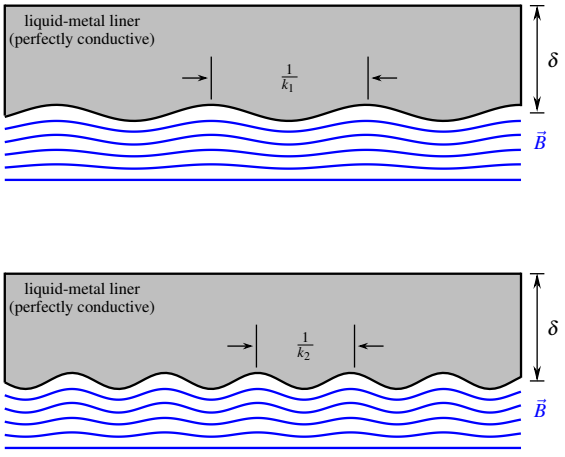

(a)

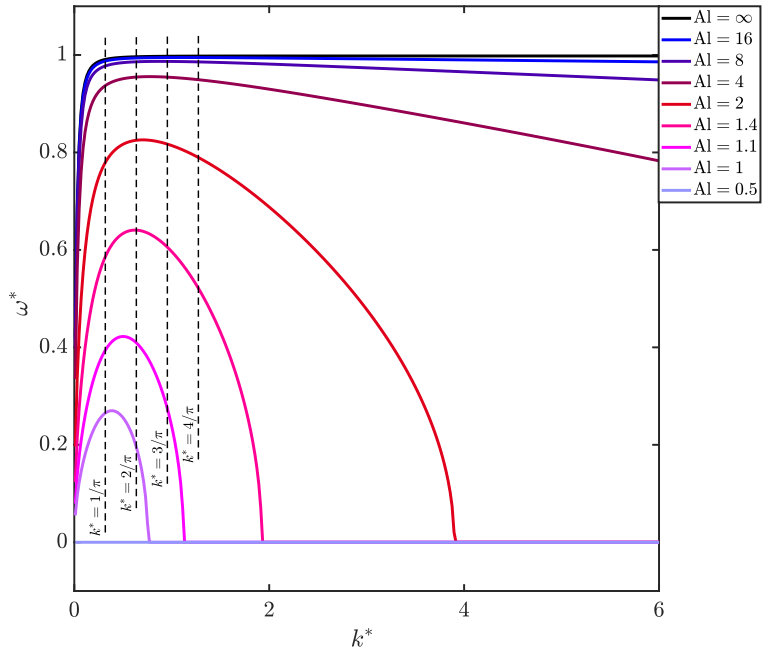

(b)

Figure 3.3: (a) Schematic of the problem for two different wavenumbers ($k_2 > k_1$). Higher wavenumbers (i.e., shorter wavelengths) result in bent magnetic field lines with greater curvature. (b) The non-dimensional MRT growth rate, ω^*, as a function of dimensionless wavenumber, k^*, for nine different Alfvén numbers of ∞, 16, 8, 4, 2, 1.4, 1.1, 1, and 0.5.

cases. Figure 3.3(b) further shows that, in general, the magnetic field exhibits a more stabilizing effect for higher wavenumbers, that is, shorter wavelengths.

The MRT growth rate and feedthrough are numerically investigated for the four wavenumbers indicated in Fig. 3.3(b), $k^* = 1/\pi$, $2/\pi$, $3/\pi$, and $4/\pi$. The results from the numerical simulations for the ideal case are compared with the analytical ones in the following section.

3.5 Results

In this section, first, the effect of the Alfvén number on the MRT growth rate and feedthrough effect is studied for the ideal case, where all regions are assumed to be perfectly conductive. This effort is then extended to the resistive MHD case, examining the effect of liner finite resistivity on instability growth for different magnetic Reynolds numbers. Additionally, the effect of electrical conductivity jump across the interface on the MRT growth rate is investigated for different wavenumbers. Finally, the effect of liquid-metal surface tension on MRT growth for both ideal and resistive cases is presented.

3.5.1 Ideal MHD case

Using the implemented two-phase ideal MHD solver, MRT instability growth was investigated for five different Alfvén numbers of 16, 8, 4, 2, and 1.4, along with the pure hydrodynamic RT case (Al $= \infty$). The numerical simulations were performed for four different wavenumbers of $k^* = 1/\pi$, $2/\pi$, $3/\pi$, and $4/\pi$. The vertical displacement of the perturbation located at the midpoint of the perturbation wavelength (i.e., spike tip), was tracked during the simulation to calculate the growth rate, as shown in Fig. 3.4(a). In Fig. 3.4(b), this perturbation displacement is plotted as a function of time using a logarithmic scale for the $y-$axis. Therefore, the slope corresponds to the numerical MRT growth rate. In this and the subsequent figures, black dashed lines are provided to assist in determining the slope, denoted by m.

The dimensionless growth rate is close to unity for all four wavenumbers in the classical RT case, as expected. For each wavenumber, it is observed that decreasing the Alfvén number results in a lower growth rate, demonstrating the stabilizing effect of the magnetic

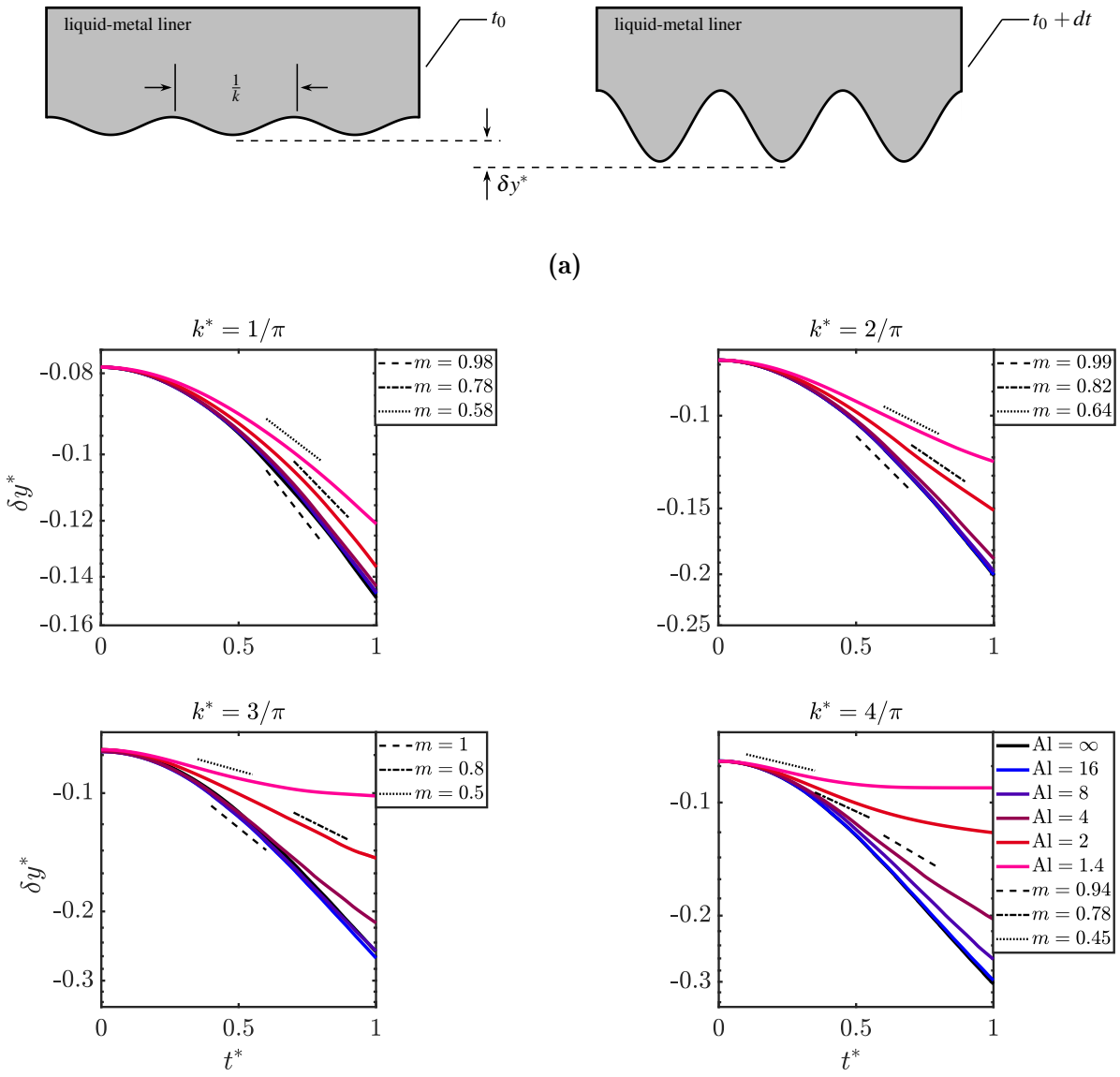

Figure 3.4: (a) The displacement of the perturbation located at the midpoint of the wavelength is measured during the simulation. (b) MRT growth of four different wavenumbers, $k^* = 1/\pi$, $2/\pi$, $3/\pi$, and $4/\pi$, for six different Alfvén numbers, i.e., Al $= \infty$, 16, 8, 4, 2, and 1.4.

field initially present in the lower layer. For $k^* = 1/\pi$, the instability growth rates for cases Al = 16 and 8 are quite close (approximately 0.9), which agrees with the analytical solution (see the $k^* = 1/\pi$ line in Fig. 3.3b). However, according to the analytical solution, the instability growth rates reduce to 0.78 and 0.58 for cases Al = 2 and 1.4, respectively, consistent with the presented numerical results.

For the case $k^* = 2/\pi$, the numerical growth rate for Al = 2 and 1.4 are given as 0.82 and 0.64, respectively. These values are greater than the corresponding ones for $k^* = 1/\pi$, as also inferred from the analytical solution. Moving to $k^* = 3/\pi$, the growth rate for the case Al = 2 reaches 0.8, slightly decreasing from the corresponding one for $k^* = 2/\pi$, as indicated by Fig. 3.4(b). This value further decreases to 0.78 for the $k^* = 4/\pi$ case. Consequently, the numerical solver also captured a decrease in the growth rate for the case Al = 2 beyond the wavenumber of $k^* = 2/\pi$, similar to the analytical solution.

For Al = 1.4, the numerical growth rates for $k^* = 2/\pi$, $3/\pi$, and $4/\pi$ are 0.64, 0.5, and 0.45, respectively, confirming the maximum growth rate for the wavenumber $k^* = 2/\pi$. However, the calculated numerical growth rates for the Alfvén number of 1.4 and wavenumbers $3/\pi$ and $4/\pi$ slightly differ from the analytical ones, which are 0.6 and 0.52 for $k^* = 3/\pi$ and $4/\pi$, respectively.

Generally, from Fig. 3.4(b), it is apparent that for test cases with greater magnetic field density (smaller Alfvén number), the numerical solution for the perturbation growth deviates from the analytical one for higher wavenumbers of $k^* = 3/\pi$ and $4/\pi$. For example, for the case with an Alfvén number and wavenumber of 1.4 and $4/\pi$, respectively, the perturbation growth differs from the predicted exponential growth of the analytical solution, as can be seen in Fig. 3.4(b), especially at the later stages of instability growth. This is explained by the fact that the presented analytical solution is mainly valid in linear regimes for relatively long wavelengths (i.e., small wavenumbers). As the wavenumber value increases and consequently the magnetic tension increases, the accuracy of the analytical solution decreases.

This section concludes with a discussion of the feedthrough effect on the upper interface of the liquid liner. Figure 3.5 illustrates the location of the upper and lower interfaces at $t^* = 1$ across wavenumbers $k^* = 1/\pi$, $2/\pi$, and $4/\pi$, for different Alfvén numbers. It is evident that for each wavenumber, decreasing the Alfvén number leads to a reduction in

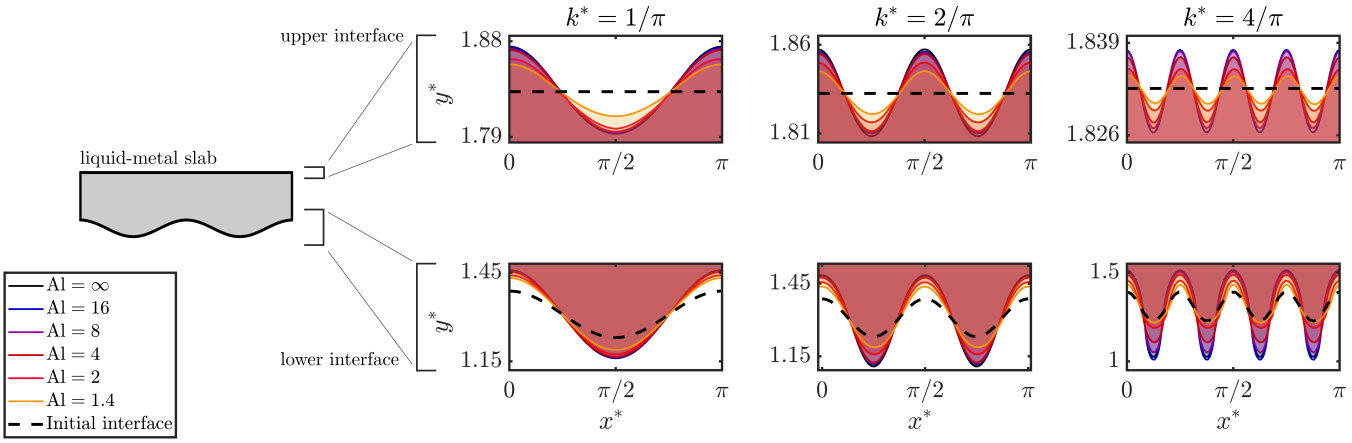

Figure 3.5: The location of upper and lower interfaces at $t^* = 1$ for three wavenumbers, $k^* = 1/\pi$, $2/\pi$, and $4/\pi$, across six different Alfvén numbers, Al = ∞, 16, 8, 4, 2, and 1.4.

perturbation growth at the initially unperturbed upper interface. This is due to the fact that the perturbation growth on the upper interface depends on the RT growth of the lower interface, and for each wavenumber decreasing the Alfvén number results in reduced RT growth. Additionally, in general, as seen in Fig. 3.5, increasing k^* results in a reduction in the feedthrough effect on the upper interface. Consequently, feedthrough is more notable for smaller k^* values, i.e., thinner slabs or smaller wavenumbers.

3.5.2 Resistive MHD case

In the preceding section, the liquid liner was assumed to be perfectly conductive. However, in real-world applications, liquid metals have finite resistivity, which impacts the growth of the MRT instability compared to the ideal case. The effect of magnetic diffusion is examined in the present section.

Figure 3.6(a) displays the schematic of the problem and qualitatively represents the difference between the configuration of the magnetic field lines for both ideal and resistive cases. Figure 3.6(b) illustrates the MRT growth rate for three different magnetic Reynolds numbers of 1000, 100, and 10, along with the ideal MHD case, $\mathrm{Re_m} = \infty$, and their pure hydrodynamic counterpart. The results are depicted for two wavenumbers, $k^* = 1/\pi$ and

$2/\pi$, and for three different Alfvén numbers of Al = 4, 2, and 1.4, with electrical conductivity ratio set to $\sigma_{e,r} = 0.1$. Figure 3.6(b) reveals a negligible difference between the ideal and resistive growth rates for the small wavenumber $k^* = 1/\pi$ (top row of Fig. 3.6b), especially for cases with lower magnetic field values. For instance, a slight difference is observed between the studied cases for Al = 2 only towards the end of the simulation time. However, the difference between the ideal and resistive cases becomes more evident for the smallest Alfvén number (Al = 1.4), and a greater growth rate of 0.7 for $\mathrm{Re_m} = 10$ is noted compared to the ideal case with the growth rate of 0.58.

For the cases with $k^* = 2/\pi$ (bottom row of Fig. 3.6b), while the growth rates of the ideal and resistive cases for Al = 4 only differ slightly in the final stages of the simulation, the results for smaller Alfvén numbers of 2 and 1.4 reveal more notable differences between the ideal and resistive cases. In the case of Al = 2, the perturbation growth of the resistive scenario with $\mathrm{Re_m} = 10$ begins to deviate from the ideal case around $t^* = 0.6$ and rises to 0.9. For higher magnetic Reynolds numbers of 1000 and 100, the perturbation growth is similar to the ideal case, with only small differences observed around the final time of the simulation. Similar behaviour is detected for Al = 1.4, where the growth rate of the resistive case with $\mathrm{Re_m} = 10$ increases to 0.9 compared to 0.64 for the ideal case.

The same results were reproduced for cases with wavenumbers of $k^* = 3/\pi$ and $k^* = 4/\pi$, shown in Fig. 3.7. This figure demonstrates that for these higher wavenumbers, even for the high Alfvén number (Al = 4), the difference between the MRT growth of ideal and resistive cases is more pronounced. Additionally, as displayed in Fig. 3.7, the magnetic Reynolds number plays an important role in determining the MRT growth rate. For all the presented cases, the MRT growth rate for $\mathrm{Re_m} = 1000$ is close to the ideal case, as this high magnetic Reynolds number corresponds to a highly conductive medium. However, by decreasing the magnetic Reynolds number, the MRT growth rate increases and becomes closer to that of the pure hydrodynamic case. For example, for an Alfvén number of 2, the growth rate of $\mathrm{Re_m} = 10$ becomes almost similar to that of the pure hydrodynamic case for both wavenumbers (see Fig. 3.7).

Based on the conducted numerical simulations, it is concluded that finite resistivity has a more pronounced effect on the MRT growth of an initially magnetic-field-free liquid liner for

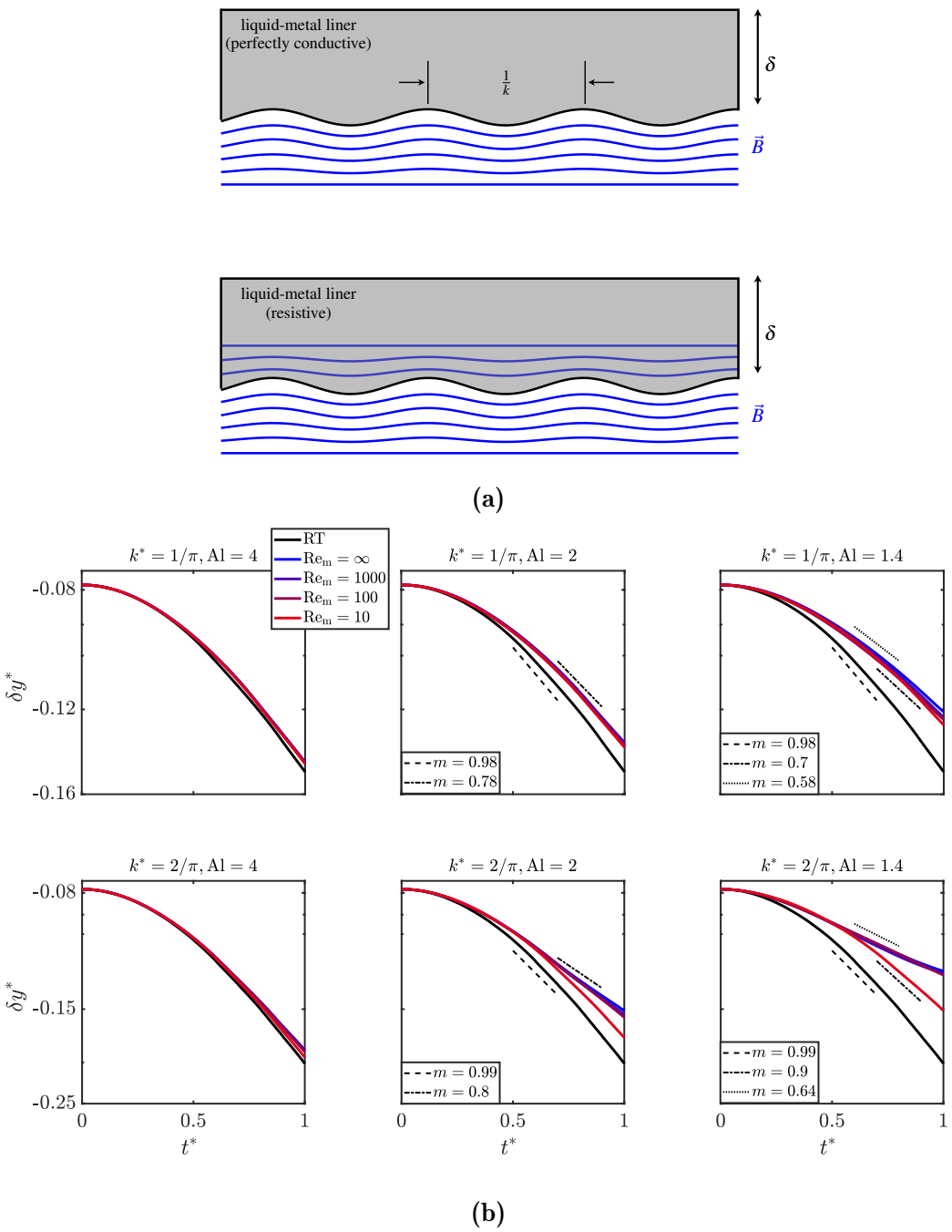

Figure 3.6: (a) The schematic of the problem qualitatively depicting the behavior of magnetic field lines for both ideal and resistive cases. (b) MRT growth of two wavenumbers, [top] $k^* = 1/\pi$ and [bottom] $k^* = 2/\pi$, with three different Alfvén numbers of 4, 2, and 1.4, from left to right, for four magnetic Reynolds numbers of ∞, 1000, 100, and 10, along with the pure hydrodynamic case.

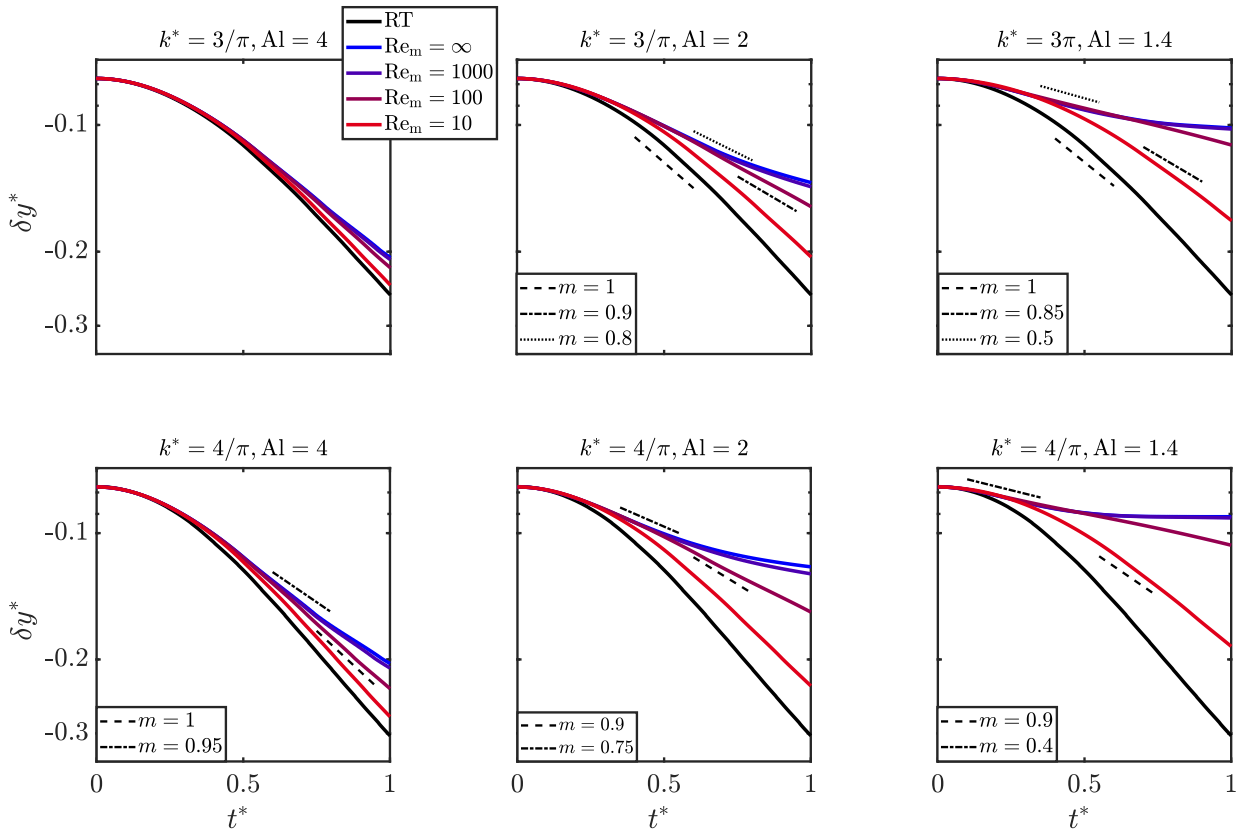

Figure 3.7: MRT growth of two wavenumbers, [top] $k^* = 3/\pi$ and [bottom] $k^* = 4/\pi$, with three different Alfvén numbers of 4, 2, and 1.4, from left to right, for four magnetic Reynolds numbers of ∞, 1000, 100, and 10, along with the pure hydrodynamic case.

perturbations with higher wavenumbers, i.e., shorter wavelengths, compared to perturbations with smaller wavenumbers. At higher wavenumbers, the difference between the ideal and resistive cases emerges at an earlier time compared to smaller wavenumbers. Secondly, for smaller Alfvén numbers, the distinction between the ideal and resistive cases develops faster, and the impact of magnetic Reynolds number becomes more noticeable. Lastly, the presence of finite resistivity increases the MRT growth rate compared to the ideal case, and for small magnetic Reynolds numbers (i.e., high magnetic diffusivity), the MRT growth rate approaches that of the pure hydrodynamic case.

To investigate the potential impact of magnetic diffusion on the morphology of the MRT instability spikes and bubbles, Fig. 3.8 displays the upper and lower interfaces of the liquid

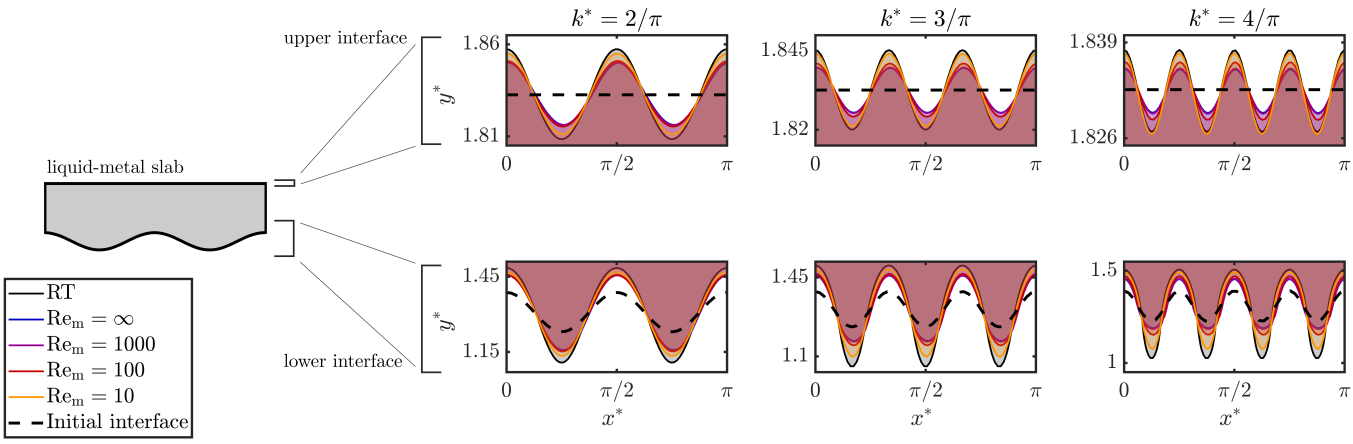

Figure 3.8: The location of upper and lower interfaces at $t^* = 1$ for three wavenumbers, $k^* = 2/\pi$, $3/\pi$, and $4/\pi$, with Alfvén number of 2, for four different magnetic Reynolds number of ∞, 1000, 100, and 10, along with the hydrodynamic case.

liner at $t^* = 1$ for three different wavenumbers, $k^* = 2/\pi, 3/\pi$, and $4/\pi$, with Al $= 2$. It can be observed that increasing magnetic diffusivity, which corresponds to decreasing the magnetic Reynolds number, leads to the spikes and bubbles of the MRT instability exhibiting growth patterns closer to those observed in pure hydrodynamic cases. Based on the presented results for the upper interface location, it is evident that, as expected, higher k^* values demonstrate less of a feedthrough effect on the upper interface. However, magnetic diffusion increases the feedthrough effect compared to the ideal case, as it enhances the instability growth of the MRT unstable interface.

Figure 3.9 depicts the magnetic field contours at $t^* = 2$ for both ideal and resistive MHD cases, considering two wavenumbers: $k^* = 2/\pi$ and $4/\pi$. The corresponding Alfvén and magnetic Reynolds numbers are 4 and 100, respectively. As can be observed from this figure, in the ideal case, no magnetic field has diffused into the liquid liner, whereas in the resistive MHD case, the magnetic field lines have penetrated the liner due to its finite resistivity. In Fig. 3.9(a), it is apparent that the peak magnetic amplitude in the ideal case is approximately 3, whereas it is around 1.4 for the resistive MHD case at $k^* = 2/\pi$. This difference confirms that magnetic diffusion results in decreased magnetic compression and, therefore, a reduction in magnetic tension in the resistive MHD case.

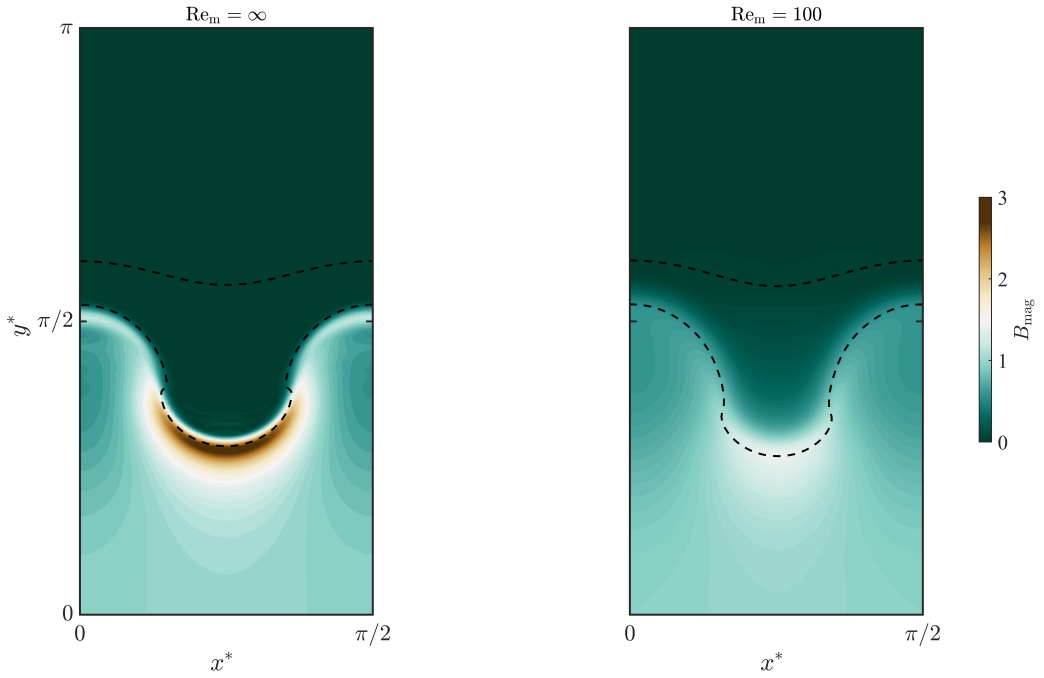

(a)

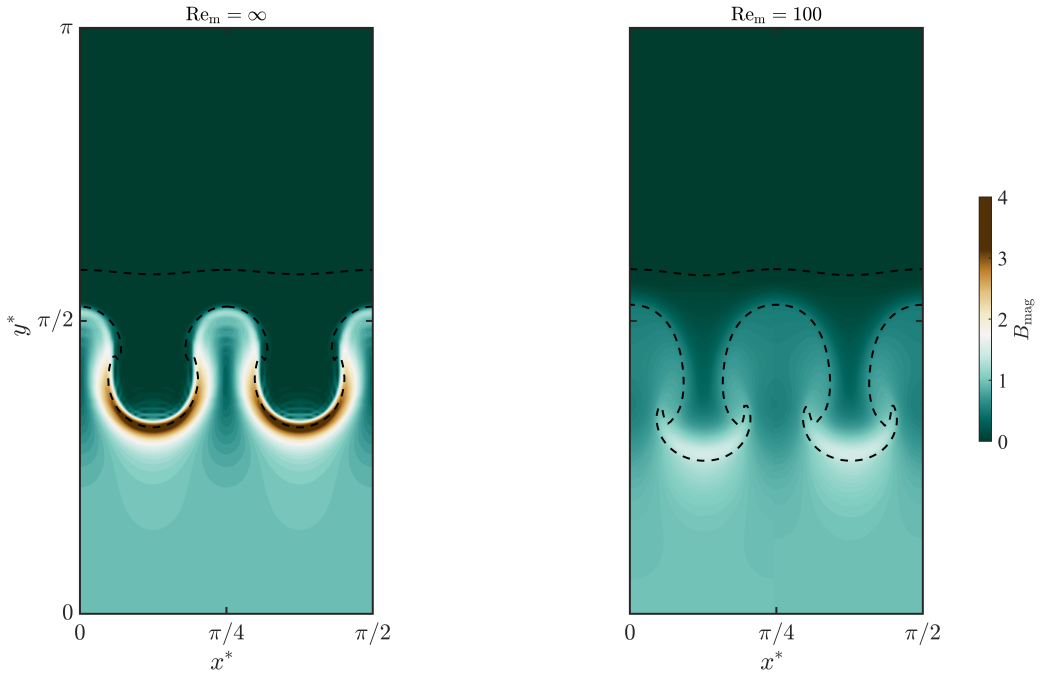

(b)

Figure 3.9: Magnetic field strength at $t^* = 2$ for two cases: ideal MHD and resistive MHD, for two wavenumbers: (a) $k^* = 2/\pi$ and (b) $k^* = 4/\pi$ with Alfvén number of 4. Dashed lines represent the liquid liner interface.

The same trend is observed in Fig. 3.9(b) for the wavenumber $k^* = 4/\pi$, with the maximum magnetic field values being almost 4 and 2 for the ideal and resistive MHD cases, respectively. Although the peak magnetic field value in the ideal MHD case is higher for $k^* = 4/\pi$ compared to $k^* = 2/\pi$, transitioning from the ideal assumption to the resistive MHD case results in reduced magnetic tension and, hence, increased RT growth.

To conclude this section, the impact of the electrical conductivity ratio across the interface on the perturbation growth rate is investigated. To this end, with Alfvén number and magnetic Reynolds number set to 2 and 100, respectively, MRT growth was simulated for four different electrical conductivity ratios of $\sigma_{e,r} = 10$, 1, 0.1, and 0.01. The results are represented in Fig. 3.10 for wavenumbers $k^* = 1/\pi$, $2/\pi$, $3/\pi$, and $4/\pi$. As indicated by this figure, for smaller wavenumbers of $k^* = 1/\pi$ and $2/\pi$, the effect of the electrical conductivity ratio on the growth rate is almost negligible, with only slight differences beginning to appear towards the end of the simulation. However, this effect is noticeable for higher wavenumbers, i.e., $k^* = 3/\pi$ and $4/\pi$. According to Fig. 3.10, for the conductivity ratio of 10, meaning the lower region has greater conductivity compared to the liquid liner, the perturbation growth closely resembles that of the ideal MHD case. Nevertheless, for conductivity ratios of $\sigma_{e,r} \leq 1$, the MRT growth begins to deviate further from the ideal MHD case. As the electrical conductivity jump across the interface increases, the growth rate tends to approach the classical RT case. This observation could be of significant importance in practical fusion applications, as the electrical conductivity ratio across the liner can become noticeable depending on the conditions. Consequently, the MRT growth rate increases, further diminishing the stabilizing effect of the magnetic field observed in the ideal case. Additionally, as one may expect from the presented results, it was observed that a higher electrical conductivity ratio resulted in an increased feedthrough effect on the upper interface.

3.5.3 Effect of surface tension

Surface tension tends to stabilize an interface against the development of RT instability by producing a restoring force, with this force increasing for perturbations with larger wavenumbers. In this section, the numerical solver was utilized to investigate MRT instability growth

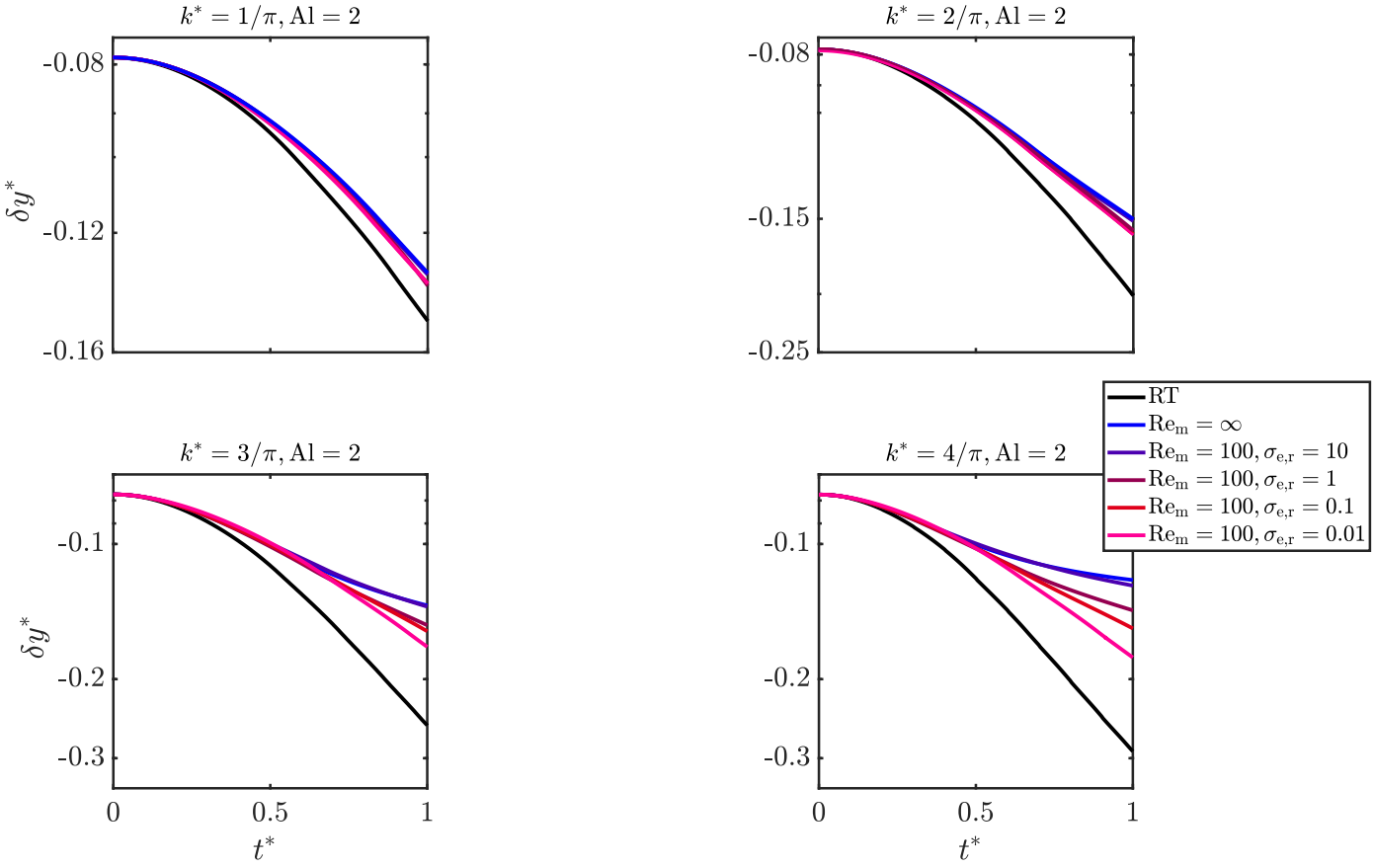

Figure 3.10: MRT growth of four wavenumbers, $k^* = 1/\pi$, $2/\pi$, $3/\pi$, and $4/\pi$, with Alfvén number and magnetic Reynolds number of 2 and 100, respectively, for four different electrical conductivity ratios of 10, 1, 0.1, and 0.01.

for both ideal and resistive MHD cases, taking into account the effect of surface tension. Our primary focus is the extent to which the value of the Bond number noticeably influences perturbation growth due to the presence of surface tension.

According to simulation results, the effect of surface tension on the MRT growth is almost negligible for Bond numbers ranging from 10^7 to 10^4, especially for perturbations with smaller wavenumbers. Due to its insignificant impact on the instability growth, the corresponding results are not shown. Therefore, numerical simulations demonstrate that within the Bond number range calculated in Table 3.1, the effect of surface tension appears to be minimal.

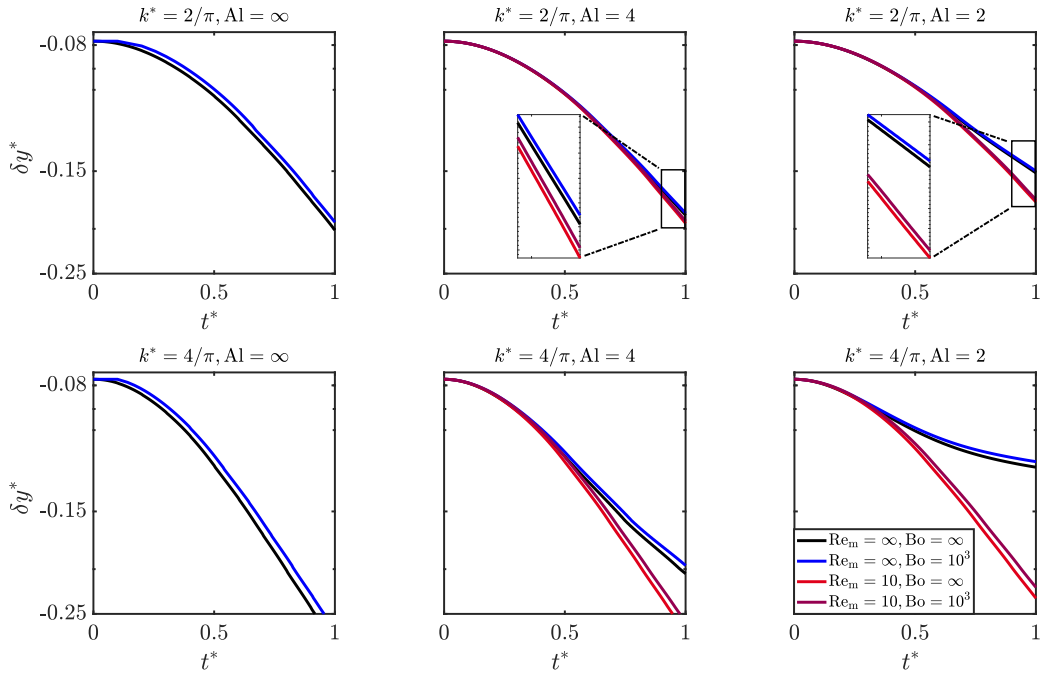

Figure 3.11: MRT growth of two wavenumbers [top] $k^* = 2/\pi$ and [bottom] $k^* = 4/\pi$ for three Alfvén numbers, ∞, 4, and 2, with a Bond number set to $\mathrm{Bo} = 10^3$, for both ideal and resistive MHD cases.

The simulation results for a Bond number of $\mathrm{Bo} = 10^3$ are presented in Fig. 3.11 for two wavenumbers of $k^* = 2/\pi$ and $4/\pi$. This figure illustrates the results for Alfvén numbers of $\mathrm{Al} = \infty$ (classical RT), 4, and 2 with two magnetic Reynolds numbers of $\mathrm{Re_m} = \infty$ (ideal MHD case) and 10 and with an electrical conductivity ratio of 0.1. As depicted in Fig. 3.11, the stabilization effect of surface tension is more pronounced for the higher wavenumber of $k^* = 4/\pi$ compared to $k^* = 2/\pi$. However, even for the case of $k^* = 2/\pi$, it can be observed that considering the effect of surface tension has led to a smaller growth rate for both ideal and resistive cases (see the insets of Fig. 3.11(top row)).

As seen in Fig. 3.11(bottom row), with the stabilization effect of surface tension being more pronounced in the case of $k^* = 4/\pi$, it becomes apparent that, for the ideal case, regardless of the Alfvén number value, the presence of surface tension leads to reduced perturbation growth. The same behaviour is evident for the resistive case, where the instability growth has decreased for $\mathrm{Bo} = 10^3$ compared to the case of $\mathrm{Bo} = \infty$. Based on the presented

results, it can be concluded that the stabilizing effect of surface tension is preserved for both ideal and resistive MHD cases. Furthermore, upon examining the evolution of the upper interface, we noted that accounting for surface tension leads to a reduced feedthrough effect on the upper interface. This reduced feedthrough effect is due not only to the reduced MRT instability growth at the lower interface but also to the presence of surface tension at the upper interface, which has a stabilizing effect on the instabilities forming at that surface. The visual presentation of surface tension impact on feedthrough at the upper interface is further elaborated in the following section.

3.6 Discussion

A discussion of the numerical results and analysis presented in Sec. 3.5 is provided here, along with an explanation of the underlying physics.

The analytical and numerical results of the MRT instability growth in the ideal MHD scenario suggest that the presence of a horizontal magnetic field in the lower layer reduces the RT instability growth of a liquid-metal liner. This reduction in MRT growth can be explained by the frozen-in law, stating that in ideal MHD flows, magnetic field lines are attached to the velocity field. Therefore, as the instability ripples begin to grow, magnetic field lines trapped in the lower layer also start to ripple and bend (see Fig. 3.3a). Consequently, the bent magnetic field lines experience tension. The resulting restoring force induced in magnetic field lines due to tension acts as a source of energy sink, thereby decreasing the MRT growth rate.

Numerical results mainly deviate from the analytical solution for smaller Alfvén numbers and higher wavenumbers. This deviation is attributed to the limitation of the analytical solution, which is primarily valid in linear regimes for relatively long wavelengths (i.e., small wavenumbers) and small magnetic tension values. As the wavenumber value increases, and consequently, the magnetic tension becomes stronger, the accuracy of the analytical solution decreases, as noted by Weis (2015). Another constraint of the analytical solution is its failure to account for the effect of finite resistivity on MRT growth, highlighting the importance of a

numerical solver in exploring the interplay between magnetic tension and magnetic diffusion across different instability development regimes.

Figure 3.12 illustrates the liquid liner interface at $t^* = 2.5$ for four different cases: pure hydrodynamic, ideal MHD with Al = 4, resistive MHD with a magnetic Reynolds number of Re = 100, and resistive MHD case with surface tension. For the latter case, the Bond number is assumed to be 100, which is reduced by approximately four orders of magnitude compared to the values reported in Table 3.1 in order to capture the effect of surface tension on the MRT instability growth. Results are depicted for two wavenumbers: $k^* = 2/\pi$ (Fig. 3.12a) and $k^* = 4/\pi$ (Fig. 3.12b). The ideal MHD case for the two studied wavenumbers indicates that the stabilizing effect of magnetic tension is more pronounced for higher wavenumbers. One may ascribe this behaviour to the induced tension in the magnetic field during the MRT growth. Through the development of the MRT instability, the bending of magnetic field lines generates Alfvén waves, and the magnetic tension part of the Lorentz force is proportional to $(\boldsymbol{k} \cdot \boldsymbol{v}_{\mathrm{Al}})^2$. Hence, as the wavenumber increases, the stabilizing effect of the magnetic field due to the greater magnetic tension becomes more pronounced, leading to further suppression of instabilities at shorter wavelengths. The schematic presented in Fig. 3.3(a) demonstrates that for shorter wavelengths, the curvature of magnetic field lines is greater, resulting in larger induced magnetic tension.

The inclusion of magnetic diffusion leads to increased instability growth for both wavenumbers, as displayed in Fig 3.12, compared to the ideal MHD case. In the presence of finite resistivity, the magnetic field lines are not confined within the boundaries of their corresponding medium (i.e., frozen-in law) any longer due to magnetic diffusion. Therefore, magnetic field lines can slip out of the lower region and diffuse into the liquid liner as shown in Fig. 3.6(a), thereby reducing the restoring force and the stabilization effect compared to the ideal case. Thus, it can be concluded that ideal MHD analysis may significantly overestimate the stabilizing effect of the magnetic field.

As indicated by Fig. 3.12, finite resistivity has a more pronounced effect on the MRT growth of an initially magnetic-field-free liquid liner for perturbations with higher wavenumbers (i.e., shorter wavelengths). This finding is analogous to that of Sun *et al.* (2023),

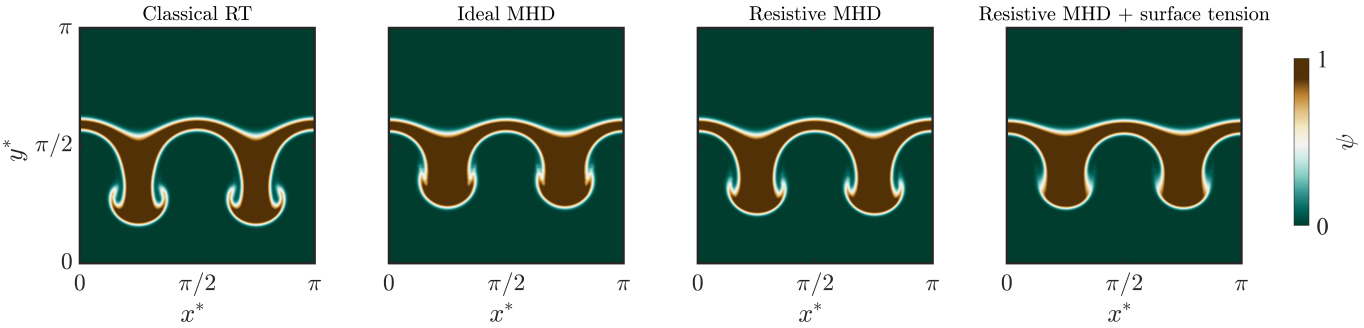

(a)

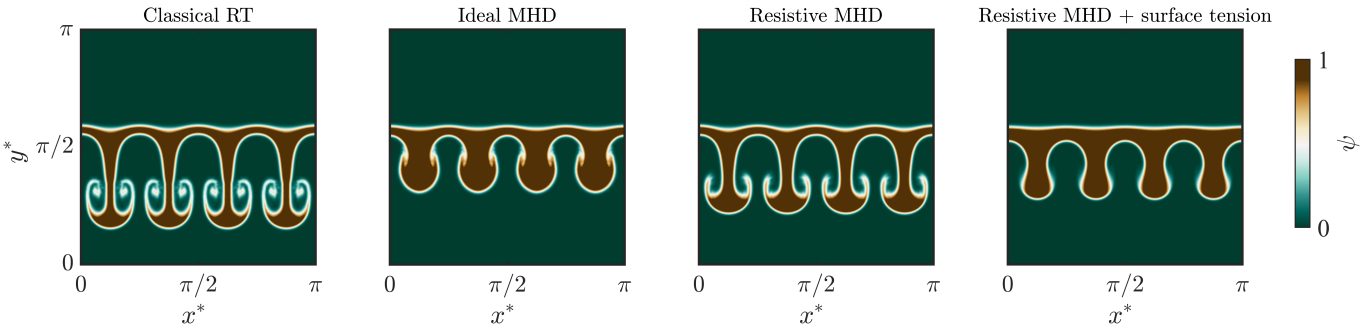

(b)

Figure 3.12: Liquid liner interface at $t^* = 2.5$ for four cases: pure hydrodynamic, ideal MHD (Al = 4), and resistive MHD (Al = 4, $\mathrm{Re_m} = 100$), without and with surface tension, from left to right, for two wavenumbers (a) $k^* = 2/\pi$ and (b) $k^* = 4/\pi$.

who investigated the effect of magnetic diffusion on the MRT growth for a single interface geometry with a constant magnetic field present in both heavy and light fluids.

In Sec. 3.5.2, it became evident that increasing magnetic diffusivity, which corresponds to decreasing the magnetic Reynolds number, leads to the spikes and bubbles of the MRT instability exhibiting growth patterns closer to those observed in pure hydrodynamic cases. This observation aligns with the findings of Samulski *et al.* (2022), who investigated MRT instability growth during the deceleration phase of ICF implosion with a constant magnetic field imposed in the domain. According to their study, the observed MRT growth and interface morphology for the resistive MHD case closely resembled the hydrodynamic case, with only slight differences noted (Samulski *et al.*, 2022).

The stabilizing mechanism of surface tension, generating restoring forces, is akin to that in the MRT case. Hence, in the literature, the effect of a magnetic field in the ideal MHD case is often considered analogous to the presence of surface tension. However, our numerical simulation showed that for high Bond numbers ($\mathrm{Bo} > 10^4$), the effect of surface tension is almost negligible. In Fig. 3.12, for a lower Bond number of $\mathrm{Bo} = 100$, the liquid-metal interface is noticeably stabilized, especially for the higher wavenumber, $k^* = 4/\pi$. Furthermore, it is visually evident that considering the surface tension effect has led to smaller perturbation growth at the upper interface.

In general, the results exhibit that increasing the wavenumber, k^*, reduces the feedthrough effect. Previous studies by Lau *et al.* (2011), Weis *et al.* (2014), and Weis (2015) have also reported that increasing k^* lessens feedthrough, and for $k^* \gg 1$, the feedthrough effect becomes virtually negligible. This observation can also be justified based on the reported feedthrough factor by Taylor (1950) for a liquid slab of finite thickness, δ. Taylor (1950) showed that the amplitude of ripples on the RT stable surface of the liquid layer grows a factor of $\mathrm{e}^{-k\delta}$ less than the perturbations on the RT unstable interface. Consequently, for larger k^* values, interpreted as thicker slabs or higher wavenumbers, the feedthrough effect on the upper interface is smaller.

The interplay between magnetic tension and magnetic diffusion can be studied across different regimes and classified as a map, which is a function of the two governing parameters,

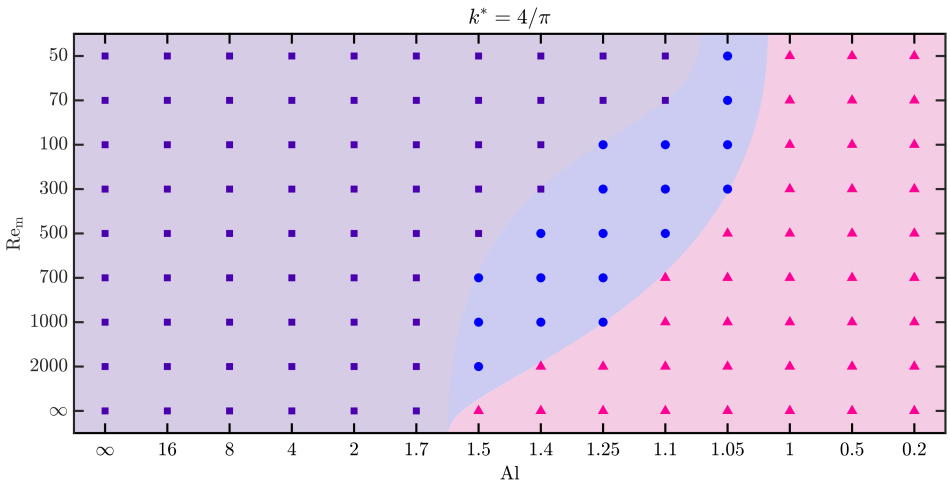

Figure 3.13: Stability analysis for $k^* = 4/\pi$ across various Alfvén numbers and magnetic Reynolds numbers, with an electrical conductivity ratio of 0.1. Purple (■), pink (▲), and blue (●) regions indicate unstable, stable, and transition from initially unstable to stable cases, respectively.

i.e., the Alfvén number and the magnetic Reynolds number. Using the established numerical toolkit, this map is represented in Fig. 3.13 for the wavenumbers $k^* = 4/\pi$.

According to this figure, three distinct behaviours are observed. The purple region (data shown with ■) illustrates an unstable region in which the RT instability develops. This region mostly corresponds to higher Alfvén numbers. In smaller Alfvén regimes, the initially perturbed interface starts to oscillate in time, and the interface is observed to be RT stable, indicated in pink (▲). One important observation is the effect of the magnetic Reynolds number on causing the stable case to become unstable. For instance, for wavenumber $k^* = 4/\pi$, in the ideal MHD case ($\mathrm{Re_m} = \infty$), the RT becomes stable for the Alfvén number of 1.4. However, decreasing the Reynolds number to $\mathrm{Re_m} = 50$, the instability starts to grow in time. The region shown in blue (with markers ●) corresponds to the regime where the perturbation starts to grow; however, after some time, it begins to oscillate, due to an increase in magnetic tension, which has a stabilizing effect on the MRT growth.

To conclude this section, the results are compared to the parameter space introduced in Table 3.1 for different applications. The studied Alfvén numbers largely fall within the ranges mentioned in Table 3.1, i.e., between 0.07 and 15 in both MTF and MagLIF approaches. Our

results suggest that for small Alfvén numbers, magnetic tension can stabilize the interface against the development of MRT instability. However, for higher Alfvén numbers, the MRT growth becomes more similar to classical RT instability. The MRT instability growth also depends on the perturbation wavenumber. The magnetic Reynolds numbers of 400 and 10 for MTF and MagLIF approaches, respectively, prove to affect the stabilizing effect of the magnetic field compared to the ideal MHD case (see Fig. 3.6b and Fig. 3.7), and the role of magnetic diffusion cannot be neglected. However, for both fusion approaches, the effect of surface tension is minimal based on the high Bond number in these regimes.

3.7 Conclusion

This study numerically investigated the MRT instability growth and feedthrough in an initially magnetic-field-free liquid-metal liner, with an axial magnetic field of arbitrary magnitude imposed in the lower layer. To this end, a novel second-order numerical solver was introduced for modelling two-phase incompressible MHD flows within the finite-difference framework. The MRT instability growth was analyzed for both scenarios of perfectly conducting and resistive liners, and the effect of the Alfvén number and magnetic Reynolds number was examined.

The results indicate that magnetic diffusion primarily affects the MRT growth rate for higher wavenumbers, while for smaller wavenumbers, the effect of finite resistivity is observed over a longer duration of instability development. Furthermore, it is demonstrated that decreasing the Alfvén number results in the faster emergence of the magnetic diffusion effect on the MRT growth. Additionally, a greater electrical conductivity jump across the liner leads to increased perturbation growth. Lastly, the surface tension effect is shown to be negligible for high Bond numbers, while for relatively smaller values of the Bond number, the stabilizing effect of surface tension is observed for both ideal and resistive MHD cases, particularly notable for higher wavenumbers.

Acknowledgments

The authors would like to thank Ivan Khalzov and Jean-Sebastien Dick for their valuable comments and suggestions. This study was supported by the Natural Sciences and Engineering Research Council (NSERC) of Canada Discovery Grant (No. RGPIN-2019-06436).

DATA AVAILABILITY

The data that support the findings of this study are available from the corresponding author upon reasonable request.

Appendix A. Evaluation of two-phase incompressible MHD numerical solver

he single interface Rayleigh–Taylor instability with a constant horizontal magnetic field, $(B_x, 0, 0)$, in both liquid and gas phases was studied as a benchmark to evaluate the accuracy, convergence, and performance of the implemented two-phase incompressible MHD solver. In this test case, a two-dimensional rectangular domain $[x, y] \in [0, 1] \times [0, 4]$, with a fluid phase filling the top half of the domain, was considered. The fluid interface at $y_0 = 2$ was initialized with a small sinusoidal perturbation with the wavelength and amplitude of 2π and 0.1, respectively. The density values were set to $\rho_{\mathrm{g}} = 1$ and $\rho_{\mathrm{l}} = 3$ with the gravity acting downwards with a magnitude of unity. The initial magnetic field value and magnetic permeability were set to $B_x = 0.1$ and $\mu_{\mathrm{m}} = 1$, respectively. The simulation was performed for four different grid resolutions of 16×64, 32×128, 64×256, and 128×512 with a constant time step of $\Delta t = 5 \times 10^{-4}/\sqrt{\mathrm{At}}$.

Figure 3.14(a) displays the results for the four different mesh resolutions at time $t\sqrt{\mathrm{At}} = 0.75$ to 2 with an increment of 0.25. As depicted in this figure, refining the mesh leads to a more accurate representation of the RT instability features, and for mesh resolutions of 64×256 and 128×512, the numerical results are closely matched. For a more thorough quantitative analysis, we compared the obtained numerical growth rate with the analytical

solution, shown in Fig. 3.14(b). The analytical growth rate is calculated as (Samulski *et al.*, 2022)

$$\omega^2 = gk\mathrm{At} - \frac{B^2k^2}{\mu_\mathrm{m}(\rho_1 + \rho_2)}, \tag{3.16}$$

which predicts a growth rate of 0.7 for this test case. From Fig. 3.14(b), it is evident that as the grid resolution increases, the numerical growth rate converges to 0.65, closely matching the analytical solution.

Assuming the solution of the finest mesh, 128×512, as an analytical solution, the convergence rate of the numerical solver is computed. To this end, the L_2 norm of the spike and bubble locations during the simulation is calculated. As indicated by Fig. 3.14(c), the obtained convergence rate is around 1.5, which is close to the expected second order, confirming the solver's accuracy and robustness.

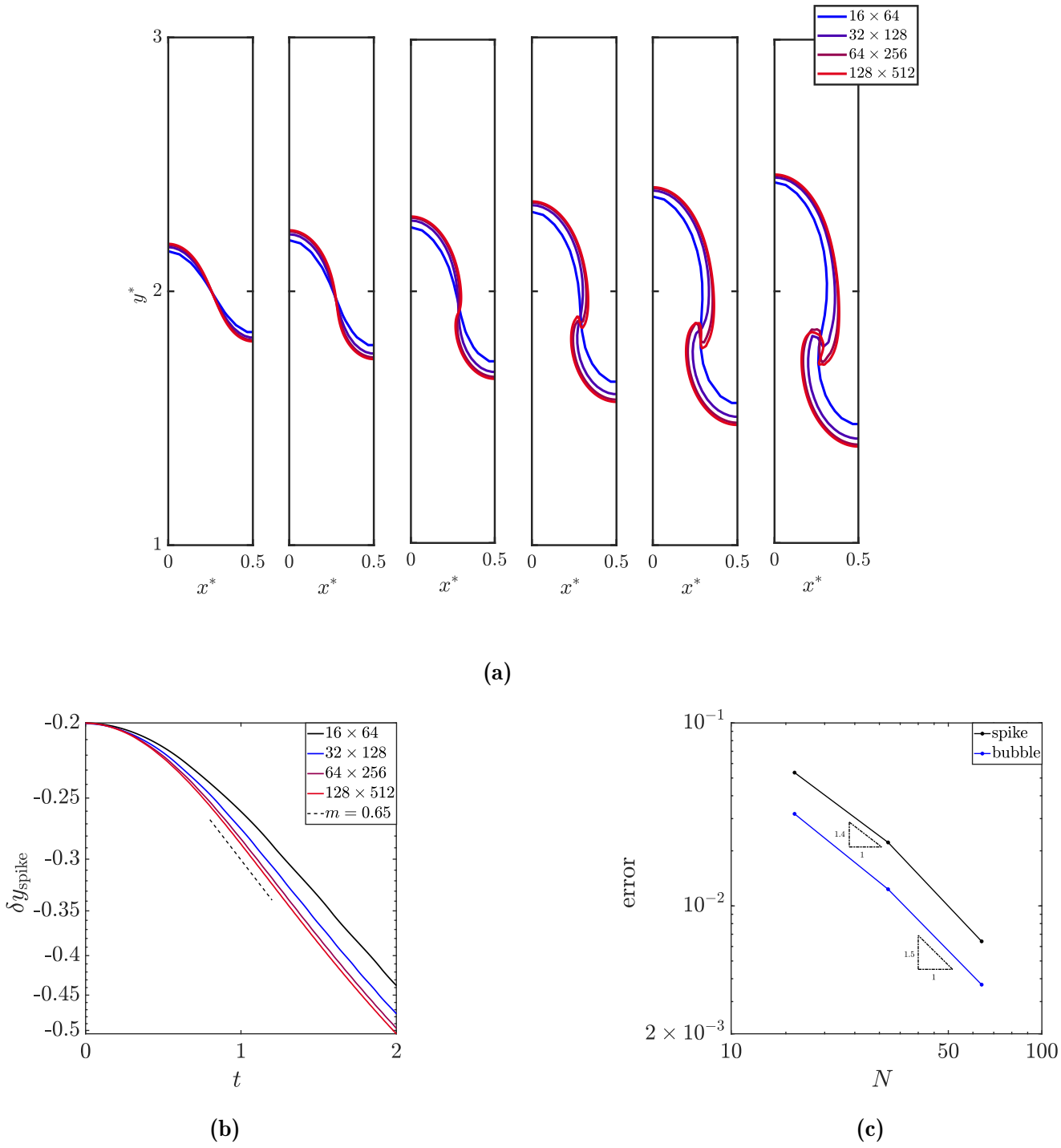

Figure 3.14: (a) The interface of the MRT instability with the density ratio of 3 at $t\sqrt{\text{At}} = 0.75, 1, 1.25, 1.5, 1.75$, and 2, from left to right, for four different mesh resolutions. (b) MRT growth rate for four different mesh resolutions. (c) Order of accuracy analysis for the implemented solver.

CHAPTER 4

Discussion

4.1 Introduction

In Chapter 1, a detailed discussion is provided on stability concerns related to liner implosion in various fusion applications, including MTF, ICF, and MagLIF. Across all these fusion approaches, preserving the instability of the liner's interface is critical. Any instabilities arising at the PLMI can significantly impair fusion reactor performance, potentially leading to plasma quenching and reduced energy production. Additionally, such instabilities may facilitate the intrusion of liner materials into the plasma, thereby introducing impurities and contaminating plasma. The RT/MRT instability is recognized as one of the intrusive instabilities occurring in fusion applications, which has been extensively studied in the literature and continues to be an active field of research.

In this thesis, the RT/MRT instability of an initially magnetic-field-free liquid liner slab surrounded by two lighter regions of the same properties (i.e., lower and upper layers) is numerically investigated. The gravitational body force is acting downward, causing the lower interface of the liner to become RT unstable. While the upper interface of the liner remains RT stable, instabilities at the lower interface propagate through the liner's finite thickness to this interface, leading to the emergence of perturbations. In the discussion presented, the upper and lower interfaces are referred to as the feedthrough interface and the RT unstable interface, respectively.

The results presented in Chapter 3 indicate that for a perfectly conductive liner, the presence of a horizontal magnetic field reduces the RT instability. This stabilizing effect appears to be more pronounced for higher wavenumbers (i.e., shorter wavelengths) and higher magnetic field values (i.e., smaller Alfvén numbers). However, it was observed that the ideal MHD assumption overestimates the stabilizing effect of the imposed magnetic field when considering the finite resistivity of the liner in the analysis. How the RT instability growth in the resistive MHD case deviates from the ideal one depends on various parameters, such as perturbation wavenumber, magnetic diffusivity, electrical conductivity ratio between the liquid-metal liner and the surrounding medium, and the time scale of interest. In this chapter, a more detailed discussion regarding resistive MRT instability and its appearance across different scenarios is provided in Sec. 4.2.

In the previous chapter, the feedthrough effect was examined only for cases where the upper interface is initially smooth, whereas perturbations might be initially present at this interface. The discussion provided in Sec. 4.3 studies how initially seeded perturbations at the upper interface affect the RT instability growth and interface coupling.

4.2 Delving deeper into the impact of magnetic diffusivity

The simulation results presented here are based on the initial conditions and simulation setup introduced in Chapter 3. For two wavenumbers, i.e., $k^* = 2/\pi$ and $4/\pi$, the RT instability growth is investigated for three scenarios: pure hydrodynamic, ideal MHD with an Alfvén number of 4, and resistive MHD with a magnetic Reynolds number of 100 and an electrical conductivity ratio of 0.1. The corresponding results illustrating the transient location of the instability spike tip from $t^* = 0$ to 2.5 are shown in Fig. 4.1. As depicted in this figure, for both of the studied wavenumbers, instability growth is lower for the ideal MRT case compared to the classical RT scenario. In the ideal MRT case, all three regions—the liquid metal liner and the upper and lower layers of air—are assumed to be perfectly conductive. Therefore, the horizontal magnetic field initially present in the lower layer remains confined to that layer and cannot diffuse into the adjacent region. The velocity field strongly influences the magnetic field when a medium is perfectly conductive or the magnetic Reynolds number

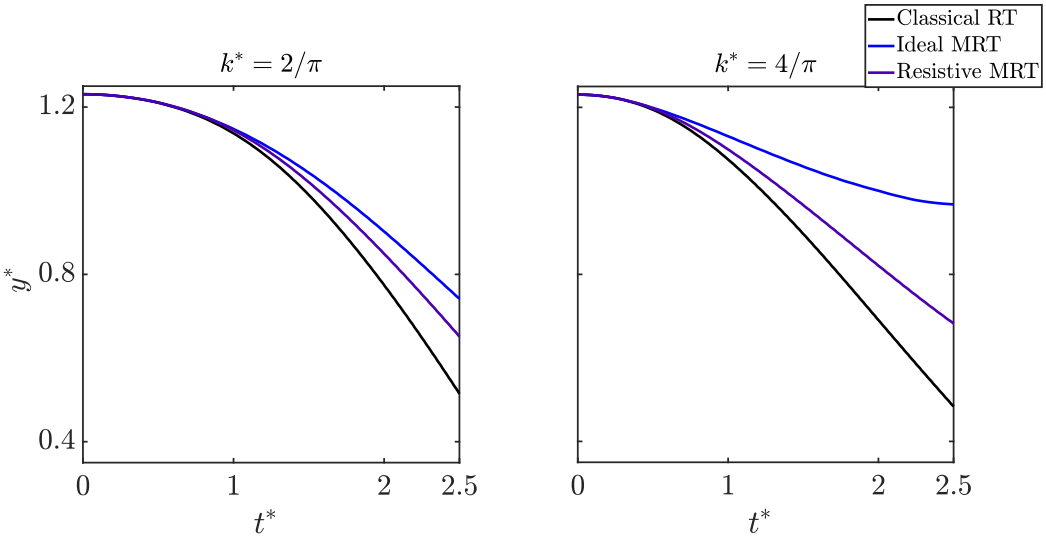

Figure 4.1: The transient location of the RT instability spike tip from $t^* = 0$ to 2.5 is represented for two wavenumbers, i.e., $k^* = 2/\pi$ and $4/\pi$, for three cases: classical RT, ideal MRT, and resistive MRT.

is high*. Therefore, magnetic field lines tend to advect with the velocity field according to Faraday's law of induction. Consequently, the movement of the fluid due to the instability growth causes the magnetic field lines to bend. Similar to an elastic band, the magnetic field lines go under tension and introduce a restoring force, which acts as an energy sink and leads to the stabilizing effect provided by the magnetic field. This restoring force is proportional to the wavenumber and is higher for perturbations with shorter wavelengths (i.e., higher wavenumbers).

To further elucidate the magnetic field behaviour during the RT instability growth, the magnetic field contours for two wavenumbers $k^* = 2/\pi$ and $4/\pi$ are represented in Fig. 4.2(a) and Fig. 4.3(a), respectively, at five different time steps, i.e., $t^* = 0.5$, 0.75, 1.25, 1.75, and 2.25. It is appreciated from these figures that during the instability growth, no magnetic field penetrates the liquid liner, consistent with the ideal MHD assumption. As the instability grows, the magnetic field strength increases in the lower layer. However, referring to

* A high magnetic Reynolds number corresponds to low resistivity values.

Fig. 4.2(a) and Fig. 4.3(a), it is observed that the peak magnetic field value is higher for the wavenumber $k^* = 4/\pi$, approximately 4, compared to the $k^* = 2/\pi$ case where the peak magnetic field value is around 3. Thus, for perturbations with smaller wavelengths, magnetic field lines experience greater bending curvature, resulting in higher magnetic field strength and increased restoring force. Consequently, this leads to a greater stabilizing impact on the RT growth. That is why in Fig. 4.1, the stabilizing effect of the magnetic field is more pronounced for the wavenumber $k^* = 4/\pi$. Additionally, this stabilizing impact begins to appear sooner for the wavenumber $k^* = 4/\pi$ compared to $k^* = 2/\pi$.

Figure 4.1 illustrates that including finite resistivity for the liquid-metal liner and the surrounding medium results in an increase in the MRT instability growth compared to the ideal MHD case. This increase is more notable for the wavenumber $k^* = 4/\pi$, with the perturbation growth deviating from the ideal MHD case and approaching the classical RT case over a shorter period of time compared to $k^* = 2/\pi$. It is noteworthy to mention that the classical RT growth rate represents the highest instability growth corresponding to the most unstable mode. Magnetic tension, akin to other mechanisms such as surface tension, viscosity, or magnetic shear, can mitigate this instability growth. Although magnetic diffusion diminishes the stabilizing effect of magnetic tension, it cannot lead to a higher instability growth compared to the classical RT case. The magnetic field contours of the resistive MHD case for wavenumbers $k^* = 2/\pi$ and $4/\pi$ are demonstrated in Fig. 4.2(b) and Fig. 4.3(b), respectively, at $t^* = 0.5$, 0.75, 1.25, 1.75, and 2.25. As depicted in these figures, in the presence of finite resistivity, magnetic field lines are no longer confined solely to the lower region and can diffuse into the liquid-metal liner. Thus, as instability ripples grow and magnetic field lines experience tension, they diffuse from the lower layer into the liquid liner to relax and release their tension. Therefore, the peak magnetic field value in this scenario is expected to be lower compared to the ideal MHD case. This is consistent with the results shown in Fig. 4.2(b) and Fig. 4.3(b), exhibiting a maximum magnetic field value of almost half compared to the ideal case for both studied wavenumbers.

The magnetic field strength across the vertical line passing through the middle of the perturbation wavelength is plotted in Fig. 4.4 for both wavenumbers, i.e., $k^* = 2/\pi$ and $4/\pi$. In both cases, under the ideal MHD assumption, the magnetic field value continues

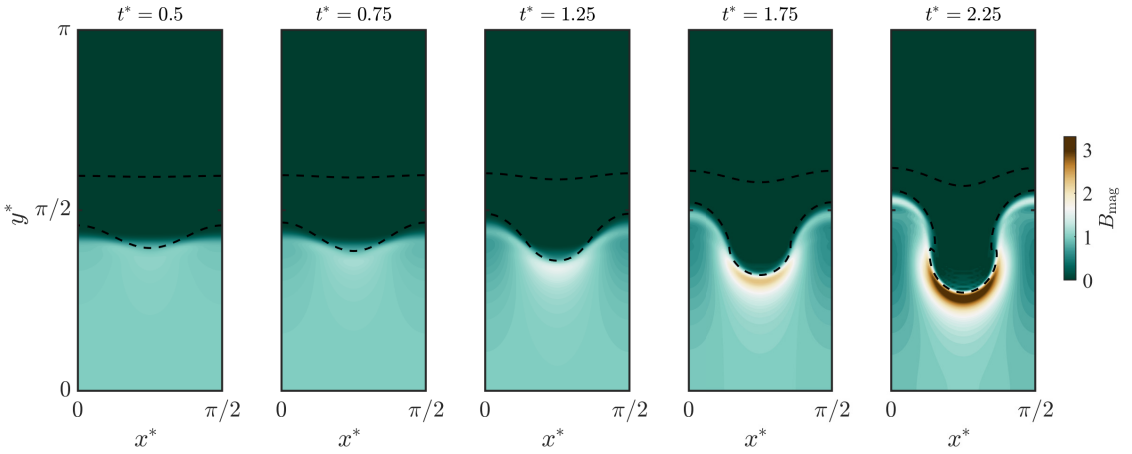

(a)

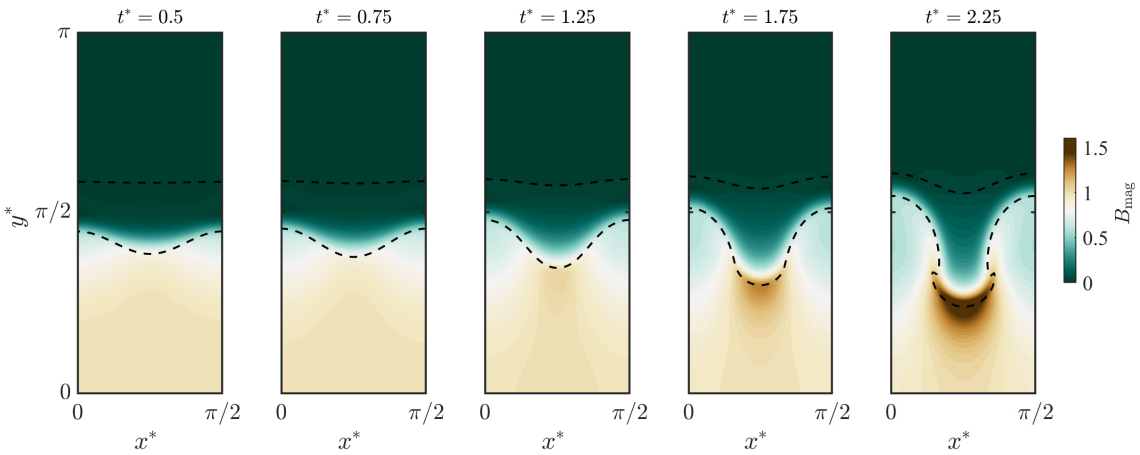

(b)

Figure 4.2: Magnetic field contours for (a) ideal MHD case (Al = 4) and (b) resistive MHD case ($\mathrm{Re_m} = 100$), with wavenumber $k^* = 2/\pi$, at $t^* = 0.5$, 0.75, 1.25, 1.75, and 2.25, from left to right, respectively.

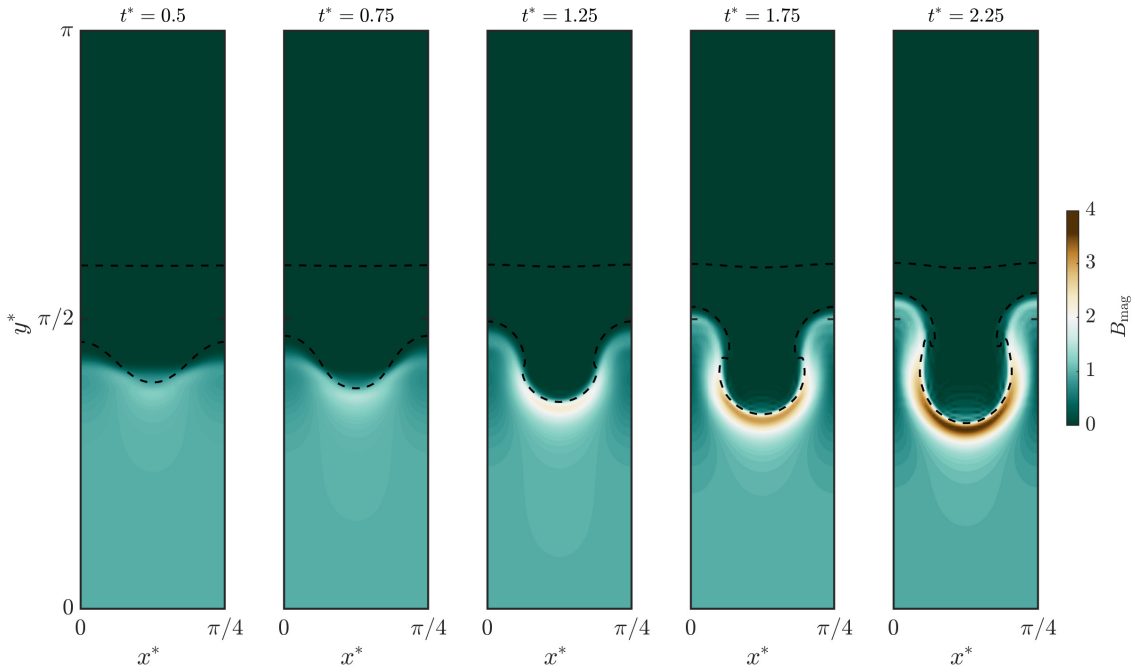

(a)

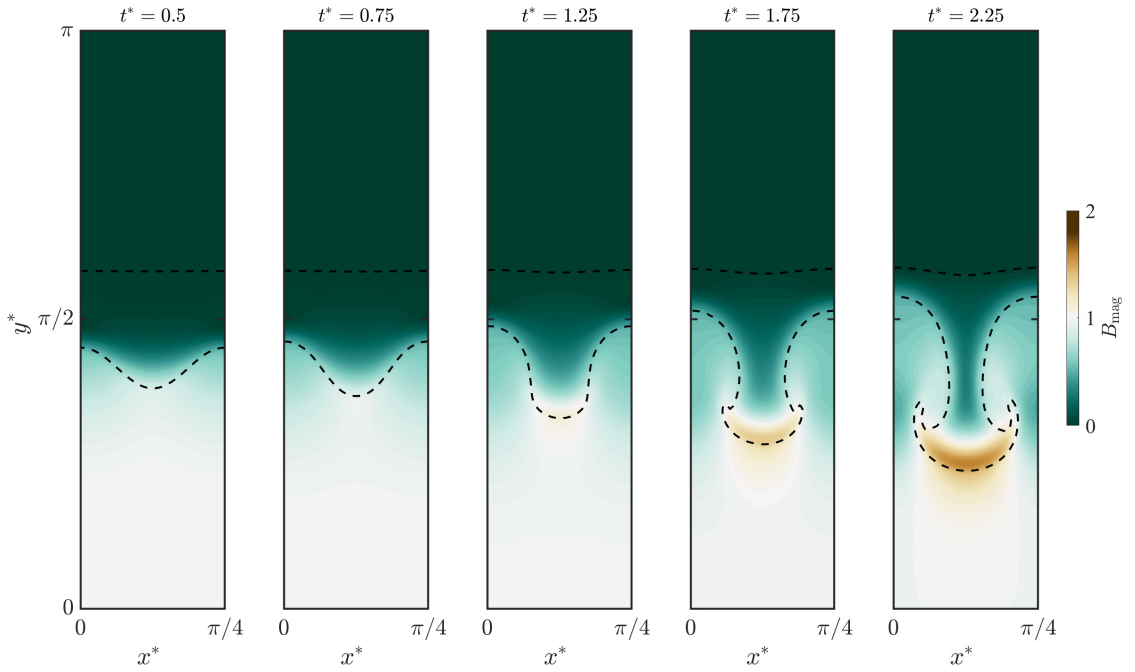

(b)

Figure 4.3: Magnetic field contours for (a) ideal MHD case (Al = 4) and (b) resistive MHD case ($\mathrm{Re_m} = 100$), with wavenumber $k^* = 4/\pi$, at $t^* = 0.5$, 0.75, 1.25, 1.75, and 2.25, from left to right, respectively.

to increase over time due to magnetic tension, and no magnetic field penetrates inside the liquid liner. However, for the resistive case, although an increase in magnetic field value is observed, the magnetic field also starts to diffuse into the liner. Hence, the magnetic peak compression is smaller in the resistive case compared to the ideal MHD case. This peak compression during the RT instability growth in the resistive MHD case and the effect of magnetic diffusion on the growth rate, depend on various factors such as magnetic diffusivity, magnetic field strength, and the time scale of interest, as studied earlier.

The presented results can also provide us with useful insight into magnetic diffusion losses during plasma compression using an imploding liner. The idea behind these plasma-liner systems is to convert the kinetic energy of an imploding liner into magnetic energy, resulting in an increase in magnetic pressure and temperature, causing plasma to reach fusion conditions. The implemented solver in this study is based on the incompressible assumption, and complete magnetic flux compression using an inward motion of the liner cannot be fully simulated. However, focusing on the initial stages of compression during which the incompressibility assumption holds, besides noting that magnetic diffusion adversely affects the magnetic field's stabilizing effect on the RT growth, it becomes apparent that during compression, the magnetic field of an initially formed plasma diffuses into the liquid-metal liner due to its finite resistivity. Therefore, the obtained peak compression of the magnetic flux within the plasma is less than the expected one derived from the ideal MHD assumption. One of the main side effects of this could be plasma energy loss if magnetic diffusion becomes noticeable during reactor operation.

In summary, these results suggest that in real-world applications where electrical resistivity cannot be neglected, the ideal MHD assumption overestimates the stabilizing effect of the magnetic field. Considering magnetic diffusion leads to an increase in the MRT growth compared to the ideal case, which is more pronounced for higher wavenumbers. The impact of magnetic diffusion on smaller wavenumbers tends to manifest over longer periods of time as opposed to higher wavenumbers. The electrical conductivity ratio between the liquid-metal liner and the surrounding air proved to be an important factor regarding the MRT growth rate in the resistive MHD case, as discussed in Chapter 3. However, the electrical conductivity ratio between the liquid metal liner and the surrounding air could be of an

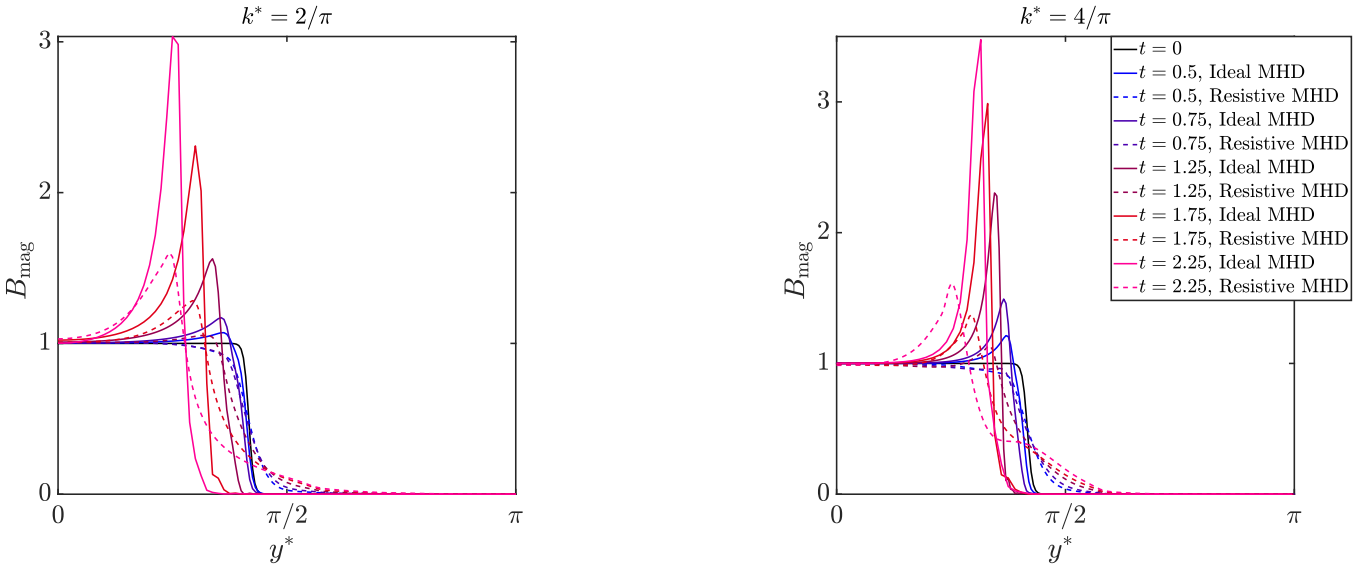

(a) **(b)**

Figure 4.4: Magnetic field value across $x = \pi/4$ and $x = \pi/8$ lines for (a) $k^* = 2/\pi$ and (b) $k^* = 4/\pi$, respectively, for both ideal and resistive MHD cases at $t^* = 0$, 0.5, 0.75, 1.25, 1.75, and 2.25.

order of $\mathcal{O}(10^{20})$, which is beyond our numerical capability to model. Consequently, one may expect that for this higher conductivity jump, the effect of magnetic diffusivity appears faster and more prominent. Increasing the electrical conductivity ratio results in instability growth approaching the classical RT limit. In similar experimental and numerical studies where the effect of magnetic diffusion on the MRT instability growth of a single interface in the presence of a background magnetic field was studied (Samulski *et al.*, 2022; Walsh, 2022), the instability growth of the resistive MHD and perturbation displacement appear to become close to the hydrodynamic case where no magnetic field exists.

4.3 Interface coupling

The perturbations at the lower interface of the liquid liner can influence the upper interface, a phenomenon known as the feedthrough effect. The feedthrough effect in a liquid liner of finite thickness has been investigated in Chapter 3. Generally, it was observed that feedthrough is dominated by smaller k^* values, and for a constant k^*, as the RT instability growth at the

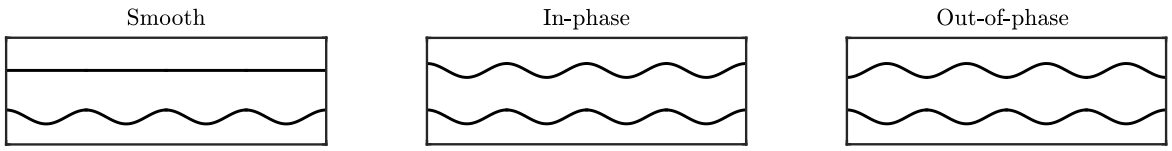

Figure 4.5: Initial configuration of the lower and upper interfaces for three scenarios where the upper interface is initially smooth, in-phase, and out-of-phase with respect to the perturbed lower interface, from left to right, respectively.

lower interface decreases, the perturbation amplitudes at the upper interface also decrease. While assumed to be initially smooth in Chapter 3, the upper interface is initially perturbed in the current chapter. Two specific cases are analyzed wherein the perturbations of the upper and lower interfaces are in-phase and out-of-phase. In the former, the peaks (troughs) of the upper interface correspond to the peaks (troughs) of its lower counterpart, whereas in the latter, the peaks (troughs) of the upper interface align with the troughs (peaks) of the lower interface (see Fig. 4.5).

The RT instability growth and its feedthrough effect are investigated across four different cases: hydrodynamic, ideal MHD, resistive MHD, and resistive MHD in the presence of surface tension, considering a wavenumber of $k^* = 4/\pi$. In the presented results, the Alfvén number, magnetic Reynolds number, and Bond number are set to 4, 100, and 100, respectively. Figure 4.6(a) depicts the upper interface location during the RT instability growth from $t^* = 0$ to 2.5. Specifically, it demonstrates the position of the perturbation at the upper interface over time for a point situated at the midpoint of the perturbation wavelength. The results suggest that the displacement of the upper interface in the smooth case is smaller compared to the in-phase and out-of-phase cases. The perturbation growth at the upper interface is observed to be larger for the classical RT case in the initially smooth scenario compared to its ideal MHD counterpart, as expected due to the decreased RT instability growth in the latter. Transitioning from the ideal MHD case to the resistive one,

the upper interface displacement increases, approaching that of the classical RT, owing to an increase in RT growth in the presence of magnetic diffusivity. Additionally, considering the surface tension effect alongside magnetic diffusivity results in smaller perturbation growth at the upper interface, confirming the mitigating effect of surface tension on the perturbation growth.

The upper interface of the liner is RT stable; therefore, initially seeded instabilities at this interface begin to oscillate, as exhibited in Fig. 4.6(a). The observed amplitude of the perturbation oscillation slightly differs among different scenarios, which is due to the difference in the RT growth rate at the lower interface that influences the feedthrough effect. For instance, considering the out-of-phase case, the perturbation displacement at $t^* = 2$ is barely smaller for the ideal MHD case as opposed to the pure hydrodynamic and resistive MHD cases. From Fig. 4.6(a), it is apparent that the perturbation growth amplitude in the out-of-phase and in-phase cases is close, with a phase lag; when the out-of-phase perturbation is at the maximum location, the in-phase is at the minimum vertical location. The results suggest that for the three cases of classical RT, ideal MHD, and resistive MHD, the oscillation periodicity is almost the same, while the oscillation frequency is higher for the case with the surface tension. This difference is attributed to the dispersive nature of the surface tension, which leads to faster oscillations of the perturbation at the interface compared to the other three cases (see Fig. 4.6a).

Figure 4.7(a) represents the liquid liner interface at $t^* = 1.75$ for the four studied cases. According to this figure, the upper interface perturbation does not have any noticeable impact on the RT instability growth at the lower interface. Consequently, referring to Fig. 4.7(a), it can be interpreted that for the studied wavenumber the feedthrough effect is relatively small. Additionally, for the in-phase and out-of-phase cases, the oscillations at the upper interface lead to the appearance of an anti-spike, resembling the jetting configuration, indicating the effect of the initial perturbations at the feedthrough interface on the morphology of the instabilities. For the case where the surface tension effect is present, the amplitude of this anti-spike is smaller compared to the other cases.

These results are reproduced for the wavenumber $k^* = 2/\pi$, as shown in Fig. 4.6(b). It is evident from this figure that for this smaller k^* value, the feedthrough effect is more

pronounced and results noticeably vary from the wavenumber $k^* = 4/\pi$. First, examining the results for the smooth case, it is apparent that the trend of perturbation growth across the four studied scenarios is similar to the previously studied wavenumber, while the difference between the classical RT and ideal MHD is more pronounced due to the higher feedthrough effect. When the ripples at the upper and lower interfaces are in-phase, the feedthrough effect is less pronounced compared to the out-of-phase scenario. In the latter, as the initial perturbation starts oscillating downward, it continues to grow in that direction due to the feedthrough effect from the RT unstable interface, leading to a higher perturbation growth during the represented time compared to the initially smooth interface case.

Figure 4.7(b) shows a snapshot of the liquid liner interface at $t^* = 1.75$, demonstrating that in this case, the upper interface impact on the RT instability growth is more noticeable due to the smaller k^* value and greater feedthrough effect. Additionally, as seen in Fig. 4.7(b), the RT instability growth is greater for the out-of-phase case. Hence, when instabilities at the lower and upper interface are out-of-phase, the feedthrough effect is amplified.

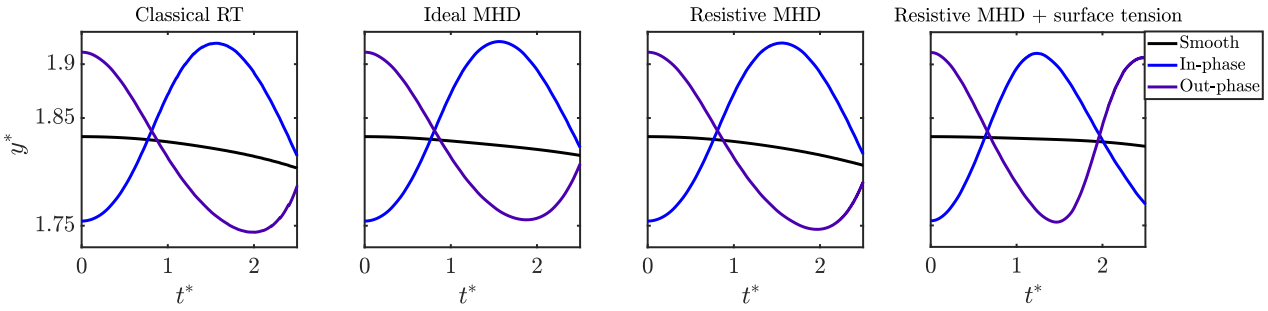

(a)

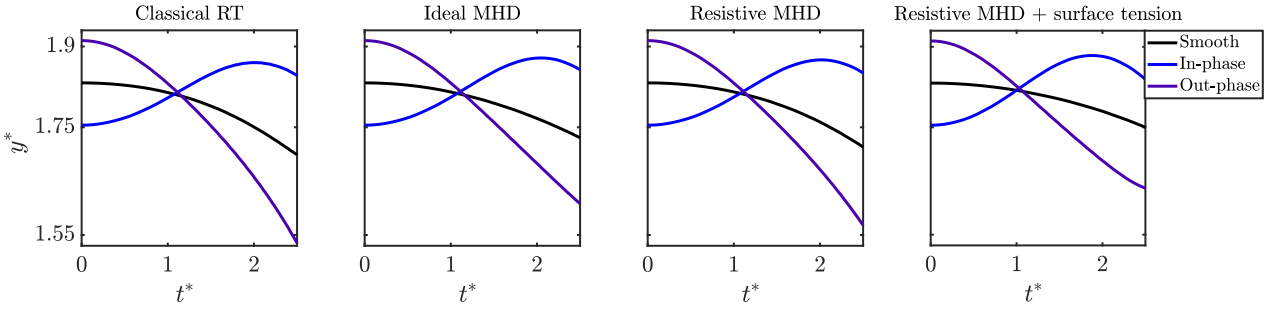

(b)

Figure 4.6: Perturbation growth at the upper interface for four cases: classical RT, ideal MHD, resistive MHD, and resistive MHD in the presence of surface tension, from left to right, respectively, with a wavenumber of (a) $k^* = 4/\pi$ and (b) $k^* = 2/\pi$.

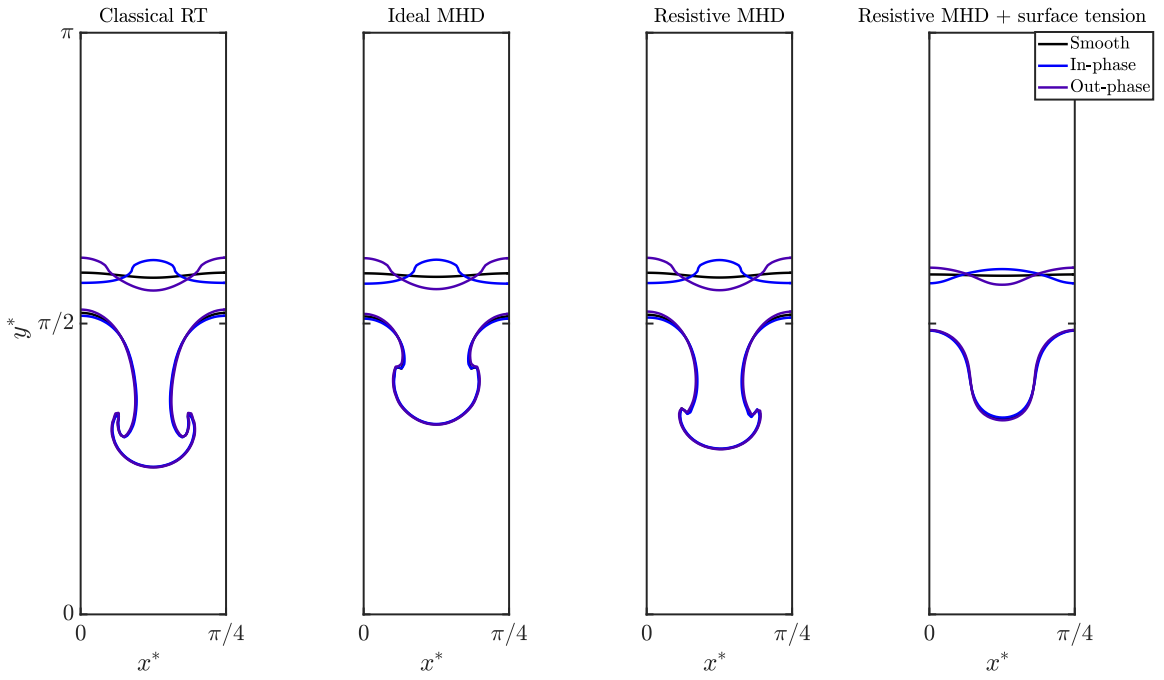

(a)

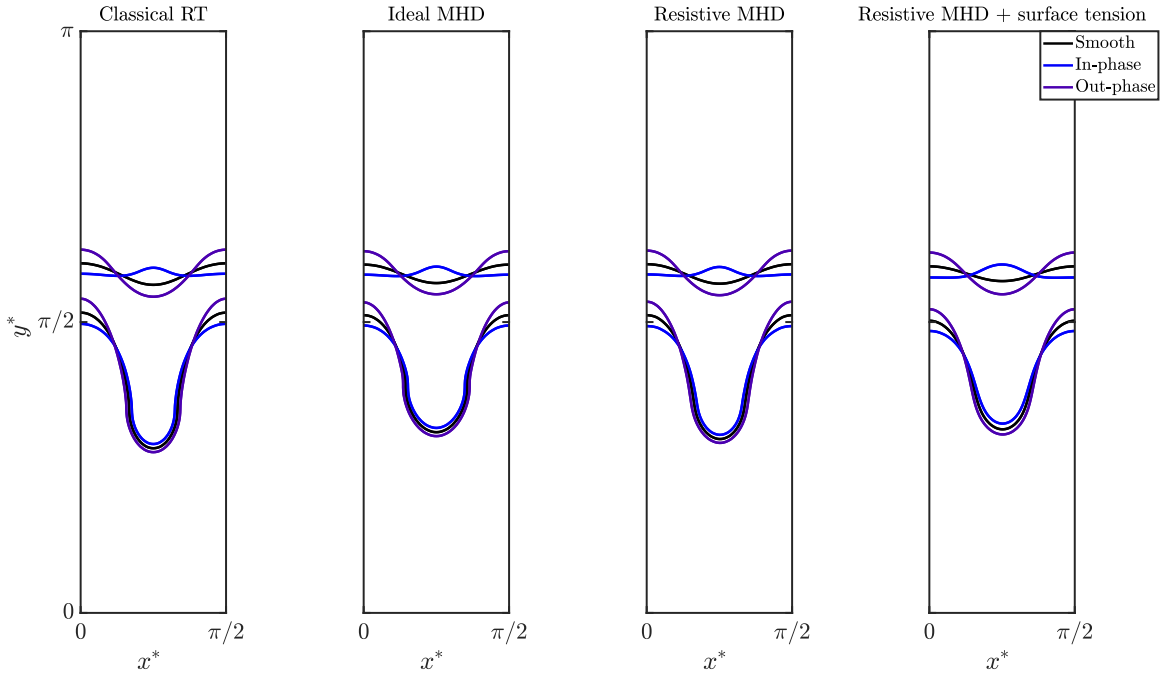

(b)

Figure 4.7: Liquid-metal liner interface at $t^* = 1.75$ for four cases: classical RT, ideal MHD, resistive MHD, and resistive MHD in the presence of surface tension, from left to right, respectively, with a wavenumber of (a) $k^* = 4/\pi$ and (b) $k^* = 2/\pi$.

CHAPTER 5

Conclusion

This chapter offers a summary of the research findings and conclusions, followed by an overview of the original contributions and suggestions for further expanding the present study.

5.1 Summary and main contributions

In this dissertation, a numerical campaign was conducted to investigate the MRT instability growth in a slab of liquid metal of finite thickness that is initally free of an internal magnetic field. A brief summary of the findings is provided below.

Two-phase solver for magnetic flows

The detailed implementation of a two-phase incompressible solver for magnetic fluids is presented in Chapter 2. In the initial stage of numerical development, a second-order two-phase incompressible solver initially designed for the hydrodynamic case was extended to accommodate magnetic flows. The proposed numerical solver coupled the Navier–Stokes equations with Maxwell's equations under the magnetostatic assumption. This two-phase solver utilized a conservative level set method within a finite-difference framework. Verification of the performance and mass conservation of the level set solver was performed through several test cases. The accuracy and robustness of the implemented two-phase solver for magnetic flows were thoroughly examined using different benchmarks, including studies on

ferrofluid deformation in quiescent and sheared flow regimes and RT instability growth in magnetic fluids. The solver exhibited excellent performance in handling various property jumps/discontinuities, such as density and magnetic permeability, across the interface separating the two fluids. Furthermore, the results demonstrated the capability of the numerical toolkit to properly model the interplay between the Lorentz force, capillary force, and inertial force at the interface across different magnetic field values.

Ferrofluid droplet

In Chapter 2, the abovementioned numerical solver was utilized to investigate the dynamics of a ferrofluid droplet in sheared flow, specifically exploring the effect of the magnetic susceptibility value of a droplet on its deformation. The results indicated that in low capillary regimes, increasing the magnetic susceptibility leads to a more pronounced deformation of the droplet with an increased inclination. The behaviour of the droplet was analyzed by studying the forces acting on its interface. In higher capillary flows, increasing the magnetic permeability ratio between the droplet and the surrounding medium resulted in a more notable rotation and elongation, potentially leading to droplet breakup based on the magnetic Bond number and susceptibility value.

Two-phase solver for ideal/resistive MHD flows

The numerical effort presented in Chapter 2 was extended and concluded in Chapter 3, where it was further developed to solve the full set of MHD equations. Consequently, a novel two-phase solver for incompressible MHD flows was introduced. Magnetic field components were defined in a staggered grid arrangement, and the divergence-free condition of the magnetic field was enforced through a projection scheme. Additionally, a dimensionless set of resistive MHD equations for two-phase flows is derived in this chapter, followed by a detailed description of the numerical discretization of the Lorentz force and the induction equation, taking into account the magnetic diffusivity jump across the interface.

MRT instability of a liquid-metal liner

Chapter 3 focused on the numerical investigation of MRT instability growth in a liquid-metal liner of finite thickness. In the studied problem, an initially magnetic-field-free liquid slab was assumed to be confined by two lower-density regions where a horizontal magnetic field was imposed in the lower layer. The results indicated that presence of the magnetic field stabilizes MRT instability growth, particularly for higher wavenumbers and smaller Alfvén numbers. Considering the finite resistivity of the liquid liner resulted in a higher instability growth compared to its ideal (i.e., perfectly conductive) counterpart. Magnetic diffusion primarily affected the MRT growth rate for higher wavenumbers, while for smaller wavenumbers, the effect of finite resistivity was only observed over a longer duration of instability development. Smaller Alfvén numbers resulted in an earlier appearance of magnetic tension effect on the instability growth. Additionally, greater electrical conductivity jumps across the liquid liner interface led to further deviation of MRT instability growth from the ideal MHD case. For the Bond numbers within the range of studied liner compression systems, the observed effect of surface tension was minimal. Finally, the feedthrough effect was observed to be smaller at higher wavenumbers and smaller Alfvén numbers, while increasing with decreasing magnetic Reynolds number.

Magnetic tension vs. magnetic diffusion

In Chapter 4, the behaviour of magnetic field lines in both ideal and resistive MHD cases was further studied across different wavenumbers. The magnetic peak compression during instability growth was shown to be greater for higher wavenumbers, resulting in a greater induced magnetic tension along the magnetic field lines. This increased magnetic tension for higher wavenumbers led to a more pronounced stabilizing effect for those wavenumbers. Transitioning from pure magnetic tension to the case where magnetic diffusion was also present, although an increase in magnetic field value was observed, the observed magnetic compression was less for all wavenumbers compared to the case where the liquid-metal liner was perfectly conductive. Lastly, the analysis highlighted the importance of the magnetic

diffusion mechanism and its adverse impact on plasma compression by comparing the peak magnetic compression values in ideal versus resistive MHD cases.

Interface coupling

The effect of initially seeded perturbations at the upper interface of the liner was studied in Chapter 4, specifically for two cases where the perturbations at the upper interface were out-of-phase and in-phase with respect to their lower counterparts. The results demonstrated that for higher wavenumbers, perturbations did not notably affect the MRT growth at the lower interface, while this effect was noticeable for lower wavenumbers. In the case of high wavenumbers, perturbation growth for both in-phase and out-of-phase scenarios seemed to be close, whereas for smaller wavenumbers, instability growth at the upper interface proved to be more pronounced in the out-of-phase scenario, which also led to increased MRT growth at the lower interface.

5.2 Recommendations for future work

This study aimed to address the research questions outlined in Chapter 1. While most of these questions have been addressed, there are other research questions worth examining in future studies. For instance, investigating the presence of a horizontal magnetic field in the upper layer to hinder instability growth due to the feedthrough effect could be potentially intriguing. Instability formation at the upper interface is undesirable in fusion applications, and using a magnetic field to dampen them presents a solution. Additionally, it is recommended to study the effect of a vertical or an inclined magnetic field on MRT instability growth and its impact on the RT instability morphology. These mentioned research questions have the potential to be addressed through the developed numerical solver in this dissertation.

This study mainly focused on the initial stages of instability growth, where the incompressibility assumption holds. However, in real fusion applications, during compression, large-amplitude acoustic and shock waves are generated, and the incompressibility assumption is no longer valid. Therefore, developing a two-phase compressible solver and exploring

the effect of compressibility on perturbation growth is a direction for future research. Additionally, in many fusion applications, convergence in cylindrical or spherical geometries is used to bring the plasma to fusion conditions. Thus, investigating the effect of convergence on MRT instability growth is an important research question to address.

Lastly, extending the implemented numerical solver to three dimensions and investigating its accuracy and robustness could be of interest. Improving code performance and CPU time by integrating implicit schemes could be avenues for further exploration. These suggestions for future work enhance the solver's suitability for studying problems involving complicated geometries, small Alfvén numbers, or small magnetic diffusion time scales.

References

Afkhami, S., Renardy, Y., Renardy, M., Riffle, J. S. & Pierre, T. St. 2008 Field-induced motion of ferrofluid droplets through immiscible viscous media. *Journal of Fluid Mechanics* **610**, 363–380.

Afkhami, S., Tyler, A. J., Renardy, Y., Renardy, M., Pierre, T. G. St., Woodward, R. C. & Riffle, J. S. 2010 Deformation of a hydrophobic ferrofluid droplet suspended in a viscous medium under uniform magnetic fields. *Journal of Fluid Mechanics* **663**, 358–384.

Avital, E., Suponitsky, V., Khalzov, I., Zimmermann, J. & Plant, D. 2020 On the hydrodynamic stability of an imploding rotating circular cylindrical liquid liner. *Fluid Dynamics Research* **52(5)**, 055505–055532.

Awasthi, M. K. 2014 Viscous potential flow analysis of magnetohydrodynamic Rayleigh–Taylor instability with heat and mass transfer. *International Journal of Dynamics and Control* **2**, 254–261.

Bacri, J.-C. & Salin, D. 1982 Instability of ferrofluid magnetic drops under magnetic field. *Journal de Physique Lettres* **43** (17), 649–654.

Bacri, J.-C., Salin, D. & Massart, R. 1982 Study of the deformation of ferrofluid droplets in a magnetic field. *Journal de Physique Lettres* **43** (6), 179–184.

Balay, S., Gropp, W. D., McInnes, L. C. & Smith, B. F. 1997 Efficient management of parallelism in object oriented numerical software libraries. In *Modern Software Tools in Scientific Computing* (ed. E. Arge, A. M. Bruaset & H. P. Langtangen), pp. 163–202. Birkhäuser Press.

Barbeau, Z., Raman, K., Manuel, M., Nagel, S. & Shivamoggi, B. 2022 Design of a high energy density experiment to measure the suppression of hydrodynamic instability in an applied magnetic field. *Physics of Plasmas* **29** (1), 012306.

Bera, R. K., Song, Y. & Srinivasan, B. 2022 The effect of viscosity and resistivity on Rayleigh–Taylor instability induced mixing in magnetized high-energy-density plasmas. *Journal of Plasma Physics* **88** (2), 905880209.

Betti, R. 2014 Magnetic fields lock in the heat for fusion. *Physics* **7**, 105.

Bijarchi, M. A., Favakeh, A., Alborzi, S. & Shafii, M. B. 2021 Experimental investigation of on-demand ferrofluid droplet generation in microfluidics using a pulse-width modulation magnetic field with proposed correlation. *Sensors and Actuators B: Chemical* **329**, 129274.

Bijarchi, M. A. & Shafii, M. B. 2020 Experimental investigation on the dynamics of on-demand ferrofluid drop formation under a pulse-width-modulated nonuniform magnetic field. *Langmuir* **36** (26), 7724–7740.

Boniou, V., Schmitt, T. & Vié, A. 2022 Comparison of interface capturing methods for the simulation of two-phase flow in a unified low-Mach framework. *International Journal of Multiphase Flow* **149**, 103957.

Book, D. L. & Turchi, P. J. 1979 Dynamics of rotationally stabilized implosions of compressible cylindrical liquid shells. *Physics of Fluids* **22** (1), 68–78.

Book, D. L. & Winsor, N. K. 1974 Rotational stabilization of a metallic liner. *Physics of Fluids* **17** (3), 662–663.

Boyd, T. J. M. & Sanderson, J. J. 2003 *The physics of plasmas*. Cambridge University Press.

Brackbill, J. U. & Barnes, D. C. 1980 The effect of nonzero $\nabla \cdot B$ on the numerical solution of the magnetohydrodynamic equations. *Journal of Computational Physics* **35** (3), 426–430.

Brackbill, J. U., Kothe, D. B. & Zemach, C. 1992 A continuum method for modeling surface tension. *Journal of Computational Physics* **100** (2), 335–354.

Brennan, D., Froese, A., Reynolds, M., Barsky, S., Wang, Z., Delage, M. & Laberge, M. 2020 Stable compression of a spherical tokamak plasma. *Nuclear Fusion* **60** (4), 046027.

Brunelli, B. 2013 *Unconventional approaches to fusion*. Springer Science & Business Media.

Bussmann, M., Kothe, D. B. & Sicilian, J. M. 2002 Modeling high density ratio incompressible interfacial flows. In *Fluids Engineering Division Summer Meeting*, pp. 707–713.

Cao, J., Wu, Z., Ren, H. & Li, D. 2009 Richtmyer–Meshkov instability of a stratified fluid in transverse magnetic field. *Physics of Plasmas* **16** (6).

Chacón, L., Knoll, D. A. & Finn, J. M. 2002 An implicit, nonlinear reduced resistive MHD solver. *Journal of Computational Physics* **178** (1), 15–36.

Chandrasekhar, S. 1981 *Hydrodynamic and Hydromagnetic Stability*. Courier Corporation.

Chen, D., Tong, X., Xie, B., Xiao, F. & Li, Y. 2023 An accurate and efficient multiphase solver based on THINC scheme and adaptive mesh refinement. *International Journal of Multiphase Flow* **162**, 104409.

Chittenden, J. P. & Jennings, C. A. 2008 Development of instabilities in wire-array Z pinches. *Physcal Review Letter* **101**, 055005.

Chorin, A. J. 1997 A numerical method for solving incompressible viscous flow problems. *Journal of Computational Physics* **135** (2), 118–125.

Clift, R., Grace, J. R. & Weber, M. E. 2005 *Bubbles, Drops, and Particles*. Courier Corporation.

Cui, X., Habashi, W. G. & Casseau, V. 2021 Multiphase SPH modelling of supercooled large droplets freezing on aircraft surfaces. *International Journal of Computational Fluid Dynamics* **35** (1-2), 79–92.

Cunha, L. H. P., Siqueira, I. R., Oliveira, T. F. & Ceniceros, H. D. 2018 Field-induced control of ferrofluid emulsion rheology and droplet break-up in shear flows. *Physics of Fluids* **30** (12).

Davidson, P. A. 2001 *An Introduction to Magnetohydrodynamics*. Cambridge University Press.

Davison, H. W. 1968 *Compilation of thermophysical properties of liquid lithium*. National Aeronautics and Space Administration.

Desjardins, O., Blanquart, G., Balarac, G. & Pitsch, H. 2008*a* High order conservative finite difference scheme for variable density low mach number turbulent flows. *Journal of Computational Physics* **227** (15), 7125–7159.

Desjardins, O., Moureau, V. & Pitsch, H. 2008*b* An accurate conservative level set/ghost fluid method for simulating turbulent atomization. *Journal of Computational Physics* **227**, 8395–8416.

Desjardins, O. & Pitsch, H. 2009 A spectrally refined interface approach for simulating multiphase flows. *Journal of Computational Physics* **228** (5), 1658–1677.

Ding, H., Spelt, P. D. & Shu, C. 2007 Diffuse interface model for incompressible two-phase flows with large density ratios. *Journal of Computational Physics* **226** (2), 2078–2095.

El-Dib, Y. O. 1994 Nonlinear hydrodynamic Rayleigh–Taylor instability of viscous magnetic fluids: effect of a tangential magnetic field. *Journal of Plasma Physics* **51** (1), 1–11.

Enright, D., Fedkiw, R., Ferziger, J. & Mitchell, I. 2002 A hybrid particle level set method for improved interface capturing. *Journal of Computational Physics* **183** (1), 83–116.

Fedkiw, R. P., Aslam, T., Merriman, B. & Osher, S. 1999 A non-oscillatory Eulerian approach to interfaces in multimaterial flows (the ghost fluid method). *Journal of Computational Physics* **152** (2), 457–492.

Finster, M., Chaves, H. & Schwarze, R. 2023 Numerical simulation of the accumulation process in modulated liquid jets of defined volume using the volume-of-fluid methodology. *International Journal of Multiphase Flow* **160**, 104356.

Fonty, T., Ferrand, M., Leroy, A., Joly, A. & Violeau, D. 2019 Mixture model for two-phase flows with high density ratios: A conservative and realizable SPH formulation. *International Journal of Multiphase Flow* **111**, 158–174.

Freidberg, J. P. 2014 *Ideal MHD*. Cambridge University Press.

Furth, H. P., Rutherford, P. H. & Selberg, H. 1973 Tearing mode in the cylindrical tokamak. *Physics of Fluids* **16** (7), 1054–1063.

Gao, D., Morley, N. B. & Dhir, V. 2004 Understanding magnetic field gradient effect from a liquid metal droplet movement. *Journal of Fluids Engineering* **126** (1), 120–124.

Gibou, F., Fedkiw, R. & Osher, S. 2018 A review of level-set methods and some recent applications. *Journal of Computational Physics* **353**, 82–109.

Glasser, A. H., Greene, J. M. & Johnson, J. L. 1975 Resistive instabilities in general toroidal plasma configurations. *Physics of Fluids* **18** (7), 875–888.

Glasser, A. H., Wang, Z. R. & Park, J.-K. 2016 Computation of resistive instabilities by matched asymptotic expansions. *Physics of Plasmas* **23** (11).

Gomes, R. B., Fernandes, H., Silva, C., Sarakovskis, A., Pereira, T., Figueiredo, J., Carvalho, B., Soares, A., Varandas, C., Lielausis, O. & others 2008 Interaction of a liquid gallium jet with the tokamak ISTTOK edge plasma. *Fusion Engineering and Design* **83** (1), 102–111.

Gomez, M. R., Slutz, S. A., Sefkow, A. B., Hahn, K. D., Hansen, S. B., Knapp, P. F., Schmit, P. F., Ruiz, C. L., Sinars, D. B., Harding, E. C. & others 2015

Demonstration of thermonuclear conditions in magnetized liner inertial fusion experiments. *Physics of Plasmas* **22** (5).

Gottlieb, S. & Shu, C.-W. 1998 Total variation diminishing Runge–Kutta schemes. *Mathematics of Computation* **67** (221), 73–85.

Guermond, J.-L. & Quartapelle, L. 2000 A projection FEM for variable density incompressible flows. *Journal of Computational Physics* **165** (1), 167–188.

Guido, S. & Villone, M. 1998 Three-dimensional shape of a drop under simple shear flow. *Journal of Rheology* **42** (2), 395–415.

Harris, E. G. 1962 Rayleigh–Taylor instabilities of a collapsing cylindrical shell in a magnetic field. *Physics of Fluids* **5** (9), 1057–1062.

Hassan, M. R. & Wang, C. 2019 Magnetic field induced ferrofluid droplet breakup in a simple shear flow at a low reynolds number. *Physics of Fluids* **31** (12).

Hassan, M. R., Zhang, J. & Wang, C. 2018 Deformation of a ferrofluid droplet in simple shear flows under uniform magnetic fields. *Physics of Fluids* **30** (9).

Hassanein, A., Allain, J. P., Insepov, Z. & Konkashbaev, I. 2005 Plasma/liquid-metal interactions during tokamak operation. *Fusion Science and Technology* **47** (3), 686–697.

Hassanein, A. & Konkashbaev, I. 1994 Erosion of plasma-facing materials during a tokamak disruption. *Nuclear Fusion* **5**, 193–224.

Herrmann, M. 2008 A balanced force refined level set grid method for two-phase flows on unstructured flow solver grids. *Journal of Computational Physics* **227** (4), 2674–2706.

Hester, J. J. 2008 The crab nebula: an astrophysical chimera. *Annual Review of Astronomy and Astrophysics* **46**, 127–155.

Hu, Y., Li, D. & Niu, X. 2018 Phase-field-based lattice Boltzmann model for multiphase ferrofluid flows. *Physical Review E* **98** (3), 033301.

Huang, H., Ying, A. & Abdou, M. 2002 3D MHD free surface fluid flow simulation based on magnetic-field induction equations. *Fusion Engineering and Design* **63**, 361–368.

Huang, Z., Lin, G. & Ardekani, A. M. 2019 A mixed upwind/central WENO scheme for incompressible two-phase flows. *Journal of Computational Physics* **387**, 455–480.

Huang, Z., Lin, G. & Ardekani, A. M. 2020 Consistent, essentially conservative and balanced-force phase-field method to model incompressible two-phase flows. *Journal of Computational Physics* **406**, 109192.

Huneault, J., Plant, D. & Higgins, A. J. 2019 Rotational stabilisation of the Rayleigh–Taylor instability at the inner surface of an imploding liquid shell. *Journal of Fluid Mechanics* **873**, 531–567.

Itoh, Y. & FUJII-E, Y. 1979 Dynamic stabilization of imploding liquid metal liner. *Journal of Nuclear Science and Technology* **16** (3), 175–189.

Itoh, Y. & FUJII-E, Y. 1980 Pressure wave propagation in an imploding liquid metal liner. *Journal of Nuclear Science and Technology* **17** (11), 801–810.

Itoh, Y., Kanagawa, T., Miyazaki, K. & FUJII-E, Y. 1982 Cavitation in cylindrical liquid metal shell imploded for axial magnetic flux compression. *Journal of Nuclear Science and Technology* **19** (1), 1–10.

Janka, H.-T. 2012 Explosion mechanisms of core-collapse supernovae. *Annual Review of Nuclear and Particle Science* **62**, 407–451.

Jesus, W. C., Roma, A. M. & Ceniceros, H. D. 2018 Deformation of a sheared magnetic droplet in a viscous fluid. *Communications in Computational Physics* **24** (2), 332–355.

Jiang, G.-S. & Shu, C.-W. 1996 Efficient implementation of weighted ENO schemes. *Journal of Computational Physics* **126** (1), 202–228.

Jiang, G.-S. & Wu, C.-C. 1999 A high-order WENO finite difference scheme for the equations of ideal magnetohydrodynamics. *Journal of Computational Physics* **150** (2), 561–594.

Jukes, J. D. 1963 On the Rayleigh–Taylor problem in magneto-hydrodynamics with finite resistivity. *Journal of Fluid Mechanics* **16** (2), 177–186.

Kennedy, M. R., Pozrikidis, C. & Skalak, R. 1994 Motion and deformation of liquid drops, and the rheology of dilute emulsions in simple shear flow. *Computers & fluids* **23** (2), 251–278.

Kerner, W., Goedbloed, J. P., Huysmans, G. T. A., Poedts, S. & Schwarz, E. 1998 Castor: Normal-mode analysis of resistive MHD plasmas. *Journal of Computational Physics* **142** (2), 271–303.

Kim, J. & Moin, P. 1985 Application of a fractional-step method to incompressible Navier–Stokes equations. *Journal of Computational Physics* **59** (2), 308–323.

Kruskal, M. D. & Schwarzschild, M. 1954 Some instabilities of a completely ionized plasma. *Proceedings of the Royal Society of London. Series A. Mathematical and Physical Sciences* **223** (1154), 348–360.

Kumikov, V. K. 1983 The measurement of the surface tension of some pure metals in the solid state. *Materials Science and Engineering* **60** (3), L23–L24.

Laberge, M. 2008 An acoustically driven magnetized target fusion reactor. *Journal of Fusion Energy* **27** (1-2), 65–68.

Laberge, M. 2019 Magnetized target fusion with a spherical tokamak. *Journal of Fusion Energy* **38** (1), 199–203.

Lai, B., Ke, Z., Wang, Z., Zhu, R., Gao, R., Mao, Y. & Zhang, Y. 2023 A lattice Boltzmann front-tracking interface capturing method based on neural network for gas-liquid two-phase flow. *International Journal of Computational Fluid Dynamics* **37** (1), 49–66.

Lau, Y. Y., Zier, J. C., Rittersdorf, I. M., Weis, M. R. & Gilgenbach, R. M. 2011 Anisotropy and feedthrough in magneto-Rayleigh–Taylor instability. *Physical Review E* **83** (6), 066405.

Lawson, J. D. 1957 Some criteria for a power producing thermonuclear reactor. *Proceedings of the Physical Society. Section B* **70** (1), 6.

Li, X., Dong, Z. Q., Li, Y., Wang, L. P., Niu, X. D., Yamaguchi, H., Li, D. C. & Yu, P. 2022 A fractional-step lattice Boltzmann method for multiphase flows with complex interfacial behaviour and large density contrast. *International Journal of Multiphase Flow* **149**, 103982.

Li, X., Yu, P., Niu, X.-D., Li, D.-C. & Yamaguchi, H. 2021 A magnetic field coupling lattice boltzmann model and its application on the merging process of multiple-ferrofluid-droplet system. *Applied Mathematics and Computation* **393**, 125769.

Linhart, J. G. 1961 Dynamic stability of a conducting, cylindrical shell in a magnetic field. *Journal of Applied Physics* **32** (3), 500–505.

Liu, X.-D., Osher, S. & Chan, T. 1994 Weighted essentially non-oscillatory schemes. *Journal of Computational Physics* **115** (1), 200–212.

Majidi, M., Bijarchi, M. A., Arani, A. G., Rahimian, M. H. & Shafii, M. B. 2022 Magnetic field-induced control of a compound ferrofluid droplet deformation and breakup in shear flow using a hybrid lattice boltzmann-finite difference method. *International Journal of Multiphase Flow* **146**, 103846.

Makaremi-Esfarjani, P. & Higgins, A. J. 2024 Magneto-Rayleigh–Taylor instability and feedthrough in a resistive liquid-metal liner of finite thickness. *Physics of Fluids* **36** (8).

Makaremi-Esfarjani, P., Higgins, A. J. & Najafi-Yazdi, A. 2023 A level set-based solver for two-phase incompressible flows: Extension to magnetic fluids. *International Journal of Computational Fluid Dynamics* **37** (7), 565–606.

Makaremi-Esfarjani, P. & Najafi-Yazdi, A. 2022 Characteristic boundary conditions for magnetohydrodynamic equations. *Computers & Fluids* **241**, 105461.

Manuel, M. J.-E., Khiar, B., Rigon, G., Albertazzi, B., Klein, S. R., Kroll, F., Brack, F.-E., Michel, T., Mabey, P., Pikuz, S. & others 2021 On the study of hydrodynamic instabilities in the presence of background magnetic fields in high-energy-density plasmas. *Matter and Radiation at Extremes* **6** (2).

Mefford, O. T., Woodward, R. C., Goff, J. DJ, Vadala, T. P., Pierre, T. G. St., Dailey, J. P. & Riffle, J. S. 2007 Field-induced motion of ferrofluids through immiscible viscous media: Testbed for restorative treatment of retinal detachment. *Journal of Magnetism and Magnetic Materials* **311** (1), 347–353.

Meng, W., Liao, L., Chen, M., Yu, C.-H., Li, J. & An, R. 2022 An enhanced CLSVOF method with an algebraic second-reconstruction step for simulating incompressible two-phase flows. *International Journal of Multiphase Flow* **154**, 104151.

Meshkov, E. E. 1969 Instability of the interface of two gases accelerated by a shock wave. *Fluid Dynamics* **4** (5), 101–104.

Mikaelian, K. O. 1982 Rayleigh–Taylor instabilities in stratified fluids. *Physical Review A* **26** (4), 2140.

Mikaelian, K. O. 1985 Richtmyer–Meshkov instabilities in stratified fluids. *Physical Review A* **31** (1), 410.

Mikaelian, K. O. 1990 Rayleigh–Taylor and Richtmyer–Meshkov instabilities in multilayer fluids with surface tension. *Physical Review A* **42** (12), 7211.

Mikaelian, K. O. 1995 Rayleigh–Taylor and Richtmyer–Meshkov instabilities in finite-thickness fluid layers. *Physics of Fluids* **7** (4), 888–890.

Miller, R. L. & Krakowski, R. A. 1980 Assessment of the slowly-imploding liner (LINUS) fusion reactor concept. *Tech. Rep.* LA-UR-80-3071; CONF-801011-55. Los Alamos National Lab. (LANL), Los Alamos, NM (United States).

Mirjalili, S., Jain, S. S. & Dodd, M. 2017 Interface-capturing methods for two-phase flows: An overview and recent developments. *Center for Turbulence Research Annual Research Briefs* **2017** (117-135), 13.

Mizuno, K., Asahara, M., Kamiya, T. & Miyasaka, T. 2022 Finite difference and reinitialization methods with level set to interfacial area transport equations for gas–liquid two-phase flows. *International Journal of Computational Fluid Dynamics* **36** (5), 361–383.

Morinishi, Y., Lund, T. S., Vasilyev, O. V. & Moin, P. 1998 Fully conservative higher order finite difference schemes for incompressible flow. *Journal of Computational Physics* **143** (1), 90–124.

Nourgaliev, R. R. & Theofanous, T. G. 2007 High-fidelity interface tracking in compressible flows: Unlimited anchored adaptive level set. *Journal of Computational Physics* **224** (2), 836–866.

Olsson, E. & Kreiss, G. 2005 A conservative level set method for two phase flow. *Journal of Computational Physics* **210** (1), 225–246.

Olsson, E., Kreiss, G. & Zahedi, S. 2007 A conservative level set method for two phase flow II. *Journal of Computational Physics* **225** (1), 785–807.

Pardo, R. M., Barua, N., Lisak, D. & Nedić, J. 2022 Jetting onset on a liquid surface accelerated past a submerged cylinder. *Flow* **2**, E36.

Pierce, C. D. 2001 Progress-variable approach for large-eddy simulation of turbulent combustion. PhD thesis, Stanford University.

Piriz, A. R., Cortazar, O. D., Lopez Cela, J. J. & Tahir, N. A. 2006 The Rayleigh–Taylor instability. *American Journal of Physics* **74** (12), 1095–1098.

Piriz, S. A., Piriz, A. R. & Tahir, N. A. 2018 Magneto-Rayleigh–Taylor instability in an elastic-medium slab. *Physics of Fluids* **30** (11).

Popinet, S. 2018 Numerical models of surface tension. *Annual Review of Fluid Mechanics* **50**, 49–75.

Prosperetti, A. 1981 Motion of two superposed viscous fluids. *Physics of Fluids* **24** (7), 1217–1223.

Prosperetti, A. & Tryggvason, G. 2009 *Computational Methods for Multiphase Flow*. Cambridge University Press.

Radman, S., Fiorina, C. & Pautz, A. 2021 Development of a novel two-phase flow solver for nuclear reactor analysis: algorithms, verification and implementation in OpenFOAM. *Nuclear Engineering and Design* **379**, 111178.

Rayleigh, L. 1882 Investigation of the character of the equilibrium of an incompressible heavy fluid of variable density. *Proceedings of the London Mathematical Society* **14** (1), 170–177.

Richtmyer, R. D. 1960 Taylor instability in shock acceleration of compressible fluids. *Communications on Pure and Applied Mathematics* **13** (2), 297–319.

Robson, A. E. 1975 Plasma confinement by megagauss magnetic fields. *Annals of the New York Academy of Sciences* **251**, 649–664.

Rosensweig, R. E. 2013 *Ferrohydrodynamics*. Courier Corporation.

Samulski, C., Srinivasan, B., Manuel, M. J.-E., Masti, R., Sauppe, J. P. & Kline, J. 2022 Deceleration-stage Rayleigh–Taylor growth in a background magnetic field studied in cylindrical and cartesian geometries. *Matter and Radiation at Extremes* **7** (2), 026902.

Scardovelli, R. & Zaleski, S. 1999 Direct numerical simulation of free-surface and interfacial flow. *Annual Review of Fluid Mechanics* **31** (1), 567–603.

Sefkow, A. B., Slutz, S. A., Koning, J. M., Marinak, M. M., Peterson, K. J., Sinars, D. B. & Vesey, R. A. 2014 Design of magnetized liner inertial fusion experiments using the Z facility. *Physics of Plasmas* **21** (7).

Seropian, G., Rust, A. C. & Sparks, R. S. J. 2018 The gravitational stability of lenses in magma mushes: Confined Rayleigh–Taylor instabilities. *Journal of Geophysical Research: Solid Earth* **123** (5), 3593–3607.

Sethian, J. A. 1999 *Level Set Methods and Fast Marching Methods: Evolving Interfaces in Computational Geometry, Fluid Mechanics, Computer Vision, and Materials Science*. Cambridge University Press.

Siemon, R. E., Lindemuth, I. R. & Schoenberg, K. F. 1999 Why magnetized target fusion offers a low-cost development path for fusion energy. *Comments on Plasma Physics and Controlled Fusion* **18** (6), 363–386.

Slutz, S. A., Herrmann, M. C., Vesey, R. A., Sefkow, A. B., Sinars, D. B., Rovang, D. C., Peterson, K. J. & Cuneo, M. E. 2010 Pulsed-power-driven cylindrical liner implosions of laser preheated fuel magnetized with an axial field. *Physics of Plasmas* **17** (5).

Song, Y. & Srinivasan, B. 2020 A survey of the effects of magnetic fields, resistivity, viscosity and thermal conduction on the Rayleigh–Taylor instability. *Radiation Effects and Defects in Solids* **175** (11-12), 1009–1014.

Su, Y. & Kim, S. H. 2018 An improved consistent, conservative, non-oscillatory and high order finite difference scheme for variable density low Mach number turbulent flow simulation. *Journal of Computational Physics* **372**, 202–219.

Sun, Y. B., Gou, J. N., Cao, C. Y., Wang, C. & Zeng, R. H. 2023 Rayleigh–Taylor instability in magnetohydrodynamics with finite resistivity in a horizontal magnetic field. *Physical Review E* **108** (6), 065208.

Sun, Y. B., Gou, J. N. & Zeng, R. H. 2022 Rayleigh–Taylor and Richtmyer–Meshkov instabilities in the presence of an inclined magnetic field. *Physics of Plasmas* **29** (7).

Suponitsky, V., Froese, A. & Barsky, S. 2014 Richtmyer–Meshkov instability of a liquid-gas interface driven by a cylindrical imploding pressure wave. *Computers & Fluids* **89**, 1–19.

Sussman, M. & Puckett, E. G. 2000 A coupled level set and volume-of-fluid method for computing 3D and axisymmetric incompressible two-phase flows. *Journal of Computational Physics* **162** (2), 301–337.

Sussman, M., Smereka, P. & Osher, S. 1994 A level set approach for computing solutions to incompressible two-phase flow. *Journal of Computational Physics* **114** (1), 146–159.

Tagawa, T. 2006 Numerical simulation of two-phase flows in the presence of a magnetic field. *Mathematics and Computers in Simulation* **72** (2-6), 212–219.

Taylor, G. I. 1932 The viscosity of a fluid containing small drops of another fluid. *Proceedings of the Royal Society of London. Series A, Containing Papers of a Mathematical and Physical Character* **138** (834), 41–48.

Taylor, G. I. 1934 The formation of emulsions in definable fields of flow. *Proceedings of the Royal Society of London. Series A, Containing Papers of a Mathematical and Physical Character* **146** (858), 501–523.

Taylor, G. I. 1950 The instability of liquid surfaces when accelerated in a direction perpendicular to their planes. I. *Proceedings of the Royal Society of London. Series A. Mathematical and Physical Sciences* **201** (1065), 192–196.

Tolias, P. 2022 Analytical expressions for thermophysical properties of solid and liquid beryllium relevant for fusion applications. *Nuclear Materials and Energy* **31**, 101195.

Tóth, G. 2000 The $\nabla \cdot B = 0$ constraint in shock-capturing magnetohydrodynamics codes. *Journal of Computational Physics* **161** (2), 605–652.

Tryggvason, G., Scardovelli, R. & Zaleski, S. 2011 *Direct Numerical Simulations of Gas-Liquid Multiphase Flows*. Cambridge University Press.

Turchi, P. J. 2008 Imploding liner compression of plasma: Concepts and issues. *IEEE Transactions on Plasma Science* **36** (1), 52–61.

Turchi, P. J., Cooper, A. L., Ford, R. & Jenkins, D. J. 1976 Rotational stabilization of an imploding liquid cylinder. *Physical Review Letters* **36** (26), 1546.

Turchi, P. J., Cooper, A. L., Ford, R. D., Jenkins, D. J. & Burton, R. L. 1980 Review of the NRL liner implosion program. *Megagauss Physics and Technology* pp. 375–386.

Unverdi, S. O. & Tryggvason, G. 1992 A front-tracking method for viscous, incompressible, multi-fluid flows. *Journal of Computational Physics* **100** (1), 25–37.

Velikovich, A. L., Cochran, F. L. & Davis, J. 1996 Suppression of Rayleigh–Taylor instability in Z-pinch loads with tailored density profiles. *Physical Review Letters* **77** (5), 853.

Velikovich, A. L. & Schmit, P. F. 2015 Bell–Plesset effects in Rayleigh–Taylor instability of finite-thickness spherical and cylindrical shells. *Physics of Plasmas* **22** (12), 122711.

Voltairas, P. A., Fotiadis, D. I. & Massalas, C. V. 2001 Elastic stability of silicone ferrofluid internal tamponade (SFIT) in retinal detachment surgery. *Journal of Magnetism and Magnetic Materials* **225** (1-2), 248–255.

Walsh, C. A. 2022 Magnetized ablative Rayleigh–Taylor instability in three dimensions. *Physical Review E* **105** (2), 025206.

Wang, L., Ye, W., He, X., Wu, J., Fan, Z., Xue, C., Guo, H., Miao, W., Yuan, Y., Dong, J. & others 2017 Theoretical and simulation research of hydrodynamic instabilities in inertial-confinement fusion implosions. *SCIENCE CHINA Physics, Mechanics & Astronomy* **60**, 1–35.

Wang, L. F., Wu, J. F., Guo, H. Y., Ye, W. H., Liu, J., Zhang, W. Y. & He, X. T. 2015 Weakly nonlinear Bell–Plesset effects for a uniformly converging cylinder. *Physics of Plasmas* **22** (8), 082702.

Weis, M. R. 2015 Magneto-Rayleigh–Taylor instability: Theory and simulation in planar and cylindrical pulsed power targets. PhD thesis, University of Michigan.

Weis, M. R., Zhang, P., Lau, Y. Y., Rittersdorf, I. M., Zier, J. C., Gilgenbach, R. M., Hess, M. H. & Peterson, K. J. 2014 Temporal evolution of surface ripples on a finite plasma slab subject to the magneto-Rayleigh–Taylor instability. *Physics of Plasmas* **21** (12), 122708.

Wu, C.-C. 2007 A high order WENO finite difference scheme for incompressible fluids and magnetohydrodynamics. *Geophysical and Astrophysical Fluid Dynamics* **101** (1), 37–61.

Yang, F., Khodak, A. & Stone, H. A. 2019*a* The effects of a horizontal magnetic field on the Rayleigh–Taylor instability. *Nuclear Materials and Energy* **18**, 175–181.

Yang, J., Mao, S., He, X., Yang, X. & He, Y. 2019*b* A diffuse interface model and semi-implicit energy stable finite element method for two-phase magnetohydrodynamic flows. *Computer Methods in Applied Mechanics and Engineering* **356**, 435–464.

Zarei Saleh Abad, M., Ebrahimi-Dehshali, M., Bijarchi, M. A., Shafii, M. B. & Moosavi, A. 2019 Visualization of pool boiling heat transfer of magnetic nanofluid. *Heat Transfer—Asian Research* **48** (7), 2700–2713.

Zhou, Y., Williams, R. J. R., Ramaprabhu, P., Groom, M., Thornber, B., Hillier, A., Mostert, W., Rollin, B., Balachandar, S., Powell, P. D. & others 2021 Rayleigh–Taylor and Richtmyer–Meshkov instabilities: A journey through scales. *Physica D: Nonlinear Phenomena* **423**, 132838.